

**APPLICATIONS OF ACOUSTO-OPTIC DEMODULATION AND DECODING
TECHNIQUES**

by

MATTHEW GRAHAM HICKS

A thesis submitted to the University of Plymouth
in partial fulfilment for the degree of

DOCTOR OF PHILOSOPHY

School of Electronic, Communication and Electrical Engineering
Faculty of Technology

In collaboration with
DRA (Funtington)

LIBRARY STORE

APRIL 1997

MATTHEW GRAHAM HICKS

**APPLICATIONS OF ACOUSTO-OPTIC DEMODULATION AND DECODING
TECHNIQUES**

ABSTRACT

This thesis describes the operation and performance of an acousto-optic demodulator system consisting of a laser source, an acousto-optic cell and a bi-cell detector. The bi-cell detector is made up of two photodiodes positioned side by side, separated by a small gap. Theory is developed to predict the following; the linear operating range for different gap sizes, absolute frequency sensitivity, system output in response to discrete phase changes, optimum gap size for phase demodulation, absolute discrete phase change sensitivity, the performance of the system in the presence of carrier noise and the effect of clipping the carrier signal on both frequency and phase modulated signals. A detailed model of the system has been written, using the software package Mathcad, which incorporates all the parameters that affect the performance of the physical system. The model has been used to study how the performance of the system changes as these parameters are varied. It is shown that the AO demodulator can be used in a number of ways; as a frequency demodulator, a phase demodulator and to demodulate digitally modulated signals, and that the optimum values of some parameters are different for each application. The model is also used to investigate the response of the system to a number of the most common forms of digital modulation. It is shown that it is possible, without any a priori knowledge of the signal, to identify each of these forms of modulation, and ultimately decode messages contained on the signals. The system can also be used to measure the frequency shift on pulse doppler radar. It is shown that the rms frequency error on a pulse using the AO demodulator is 150% better than that of existing systems. Experimental results are presented that are in good agreement with the results gained from both the theoretical and modelled analysis of the system. Finally suggestions are made for areas of further work on the signal processing of the output signals and possible uses of the demodulator in the future.

ACKNOWLEDGEMENTS

The author would like to express his appreciation to the following people for their help and advice throughout this period of research and in the preparation of this thesis.

To Dr Kit Reeve of the University of Plymouth for his tremendous support and guidance in his role as supervisor.

To Warren Houghton for his guidance in modelling the system.

To Juliet Dunn-Rogers and Keith Youern at the Defence Research Agency, Funtington for the Research contract.

To Dan Spong and Michael Gildea for their friendship and distraction.

Finally to my parents, without whose support and encouragement I would not have been able to embark on this PhD.

TABLE OF CONTENTS

Abstract	i
Acknowledgements	ii
Table of contents	iii
Lists of diagrams and graphs	ix
Authors declaration	xii
1. INTRODUCTION	1
2. MODULATION TECHNIQUES	4
2.1 Angle modulation	4
2.2 FM demodulators	7
2.2.1 Amplitude limiting	7
2.2.2 Slope detection	7
2.2.3 Balanced slope detector	8
2.2.4 Phase discriminator	9
2.2.5 Ratio detector.	9
2.2.6 The phase locked loop	10
2.2.7 Digital Demodulators	10
2.3 Digital modulation	11
2.3.1 Frequency shift key (FSK)	11
2.3.2 Phase shift keying (PSK).	13
2.3.3 Differential PSK	14
2.3.4 Quaternary PSK	15
2.3.5 Offset QPSK	16
2.3.6 MSK	17
2.4 Applications of Demodulators	20
3. RADAR TECHNIQUES AND ELECTRONIC WARFARE	22
3.1 Radar	22
3.2 Radar / electronic warfare (EW) Introduction	24

3.2.1	Definitions	24
3.2.2	ESM	25
3.2.3	System components	27
3.2.4	The instantaneous frequency measurer (IFM)	29
4.	ACOUSTO-OPTICS	31
4.1	Theory	31
4.1.1	Particle analysis	32
4.1.2	Thin-phase grating approximation	34
4.1.3	Thick-phase grating approximation	36
4.1.4	Raman Nath mode	37
4.1.5	The Bragg Mode	39
4.1.6	Time Bandwidth product	40
4.2	Applications of acousto-optic devices	41
5.	ACOUSTO-OPTIC DEMODULATOR - SYSTEM DESCRIPTION	44
5.1	Component selection	46
5.1.1	The Laser source	46
5.1.2	The AO-cell	46
5.1.3	The detector assembly	47
5.2	Experimental Procedure	48
6.	THE COMPUTER SIMULATION	50
6.1	System components	50
6.1.1	Laser	50
6.1.2	AO-cell	50
6.1.3	Lens	51
6.1.4	Detector	51
6.2	Relevant equations used in the computer model	53
6.3	Implementation of the model	54
7.	FM SYSTEM ANALYSIS	61

7.1 Deflection measurement	61
7.2 The system linear range for FM.	62
7.3 Shot noise limited resolution for FM demodulation	68
7.3.1 Analysis for very small gap	69
7.3.2 Effect of a finite gap size	73
7.4 Effect of noise on an FM carrier signal	74
7.4.1 The effect of clipping on the spectrum of a noisy signal.	75
7.4.2 The optimum clipping level	77
7.4.3 System SNR loss	79
7.5 Summary and conclusions	81
8. PM SYSTEM ANALYSIS	83
8.1 Variation of output of bicell system for discrete phase shift	83
8.2 Optimum gap size for phase demodulation	87
8.3 Shot noise limited resolution for PM	89
8.3.1 Sum channel	89
8.3.2 Difference channel	91
8.4 The effect of clipping on PM	92
8.5 Summary and conclusions	94
9. SIMULATED RESULTS FROM THE MODEL	96
9.1 Digital phase modulation	96
9.1.1 Phase shift of π .	97
9.1.2 Phase shift of $\pi/2$	98
9.1.3 $\pm \pi/4$ and $\pm 3\pi/4$ phase shifts	99
9.1.4 Summary	100
9.2 Digital frequency modulated signals	101
9.2.1 Continuous Phase - Frequency Shift Keying (CP-FSK)	101
9.2.2 Frequency shift keying (FSK)	102
9.3 Practical Phase Shift Keying signals	103

9.3.1 Binary Phase Shift Keying (BPSK) / Differential phase shift keying (DPSK)	104
9.3.2 Quadrature phase shift keying (QPSK)	105
9.3.3 Offset quadrature phase shift keying (OQPSK)	106
9.4 Truth Table	107
9.5 Pulse Doppler measurement	108
9.6 AM noise analysis	111
9.7 System response to phase changes	112
10. EXPERIMENTAL RESULTS	115
10.1 Modulation transfer function	115
10.2 Phase transfer function	116
10.3 Digital modulation	117
10.3.1 Digital phase modulated signals	118
10.3.2 Digital frequency modulated signals	120
10.3.3 Practical Phase Shift Keying (PSK) signals	121
10.4 Shot noise limited frequency resolution	124
10.5 Shot noise limited phase resolution	127
10.6 Pulse Doppler measurement	128
11. CONCLUSIONS	129
11.1 FM AO demodulator	129
11.2 Phase modulation	130
11.3 Digital modulation	131
11.4 Future work	133
11.5 Overall conclusions	134
APPENDIX A.	136

1. Matched Filters	136
2. Carrier recovery in QPSK	138
3. Probability of error in transmission	139
4. Likelihood ratio	142
APPENDIX B. Optical Fourier transform	143
APPENDIX C. Mathcad files	146
1. The model	146
2. PSD file	152
3. Optimum gap size	154
4. Linearity of the MTF	158
5. MTF for different gap sizes	161
6. Calculating values for a_1 , a_2 , and a_3	163
7. Modelled phase transfer characteristic	165
APPENDIX D. RESPONSE TO BANDLIMITED NOISE	168
REFERENCES	174
BIBLIOGRAPHY	176
PAPERS	177

INDEX

190

Abbreviations

190

LIST OF DIAGRAMS AND GRAPHS

FIGURE 2.1 AMPLITUDE LIMITER	7
FIGURE 2.2 SLOPE DETECTOR	8
FIGURE 2.3 BALANCED SLOPE DETECTOR	8
FIGURE 2.4 PHASE DISCRIMINATOR	9
FIGURE 2.5 THE RATIO DETECTOR	10
FIGURE 2.6 BLOCK DIAGRAM OF A PHASE LOCKED LOOP	10
FIGURE 2.7 (A) THE MATCHED FILTER RECEIVER (B) THE CORRELATOR RECEIVER	12
FIGURE 2.8 PROBABILITY DENSITY FUNCTIONS FOR BINARY PSK WAVEFORMS.	12
FIGURE 2.9 A CORRELATION DETECTOR FOR ANTIPODAL SIGNALS	13
FIGURE 2.10 PROBABILITY DENSITY FUNCTION FOR PRK	14
FIGURE 2.11 SIMPLIFIED BLOCK DIAGRAM OF A QPSK DEMODULATOR.	15
FIGURE 2.12 EXCESS PHASE TRELLIS FOR MSK	17
FIGURE 2.13 MSK WAVEFORMS.	19
FIGURE 3.1 BLOCK DIAGRAM OF AN ESM SYSTEM	27
FIGURE 3.2 BLOCK DIAGRAM OF AN IFM SYSTEM	29
FIGURE 4.1 ACOUSTO-OPTIC CELL DIAGRAM.	32
FIGURE 4.2 THE MOMENTUM-CONSERVATION RELATION.	33
FIGURE 4.3 BESSEL FUNCTIONS OF ORDER 0, 1, AND 2.	38
FIGURE 4.4 ACOUSTO-OPTIC SCANNER	43
FIGURE 5.1 THE BI-CELL DETECTOR	45
FIGURE 5.2 BLOCK DIAGRAM OF THE DETECTOR SYSTEM.	47
FIGURE 5.3 EXPERIMENTAL SET-UP	49
FIGURE 6.1 FLOW CHART OF MATHEMATICAL MODEL	52
FIGURE 6.2 RESPONSE OF THE BANDPASS FILTER	55
FIGURE 6.3 10 μ S OF GENERATED NOISE	55
FIGURE 6.4 SPECTRUM OF UNFILTERED NOISE	56
FIGURE 6.5 1 μ S OF PSK MODULATION $f_c = 50$ MHZ	56
FIGURE 6.6 SPECTRUM OF UNFILTERED SIGNAL	56
FIGURE 6.7 UNFILTERED SIGNAL + NOISE WITH AN SNR OF 13DB	57
FIGURE 6.8 UN FILTERED AND UNCLIPPED SIGNAL + NOISE FREQUENCY SPECTRUM	57

FIGURE 6.9 BANDLIMITED SIGNAL + NOISE	58
FIGURE 6.10 BANDLIMITED SIGNAL + NOISE SPECTRUM	58
FIGURE 6.11 CLIPPED SIGNAL	58
FIGURE 6.12 GAUSSIAN BEAM	59
FIGURE 6.13 GAUSSIAN MULTIPLIED WITH SIGNAL	59
FIGURE 6.14 FOURIER TRANSFORM OF SIGNAL AND GAUSSIAN WINDOW	60
FIGURE 6.15 OUTPUT OF EACH BI-CELL	60
FIGURE 6.16 SUM AND DIFFERENCE OF THE BI-CELL OUTPUTS	60
FIGURE 7.1 DISPLACEMENT OF THE BEAM IN THE FOCAL PLANE OF A LENS	62
FIGURE 7.2 DEVIATION OF THE BEAM WITH RESPECT TO THE GAP SIZE	63
FIGURE 7.3 MODULATION TRANSFER FUNCTION FOR VARYING GAP SIZES	65
FIGURE 7.4 ERROR IN LINEAR APPROXIMATION TO MTF	67
FIGURE 7.5 BLOCK DIAGRAM OF BI-CELL DETECTOR	68
FIGURE 7.6 THE AFFECT OF INCREASING THE BEAMWIDTH IN THE AO CELL	72
FIGURE 7.7 SYSTEM RESOLUTION VERSUS DIFFRACTED LIGHT POWER	72
FIGURE 7.8 HOW THE ASSUMPTION FOR PDIFF COMPARES WITH ACTUAL VALUES	73
FIGURE 7.9 THE EFFECT OF CLIPPING ON THE FREQUENCY SPECTRUM OF SIGNALS	76
FIGURE 7.10 THE EFFECT OF CLIPPING ON THE OUTPUT SNR	77
FIGURE 7.11 HOW THE OPTIMUM CLIPPING LEVEL CHANGES WITH CNR_{IN}	78
FIGURE 7.12 HOW THE CLIPPING LEVEL IS AFFECTED BY δF .	78
FIGURE 7.13 GRAPH SHOWING HOW FIGURE 7.12 AFFECTS FIGURE 7.11.	79
FIGURE 7.14 EFFECT OF DIFFERENT CLIPPING LEVELS ON SNR_{OUT} AS SNR_{IN} VARIES	80
FIGURE 7.15 SNR LOSS VERSUS DEVIATION δF .	80
FIGURE 8.1 GAUSSIAN WINDOW FUNCTION FOR WL AND WR .	84
FIGURE 8.2 NUMERICAL SOLUTION OF EQUATION 8.16.	86
FIGURE 8.3 PSD OF THE GAUSSIAN FOR PHASE CHANGES OF $0, \pi/4, \pi/2, \pi$	87
FIGURE 8.4 PULSE AMPLITUDE VERSUS GAP SIZE.	88
FIGURE 8.5 GRAPH SHOWING $\Delta PSUM, PSUM(\phi),$ AND $PSUM(0)$.	89
FIGURE 8.6 OPTIMUM CLIPPING LEVEL VERSUS CNR_{IN}	93
FIGURE 8.7 OPTIMUM CLIPPING FOR THE SUM AND THE DIFFERENCE CHANNEL.	93
FIGURE 8.8 EFFECT OF DIFFERENT LEVELS OF CLIPPING SNR_{OUT} VERSUS SNR_{IN} .	94
FIGURE 9.1 BEAM SPECTRAL DENSITY IN RESPONSE TO BPSK INPUT SIGNAL.	97
FIGURE 9.2 RESPONSE TO π PSK INPUT, ON A 50 MHZ CARRIER FREQUENCY.	97
FIGURE 9.3 BEAM SPECTRAL DENSITY IN RESPONSE TO $+\pi/2$ INPUT SIGNAL.	98
FIGURE 9.4 BEAM SPECTRAL DENSITY IN RESPONSE TO $-\pi/2$ INPUT SIGNAL.	98

FIGURE 9.5 RESPONSE TO $+\pi/2$ AND $-\pi/2$ INPUT ON A 50 MHZ CARRIER FREQUENCY.	99
FIGURE 9.6 BEAM SPECTRAL DENSITY IN RESPONSE TO $-\pi/4$ INPUT SIGNAL.	99
FIGURE 9.7 BEAM SPECTRAL DENSITY IN RESPONSE TO $-3\pi/4$ INPUT SIGNAL.	100
FIGURE 9.8 A 50 MHZ CARRIER MODULATED BY $\pm\pi/4$ AND $\pm 3\pi/4$.	100
FIGURE 9.9 BEAM SPECTRAL DENSITY IN RESPONSE TO CP-FSK INPUT SIGNAL.	102
FIGURE 9.10 RESPONSE TO CP-FSK INPUT ON 50 MHZ CARRIER FREQUENCY.	102
FIGURE 9.11 BEAM SPECTRAL DENSITY IN RESPONSE TO FSK INPUT SIGNAL.	103
FIGURE 9.12 RESPONSE TO FSK INPUT ON 50 MHZ CARRIER FREQUENCY	103
FIGURE 9.13 SIMULATION RESULTS OF PHASE CHANGES USING π AND 0.	105
FIGURE 9.14 SIMULATION RESPONSE TO A QPSK SIGNAL	105
FIGURE 9.15 SIMULATION RESPONSE OF AN OQPSK SIGNAL	106
FIGURE 9.16 BEAM SPECTRAL DENSITY IN RESPONSE TO A 2 μ S PULSE OF A 50 MHZ	109
FIGURE 9.17 A 2 μ S PULSE OF A 50 MHZ	109
FIGURE 9.18 A 2 μ S PULSE OF A ± 50.01 MHZ	110
FIGURE 9.19 IMPROVEMENT IN RMS FREQUENCY ERROR FOR A 1 μ S PULSE	111
FIGURE 9.20 IMPROVEMENT IN RMS FREQUENCY ERROR FOR A 2 μ S PULSE	111
FIGURE 9.21 INPUT SIGNAL 50 MHZ, NO MODULATION, 10 MHZ AM NOISE.	112
FIGURE 9.22 SIMULATED PHASE RESPONSE OF THE DIFFERENCE CHANNEL.	113
FIGURE 9.23 SIMULATED PHASE RESPONSE OF THE SUM CHANNEL.	113
FIGURE 9.24 PHASE RESPONSE FOR THE DIFFERENCE CHANNEL.	113
FIGURE 9.25 PHASE RESPONSE FOR THE SUM CHANNEL.	114
FIGURE 10.1 MODULATION TRANSFER FUNCTION FOR VARYING GAP SIZES	116
FIGURE 10.2 EXPERIMENTAL VERIFICATION OF EQ. (8.16). (SUM)	117
FIGURE 10.3 EXPERIMENTAL VERIFICATION OF EQ. (8.16). (DIFF)	117
FIGURE 10.4 EXPERIMENTAL RESPONSE TO A π PHASE SHIFT	118
FIGURE 10.5 EXPERIMENTAL RESPONSE TO PHASE SHIFTS OF $\pm\pi/2$	119
FIGURE 10.6 EXPERIMENTAL RESPONSE TO $\pm \pi/4, \pm 3\pi/4$ PHASE SHIFTS	119
FIGURE 10.7 EXPERIMENTAL RESPONSE TO A CP-FSK SIGNAL	120
FIGURE 10.8 EXPERIMENTAL RESPONSE TO AN FSK SIGNAL	121
FIGURE 10.9 EXPERIMENTAL RESPONSE TO A BPSK SIGNAL	122
FIGURE 10.10 EXPERIMENTAL RESPONSE TO A QPSK SIGNAL	123
FIGURE 10.11 EXPERIMENTAL RESPONSE TO AN OQPSK SIGNAL	124
FIGURE 10.12 1 KHZ SIN WAVE WITH VARIOUS DEVIATIONS	125
FIGURE 10.13 SHOT NOISE LIMITED FSK SIGNAL FOR VARIOUS DEVIATIONS	126
FIGURE 10.14 EXPERIMENTAL RESPONSE TO VARIOUS PHASE SHIFTS	127
FIGURE 10.15 EXPERIMENTAL RESPONSE TO VARIOUS PHASE SHIFTS	128
FIGURE 10.16 5 μ S PULSES OF 45 MHZ ± 10 KHZ SIGNAL SEPARATED BY 5 μ S.	128

AUTHOR'S DECLARATION

At no time during the registration for the degree of Doctor of Philosophy has the author been registered for any other University award.

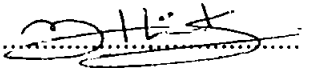
This study was carried out in collaboration with DRA (Funtington)

Relevant conferences were attended at which work was presented.

Presentation and conferences attended :

Radio Receivers and associated systems, University of Bath, 26-28 September 1995.

Aerosense Aerospace/ Defense Sensing and controls, Orlando, Florida, 8-12 April 1996.

Signed.....
Date.....23-1-97

1. Introduction

The concept of acousto-optic (AO) FM demodulation was introduced by Pieper and Poon [1] who described an acousto-optic receiver for commercial FM radio transmissions. The performance of a similar system, applied to radar processing was studied by Brooks [2]. Two types of detector assembly were considered: the first a knife edge detector as described by Pieper and Poon[1] , and the second a bi-cell system consisting of two photodiodes separated by a small gap. Brooks [2] showed that the bi-cell system has the ability to reduce or cancel AM and laser intensity noise effects, and suggested theoretical minimum detectable values for frequency deviations, based on the receiver noise characteristics for the knife edge detector assembly.

It has also been demonstrated by Reeve and Houghton [3] that a signal containing a π phase change may be detected by a system similar to the AO FM demodulator, except that the detector is covered by a slit instead of a knife edge. The phase change can be detected, since the light amplitude distribution at the detector is proportional to the instantaneous Fourier transform of the signal in the AO-cell. Therefore, as the phase change travels through the cell, the intensity distribution of the beam at the detector is no longer Gaussian; power is taken away from the centre of the beam and redistributed symmetrically either side. With the beam centred on the slit at the detector, this effect causes the output to fall as the phase change passes through the AO-cell.

It will be shown that the performance of the bi-cell system described by Brooks [2] can be improved and used in a surveillance receiver for electronic warfare (EW) applications. Electronic support measures (ESM) is the tactical reception of signals to locate, identify and analyse signals so that their effects can be avoided, countered or exploited.

ESM from the standpoint of narrow pulse radar has three functions; interception (detection) of radar emissions, analysis of radar signals and direction finding to the origin of radar signals. This narrow pulse, high power radar is easy to detect and, as a consequence, is of no interest to this work. Pulse compression radar is more difficult to detect because the energy of the pulse is spread over a wide bandwidth and time period. The pulse is either phase or frequency modulated so it is important that the receiver can identify and analyse modulation on a pulse. Continuous wave (CW) spread spectrum radar and communication

transmission basically amount to the same thing, a continuous carrier signal with some form of frequency or phase modulation on it. It will be shown that AO demodulator can be used to identify and analyse signals coming from pulse compression and CW radar and communication transmissions. This is discussed in more detail in section 3.2. A general purpose surveillance receiver will have no a priori knowledge of the signal characteristics. The requirements for such a receiver would be threefold: (i) to detect the presence of a signal and measure its carrier frequency, (ii) to identify the type of modulation being used, and (iii) to demodulate/decode the signal. The first of these requirements can be achieved using scanning superhet or channellised receivers, but automatic techniques for (ii) and (iii) are more difficult. It will be shown that the AO demodulator can be used for identifying different types of digital modulation and also effectively demodulates the signal and enables decoding. Such a system will operate in real time at carrier frequencies or intermediate frequencies (IF) from around 20 MHz to several GHz, depending on the type of AO-cell used.

There are various forms of modulation used in CW radar, and communication applications, a review of which can be found in chapter 2. Amplitude shift keying, (ASK) which as its name suggests modulates the amplitude envelope of the carrier, is very easy to detect, by this method and others, and is therefore rarely used for the types of transmission that a surveillance receiver would be interested in. This study will concentrate on frequency shift keying (FSK) and phase shift keying (PSK) modulation and their variations. In PSK and FSK signals the amplitude of the signal is constant so any receiver that detects only variations in the power of the signals will see no modulation. It is only when the signals are examined in the frequency domain that the modulation becomes evident. The power spectrum is examined using a bi-cell detector, in a similar way to that in which the slit was used by Reeve and Houghton [3]. The output from the two elements of the bi-cell detector show how the power in the signal varies within two frequency bands defined by the size and position of the elements. It will be shown that comparison of the sum and difference of the signals from the two detectors enables the different types of modulation to be identified and ultimately decoded.

The performance of the bi-cell system has been accurately modelled for frequency and phase demodulation of real signals (i.e. signals containing AM and FM noise) using the software package Mathcad. The analysis includes characterisation of the effect of changing

key system parameters such as; the gap size of the bi-cell, the standard deviation of the beam in the AO-cell, the standard deviation of the beam at the detector (focal length of the lens), laser intensity and laser wavelength. It will be shown that as a frequency demodulator the system can detect frequency deviations of between 25 Hz and 1 MHz on a 50 MHz carrier signal, and phase changes down to a fraction of a degree. The signal to noise ratio gain is shown graphically for both the sum and the difference channels, and the consequences of 'clipping' or 'limiting' on the signal is discussed in detail.

All the results from the analysis are substantiated by the results from the model and those in turn have been verified with practical results, obtained using an optical breadboard system. The system parameters of the model were identical to those used in the breadboard system so that its results should be identical to those gained from a practical system. The accuracy of the model has been proven by passing the same signal through the experimental system as has been used for the models results and comparing the outputs of the sum and difference channels.

2. Modulation techniques

2.1 Angle modulation

A CW sinusoidal signal with amplitude and phase modulation can be expressed as

$$\phi(t) = a(t) \cos[\omega_c t + \gamma(t)]. \quad (2.1)$$

Consider the case where $a(t) = A$ (a constant) and the phase angle $\gamma(t)$ is varied in proportion to a signal $f(t)$. This introduces the concept of angle modulation. The angle of a sinusoidal signal is described in terms of its frequency and/or a phase angle. Detailed analysis of angle modulation which incorporates phase and frequency modulation techniques can be found in any communications textbook[4,5,6]. Here will be given a brief summary.

If the phase angle $\theta(t)$ is varied linearly with the input signal $f(t)$, we can write

$$\theta(t) = \omega_c t + k_p f(t) + \theta_0 \quad (2.2)$$

where ω_c , k_p , θ_0 are constants. Because the phase is linearly related to $f(t)$, this type of modulation is known as phase modulation, (PM).

Another possibility is to make the instantaneous frequency proportional to the input signal,

$$\omega_i = \omega_c + k_f f(t), \quad (2.3)$$

where ω_c , k_f are constants. This is called frequency modulation, (FM), the phase angle of this signal is

$$\theta(t) = \int_0^t \omega_i(\tau) d\tau = \int_0^t k_f f(\tau) d\tau + \theta_0 \quad (2.4)$$

Comparisons of Eqs. (2.2) and (2.4) shows that PM and FM are closely related, such that if a signal is first integrated and then used to phase modulate a carrier, the result will be a frequency modulated signal. Unlike AM signals, angle modulated signals are not always linear as can be seen from the following.

A general PM signal can be represented by

$$\phi_{PM}(t) = A e^{j\theta(t)} = A e^{j(\omega_c t + \theta_0)} e^{jk_p f(t)} \quad (2.5)$$

using a series expansion for the exponential modulation factor in Eq. (2.5) gives

$$\phi_{PM}(t) = A e^{j(\omega_c t + \theta_0)} \left[1 + jk_p f(t) - \frac{1}{2!} k_p^2 f^2(t) - j \frac{1}{3!} k_p^3 f^3(t) + \dots \right] \quad (2.6)$$

From this it can be concluded that unless $|k_p f(t)| \ll 1$, angle modulation -in this case PM is not linear. Therefore the sidebands arising in angle modulation will not, in general, obey the principle of superposition. An analysis of spectra will have to be carried out using a particular waveform.

In this case let

$$f(t) = a \cos \omega_m t . \quad (2.7)$$

From Eq. (2.3) for FM we have

$$\omega_i = \omega_c + a k_f \cos \omega_m t , \quad (2.8)$$

where k_f is the frequency modulation constant. By defining a new constant called the peak frequency deviation,

$$\Delta\omega = a k_f , \quad (2.9)$$

we can write

$$\omega_i = \omega_c + \Delta\omega \cos \omega_m t . \quad (2.10)$$

From Eq. (2.4) the phase of this FM signal is therefore

$$\theta(t) = \omega_c t + \Delta\omega/\omega_m \sin \omega_m t = \omega_c t + \beta \sin \omega_m t , \quad (2.11)$$

where $\beta = \Delta\omega/\omega_m$ is a dimensionless ratio of the peak frequency deviation to the modulating frequency.

The resulting FM signal is

$$\begin{aligned} \phi_{FM}(t) &= \Re\{Ae^{j\theta(t)}\} \\ \phi_{FM}(t) &= \Re\{Ae^{j\omega_c t} e^{j\beta \sin \omega_m t}\} \end{aligned} \quad (2.12)$$

which may be written as

$$\phi_{FM}(t) = A \cos (\omega_c t + \beta \sin \omega_m t) . \quad (2.13)$$

Eq. (2.13) can be rewritten using identities as

$$\phi_{FM}(t) = A \cos \omega_c t \cos(\beta \sin \omega_m t) - A \sin \omega_c t \sin (\beta \sin \omega_m t). \quad (2.14)$$

For small values of β we can approximate that

$$\cos (\beta \sin \omega_m t) \approx 1, \quad (2.15)$$

$$\sin (\beta \sin \omega_m t) \approx \beta \sin \omega_m t . \quad (2.16)$$

The condition where β is small enough for these approximations is the condition for narrowband FM (NBFM). Usually a value of $\beta < 0.2$ is taken to be sufficient. Combining Eqs. (2.15), (2.16) in (2.14) we can write

$$\phi_{NBFM}(t) = A \cos \omega_c t - \beta A \sin \omega_c t \sin \omega_m t \quad (2.17)$$

which like an AM waveform has a spectrum consisting of a carrier and two sidebands. For values of $\beta > 1$ we proceed as before to get Eq. (2.12) The second exponential in Eq. (2.12) is a periodic function of time with a fundamental frequency of ω_m rad/sec. It can be expanded in a Fourier series,

$$e^{j\beta \sin \omega_m t} = \sum_{n=-\infty}^{\infty} F_n e^{jn\omega_m t} \quad (2.18)$$

where

$$F_n = \frac{1}{T} \int_{-T/2}^{T/2} e^{j\beta \sin \omega_m t} e^{-jn\omega_m t} dt \quad (2.19)$$

making a change of variable $\xi = \omega_m t = (2\pi/T)t$, we get

$$F_n = \frac{1}{2\pi} \int_{-\pi}^{\pi} e^{j(\beta \sin \xi - n\xi)} d\xi, \quad (2.20)$$

This integral can be evaluated numerically in terms of the parameters n and β , and is called the Bessel function of the first kind. From these results it is obvious that a FM waveform with sinusoidal modulation has an infinite number of sidebands. However the magnitudes of the spectral components of the higher order sidebands become negligible, and for all practical purposes, the power is contained in a finite bandwidth. A general rule for approximating this bandwidth was given by Carson and is given by

$$W \approx 2\omega_m(1 + \beta) \quad (2.21)$$

As mentioned previously there is no basic difference between the generation of FM and PM signals. The slight modification will be pointed out here.

Eq (2.8) gives us the instantaneous frequency for an FM signal with sinusoidal modulation, for PM with the same modulating signal we have

$$\begin{aligned} \theta(t) &= \omega_c + ak_p \cos \omega_m t + \theta_0 \\ &= \omega_c + \Delta\theta \cos \omega_m t + \theta_0 \end{aligned} \quad (2.22)$$

where $\Delta\theta$ is the peak phase deviation (in radians) and k_p is the phase modulator constant (in radians per volt). The instantaneous frequency is

$$\omega_i(t) = \frac{d\theta}{dt} \quad (2.23)$$

$$= \omega_c - ak_p \omega_m \sin \omega_m t \quad (2.24)$$

$$= \omega_c - \Delta\omega \sin \omega_m t \quad (2.25)$$

Thus we see that the peak frequency deviation in PM is proportional not only to the amplitude of the modulating signal but also to its frequency. Aside from this we can take $\Delta\omega = ak_p \omega_m = \Delta\theta \omega_m$ and then proceed as if the modulation were FM as far as bandwidth, sidebands etc. are concerned.

2.2 FM demodulators

There are a number of ways to recover the modulating signal from the FM waveform, there follows a brief overview of the most common. The overall characteristic must be the same, to provide an output signal whose amplitude is proportional to the instantaneous frequency of the input waveform.

2.2.1 Amplitude limiting

In order to make full use of the advantages offered by FM, a demodulator must be preceded by an amplitude limiter (Figure 2.1), on the grounds that any amplitude changes on the signal are spurious, and must therefore be removed to avoid distortion. This is important as most FM demodulators react to amplitude changes as well as frequency changes. The limiter is obviously a form of clipping device, a circuit whose output tends to remain constant despite changes in the input. Most limiters will behave in this fashion so long as the input voltage stays within a certain range.

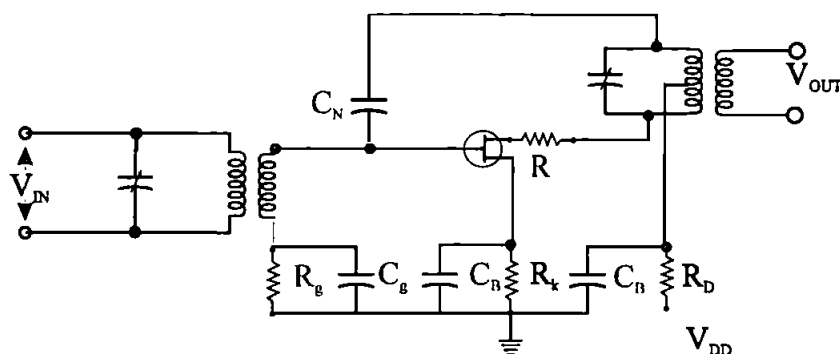


Figure 2.1 Amplitude limiter

2.2.2 Slope detection

A frequency modulated signal fed into a tuned circuit whose resonant frequency is to one side of the centre frequency of the FM signal will have an output whose amplitude that

depends on the frequency deviation of the input signal. This produces an output voltage proportional to the frequency deviation of the carrier. The output is then applied to a diode detector with an RC load of suitable time constant. The slope detector is only linear over a very limited range and is obviously very sensitive to amplitude variations in the signal.

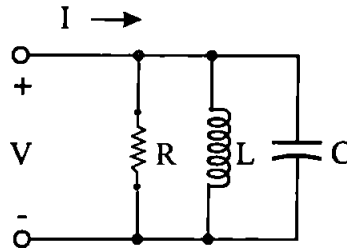


Figure 2.2 slope detector

2.2.3 Balanced slope detector

This uses two slope detectors connected back to back, to the opposite ends of a centre-tapped transformer, and hence fed 180° out of phase. The top secondary circuit is tuned above the IF and the bottom circuit is tuned below the IF by the same amount. Each circuit is connected to a diode detector with an RC load. The output is taken from across the series combination of the two loads, so that it is the sum of the two individual outputs.

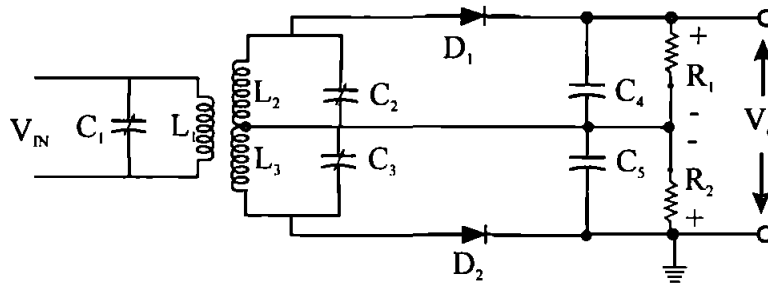


Figure 2.3 Balanced slope detector

The S-shaped characteristic of the balanced slope detector is an improvement on the slope detector, but is even more difficult to align and there is still no amplitude limiting.

2.2.4 Phase discriminator

It is possible to obtain the same S-shaped response curve from a circuit which is tuned to the centre frequency of the incoming signal in both the primary and secondary windings. This helps simplify the alignment and gives far better linearity than slope detection.

This circuit shown in 2.3. Uses the same diode and load arrangement, but the method of insuring that the voltages fed to the diodes vary linearly with the input signal has been completely changed. The primary and secondary voltages are:

exactly 90° out of phase when f_{in} is f_c

less than 90° out of phase when f_{in} is higher than f_c

more than 90° out of phase when f_{in} is less than f_c

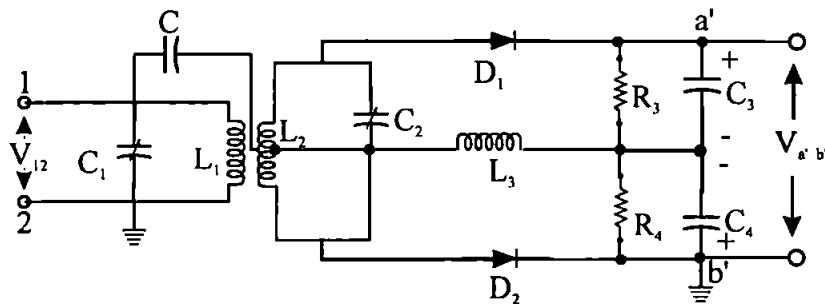


Figure 2.4 Phase discriminator

Thus, although the voltages will be the same at the diodes at all frequencies, the vector sums will differ. Therefore the individual output voltages will only be equal when the input is at f_c .

2.2.5 Ratio detector.

The phase discriminator also called the Foster-Seeley discriminator is still sensitive to changes in the amplitude of the input signal. This makes prior limiting necessary. It is possible to modify the discriminator to provide limiting, such a circuit is called a ratio detector.

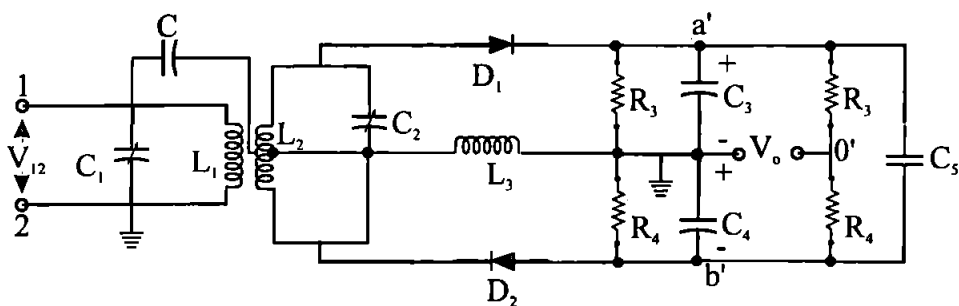


Figure 2.5 The ratio detector

The ratio detector shown in Figure 2.5. Is very similar to the phase discriminator circuit, but three important changes have been made: one of the diodes has been reversed, a large capacitor has been placed across what used to be the output, and the output is now taken from a different point.

2.2.6 The phase locked loop

The phase locked loop demodulator, shown in Figure 2.6, offers many advantages over the tuned circuit demodulators. It uses the error voltage in a PLL driven by the input signal as the output. The error voltage will vary linearly with the input signal as long as the PLL stays in 'lock'. The lock range and capture range can be easily changed by altering the system parameters, to suit specific applications. PLL's offer high AM rejection and very good signal to noise ratios. They are fast becoming the most popular FM demodulator.

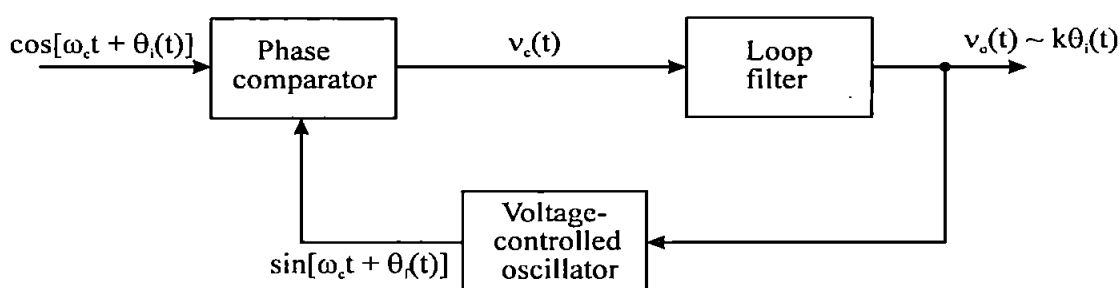


Figure 2.6 Block diagram of a phase locked loop

2.2.7 Digital Demodulators

DSP techniques have been used to create digital FM demodulators for FM, TV and wireless in software [7]. The proposed demodulation system for existing FM broadcast receiver and TV audio applications has been shown to be very accurate and able to

suppress AM to 70 dB. To date this all digital FM demodulator has not been implemented. More simple digital demodulators, implemented using DSP techniques, are already in common use in modems.

2.3 Digital modulation

There is a variety of techniques currently in use for digital modulation of communications signals. These fall under the broad headings of amplitude, frequency and phase shift keying (ASK, FSK and PSK) but many variations exist, such as phase reversal keying (PRK), quaternary phase shift keying (QPSK), offset-keyed QPSK and minimum shift keying (MSK). These techniques are used, not only in general communications applications but also in spread spectrum systems; similar techniques are also used in low probability of intercept radar. A co-operating receiver will know the details of the type of modulation being employed and will have the appropriate matched filter and demodulation systems. Here is given a brief overview of the most popular forms of FSK and PSK.

2.3.1 Frequency shift key (FSK)

FSK is binary frequency modulation of the analogue carrier. Thus a voltage controlled oscillator can be used with the two voltage levels of the data, shifting the carrier to two discrete frequencies, one of which represents binary 1 and the other binary 0.

The two received signal waveforms are different and so two matched filters are used, one for each waveform. If the two waveforms are given by

$$\phi_1(t) = A \sin m\omega_0 t \quad (2.26 \text{ a})$$

$$\phi_2(t) = A \sin n\omega_0 t \quad (2.26 \text{ b})$$

Two possible receivers for FSK are shown in Figure 2.7. (a) The matched filter receiver and (b) the correlator receiver. The effect of both is identical-to select the output with the largest degree of similarity between the received signal and possible transmitted signals. Thus both these receivers are maximum likelihood (Appendix A4). The operation of these receivers is described in Appendix A1.

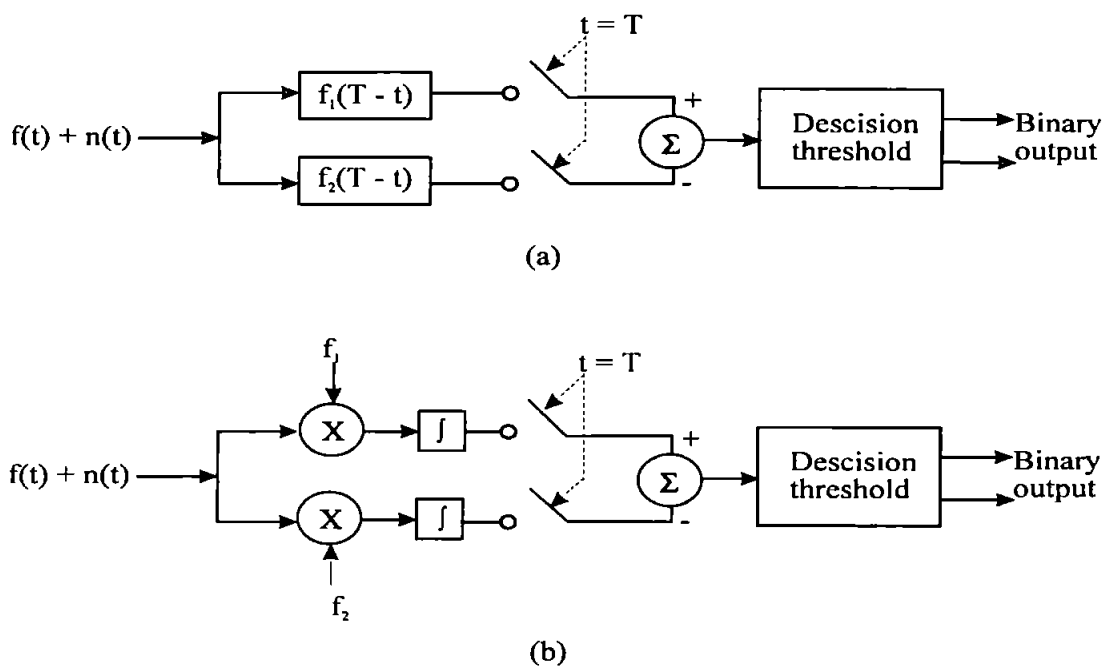


Figure 2.7 . (a) The matched filter receiver (b) The correlator receiver

The average energy per binary bit is [4]

$$E = \int_0^T A^2 \sin^2 m\omega_o t dt = A^2 T / 2 \quad (2.27)$$

If one only signalling frequency is present then it is assumed that the output from one matched filter will be E and the other zero. Conversely if the other frequency is present the output of the first matched filter is zero and the result of the subtraction is -E. As shown in Figure 2.8.

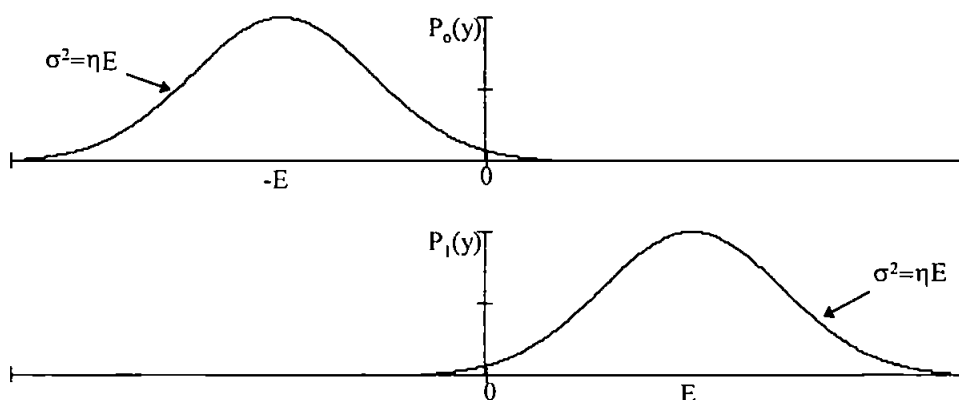


Figure 2.8 Probability density functions for binary PSK waveforms.

This is similar to the polar-binary case, see Appendix A, except for the fact that the noise voltages are subtracted at the output of the filters. If we assume that the two frequencies do not overlap then the output noise voltages are statistically independent and hence add on a power (mean-square) basis. Therefore we can simply double the variance, assuming the two filter bandwidths are the same, and proceed as before, giving [4]

$$P_{\epsilon} = \int_0^{\infty} \frac{1}{\sqrt{2\pi\eta E}} e^{-(y+E)^2 / (2\eta E)} dy$$

$$= Q\left(\sqrt{\frac{E}{\eta}}\right) \quad (2.28)$$

where E is the (average) energy per binary digit.

2.3.2 Phase shift keying (PSK).

In phase shift keying the phase of the carrier signal is switched between two or more values in response to a binary message. For binary modulation a 180° phase shift is often used because it simplifies the modulator design, this is known as phase-reversal keying (PRK), and can be written as

$$\phi_1(t) = A \sin \omega_c t \quad (2.29 a)$$

$$\phi_2(t) = -A \sin \omega_c t \quad (2.29 b)$$

The correlation detector shown in Figure 2.9 gives an output of $y(t) = E + n_o(T)$ at time $t = T$ given an input of $[\phi_1(t) + n(t)]$, and $y(t) = -E + n_o(T)$ for an input of $[\phi_2(t) + n(t)]$. The variance of the noise is [cf. Eq. (A3.16)] $\overline{n_o^2(t)} = \eta E / 2$ [4] and the corresponding probability density functions are shown in Figure 2.10.

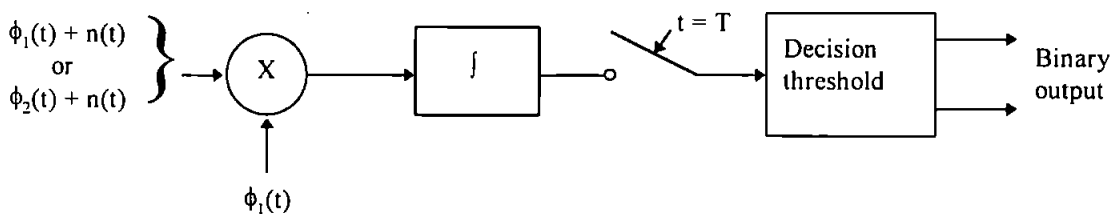


Figure 2.9 A correlation detector for antipodal signals

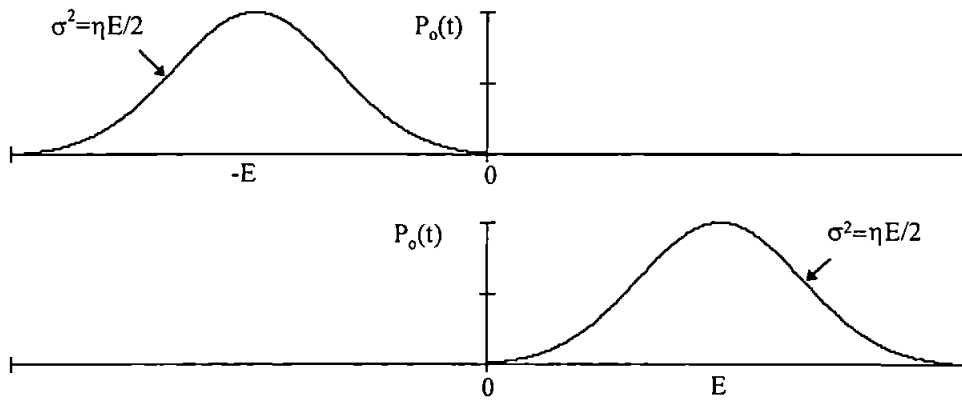


Figure 2.10 Probability density function for PRK

It is clear from Figure 2.10 that the optimum decision threshold is zero. Therefore the net probability of error is given by [4]

$$\begin{aligned}
 P_E &= \int_0^{\infty} \frac{1}{\sqrt{\pi\eta E}} e^{-(y+E)^2 / (\eta E)} dy \\
 &= Q\left(\sqrt{\frac{2E}{\eta}}\right) \quad (2.30)
 \end{aligned}$$

By comparing Eq. (2.30) and Eq. (A.3.19) it can be seen that PRK has the same probability of error performance as polar baseband systems, although it can be seen that it needs half the average power of FSK by comparing Eq. (2.30) and Eq. (2.28).

2.3.3 Differential PSK

Carrier synchronisers often cannot distinguish whether they are locked to the carrier phase or to the phase plus a multiple of π/M , where M is the number of states in the modulation scheme. This makes it difficult to encode data into the absolute transmitted phase levels. In a differential scheme, the data are encoded into the transition from interval to interval.

DPSK uses the difference between successive bits to encode the information as illustrated in Table 2.1 DPSK encoding. Differential encoding uses the rule that there is no change in the output state if a 1 is present at the input and there is a change if a 0 is present. The table assumes an initial arbitrary state of 1. The obvious advantage is that the receiver can use the phase of the previous digit as a reference signal.

PCM code input		1	1	0	0	0	1	0	1	0
Differential code	1	1	1	0	1	0	0	1	1	0
Phase	0	0	0	π	0	π	π	0	0	π

Table 2.1 DPSK encoding

The probability error of DPSK is [4]

$$P_e = \frac{1}{2} \exp \frac{-E}{\eta} \quad (2.31)$$

2.3.4 Quaternary PSK

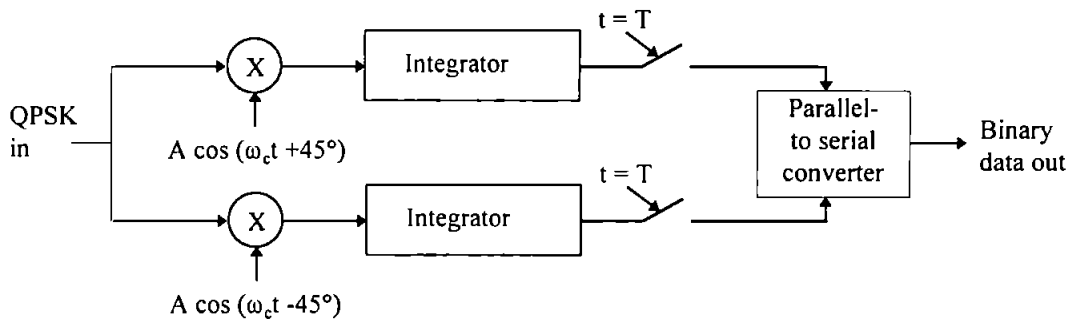


Figure 2.11 Simplified block diagram of a QPSK demodulator.

QPSK modulation carries four symbols, each with a different phase. These phases are spaced by 90° and normally are $\psi = \{45^\circ, 135^\circ, 225^\circ, 315^\circ\}$; this corresponds to the RF signal $\sqrt{2E_s / T} \cos(\omega_o t + \psi)$, which is

$$\text{Send 00: } s(t) = \sqrt{\frac{2E_s}{T}} \left[+\frac{1}{\sqrt{2}} \cos(\omega_o t) - \frac{1}{\sqrt{2}} \sin(\omega_o t) \right]$$

$$\text{Send 10: } s(t) = \sqrt{\frac{2E_s}{T}} \left[-\frac{1}{\sqrt{2}} \cos(\omega_o t) - \frac{1}{\sqrt{2}} \sin(\omega_o t) \right]$$

$$\text{Send 11: } s(t) = \sqrt{\frac{2E_s}{T}} \left[-\frac{1}{\sqrt{2}} \cos(\omega_o t) + \frac{1}{\sqrt{2}} \sin(\omega_o t) \right]$$

$$\text{Send 01: } s(t) = \sqrt{\frac{2E_s}{T}} \left[+\frac{1}{\sqrt{2}} \cos(\omega_o t) + \frac{1}{\sqrt{2}} \sin(\omega_o t) \right]$$

Because the transmitted QPSK signal can be regarded as two orthogonal BPSK signals it can be demodulated by two BPSK receivers, or correlators, in parallel, one for each quadrature. The block diagram of such a system is shown in Figure 2.11.

The probability error function for each of the receivers would therefore be given by [4]

$$\begin{aligned}
 P_e &= \int_0^{\infty} \frac{1}{\sqrt{\pi\eta E}} e^{-(y+E/\sqrt{2})^2/(\eta E)} dy \\
 &= Q\left(\sqrt{\frac{E}{\eta}}\right)
 \end{aligned} \tag{2.32}$$

The probability that the output of the receiver is correct is the product of the probabilities of both correlators being correct or

$$\begin{aligned}
 P_c &= (1 - P_e)(1 - P_e) \\
 &= 1 - 2P_e + P_e^2
 \end{aligned} \tag{2.33}$$

which for small values of P_e ($P_e \ll 1$) gives

$$P_c = 1 - 2P_e \tag{2.34}$$

The probability of symbol error, P_{es} , for the QPSK system is therefore

$$\begin{aligned}
 P_{es} &= 1 - P_c \\
 P_{es} &\approx 2P_e = 2Q\left(\sqrt{\frac{E_s}{\eta}}\right)
 \end{aligned} \tag{2.35}$$

2.3.5 Offset QPSK

OQPSK is similar to QPSK except that the carrier phase transitions are transmitted in two periods. This results in instantaneous carrier phase transitions of only $\pm\pi/2$ from the previous phase state, as compared to QPSK (and BPSK) that contain π transitions. Hence, OQPSK does not have the complete phase-reversal transients of QPSK which are badly affected by filters and the nonlinearities present in practical systems. A OQPSK receiver is similar to the QPSK receiver shown in Figure 2.11, except that the quadrature channel is delayed by $T/2$. Since staggering the bit streams does not change the properties of the quadrature modulation process, OQPSK has the same average probability of error as QPSK. Furthermore it has been shown that offsetting the two bit streams gives an optimum immunity to phase jitter in the presence of additive Gaussian noise [8].

2.3.6 MSK

It is beneficial in FSK systems for some form of continuous phase FSK (CP-FSK) to be used to minimise phase discontinuities and the resultant phase transients. These are caused if the modulation system being used switches frequency irrespective of the position of the phase. This offers the same bandwidth efficiency as QPSK and OQPSK, but its power spectral density decreases more rapidly beyond the minimum bandwidth.

An example of a CP-FSK modulation system is minimum shift keying (MSK), here the frequency separation between f_1 and f_2 is required to be such that there is one-half cycle difference in one bit interval. This can be written as

$$\phi_{MSK}(t) = A \cos \left[\omega_c t \pm \frac{\pi}{2T_b} + \gamma(0) \right], \quad 0 \leq t < T_b. \quad (2.36)$$

where $\gamma(0)$ is the initial phase of the signal, dependant on the past history of the modulation process. The instantaneous frequency is

$$\omega_i = \omega_c \pm \frac{\pi}{2T_b}, \quad (2.37)$$

or

$$f_i = f_c \pm \frac{1}{4T_b}. \quad (2.38)$$

This ensures that all frequency changes take place when the phase is 0.

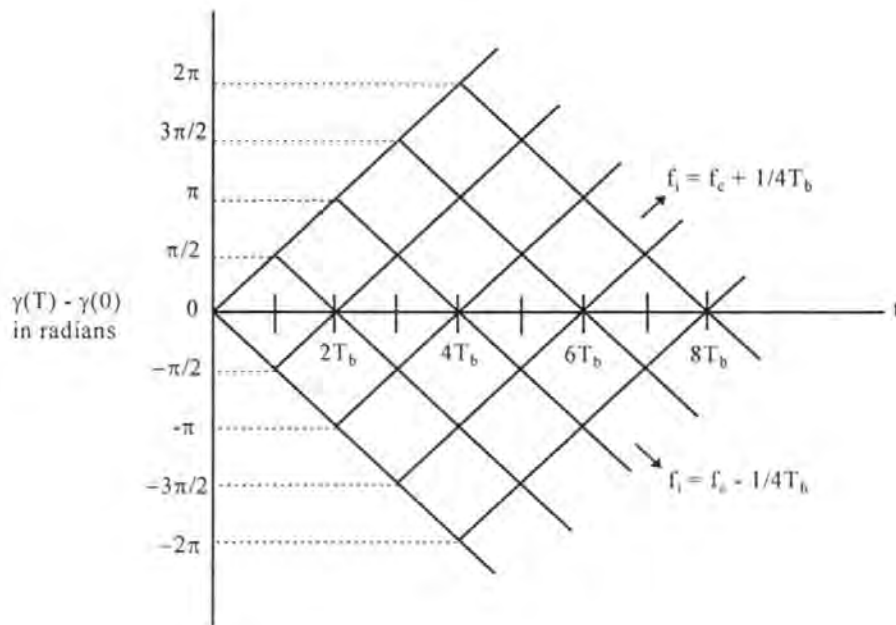


Figure 2.12 Excess phase trellis for MSK

Figure 2.12 shows the trellis diagram for all the possible values of $\gamma(t)$ for $t > 0$ over several successive bit intervals, assuming that $\gamma(0) = 0$. Each path from left to right through the phase trellis corresponds to a specific binary sequence. Over each bit interval the phase is advanced or retarded exactly 90° depending on whether the data for that interval is 1 or 0. It can be shown that [4] p644 Eq. (2.36) can be expressed in terms of in-phase and quadrature components as

$$\phi_{MSK}(t) = A \left\{ a_I(t) \cos \frac{\pi t}{2T_b} \cos \omega_c t - a_Q(t) \sin \frac{\pi t}{2T_b} \sin \omega_c t \right\} \quad (2.39)$$

where $a_I(t) = \cos \gamma_k$, and $a_Q(t) = p_k \cos \gamma_k$, and ensuring that $\gamma_k = 0, \pi$, modulo 2π , gives

$$p_k = a_I(t)a_Q(t) \quad (2.40)$$

Now MSK can be thought of as a special case of OQPSK with sinusoidal pulse weighting (rather than rectangular weighting). The various components of the MSK signal are illustrated in Figure 2.13 for an input sequence 1110100.

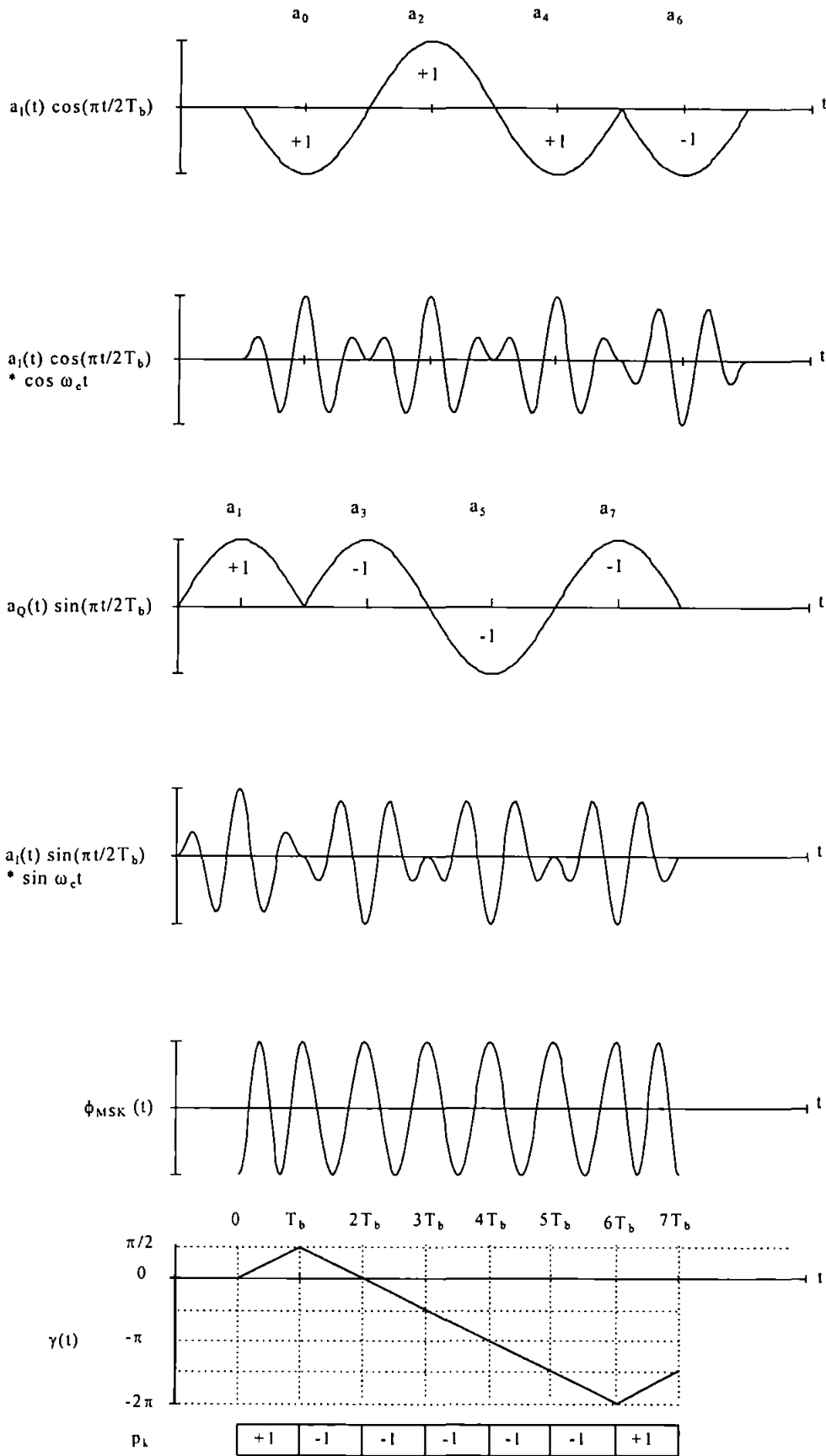


Figure 2.13 MSK waveforms.

2.4 Applications of Demodulators

The most obvious use for an FM demodulator is for the demodulation of wideband FM and narrowband FM. Wideband FM is used for broadcast transmissions, and for the sound accompanying TV transmissions. Narrowband FM is used for communications, in competition with SSB, having its applications in various forms of mobile communications, generally at frequencies above 30 MHz. It is also used in conjunction with SSB in frequency division multiplexing (FDM). FDM is a technique for combining large numbers of channels in broadband links used for terrestrial or satellite communications.

FM demodulators are commonly used for radar interception in EW especially radars with low probability of intercept (LPI) features. These may include low sidelobe antennas, infrequent scanning, reducing the radar power when tracking a closing target (as range is reduced, radar power is also reduced), making use of waveform coding to provide transmitting duty cycles approaching one (to reduce the peak power while maintaining the average power) and using frequency hopping to force the interceptor to consider more of the spectrum in attempting to characterise the radar. Chapter 3 provides a brief introduction to radar and EW

Digital modulation methods are used for transmission of binary symbols through bandpass channels. Binary modulation methods used are Amplitude shift keying (ASK), frequency shift keying (FSK), and phase shift keying (PSK). In these methods, the amplitude, frequency or phase of a sinusoid is switched in response to a PCM input.

Using matched filter detection in additive white Gaussian noise, PSK requires up to 3 dB less power than ASK or FSK, although ASK and FSK can use coherent or non-coherent detection. Differential PSK (DPSK) can be used to gain most of the advantages of PSK and yet avoid the requirements for coherent detection. The most popular choices for communication systems are PSK, DPSK and FSK.

Quadrature PSK (QPSK) uses quadrature multiplexing principles to offer twice the bit rate capability as that of the binary methods. Delaying either the I or Q channel will result in offset QPSK (OQPSK) which has the advantage that it has a more constant envelope than QPSK.

Minimum-shift keying (MSK) is an example of coherent FSK in which the phase in the modulated waveform is continuous, and the frequency shift is such that there is a one-half cycle difference in one bit interval. MSK has similar characteristics to those of OQPSK.

Spread spectrum systems modulate a signal a second time using a wideband spreading waveform. This is done so that the system's transmitted energy occupies a larger bandwidth than the information bit rate, (usually much larger) and is relatively independent of the information bit rate. Communication systems using direct modulation of a modulated carrier by a wideband spreading signal for purposes of bandwidth spreading are called direct-sequence (DS) spread spectrum systems. The simplest form of DS spread spectrum employs BPSK as the spreading modulation. For the common choice of $\Delta\theta = \pi$, an expression for the BPSK waveform is:

$$\phi(t) = Ap(t) \cos \omega_c t, \quad (2.41)$$

where $p(t)$ is a binary switching function with possible states ± 1 and governed by the modulating (input signal). The resulting DS spread spectrum signal is

$$x(t) = Ac(t)p(t) \cos \omega_c t, \quad (2.42)$$

where $c(t)$ is the spreading modulation waveform. A popular choice for $c(t)$ is that of a pseudorandom noise (PN) binary sequence having values ± 1 .

Demodulation in such systems, at least in part, is achieved by correlation of the received signal with the spreading waveform, $c(t)$.

3. Radar techniques and electronic warfare

3.1 Radar

A radar detects the presence of objects and locates their position in space by transmitting electromagnetic energy and observing the returned echo. A pulse radar transmits a relatively short burst of electromagnetic energy, after which the receiver is turned on to listen for the echo. The echo not only indicates that a target is present, but the time that elapses between the transmission of the pulse and the receipt of the echo is a measure of the distance to the target. Separation of the echo signal and the transmitted signal is made on the basis of differences in time.

The radar transmitter may be operated continuously rather than pulsed if the strong transmitted signal can be separated from the weak echo. The received echo signal power is considerably smaller than the transmitter power. Separate antennas for transmission and reception help segregate the weak echo from the strong leakage signal, but the isolation is usually not sufficient. A feasible technique for separating the received signal from the transmitted signal when there is relative motion between target and radar is based on recognising the change in the echo signal frequency caused by the doppler effect.

It is well known that if either the source of oscillation or the observer of the oscillation is in motion, an apparent shift in frequency will result. This is the doppler effect and is the basis of MTI and CW doppler radar. The doppler frequency shift f_d is given by [9]

$$f_d = \frac{2v_r}{\lambda} = \frac{2v_r f_o}{c} \quad (3.1)$$

where v_r = relative or radial velocity of target with respect to radar, f_o = transmitted frequency and c = velocity of propagation = 3×10^8 m/s.

Simple CW radar is unable to measure range, therefore some sort of timing mark must be applied to a CW carrier if range is to be measured. The spectrum of a CW transmission can be broadened by the application of modulation, either amplitude, frequency or phase. An example of amplitude modulation is the pulse radar, the narrower the pulse the better the measurement. A widely used technique to broaden the spectrum of CW radar is to frequency modulate the carrier. The timing mark is the changing frequency. The transit time is proportional to the difference frequency between the echo signal and the transmitter

signal. The greater the transmitter frequency deviation in a given time interval, the more accurate the measurement of the transit time and the greater will be the transmitted spectrum.

Pulse compression allows a radar to utilise a long pulse to achieve large radiated energy, but simultaneously to obtain the range resolution of a short pulse. It accomplishes this by employing frequency or phase modulation to widen the signal bandwidth. (Amplitude modulation is also possible, but is seldom used.) The choice of a pulse compression radar system is dependant on the type of waveform selected and the method of generation and processing. The waveforms used fall into three categories; linear FM, non linear FM and phase coded and can all be generated and processed actively or passively. Active generation involves modulation of a carrier signal without time expansion, whereas passive generation involves exciting a device such as a surface acoustic wave, SAW, structure to produce a time-expanded coded waveform. Active processing involves mixing delayed replicas of the transmitted signal with the received signal and is a correlation processing approach. Passive processing involves the use of a compression network that is the conjugate of the expansion network and is a matched filter approach. The received signal is processed such that it compresses the long pulse to a duration $1/B$, where B is the modulated-pulse spectral bandwidth.

The doppler frequency shift produced by a moving target may be used in a pulse radar, just as in the CW radar, to determine the relative velocity of a target or to separate desired moving targets from undesired stationary objects (clutter). A pulse radar that utilises doppler frequency shift as a means for discriminating moving from fixed targets is called an MTI (moving target indication) or pulse doppler radar.

3.2 Radar / electronic warfare (EW) Introduction

Electronic warfare systems are operated by both sides in a conflict. The two sides can be considered the 'Threats' and the 'Defenders'. The EW objectives of the threats and defenders are listed below [10]

Threat objectives :

- Prevent detection of the presence of the threat
- Prevent the determination of the intentions of the threat
- Prevent the detection of the threat's electromagnetic (EM) radiation by the defenders
- Prevent location of the threat by location of its EM signals
- Prevent recovery of the information content of the threat's EM signals
- Prevent interference with the threat's use of the EM spectrum

Defender objectives :

- Detect the presence of threats
- Determine the location and intentions of threats using defenders EM radiation
- Detect the presence of the threat's EM radiation
- Identify the threat's EM radiation
- Identify the threat's intentions through analysis of the threat's EM radiation
- Determine the threat's location through the threats EM radiation
- Determine the information content of the threat's EM radiation
- Deny the use of the EM spectrum by the threat.

3.2.1 Definitions

a. Electronic support measures (ESM) :ESM is that division of electronic warfare involving actions taken under direct control of an operational Commander to search for, intercept, and identify / locate sources of radiated electromagnetic energy for the purpose of immediate threat recognition.

Thus, electronic warfare support measures provide a source of information required for immediate decisions involving electronic counter measures, electronic counter-counter measures, avoidance, targeting and other tactical employment of forces.

b. Electronic counter measures (ECM) : ECM is that division of electronic warfare involving actions taken to prevent or reduce an enemy's effective use of the electromagnetic spectrum. Electronic counter measures include :

Electronic Jamming - the deliberate radiation, reradiation, or reflection of electromagnetic energy with the object of impairing the use of electronic devices, equipment, or systems being used by an enemy.

Electronic deception - The deliberate radiation, reradiation, alteration, absorption or reflection of electromagnetic energy in a manner intended to mislead an enemy in the interpretation or use of information received by the enemy's electronic systems

c. Electronic counter-counter measures (ECCM) : ECCM is that division of electronic warfare involving actions taken to retain effective friendly use of the electromagnetic spectrum.

Of the categories mentioned above the one of relevance to this work is ESM which will now be explained in more detail

3.2.2 ESM

ESM is arguably the most valuable EW category because it offers something for nothing. Only passive techniques are used so that information can be obtained about the enemy without the need to risk giving away your own position and identity by transmitting. In addition ECM systems rely upon ESM for initial threat location and analysis.

An ESM system must aim to achieve 100% probability of intercept: therefore as well as having the sensitivity to detect the smallest signal received it must also have instantaneous coverage of the entire frequency band of interest. It must also have sufficient instantaneous dynamic range to be able to deal simultaneously with a pulse compression or CW radar at the limit of detection and a high power surveillance radar 500 m away.

The more parameters an ESM system can measure the better chance it has of successfully identifying the intercept. The following is a list of the parameters of a radar pulse that can be measured :

a. Bearing or Angle of arrival (AOA)

- b. Radio Frequency (RF)
- c. Time of arrival (TOA)
- d. Pulse width (PW)
- e. Pulse amplitude (PA)
- f. Modulation on a pulse
- g. Signal polarisation

For CW radar and communication signals the parameters that need to be analysed change :

- a. Bearing or Angle of arrival (AOA)
- b. Radio frequency
- c. Type of modulation
- d. Coding used
- e. Message information

3.2.3 System components

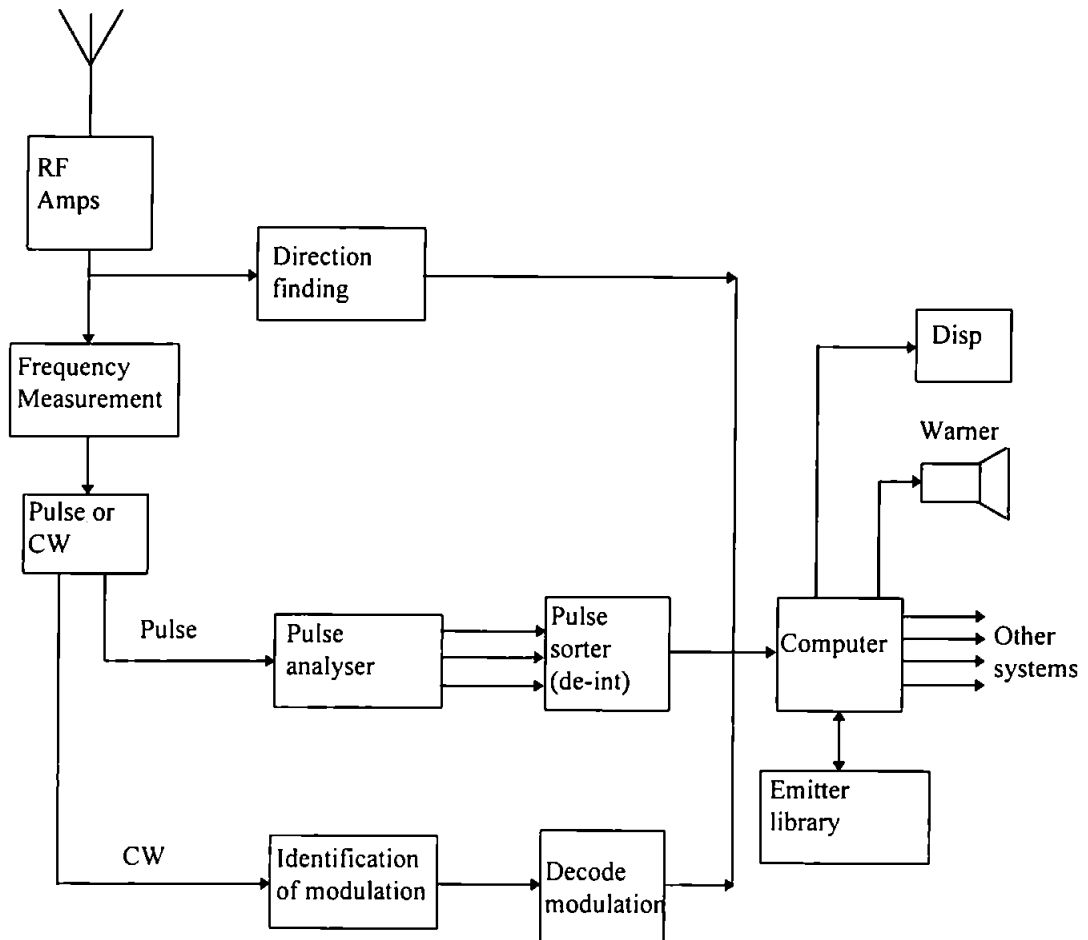


Figure 3.1 Block diagram of an ESM system

Antenna systems

These include both the directional antennas required for bearing measurement and the omnidirectional antennas which feed the RF measurement and pulse analyser systems.

RF amplifiers

Travelling wave tube or solid state amplifiers may be used to increase sensitivity and dynamic range

Direction finding, frequency measuring and pulse analyser.

These systems measure the primary parameters, the system of interest here being the frequency measuring system the most common of which the instantaneous frequency measurer (IFM), is discussed in section 3.2.4.

Deinterleaving system

This is a fast dedicated processor which derives the secondary parameters from the primary measurements after sorting the deinterleaved pulse chains.

Identification of modulation

Identify the type of modulation being used. i.e. frequency modulation / phase modulation (FSK, BPSK etc.)

Decode modulation

Demodulates/decodes the information on the signal, making various assumptions from the identification of the modulation.

Computer/emitter library

A general purpose computer compares the measured primary and secondary parameters with data stored in the emitter library and attempts to make an identification. The computer may be linked to other systems such as ECM, weapons, radars and Operations room.

Output/Warner

High threat intercepts should activate immediate warner signals in the operations room and EW office. Normal contacts will be displayed on tabular displays.

3.2.4 The instantaneous frequency measurer (IFM)

The basic concept of the IFM is illustrated in Figure 3.2

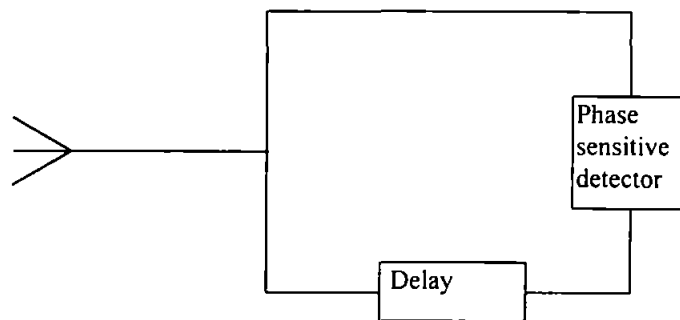


Figure 3.2 Block diagram of an IFM system

The incoming signal is split into two. One half is delayed by T secs and fed to one input of a phase sensitive detector (PSD). The other half is fed directly to the other input of the PSD. If the input is at f Hz then the phase difference between the delayed and undelayed signals is

$$\phi = 2\pi fT \text{ rads} \quad (3.2)$$

hence the measured phase difference is proportional to the signal frequency. The choice of the time delay T is governed by two factors:

(1.) The phase difference for any frequency of interest cannot exceed 2π rads. $2\pi+x$ rads would be measured as x rads giving a false result. Hence

$$2\pi fT \leq 2\pi$$

giving

$$T \leq 1/f$$

In practice since any frequency band can be mixed down to baseband, the time delay T must be no greater than the reciprocal of the bandwidth of the device.

(2.) In digital IFMs several delay lines of different lengths are used to generate more accurate results. Phase ambiguities in the longer lines are resolved by the shorter ones [11]. There is however, a limit to the length of delay line that can be used. The maximum delay

can be no longer than the length of the shortest pulse to be measured. Otherwise the undelayed half of the signal will be finished before the delayed half arrives at the PSD.

The IFM system can be used to identify either phase or frequency modulation on a pulse and by careful analysis of its output could be used to demodulate the signal. However this is seldom if ever done in a practical system, most confine themselves to a simple indication of the presence of FMOP or PMOP.

Although in most ways the IFM is an excellent system for ESM applications it suffers from one major drawback. It cannot cope with two simultaneous signals in the same frequency band. For low duty cycle signals such as pulse radar this is not generally a problem but with the increasing trend towards high duty cycle or CW radars it renders the IFM practically useless

4. Acousto-optics

Diffraction of light by sound was predicted by Brillouin in 1922 [12] and was demonstrated experimentally some ten years later [13]. The development of the laser caused renewed interest in this field because the scattering of light by sound provides a convenient way of controlling the frequency, intensity and direction of an optical beam.

Recently, as new technology has been developed, optical signal processing has become increasingly important. Acousto-optic devices have an important role in this type of processing. For example, acousto-optic devices have been developed for performing fundamental operations such as convolution, correlation, light modulation and matrix algebra. Such devices may offer unique capabilities for applications in communication systems, with real time signal processing, faster speeds and higher bandwidths. The desire to process ever increasing amounts of data has led to the extension of carrier frequencies into the optical region. These types of interaction have opened new ways to perform convolution, correlation and other types of optical signal processing. Because most of these techniques can be realised using various technologies, acousto-optics has been forced to compete not only with digital signal processing, but with rival optical systems such as electro optics or charge coupled devices.

4.1 Theory

An acousto-optic device consists of an optically transparent medium, usually a crystal, see Figure 4.1, in which ultrasonic waves propagate. The acoustic wave is launched into the medium using a piezoelectric transducer. By applying an electric field to the transducer the piezoelectric material is deformed, producing an internal strain, thus converting the electrical signal into an acoustic strain wave in the medium. As the sound wave propagates through the medium, it causes a periodic change in the refractive index, producing regions of compression in the crystal lattice, followed by regions in which the lattice is relaxed. The index variations for a periodic signal, such as a sine wave, are periodic causing them to act as a diffraction grating when the laser beam passes through the cell. [14]

The net result is that light passing through the acousto-optic cell is phase modulated according to these changes in the optical path.

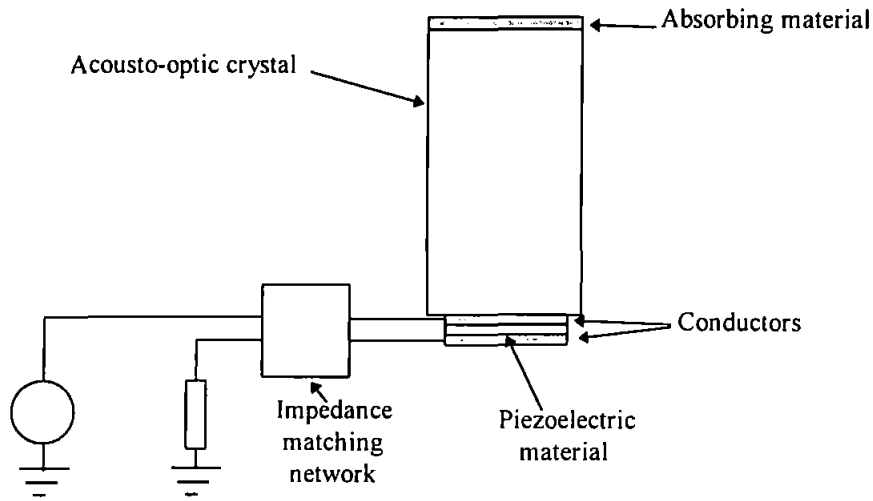


Figure 4.1 Acousto-optic cell diagram.

4.1.1 Particle analysis

The interaction between light and sound can be described in terms of wave interactions or particle collisions. The easier of the two approaches is the particle analysis. According to this picture, light consists of photons and sound consists of phonons. Each photon has momentum $h\mathbf{k}$ and energy $h\omega$, and each phonon has momentum $h\mathbf{k}_s$ and energy $h\omega_s$, where \mathbf{k} is the wave vector and ω is the optical frequency and h is planck's constant. The diffraction of light by an approaching sound can be described as a series of collisions, each of which involves a annihilation of one incident photon at ω_i and one phonon and a simultaneous creation of a new diffracted photon at a frequency ω_d , which propagates along the direction of the scattered beam. The conservation of momentum requires that the momentum $h(\mathbf{k}_s + \mathbf{k}_i)$ of the colliding particles is equal to the momentum $h\mathbf{k}_d$ of the scattered photon, so

$$\mathbf{k}_d = \mathbf{k}_s + \mathbf{k}_i \quad (4.1)$$

the conservation of energy takes the form

$$\omega_d = \omega_i + \omega_s \quad (4.2)$$

From Eq. (4.2) it can be seen that the diffracted beam is shifted in frequency by an amount equal to the sound frequency. Since the collision involves the annihilation of a phonon, conservation of energy decrees that the shift in frequency is such that $\omega_d > \omega_i$ and the phonon energy is added to that of the annihilated photon to form a new photon. Using this argument it follows that if the direction of the sound beam were reversed so that it was

receding from the incident optical wave, the scattering process could be considered as one in which a new photon (diffracted photon) and a new phonon are generated while the incident photon is annihilated. In this case, the conservation-of-energy principle yields

$$\omega_d = \omega_i - \omega_s \quad (4.3)$$

The conservation-of-momentum condition Eq. (4.1) is equivalent to the Bragg condition which can be shown to be [15]

$$2\lambda_s \sin\theta = \lambda / n_o \quad (4.4)$$

where n is the refractive index of the crystal, and λ is the wavelength of the light. To show why this is true, consider Figure 4.2. Since the sound frequencies of interest are below 10^{10} Hz and those of the optical beam are usually above 10^{13} Hz, we have

$$\omega_d = \omega_i + \omega_s \approx \omega_i, \text{ so } |k_d| \approx |k_i| \quad (4.5)$$

due to the relationship

$$k = \frac{2\pi}{\lambda} = \frac{2\pi f}{c} = \frac{\omega}{c} \quad (4.6)$$

and the magnitude of the two wave vectors is taken as k . The magnitude of the sound wave vector is thus

$$k_s = 2k \sin\theta \quad (4.7)$$

It will later be shown that this diffracted light is also doppler shifted by an amount proportional to the applied frequency.

Using $k_s = 2\pi/\lambda_s$, this equation is the same as Eq. (4.4).

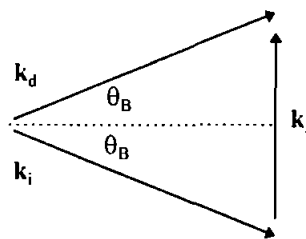


Figure 4.2 The momentum-conservation relation, Eq. (4.1), used to derive the Bragg condition $2\lambda_s \sin\theta_B = \lambda/n$, for an optical beam that is diffracted by an approaching sound wave. θ_B is the angle between the incident or diffracted beam and the acoustic wavefront.

It should be noted that k_i and k_d can be switched in Figure 4.2 giving a - sign in Eq. (4.7).

4.1.2 Thin-phase grating approximation

A simple co-ordinate system is defined for this example; the acoustic wave is propagating along the x-direction. Assuming a continuous sinusoidal wave and neglecting attenuation and diffraction effects for the moment, the resulting perturbation of the refractive index is given by

$$\Delta n(x,t) = \Delta n_0 \sin(\omega_s t - k_s x + \delta) \quad (4.8)$$

where the angular frequency is $\omega_s = 2\pi f_s$, f_s is the acoustic frequency, $k_s = 2\pi/\lambda_s$ is the acoustic wave vector, $\lambda_s = V_a/f_s$ is the acoustic wavelength, V_a is the velocity of the acoustic wave and δ is an arbitrary phase difference. The refractive index is a function of both position and time the magnitude of its change given by

$$\Delta n_0 = n_0^3 ps/2 \quad (4.9)$$

where s is the induced strain caused by the acoustic wave, and p is the elasto-optic coefficient. If we consider the ultra sonic beamwidth, L , to be narrow, the effect of the acoustic beam is to form a thin-phase grating whose phase dependence is given by

$$\Delta f(x,t) = 2\pi\Delta n_0 L/\lambda_0 \sin(\omega_s t - k_s x + \delta) \quad (4.10)$$

The electric field E_i , of a beam incident on this grating may be expressed as

$$E_i = E_0 e^{j\Delta f(x,t)} \quad (4.11)$$

where E_0 is the amplitude, $\omega_1 = 2\pi f_1$, $k_1 = 2\pi n/\lambda$, f_1 is the optical frequency $= c/\lambda$, λ is the optical wavelength, c is the speed of light in vacuum and n is the refractive index of the medium. After passing through the acoustic phase grating, the emerging output light, E_{out} , may be expressed as

$$E_{out} = E_0 e^{j[\omega_1 t - k_1 z + \Delta f(x,t)]} \quad (4.12)$$

This can also be expanded into a series of Bessel functions [16]

$$E_{out} = E_0 \sum_{q=-\infty}^{+\infty} J_q(2\pi\Delta n_0 L / \lambda_0) e^{j((\omega_1 + q\omega_s)t - k_1 z - qk_s x)} \quad (4.13)$$

which is simply the sum of the amplitudes of the q th order light resulting from the interaction. The physical interpretation of Eq. (4.13) is simply that each term in the summation gives rise to a plane wave; the electric field of the output light can be decomposed into a set of such plane waves. The amplitude of the q th order, E_q , is proportional to the electric field as well as the q th order Bessel function and is given by

$$E_q = E_0 J_q(2\pi\Delta n_0 L / \lambda_0) e^{j((\omega_1 + q\omega_s)t - k_1 z - qk_s x)} \quad (4.14)$$

the frequency of the qth order being

$$\omega_q = \omega_l + q\omega_s \quad (4.15)$$

so that the diffracted light is frequency shifted. This frequency shift is proportional to the diffracted order, and can be thought of as resulting from the doppler shift of the light as it diffracts from a moving grating. Note that each order propagates in a different direction, from the dependence of the propagation on q:

$$\mathbf{k}_q = i_z \mathbf{k}_l + i_x q \mathbf{k}_s \quad (4.16)$$

where the notation i_x refers to a unit vector in the x direction.

Of particular interest is to consider the first order, given by

$$E_{+1} = E_0 J_1(2\pi\Delta n_0 L / \lambda_0) e^{j(\omega_l + \omega_s)t} e^{-jk_l(z i_z \cos\theta_z + x i_x \sin\theta_x)} \quad (4.17)$$

The diffraction efficiency, or ratio of the intensities between the zero order and the first order is given by

$$I_1/I_0 = (J_1(2\pi\Delta n_0 L / \lambda_0))^2 / (J_0(2\pi\Delta n_0 L / \lambda_0))^2 \quad (4.18)$$

when $2\pi\Delta n_0 L / \lambda_0 \ll 1$ this simplifies to

$$I_1/I_0 = (2\pi\Delta n_0 L / \lambda_0)^2 \quad (4.19)$$

substituting in for Δn_0 gives

$$I_1/I_0 = \pi^2 n_0^6 L^2 p^2 s^2 / \lambda_0^2 \quad (4.20)$$

The acoustic power P_a can be defined as

$$P_a = \frac{1}{2}(\rho V_a^2 s^2) \quad (4.21)$$

where ρ is the density of the medium, taking this as a factor in Eq. (4.18).

$$I_1/I_0 = (2\pi^2 n_0^6 L^2 p^2 / \rho V_a^2 \lambda_0^2) P_a \quad (4.22)$$

A cell of width L, its interaction length, and height H will have a total acoustic power

$$P_{tot} = P_a(LH) \quad (4.23)$$

giving

$$I_1/I_0 = 2\pi^2 n_0^6 L p^2 P_{tot} / H \rho V_a^2 \lambda_0^2 \quad (4.24)$$

or

$$I_1/I_0 = (2\pi^2 L P_{tot} / H \lambda_0^2) M_2 \quad (4.25)$$

M_2 is a figure of merit used to evaluate acousto-optic configurations. The figure of merit is defined as

$$M_2 = \frac{n_0^6 p^2}{\rho V_a^3} \quad (4.26)$$

where n_0 is the refractive index of the material, p is strain-optic coefficient, ρ is the density of the material, and V_a is the sound velocity. As the diffraction efficiency is proportional to M_2 (Eq. (4.25)), it can be seen from Eq. (4.26) that low acoustic-wave velocities and high indices of refraction will give high diffraction efficiencies.

4.1.3 Thick-phase grating approximation

In many cases the grating is made much thicker than assumed in section 4.2.2. in order to improve interaction efficiency. To analyse the thick grating problem, it is necessary to solve the wave equation which takes the form

$$\nabla^2 E = [n(x,t)^2 / C^2] \frac{d^2 E}{dt^2} \quad (4.27)$$

where the refractive index is a function of both space and time

$$\Delta n(x,t) = \Delta n_0 \sin(\omega t + t - k_a Z + \varphi) \quad (4.28)$$

To solve this equation, a form for the electric field of the diffracted light E , in terms of the incident light E_0 is required. The electric field can be expressed by the following Fourier series expansion

$$E = E_0 \sum_{q=-\infty}^{\infty} A_q(Z) e^{j(\omega_q t - \mathbf{k}_q \cdot \mathbf{r})} \quad (4.29)$$

where $A_q(Z)$ is the amplitude of the q th Fourier component of the light, and the propagation vector is given by the vector dot product

$$\mathbf{k}_q \cdot \mathbf{r} = K(z \cos \theta + x \sin \theta) + q k_a x \quad (4.30)$$

where \mathbf{r} indicates a general propagation vector, \mathbf{k}_q comes from Eq. (4.16) and we have assumed that the incident light is propagating in the xz plane at an angle θ with respect to the optical axis. If we now substitute our expression for the electric field E , into the wave equation we obtain a series of coupled differential wave equations in the diffracted amplitudes, A_q

$$\frac{dA_q}{dz} - \frac{\pi \Delta n_0}{\lambda} (A_{q-1} - A_{q+1}) = jqQ(q - 2\alpha) \frac{A_q}{2L} \quad (4.31)$$

where

$$Q = \frac{2\pi \lambda Z}{n_0 \Lambda^2} \quad (4.32)$$

and

$$\alpha = -\frac{n_o \Lambda}{\lambda} \sin \theta \quad (4.33)$$

where Λ is the acoustic wavelength. This is related to the applied drive frequency f by $\Lambda = V_a/f$ where V_a is the acoustic velocity

The transition from Raman-Nath mode of operation to Bragg mode is characterised by defining a Q factor.. The boundary between the two modes of operation is $Q \approx 2\pi$. So that if $Q \ll 2\pi$ the cell is operating in Raman-Nath mode, and if $Q \gg 2\pi$ the cell is operating Bragg mode.

It is assumed that the second derivative of A_q with respect to z is negligible in comparison with other terms.

The first term in our coupled differential equation ($\pi \Delta n_o / \lambda$) is the coupling efficient between adjacent modes. A given mode can couple energy only into an adjacent mode; for instance , if $q = 0$ then only a zero and first order modes appear.

The amount of energy transfer between adjacent modes depends not only on the coupling coefficient, but also on the degree of phase matching between modes. If two adjacent modes are not phase matched there can be no energy transfer.

If the phase difference is small then there can be transfer between the diffracted orders. We have noted that the zero order ($q=0$) is coupled only to the first order ($q=\pm 1$); good energy transfer from the zero order will only occur when the term

$$jqQ(q - 2\alpha) \frac{A_q}{2L} \quad (4.34)$$

is small for $q = \pm 1$. This can be accomplished in two ways.

- 1) Q very small and $\theta \approx 0$ (Raman-Nath)
- 2) operating at angles of incidence such that $\alpha = \pm 1/2$ so that Q can be arbitrarily large. (Bragg regime)

4.1.4 Raman Nath mode

If a wave passes through an element whose response is $|a(x)|e^{j\phi(x)}$ it will have the form $|a(x)|\cos[2\pi f_1 t + \phi(x)]$, where f_1 is the frequency of the light. In a similar fashion, light passing through an acousto-optic cell when driven by a pure sinusoidal frequency f_j , is phase modulated so that

$$A(x,t) = A_o \cos \left[2\pi f_1 t + \frac{2\pi Z}{\lambda} \left\{ n_o + \Delta n_o \cos \left[2\pi f_j \left(t - \frac{T}{2} - \frac{x}{V_a} \right) \right] \right\} \right] \quad (4.35)$$

where $A(x,t)$ is the amplitude of the output wave in space and time, A_o is the amplitude of the incident light wave, and Δn_o is the change in the refractive index within the interaction medium induced by the travelling strain wave. The argument $t - T/2 - x/V_a$ shows that $A(x,t)$ is a wave travelling in the positive x direction with velocity v and that the cell has a transit time of $T = L/V_a$, where L is the length of the acousto-optic cell. The strain wave is proportional to the amplitude of the acoustic wave. A sinusoidal input to the cell causes the cell to act as a phase diffraction grating travelling in the x direction. Light is diffracted by the grating to produce several positive and negative diffracted orders. Analysis of the operation of the acousto-optic cell yields the Raman-Nath equation for the amplitude of the i th diffracted order [17]

$$|A_i| = |A_o J_i(\gamma)|, \quad (4.36)$$

where A_o is the amplitude of the incident light, J_i is the i th order Bessel function, and γ is the phase shift of the light induced by the refractive index change. The normalised diffracted amplitude of the i th wave is indicated by m_i [17]

$$m_i = \frac{A_i}{A_o} = (-j)^i J_i \left[\frac{2\pi Z \Delta n}{\lambda} \right], \quad (4.37)$$

where $J_i(\bullet)$ is an i th order Bessel function of the first kind. m_i is defined as the modulation index for the i th order; it is defined as the ratio of the diffracted light amplitude to the incident light amplitude. The amplitude of the diffracted light, as a function of the phase shift of the Bessel function, is shown in Figure 4.3. For the undiffracted light and the first two diffracted orders.

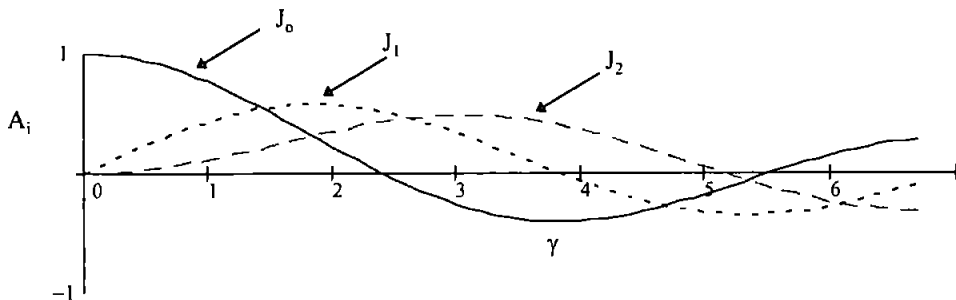


Figure 4.3 Bessel functions of order 0, 1, and 2.

4.1.5 The Bragg Mode

From Eq. (4.37). We see that large values of Δn and Z lead to high diffraction efficiencies. As light is wasted when multiple orders are generated the interaction width Z of the crystal is increased until the Bragg mode of operation is reached. For optical signal processing the Bragg mode is usually used because more of the optical power is coupled into the desired order. It is possible to have only two orders present the zero and one negative diffracted order.

The Bragg angle is defined as

$$\sin\theta_B = \frac{\mathbf{k}_a}{2\mathbf{K}} \quad (4.38)$$

where \mathbf{k}_a is the wave vector of the acoustic wave and \mathbf{K} is the wave vector of the light wave, or in terms of wavelength

$$\sin\theta_B = \frac{\lambda}{2\Lambda} \quad (4.39)$$

where $\Lambda = V_a/f$. The optimum illumination for the Bragg mode is therefore at the off-axis Bragg-angle θ_B , whereas the illumination is normal to the surface of the acousto-optic cell in the Raman-Nath- mode.

From Eq. (4.39) the angle between the incident and diffracted light waves, known as the deflection angle α , is given by

$$\alpha = \theta_i + \theta_d = 2\theta_B \approx \frac{\lambda}{\Lambda} = \frac{\lambda}{V_a} f \quad (4.40)$$

Thus the deflection angle is proportional to the frequency of the acoustic wave f . The direction of the laser beam is controlled by the change in frequency of the acoustic wave, which in turn equals the frequency of the electrical signal driving the piezoelectric transducer. If the frequency change is given by Δf , then the scan angle of the beam will be

$$\Delta\alpha = \frac{\lambda}{V_a} \Delta f \quad (4.41)$$

Although in practical applications the Bragg mode of operation is almost always used to produce the highest diffraction efficiency, there are advantages in using the Raman-Nath mode in explaining basic optical signal processing theory. The symmetry of the Raman-Nath mode in the positive and negative orders is useful.

Having discussed the cases where $Q \ll 1$ and $Q \gg 1$ arising from coupled mode theory, the case for $Q \approx 1$ has not been considered. This condition known as the transit region has no analytical solution, numerical computations of diffracted light intensities are relied upon to show the response from (4.31) [18]. Physically, the diffracted light in this region exhibits some properties of both Bragg and Raman-Nath cases, depending on the exact value of Q . At this point it is possible to deal with the Bragg regime by restricting the analysis to simple cases. The Bragg regime is often used for signal processing applications because all of the diffracted light is diffracted in a single order, and no optical power is lost in higher diffracted orders.

4.1.6 Time Bandwidth product

The time bandwidth product is the product of the bandwidth and the time duration of the processed signal. It tells us the degree of complexity of a signal, its derivation begins by relating the total angular deflection range $\Delta\theta$ to the bandwidth Δf :

$$\Delta\alpha = \frac{\lambda}{V_a} \Delta f \quad (4.42)$$

so that the deflection angle is linear in applied frequency. The number M of resolvable angles produced by the cell is

$$M = \frac{\text{Angular Range}}{\text{Angular Resolution}} = \frac{\Delta\alpha}{\lambda / L} \quad (4.43)$$

where L is the length of the acousto-optic cell and λ/L is the intrinsic angular resolution of any physical system. Using Eq. (4.42) in Eq. (4.43) we find

$$M = \frac{\lambda \Delta f / V_a}{\lambda / L} = \frac{L}{V_a} \Delta f = T \Delta f = TW \quad (4.44)$$

remembering that $L = V_a T$ and the total bandwidth of the cell is $\Delta f = W$. T is the transit time of the cell.

4.2 Applications of acousto-optic devices

Acousto-optic cells are configured in different ways for different functions. These configuration can be split into three categories. They can be used to modulate light temporally, deflect light (modulate it spatially), or be used as an acousto-optic tuneable filter.

The acousto-optic tuneable filter is a device which can be electronically tuned to pass a selected optical wavelength within a specific spectral range. This gives the AOTF the ability to rapidly scan across the entire operational spectral range. It should be noted that while the AO deflectors and modulators use a narrowband incident light beam (i.e. laser) tuneable filters are designed as dispersive elements and therefore require broadband lights sources. Therefore the performance parameters of AOTFs are quite different from the modulators and deflectors and not relevant to this research. For more details on these devices see [19]

When used as modulators the illumination must be a narrow beam because the rise time associated with the modulation bandwidth is proportional to the time τ required for the acoustic beam to travel across the optical beam. As the acoustic transit time decreases, the risetime decreases so that the corresponding bandwidth increases.

The 10-90% rise time t_r for an acousto-optic modulator is a function of the transit time τ . For a Gaussian input beam profile, truncated at the $1/e^2$ points in intensity $t_r \approx \tau/1.5$ and the frequency response roll off R , defined in decibels is [20]

$$R = 10 \log \left[e^{-\pi^2 f^2 \tau^2 / 8} \right] \quad (4.45)$$

The modulation bandwidth f_m associated with a response fall off R is simply the value of modulation frequency which satisfies Eq. (4.45).

$$f_m = c\sqrt{R/\pi\tau} \quad (4.46)$$

where $c = \sqrt{(0.8 \ln 10)} \approx 1.4$. The relationship between modulation bandwidth and acoustic transit time is

$$f_m = 0.445\sqrt{R/\tau} \quad (4.47)$$

This can be expressed in terms of risetime t_r ,

$$f_m = 0.29\sqrt{R/t_r} \quad (4.48)$$

The modulation rate required for the response to fall below the -3dB level is now

$$f_m = 0.77/\tau \quad (4.49)$$

or in terms of risetime

$$f_m = 0.5/t_r \quad (4.50)$$

When driven by a CW frequency, the AO cell behaves as a random access beam deflector which addresses a specific point in the focal plane of the lens. It is in this mode of operation that the AO cell is used in the acousto-optic demodulator. Figure 4.4 shows an acousto-optic cell at plane P_1 with an acoustic velocity V_a and a length $L = V_a T$. The cell is driven with a signal

$$f(t) = \cos(2\pi f_k t) \quad (4.51)$$

to access the k th spot position in the scan line. This signal produces a positive diffracted order whose Fourier transform is generated by a lens with focal length F :

$$F_+(\xi, t) = \int_{-\infty}^{\infty} f_+(x, t) e^{j(2\pi/\lambda F)\xi x} dx \quad (4.52)$$

where $f_+(x, t) = \text{rect}(x/L) \exp[j2\pi f_k(t - T/2 - x/V_a)]$. The Fourier transform of $f_+(x, t)$ is

$$\begin{aligned} F_+(\xi, t) &= \int_{-L/2}^{L/2} e^{j2\pi f_k(t - T/2 - x/V_a)} e^{j(2\pi/\lambda F)\xi x} dx \\ &= e^{j2\pi f_k(t - T/2)} \text{sinc} \left[\left(\frac{\xi}{\lambda F} - \frac{f_k}{V_a} \right) L \right] \end{aligned} \quad (4.53)$$

ignoring amplitude scaling factors from Eq. (4.53), we find that the lens focuses light at the spatial position

$$S_k = \frac{\lambda F}{V_a} f_k \quad (4.54)$$

at plane P_2 . This result shows that the spot position is linearly proportional to the applied frequency.

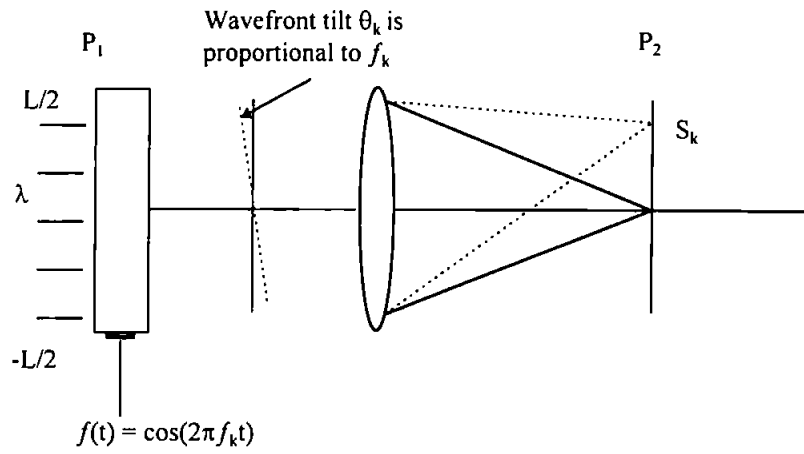


Figure 4.4 Acousto-optic scanner

5. Acousto-optic demodulator - System description

A schematic diagram of the AO demodulator system is shown in Figure 5.1. Similar systems, using only a single photodiode detector, have been described by Pieper and Poon [1] and Brooks and Reeve [21] for FM demodulation and by Reeve and Houghton [3] for demodulation of phase-reversal keying PRK signals.

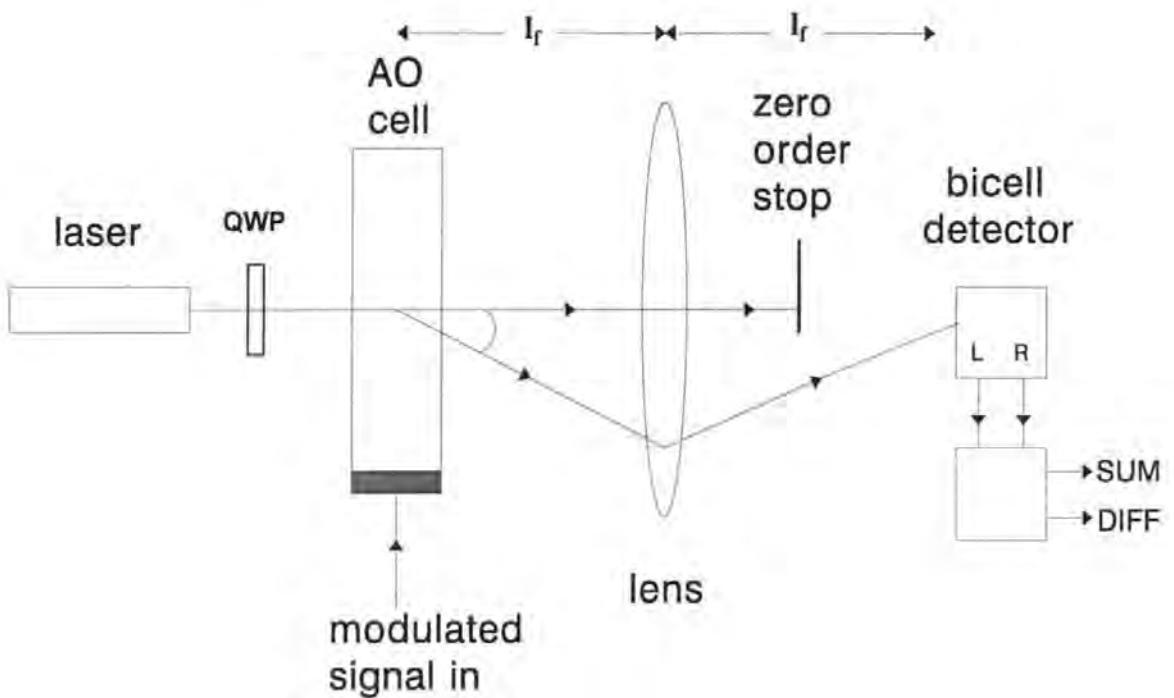


Figure 5.1 The acousto-optic demodulator

The detector assembly employed in this case is a bi-cell device (Figure 5.1) consisting of two photodiodes separated by a narrow gap of width g .

The signal under investigation is applied to the AO-cell. The properties of AO-cells are well known; a review is given in chapter 4 and more detailed descriptions can be found in text books such as Vanderlugt [4] and Stroud [5]. A narrow laser beam passing through the cell is deflected through an angle proportional to the signal carrier frequency. In this first order diffracted light, the beam is spatially modulated by the signal instantaneously in that

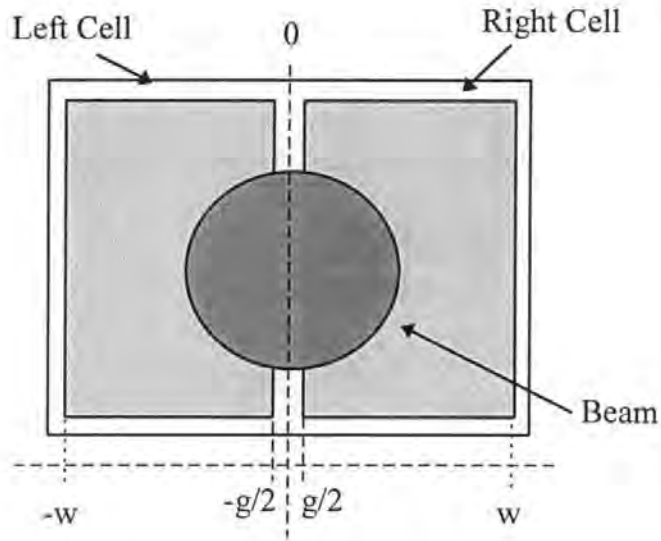


Figure 5.1 The bi-cell detector

part of the cell that is illuminated by the laser beam. The spatial distribution of light amplitude in the focal plane of the lens is therefore proportional to the Fourier transform of that part of the signal within the window formed by the laser beam passing through the AO-cell (Appendix B). Since the photodiodes respond to the light intensity, their output will be proportional to the power spectral density of the signal integrated over the illuminated part of the detector. The system therefore monitors changes in the power in the windowed signal over two frequency bands defined by the size and position of the bi-cell elements. The signal from the left and right elements of the bi-cell detector are:

$$s_L = k \int_{-\infty}^{-g/2} |F(x)|^2 dx \quad \text{and} \quad s_R = k \int_{g/2}^{\infty} |F(x)|^2 dx \quad (5.1)$$

where k is a constant and $F(x)$ is the spatial light distribution in the focal plane of the lens, which as previously stated, is proportional to the Fourier transform of the windowed signal. Strictly the limits of Eq. (5.1) should not be written as $\pm\infty$, but $\pm w$, where $\pm w$ are the edges of the bi-cell, although in practice provided that the focal length of the lens is chosen suitably any light lost off the edge of the bi-cell is negligible, and the results will be the same. These equations do not generally lend themselves easily to an analytic solution; the response of the system has therefore been simulated using a computer model (see chapter

6), these results were used to predict how a practical system would perform under various conditions.

5.1 Component selection

5.1.1 The Laser source

In section 7.3 a graph of frequency resolution versus optical power shows how the resolution improves with more power. This suggests that a more powerful laser would improve the performance of the system, but due to the small size of the photodetectors, the optical power required to saturate them is still small ; 0.196 μW for the small detector and 4.16 mW for the larger one (based on the maximum power density of the cells of $10\text{mW}/\text{cm}^2$). Therefore a powerful laser (i.e. $> 5 \text{ mW}$) could not be used for the small detector. The higher power HeNe lasers available are not frequency stabilised, and this frequency drift causes low frequency noise on the output meaning that the beam will not stay centred on the bi-cell detector.

Changing the wavelength of the laser from visible to infra-red ($\approx 850 \text{ nm}$) would mean that the silicon photodetectors would be working on the most sensitive part of their responsivity curve. To operate at this wavelength would require the use of laser diodes as sources. Unfortunately laser diode technology has not yet progressed to the stage where a constant power frequency stabilised beam is readily available, the cost of this sort of quality laser diode was too much for this project. The results gained from the infra-red system used, were all limited by the laser source rather than any other effects.

The laser source used to obtain the practical results was a He-Ne laser, frequency stabilised to one part in 10^9 with an operating wavelength λ , of 632.8 nm, this is in the red part of the visible spectrum. The laser had a nominal maximum optical power output of 1 mW and a quoted beamwidth of 0.49mm at the $1/e^2$ intensity points.

5.1.2 The AO-cell

There were many factors affecting the choice of AO-cell; cost of high frequency cells, diffraction efficiency, acoustic velocity, wavelength of the light, bandwidths of all the signal generating and logging equipment. The 2045 signal generator can produce signals at data rates up to 800 MHz, giving a bandwidth of 400 MHz and the 6100 waveform

digitiser and analyser can capture signals with bandwidths of up to 100 MHz. Therefore it was only realistic to use a $\text{TeO}_2(\text{SS})$ crystal which generally have centre frequencies of 45 or 90 MHz rather than $\text{GaP}(\text{L})$ or $\text{LiNbO}_3(\text{L})$ which can operate at centre frequencies of 2 GHz ((SS) and (L) denote slow shear and longitudinal respectively, these represent the type of acoustic wave used in the AO device).

The AO-cell used was an Isomet OPT-1 TeO_2 crystal operating in the slow shear mode (for good aperture and high diffraction efficiency) at an acoustic velocity V_a of 617m/s. It has a centre frequency of 45 MHz and a bandwidth of 30 MHz. It is quoted as having a diffraction efficiency η of 50%/Watt (RF power) which means we can expect up to half a milliwatt of optical power diffracted into the first order at the detector.

5.1.3 The detector assembly

The detector assembly consisted of a bi-cell detector, two similar transimpedance amplifiers and a sum and a difference amplifier to give the required output signal, Figure 5.2. Two bi-cell detectors were used, one with a gap of $80\mu\text{m}$ and the other with a gap of $10\mu\text{m}$. The relationship between the gap size and the standard deviation of the beam at the detector σ_p , is critical and is described in chapters 7 and 8 .

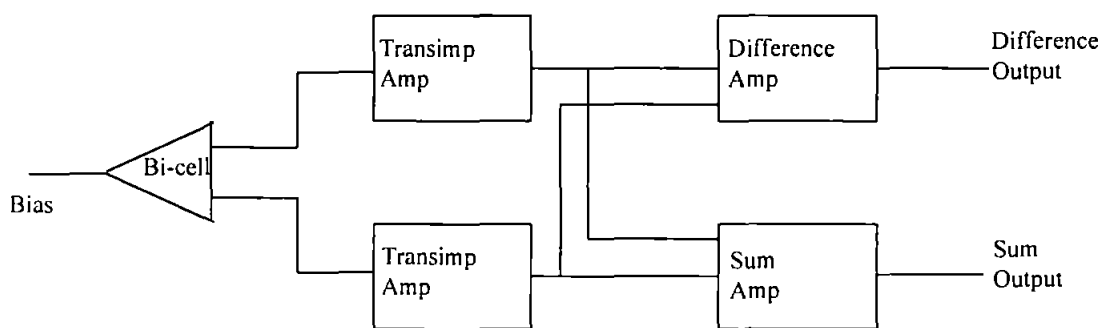


Figure 5.2 Block diagram of the detector system.

The specifications for the detector were sent to a company specialising in the production of low noise transimpedance amplifiers, as it was important that for small frequency deviations the output was limited by the shot noise on the signal and not amplifier noise. The detector used had calculated shot noise at maximum output of $600\ \mu\text{V rms}$ ($3.5\ \text{mV p-p}$)

5.2 Experimental Procedure

In order to gain maximum diffraction efficiency from an AO cell operating in slow shear mode, circularly polarised light is required, achieved by inserting a quarter wave plate between the linearly polarised laser and the AO-cell. The cell was driven by a 1 watt wideband amplifier which in turn was driven by a variable gain preamplifier. The zero order light was then blocked so that only the first order passed through the lens onto the detector assembly. The focal length of the lens depended on the gap size of the bi-cell and application that the system was being set-up for (i.e. FM or digital demodulation). See chapters 7 and 8.

A frequency of 50 MHz was used as the centre frequency of the undeviated carrier. The detector assembly was then positioned such that, with no modulation on the carrier the first order diffracted light fell equally on the two halves of the bi-cell. This was accurately achieved by inverting one trace on the scope and adding it to the other, the detector was then moved until the difference of the two detectors was zero. Finally the AO-cell was rotated on a turntable until the maximum light was diffracted into the first order. This is done in order to ensure the optimum Bragg diffraction condition is met .

The test signal could be generated in one of two ways; the simplest was to program the required waveform directly onto the Analogic 2045, and add any noise using its own noise generator. The second was to generate a sampled signal on the PC using Mathcad, and download the digitised signal to the 2045, where the analogue signal would be produced. The advantage of the second method was that the signal generated on the PC could also be analysed using the model, so an exact comparison of the results from the two systems was possible. The output from the detector assembly was captured by an Analogic Data 6100 waveform analyser which stores the data, until it could be down loaded back onto the computer. Once the results were on the computer they could be analysed more thoroughly in terms of spectral content, signal to noise ration, standard deviation and variance. Figure 5.3 shows a block diagram of the experimental set-up.

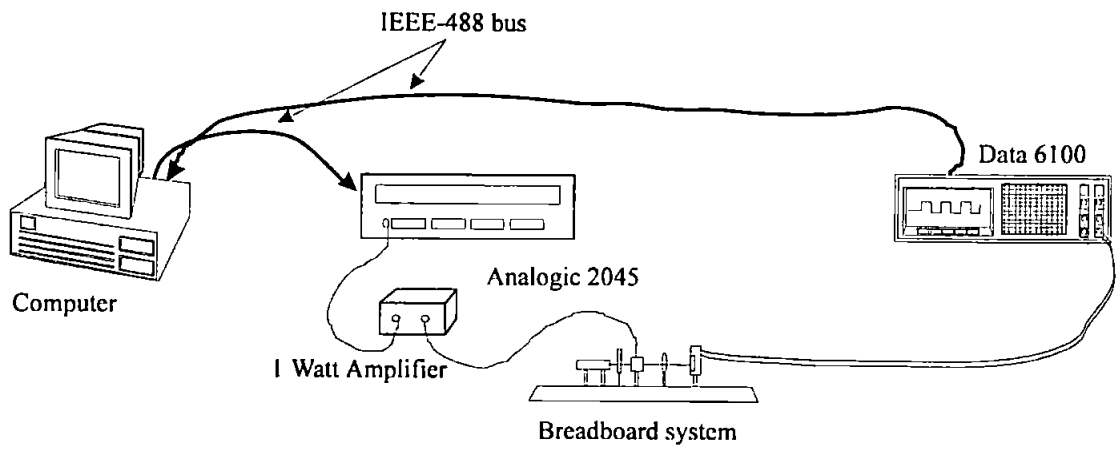


Figure 5.3 Experimental set-up

6. The computer simulation

In order to create a computer model of the AO-demodulator system it was necessary to look at the operation of each component in the system. This section shows how each component was analysed and how the significant parameters were extracted so that they could be easily changed and their effect on the system noted.

6.1 System components

The following describes in detail the action and important parameters of each of the components in the system. Figure 6.1 shows a flow diagram of the operation of the computer model. It also shows how these sections of the model are combined to represent the operation of each of the components listed below :

6.1.1 Laser

The laser generates a collimated beam of light, the beam profile or intensity distribution of which is Gaussian. The specifications of the laser that are important to the system are its wavelength, its beamwidth and its power. The beamwidth of the laser is usually quoted as the distance between the e^{-2} points on the intensity profile, this corresponds to $4\sigma_0$, where σ_0 is the standard deviation of the Gaussian. Obviously the laser is not truncated at the e^{-2} points. In the model the laser beam is represented as having a width of $6\sigma_0$, which yields results virtually indistinguishable from those obtained calculating the width to $20\sigma_0$.

6.1.2 AO-cell

The AO-cell is the transducer that converts the RF signal into an optical signal. It diffracts a percentage of the laser beam into the first order, the amount of light diffracted is given by the diffraction efficiency of the cell. The spatial distribution of light in the first order is proportional to the signal in the laser beam window of the cell, if the cell is being operated within its linear range. The width of this window, in the time domain, depends on σ_0 and V_a (the acoustic velocity of the cell).

6.1.3 Lens

By placing a lens between the AO-cell and the detector the instantaneous Fourier transform of the light amplitude in the first order diffracted beam appears in the focal plane of the lens. The choice of focal length l_f , of this lens is dependent on the beamwidth of the laser σ_0 and the size of the gap in the bi-cell Eq. (6.5)

6.1.4 Detector

The bi-cell responds to the integral of the light intensity, i.e. (amplitude)², falling on each element. Since the spatial distribution of light in the focal plane of the lens is the Fourier transform of the signal in the AO-cell, this is effectively integrating the power spectral density, (PSD) of the signal over frequency limits defined by the position and size of the bi-cell elements. As mentioned earlier the gap size of the bi-cell affects the choice of the lens, it is also important that the elements are big enough to catch all the light as the beam is deflected left and right. The bi-cell also sets the maximum laser power for the system, which is limited by the maximum optical power the detector can take without saturating, normally expressed in mW/cm^2 .

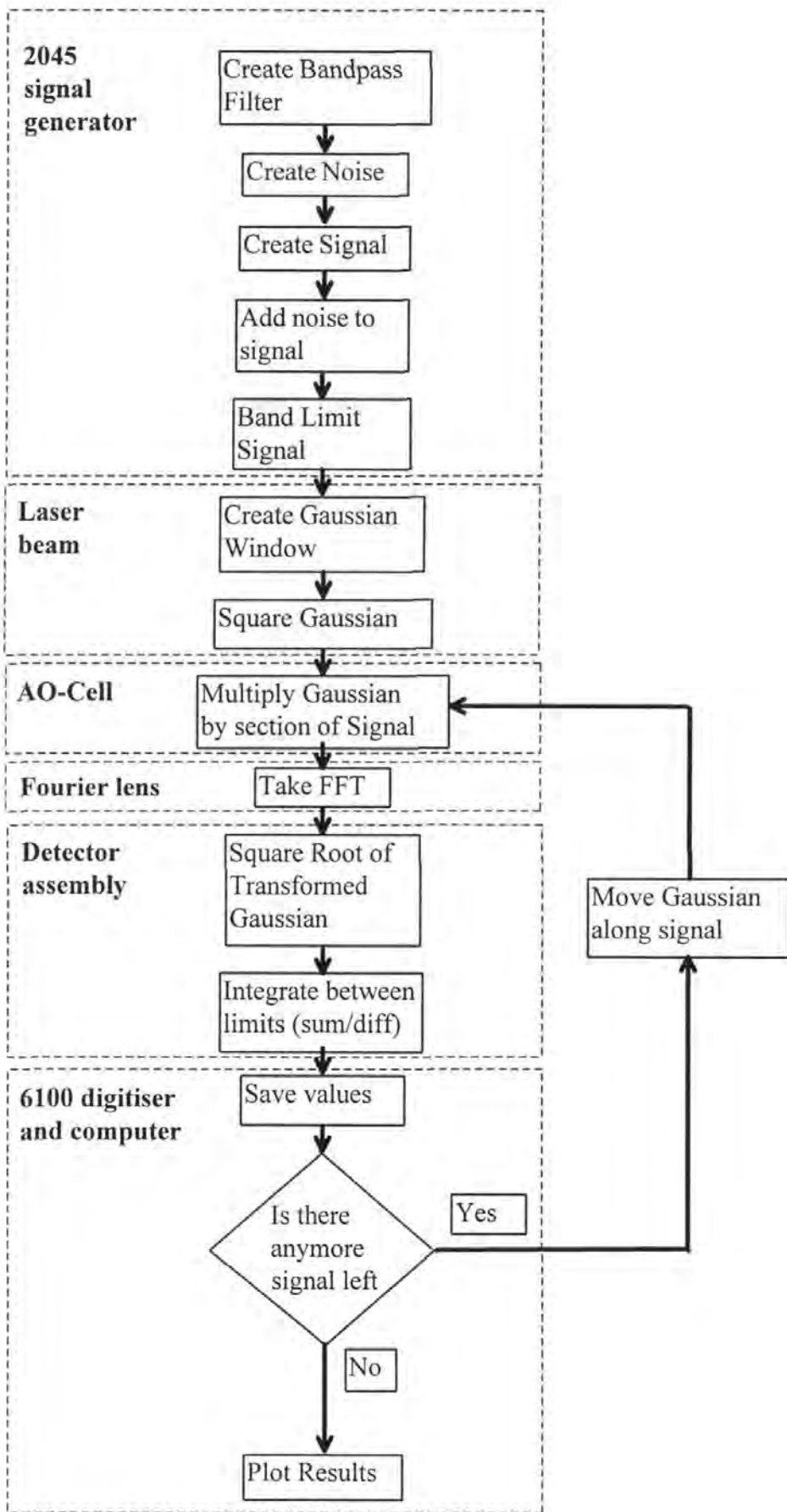


Figure 6.1 Flow chart of mathematical model

6.2 Relevant equations used in the computer model

A standard Gaussian beam intensity profile was created using the equation

$$I_s(x) = \frac{P}{\sqrt{2\pi\sigma_o^2}} e^{-\frac{x^2}{2\sigma_o^2}} \quad (6.1)$$

where P is the total power in the laser beam.

In order to maintain the relationships between the time aperture of the system which is proportional to σ_o/V_a and the frequency of the modulated signal, the number of points calculated for each standard deviation in Eq. (6.1) was related to the sampling frequency, used to generate the test signals

$$\text{StdDevPoints} = \frac{\sigma_o}{V_a} * f_s \quad (6.2)$$

Eqs. (6.3) and (6.4) are examples of the signals used to test the system, the FSK signal was created using

$$\begin{aligned} FSK(t) &:= \sin[2\pi(f_c - f_{dev})t] & t = 0 - 1 \mu\text{s} \\ FSK(t) &:= \sin[2\pi(f_c + f_{dev})t] & t = 1 - 2 \mu\text{s} \end{aligned} \quad (6.3)$$

and the Biphase signal

$$\begin{aligned} BPSK(t) &:= \sin[2\pi f_c t] & t = 0 - 1 \mu\text{s} \\ BPSK(t) &:= \sin[2\pi f_c t + \pi] & t = 1 - 2 \mu\text{s} \end{aligned} \quad (6.4)$$

It may be shown (Appendix B) for an unmodulated carrier applied to the AO-cell, that the intensity profile of the beam in the focal plane of the lens is also Gaussian with the standard deviation σ_t given by

$$\sigma_l = \frac{\lambda l_f}{4\pi\sigma_o} \quad (6.5)$$

where λ is the wavelength of the light and l_f is the focal length of the lens. This is obtained by squaring the Fourier transform of the square root of the intensity profile.

When a modulated signal is applied to the Bragg cell, the light amplitude profile at the detector is proportional to $F(x)$ the Fourier transform of the applied signal. The signal from the left and right elements of the bi-cell are

$$S_L = k \int_{-\infty}^{-g/2} P(x) dx \quad S_R = k \int_{g/2}^{\infty} P(x) dx \quad (6.6)$$

where $P(x)$ is the PSD of the signal instantaneously within the cell (i.e. $|F(x)|^2$) and k is a constant dependant on the responsivity of the cell.

From Eq. (4.8) the displacement δx of the diffracted spot at the detector due to a change in frequency δf can be shown to be

$$\delta x = l_f \delta \theta = \frac{\lambda l_f}{V_a} \delta f \quad (6.7)$$

if we divide Eq. (6.7) by Eq (6.5) we obtain

$$\frac{\delta x}{\sigma_l} = \frac{4\pi\sigma_o}{V_a} \delta f \quad (6.8)$$

This ratio, which expresses lateral deviation δx of the diffracted spot at the detector due to applied frequency δf , in terms of the spot size, is independent of the laser wavelength and the focal length of the lens. Therefore the model refers all measurements at the detector, including the size of the bi-cell gap to the standard deviation of the unmodulated beam at the detector σ_l .

6.3 Implementation of the model

Once the sampling frequency has been set-up and the number of samples decided, the IIR digital bandpass filter can be generated. The filter generated is an eighth order Butterworth filter, set to the required bandwidth, normally 1 MHz, at a centre frequency of 50 MHz.

The function used to generate this filter is contained in Mathcad, the design procedure is an implementation of algorithms by Stearns and David [22] and produces the response shown in Figure 6.2.

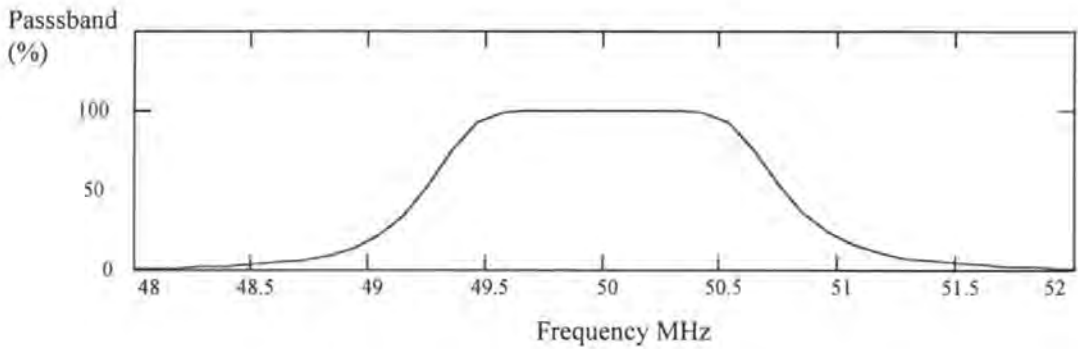


Figure 6.2 Response of the bandpass filter

The noise was randomly generated by a Mathcad function. The vector generated is viewed as the output of N independent noise sources each following a Gaussian probability distribution of mean 0 and standard deviation 1. Figure 6.3 shows a $10\ \mu\text{s}$ sample of generated noise signal.

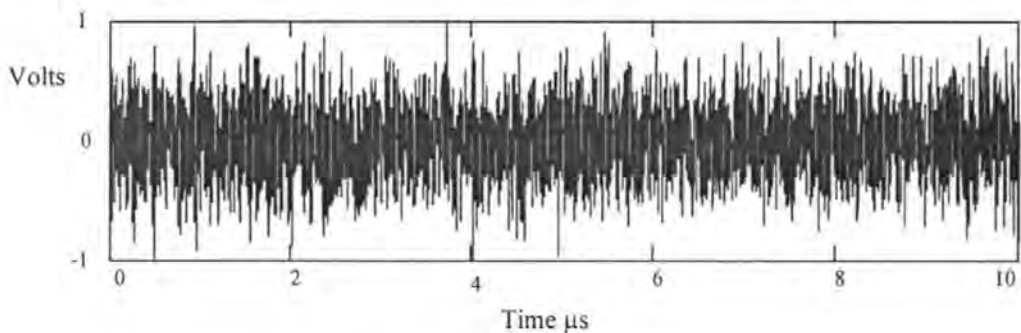


Figure 6.3 $10\ \mu\text{s}$ of generated noise

The Gaussian noise has a uniform spectrum over the entire range so that a portion of it will always affect the spectrum of the signal being demodulated, Figure 6.4 shows the frequency spectrum of the signal shown in Figure 6.3.

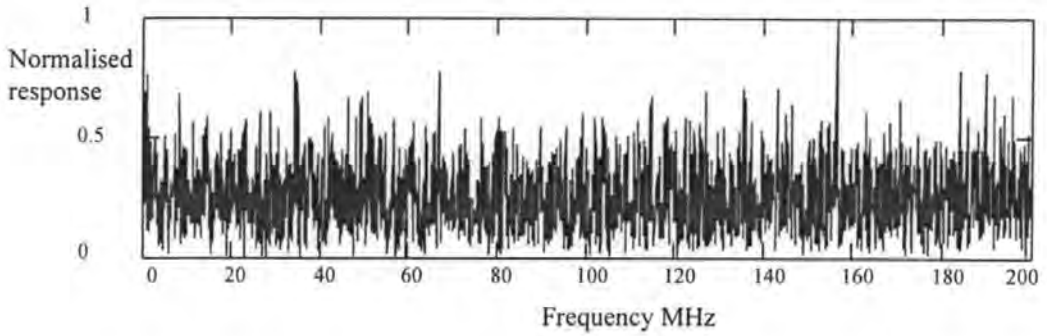


Figure 6.4 Spectrum of unfiltered noise

The signal was then created according to the type of modulation to be modelled. The signal used a carrier frequency of 50 MHz, as would the experimental system, and the modulation was then added accordingly. Figure 6.5 shows 1 μ s of PSK modulation with a modulation rate of 1.25 Mbps.

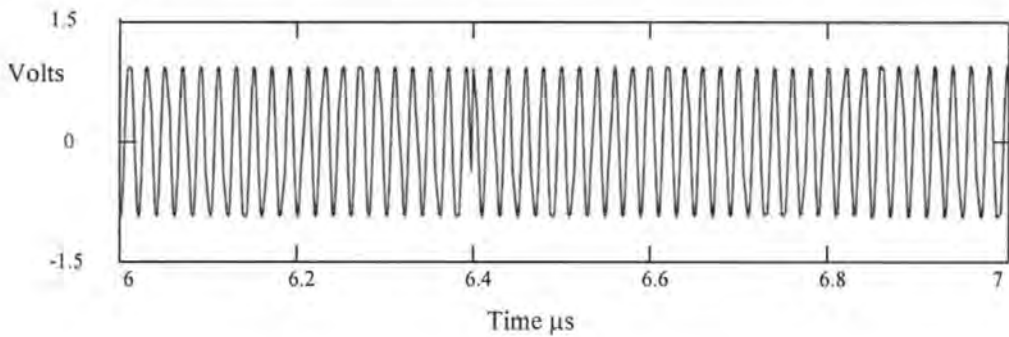


Figure 6.5 1 μ s of PSK modulation $f_c = 50$ MHz

Figure 6.6 shows the spectrum of 20 μ s of randomly modulated PSK signal. It can be seen that an approximation to the expected sinc function is formed although because the length of signal taken was only 20 μ s it is not a particularly close approximation.

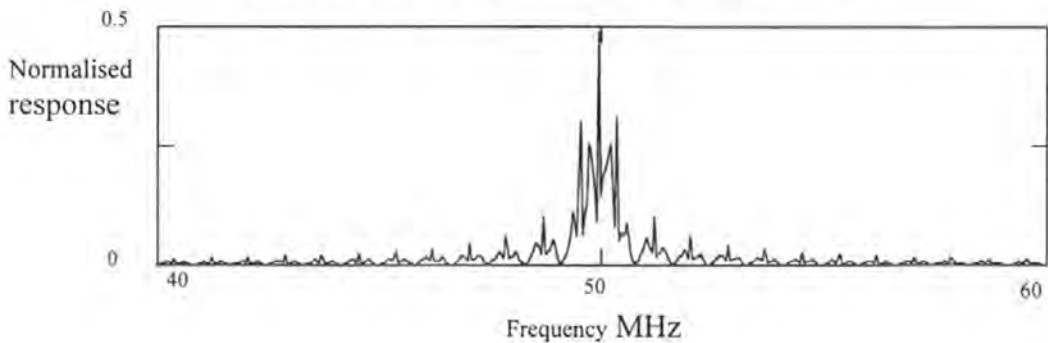


Figure 6.6 Spectrum of unfiltered signal

The normalised plot has been clipped to half of the normalised amplitude, in Figure 6.6 to show greater detail of the outer frequencies on the figure. A longer signal would have given a more representative power spectra, unfortunately the limits of the software did not allow this.

The signal is added to the noise in such a way that the signal to noise ratio can be easily changed. The bandwidth of the noise is limited by the bandpass filter shown in Figure 6.2. Obviously the narrower the filter the better, unfortunately the minimum bandwidth for the filter is set by the type of modulation used. In this example the bandwidth was 1 MHz. The SNR was set by calculating the unscaled SNR of the signal + noise using

$$\frac{\text{var}(\text{noise})}{\text{var}(\text{signal})}$$

where var takes the variance of the data, and multiplying it by the desired SNR

$$\frac{\text{SNR}_{\text{desired}}}{10} \cdot 10$$

and taking the square root, thus calculating the factor by which the noise should be divided to obtain the desired SNR. The filtered signal shown in Figure 6.9 has an SNR of 13 dB

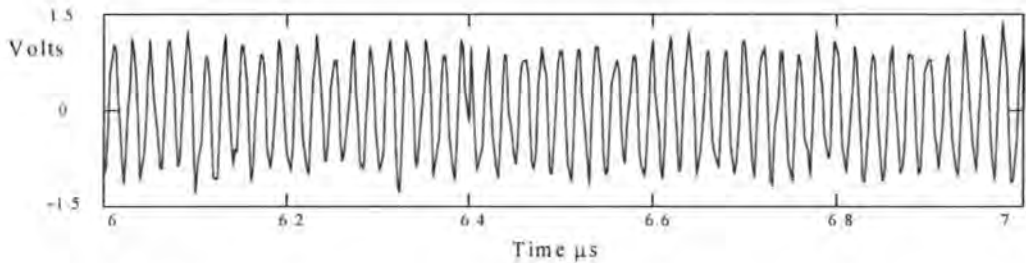


Figure 6.7 Unfiltered signal + noise

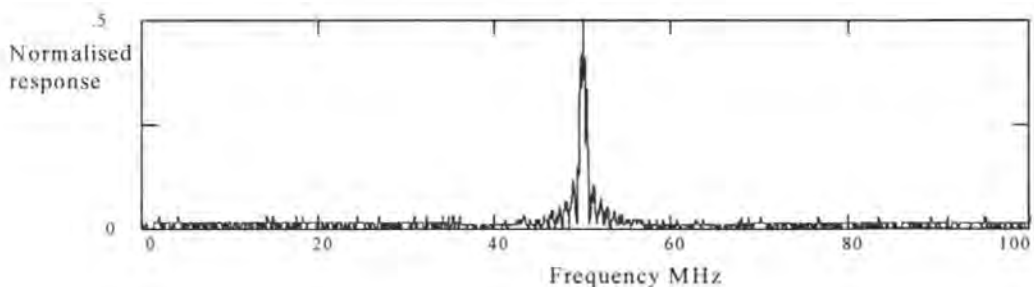


Figure 6.8 Unfiltered and unclipped Signal + Noise frequency spectrum

Figure 6.9 and Figure 6.10 show the effect that the filter has on the amplitude of the signal + noise, and its spectrum

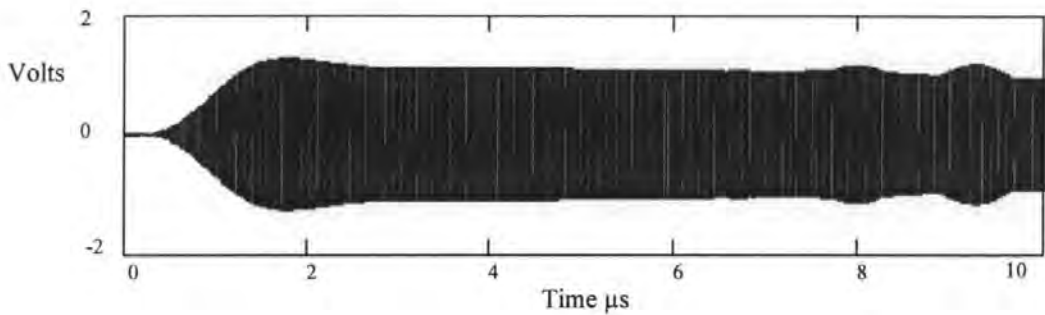


Figure 6.9 Bandlimited signal + noise with an SNR of 13dB

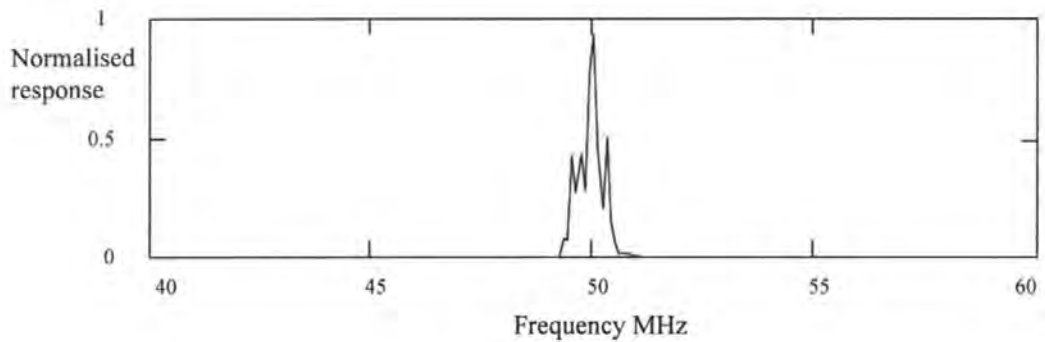


Figure 6.10 Bandlimited signal + noise spectrum

In order to remove the majority of the amplitude noise on the signal it is limited or clipped, the effect of this on the signal is shown in Figure 6.11, the extent of this clipping is discussed in chapter 8.

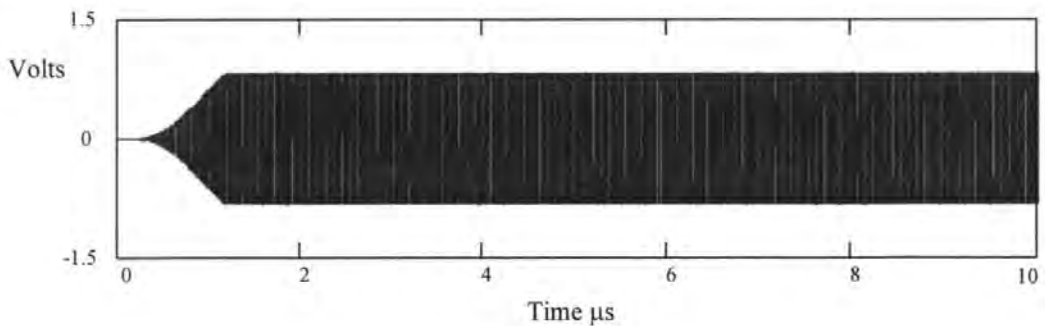


Figure 6.11 clipped signal

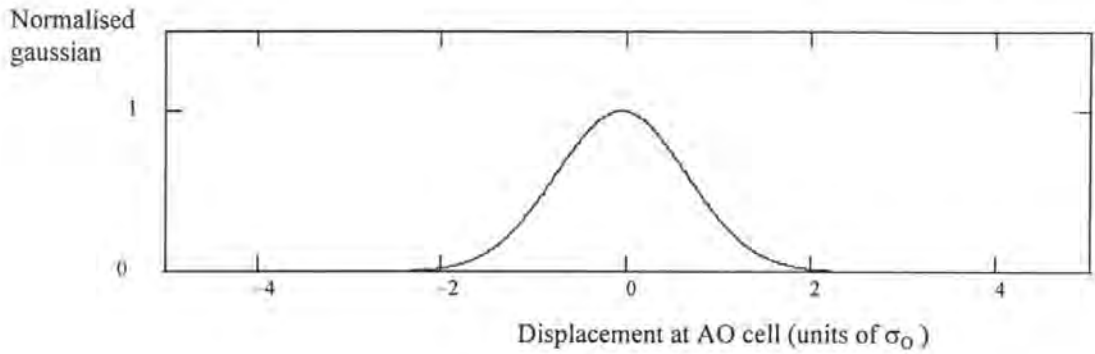


Figure 6.12 Gaussian beam

The Gaussian distribution is multiplied by the first part of the signal, as shown in Figure 6.13. The Gaussian is then moved across the signal from left to right to represent the action of the signal propagating through the AO-cell.

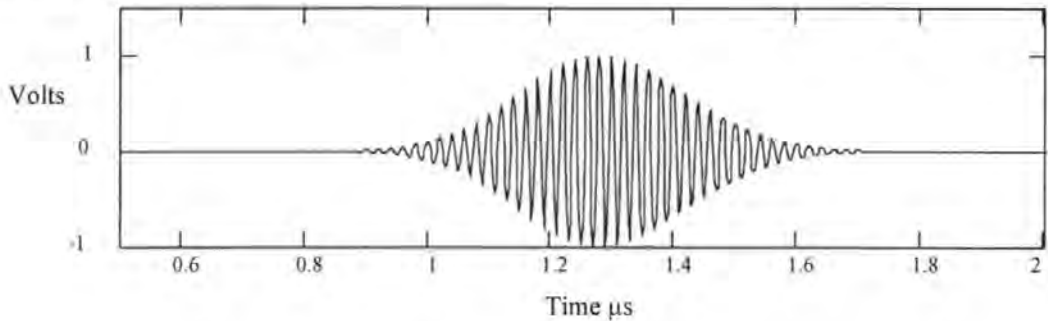


Figure 6.13 Gaussian multiplied with signal

The Fourier transform of the signal shown in Figure 6.13 is shown in Figure 6.14. This represents the Gaussian beam in the focal plane of the lens, on the bi-cell. The two dotted lines represent the two detectors of the bi-cell, over which the amplitude of the Gaussian is summed.

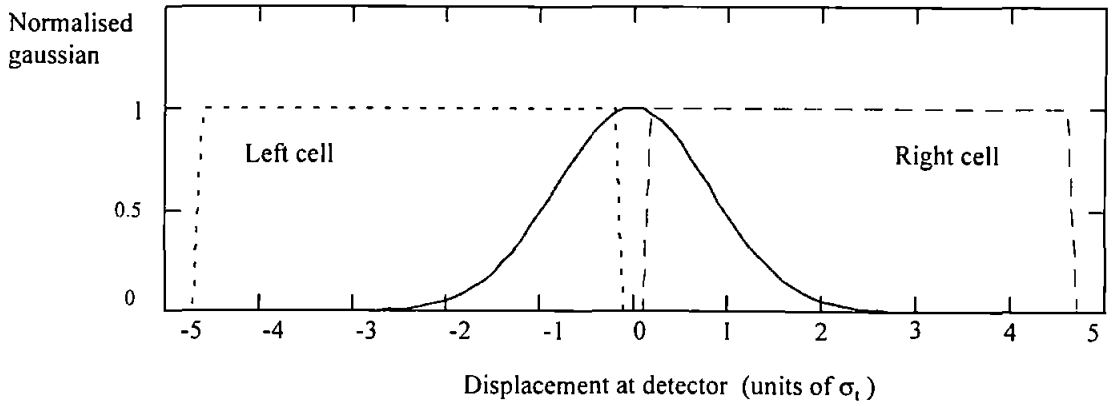


Figure 6.14 Fourier transform of signal and Gaussian window, with the two detectors of the bi-cell marked

The results of the summations across the two detectors are stored as the Gaussian is moved across the signal, and plotted as shown in Figure 6.15.

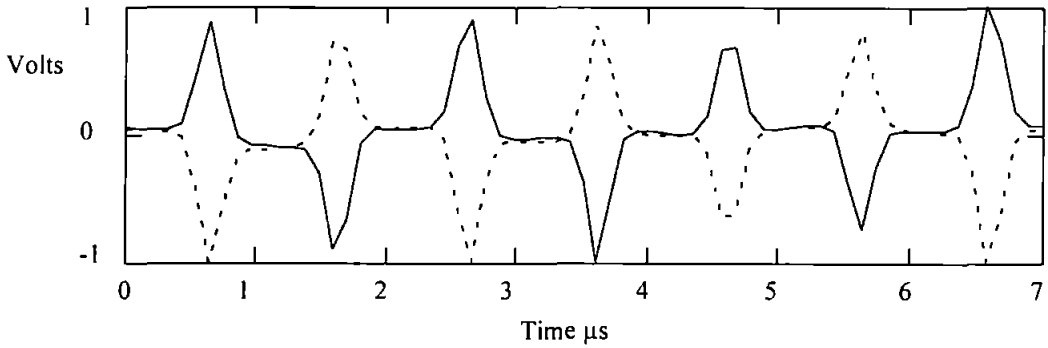


Figure 6.15 output of each bi-cell

Finally the sum and difference of the two traces shown in Figure 6.16 are plotted and analysed in terms of spectrum, standard deviation, variance and SNR.

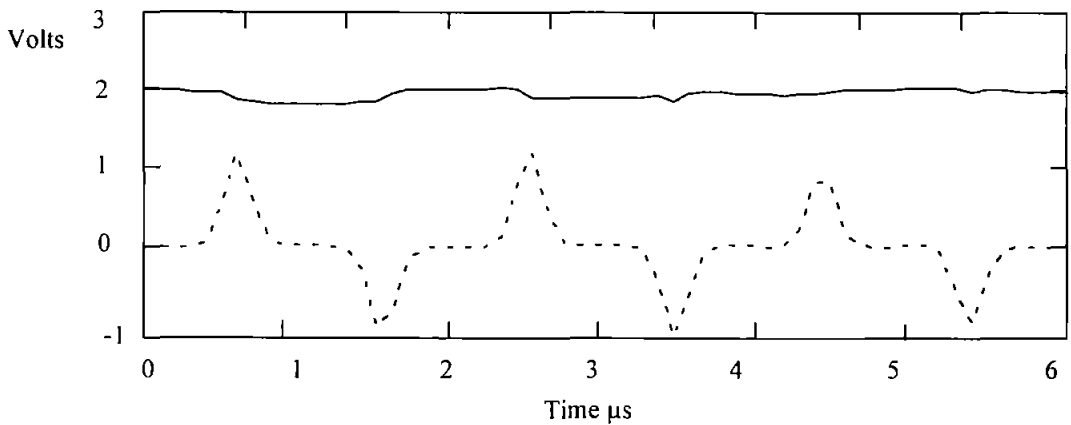


Figure 6.16 Sum and difference of the bi-cell outputs

7. FM System analysis

This chapter analyses and in most cases develops theory for several areas of the FM demodulation process, these are:

1. The frequency dependent deflection of the beam and its displacement at the detector assembly.
2. The effect of the Gaussian beam on the linearity of the system when it is swept across the bi-cell detector, and how different gap sizes affect the linearity of the system.
3. The minimum detectable frequency deviation, limited by the detector noise.
4. The effect of introducing FM noise onto the carrier signal on the response of the system, and optimum levels for clipping these 'noisy' signals.

7.1 Deflection measurement

Chapter 4 provided a brief introduction to the theory behind AO devices, it was shown (Eq. (4.41)) that a change in applied frequency results in a proportional change in the deflection angle of the beam from the AO cell. This change in deflection angle is measured as the beam moves across the bi-cell. The magnitude of this detected signal depends on the optical geometry of the system.

The simple lens and detector arrangement used in the AO modulator is shown in Figure 7.1. The detector is in the back focal plane of the lens so that δx is affected only by the angular displacement of the beam α , which for small angles is given by the equation

$$\alpha = \frac{\delta x}{l_f} \text{ (rads)} \quad (7.1)$$

where δx is the displacement at the detector and l_f is the focal length of the lens. If Eq. (7.1) is substituted in Eq. (4.41) for α we get

$$\delta x = \frac{\lambda l_f}{V_a} \delta f \quad (7.2)$$

agreeing with Eq. (4.54) and which is frequently used in the forthcoming analysis.

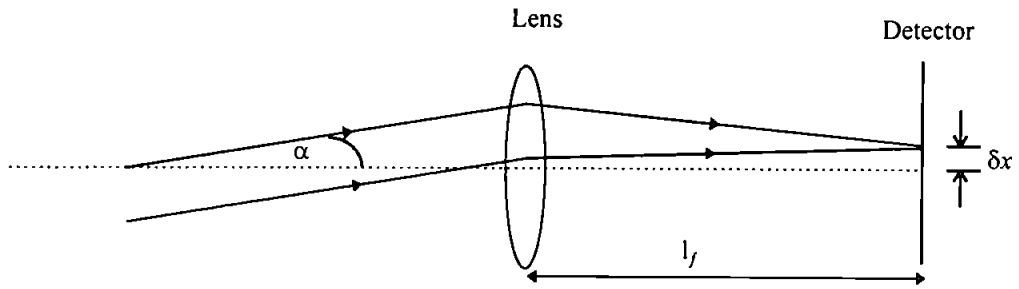


Figure 7.1 Displacement of the beam in the focal plane of a lens

7.2 The system linear range for FM.

The raw beam pattern from a normal laser operating in TEM(0,0) mode is a truncated Gaussian. In the (u,v) plane this can be expressed as

$$I_s(u, v) = \frac{P}{2\pi\sigma_o^2} \exp\left[-\frac{u^2 + v^2}{2\sigma_o^2}\right] \quad (7.3)$$

where P is the total power in the beam and σ_o is the standard deviation of the Gaussian in both the u and v direction. It does not matter if the standard deviation into the v direction is not identical to that of u, as the bi-cell integrates across the whole of the beam in the v direction. The beam profile at the bi-cell after the beam has been deflected and focused by the lens is still Gaussian,

$$I_t(x, y) = \frac{P_1}{2\pi\sigma_t^2} \exp\left[-\frac{x^2 + y^2}{2\sigma_t^2}\right] \quad (7.4)$$

where P_1 is the power in the deflected beam and it is shown in Appendix B that

$$\sigma_t = \frac{\lambda l_f}{4\pi\sigma_o} \quad (7.5)$$

When the carrier is unmodulated the beam is centred on the bi-cell, and since the deflection from the modulation is equally likely to be positive as negative the average background light intensity, P_b , falling on each detector is

$$P_b = \int_{-\infty}^{\infty} \int_{-g/2}^{g/2} I_t(x, y) dx dy = P_1 Q\left(\frac{g}{2}\right) \quad (7.6)$$

where g is the gap size expressed in units of σ_t and the Q function is defined as

$$Q(x) = \frac{1}{\sqrt{2\pi}} \int_x^{\infty} e^{-\frac{y^2}{2}} dy \quad (7.7)$$

The modulation transfer function can be modelled by calculating the signal power, P_s , which is the change in light intensity as the beam is deflected by a distance δx from the central undeviated position, (see Figure 7.2).

$$P_{sL} = \int_{-\infty}^{\infty} \int_{-\infty}^{\delta x - g/2} I_t(x, y) dx dy \quad (7.8)$$

and

$$P_{sR} = \int_{-\infty}^{\infty} \int_{-\infty}^{\delta x + g/2} I_t(x, y) dx dy \quad (7.9)$$

where δx is given by Eq. (7.2)

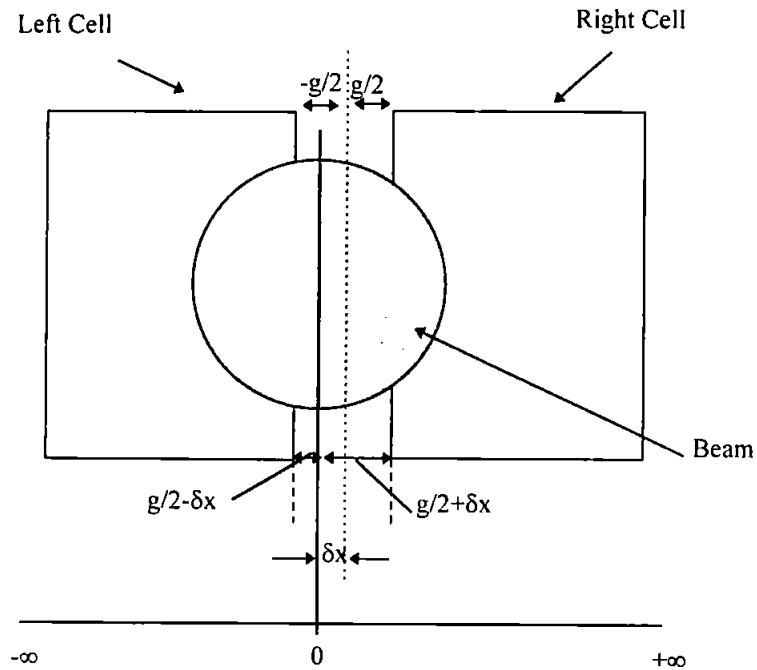


Figure 7.2 Deviation of the beam with respect to the gap size

This is the deflection equation for an AO cell with a lens of focal length l_f in the optical path. The double integrals of Eqs. (7.8) and (7.9) can be split up in terms of x and y

$$P_{sL} = \frac{P_1}{\sqrt{2\pi\sigma_t^2}} \int_{-\infty}^{\infty} \exp\frac{-y^2}{2\sigma_t^2} dy \frac{P_1}{\sqrt{2\pi\sigma_t^2}} \int_{-\infty}^{\delta x - g/2} \exp\frac{-x^2}{2\sigma_t^2} dx \quad (7.10)$$

and

$$P_{sR} = \frac{P_1}{\sqrt{2\pi\sigma_t^2}} \int_{-\infty}^{\infty} \exp\frac{-y^2}{2\sigma_t^2} dy \frac{P_1}{\sqrt{2\pi\sigma_t^2}} \int_{\delta x + g/2}^{\infty} \exp\frac{-x^2}{2\sigma_t^2} dx \quad (7.11)$$

The integrals with respect to y in the above equations are constant and equal to unity. This leaves a much simpler 1-d integral

$$P_{sL} = \frac{P_1}{\sqrt{2\pi\sigma_t^2}} \int_{-\infty}^{\delta x - g/2} \exp\frac{-x^2}{2\sigma_t^2} dx \quad (7.12)$$

$$P_{sR} = \frac{P_1}{\sqrt{2\pi\sigma_t^2}} \int_{\delta x + g/2}^{\infty} \exp\frac{-x^2}{2\sigma_t^2} dx \quad (7.13)$$

The total area of the Gaussian is P_1 , therefore Eqs. (7.12) and (7.13) can be rewritten

$$P_{sL} = \frac{P_1}{2} - \frac{P_1}{\sqrt{2\pi\sigma_t^2}} \int_{\delta x - g/2}^0 \exp\frac{-x^2}{2\sigma_t^2} dx \quad (7.14)$$

$$P_{sR} = \frac{P_1}{2} - \frac{P_1}{\sqrt{2\pi\sigma_t^2}} \int_0^{\delta x + g/2} \exp\frac{-x^2}{2\sigma_t^2} dx \quad (7.15)$$

The difference of P_L and P_R was calculated numerically for various values of δx between the limits of $\pm\sigma_t$, using Mathcad, for three different gap sizes shown in Figure 7.3.

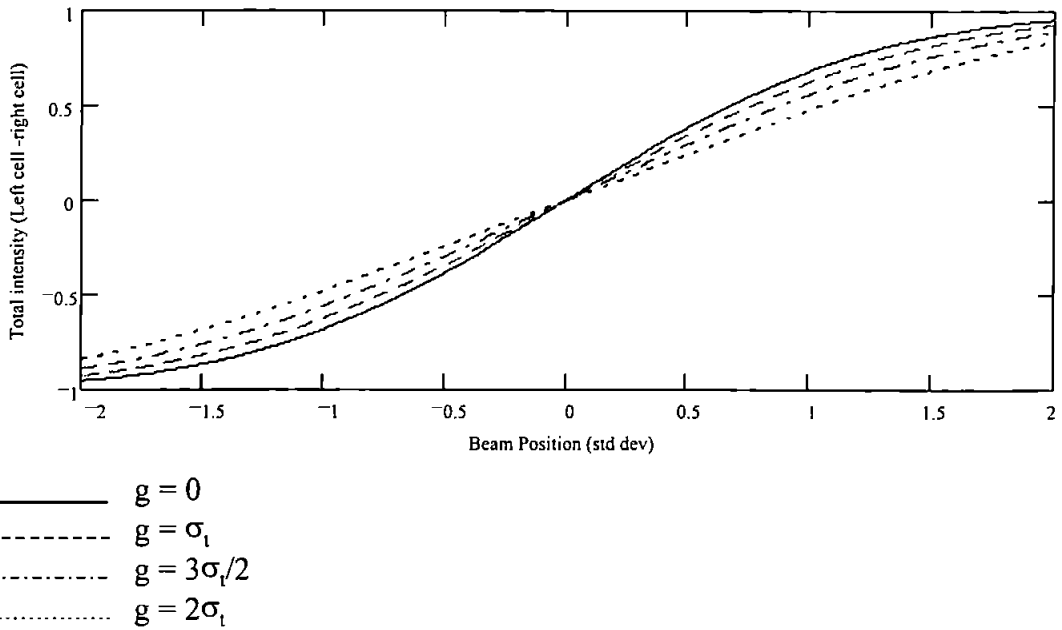


Figure 7.3 Modulation Transfer Function for varying gap sizes

This shows that with no gap we gain the same modulation transfer function as for the knife edge detector [2], but as the gap size increases the linear range increases slightly, as verified in Figure 7.4.

The integral analysis of the modulation transfer function requires a large number of numerical integrations to be performed and does not lend itself easily to finding a linear approximation to the transfer function.

As shown by Brooks [2] if we limit the ratio of δx to σ_1 to less than unity i.e.

$$\left| \frac{\delta x}{\sigma_1} \right| < 1 \quad (7.16)$$

then we can evaluate the integral by expanding the exponential as a power series and integrating term by term.

Knowing that

$$e^z = 1 + z + \frac{z^2}{2!} + \frac{z^3}{3!} + \frac{z^4}{4!} + \dots \text{for } |z| < 1 \quad (7.17)$$

Then substituting z for

$$z = -\frac{x^2}{2\sigma_t^2} \quad (7.18)$$

which gives us

$$e^{-\frac{x^2}{2\sigma_t^2}} = 1 - \frac{x^2}{2\sigma_t^2} + \frac{x^4}{8\sigma_t^2} - \frac{x^6}{48\sigma_t^2} + \frac{x^8}{384\sigma_t^2} - \dots \quad (7.19)$$

substituting Eq. (7.19) into Eqs. (7.14) and (7.15) we obtain

$$P_{sL} = \frac{P_1}{2} - \frac{P_1}{\sqrt{2\pi\sigma_t^2}} \left(g/2 - \delta x - \frac{(g/2 - \delta x)^3}{6\sigma_t^2} + \frac{(g/2 - \delta x)^5}{40\sigma_t^4} - \frac{(g/2 - \delta x)^7}{336\sigma_t^6} + \dots \right) \quad (7.20)$$

and

$$P_{sR} = \frac{P_1}{2} - \frac{P_1}{\sqrt{2\pi\sigma_t^2}} \left(g/2 + \delta x - \frac{(g/2 + \delta x)^3}{6\sigma_t^2} + \frac{(g/2 + \delta x)^5}{40\sigma_t^4} - \frac{(g/2 + \delta x)^7}{336\sigma_t^6} + \dots \right) \quad (7.21)$$

giving

$$P_{sL} = \frac{P_1}{2} - \left[\frac{P_1}{\sqrt{2\pi}} \left(\frac{g/2 - \delta x}{\sigma_t} - \frac{1}{6} \left(\frac{g/2 - \delta x}{\sigma_t} \right)^3 + \frac{1}{40} \left(\frac{g/2 - \delta x}{\sigma_t} \right)^5 - \frac{1}{336} \left(\frac{g/2 - \delta x}{\sigma_t} \right)^7 + \dots \right) \right] \quad (7.22)$$

$$P_{sR} = \frac{P_1}{2} - \left[\frac{P_1}{\sqrt{2\pi}} \left(\frac{g/2 + \delta x}{\sigma_t} - \frac{1}{6} \left(\frac{g/2 + \delta x}{\sigma_t} \right)^3 + \frac{1}{40} \left(\frac{g/2 + \delta x}{\sigma_t} \right)^5 - \frac{1}{336} \left(\frac{g/2 + \delta x}{\sigma_t} \right)^7 + \dots \right) \right] \quad (7.23)$$

These expressions were expanded, P_{sL} was subtracted from P_{sR} to give P_{DIFF} , and the linear terms (i.e those in δx were extracted from the resulting function. Using these linear terms only we get

$$P_{DIFF} = P_{sR} - P_{sL} = P_1 \frac{1}{\sqrt{2\pi}} \left(2 \frac{\delta x}{\sigma_t} - \frac{1}{4} \frac{\delta x}{\sigma_t} \frac{g^2}{\sigma_t^2} + \frac{1}{64} \frac{\delta x}{\sigma_t} \frac{g^4}{\sigma_t^4} - \frac{1}{1536} \frac{\delta x}{\sigma_t} \frac{g^6}{\sigma_t^6} + \dots \right) \quad (7.24)$$

or

$$P_{DIFF} = \frac{P_1}{\sqrt{2\pi}} \frac{\delta x}{\sigma_t} \left(2 - \frac{1}{4} \frac{g^2}{\sigma_t^2} + \frac{1}{64} \frac{g^4}{\sigma_t^4} - \frac{1}{1536} \frac{g^6}{\sigma_t^6} + \dots \right) \quad (7.25)$$

The difference between this power series approximation and the value obtained from the full integral of the MTF is simply the sum of all the higher order terms omitted from Eq. (7.25) This difference is plotted as an error for different gap sizes in Figure 7.4. It is clear from this figure that the system becomes more linear as the gap size increases, although it must be remembered that this is at the expense of the resolution of the system (see Figure 7.6)

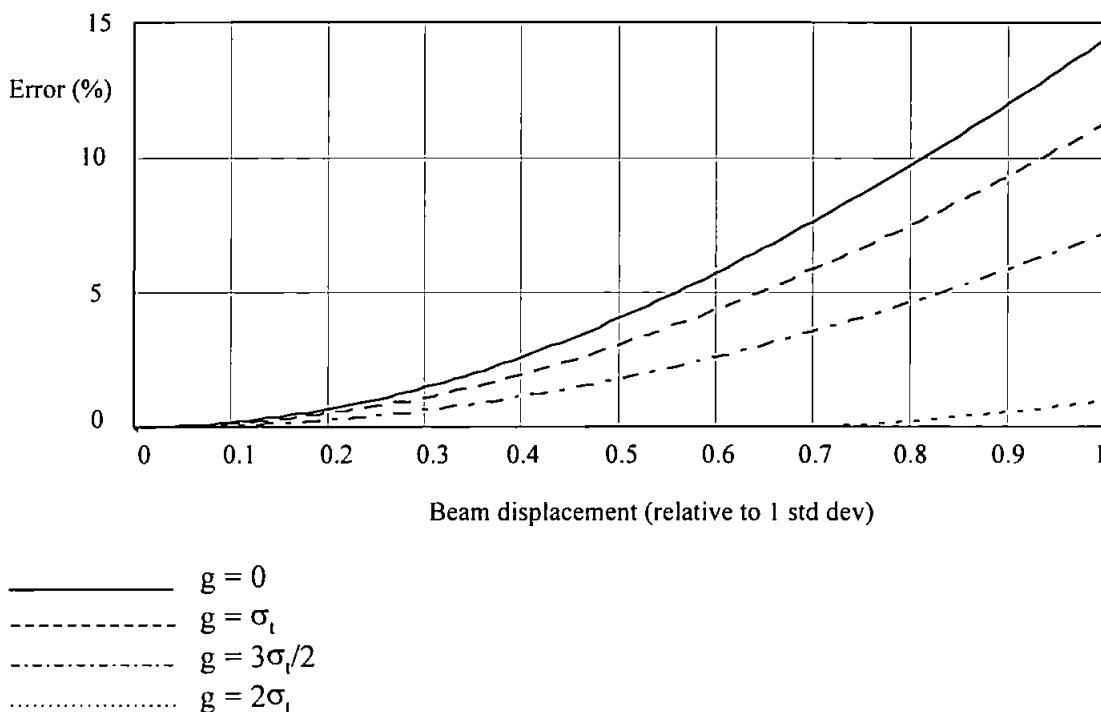


Figure 7.4 Error in linear approximation to MTF

If an error of less than 1% was required it can be seen that for a gap size of zero this would limit the value of $|\delta x/\sigma_t|$ to 0.2 whereas for a gap size of $2\sigma_t$ the value of $\delta x/\sigma_t$ would only be limited to 1. This allows us to calculate the maximum frequency deviation for a given system before the MTF causes significant non-linearity and distortion.

7.3 Shot noise limited resolution for FM demodulation

It has been shown in section 7.2 that there is a direct relationship between the change in the optical power falling on each detector and the applied frequency. The smallest detectable frequency deviation will be when the signal level due to the change in optical power is equal to the signal level due to the combined noise of the two detectors. To calculate this minimum deviation we first examine the detector noise.

It has been shown [2] that it is valid in all practical cases to ignore the thermal noise component of the system (i.e. when $2eB_nR_\lambda P_b \gg 4kTB_n/R_L$) as the large amount of background illumination due to the laser beam gives rise to a large shot noise signal. For a laser power of 1 mW Brooks [2] showed that the shot noise was a factor of 10^4 greater than the thermal noise. The signal current at the output of the photodiodes is given by

$$i_{sL} = R_\lambda (P_b + P_{sL}) \quad (7.26)$$

and

$$i_{sR} = R_\lambda (P_b + P_{sR}) \quad (7.27)$$

Where i_{sL} and i_{sR} are the signal currents for the left and right bi-cell elements, R_λ is the diode responsivity and P_{sL} and P_{sR} are the optical signal powers falling on the left and right bi-cell elements. The shot noise currents in the two photodetectors are given by

$$i_{nL}^2 = 2eB_nR_\lambda (P_b + P_{sL}) \quad (7.28)$$

and

$$i_{nR}^2 = 2eB_nR_\lambda (P_b + P_{sR}) \quad (7.29)$$

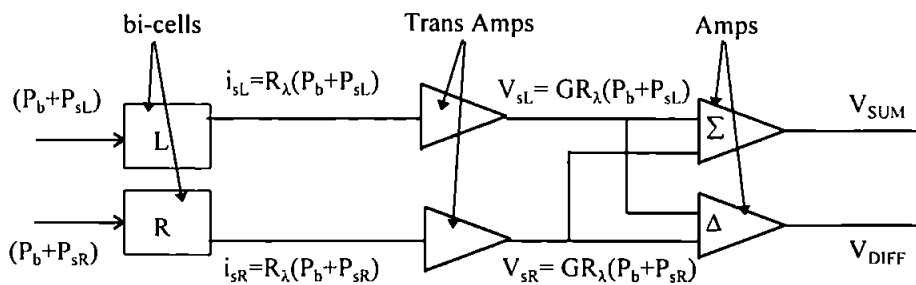


Figure 7.5 Block diagram of bi-cell detector

Assuming for now that the gap size of the bi-cell is zero, makes the analysis possible. Later the case when the gap size is not equal to zero will be solved numerically. When the gap size is zero, $P_{sL} = -P_{sR}$ and so

$$i_n^2 = 2eB_n R_\lambda (2P_b) \quad (7.30)$$

where B_n is the system noise bandwidth and P_b is the background optical power.

The ratio of background power P_b to signal power P_s can be written as

$$K = \frac{P_s}{P_b} \quad (7.31)$$

where $|K| \ll 1$. Since P_s represents the signal and P_b is proportional to the shot noise, P_s/P_b is related to the signal to noise ratio. P_s can be represented by P_{DIFF} or P_{SUM} depending on whether we are considering the sum or difference channel, where

$$P_{DIFF} = (P_b + P_{sL}) - (P_b + P_{sR}) \quad (7.32)$$

and

$$P_{SUM} = (P_b + P_{sL}) + (P_b + P_{sR}) \quad (7.33)$$

7.3.1 Analysis for very small gap

For this case where the gap in the bi-cell is assumed to be zero and $P_{sL} = -P_{sR}$, P_{SUM} from Eq. (7.33) will be constant, (equal to $2P_b$) and is therefore ignored. We now consider the case for the difference, in this case $P_s = P_{DIFF}$. K can be positive or negative depending on whether the deflection is to the left or the right. To get an absolute limit we must see how K varies with applied frequency for a given geometry and how it is related to the output SNR. We will find the value for K for $SNR = 1$. This will be taken as the limit of frequency resolution

The SNR (in terms of electrical power) is given by

$$SNR = \frac{i_s^2}{i_n^2} = \frac{(R_\lambda P_{DIFF})^2}{4eB_n R_\lambda P_b} \quad (7.34)$$

but Eq. (7.31) allows us to substitute for P_{DIFF} (equal to P_s) to give

$$SNR = \frac{(KR_{\lambda} P_b)^2}{4eB_n R_{\lambda} P_b} \quad (7.35)$$

If we set a unity SNR (equal signal and noise powers) as the minimum SNR limit on sensitivity then

$$\frac{(K_{SNR=1} R_{\lambda} P_b)^2}{4eB_n R_{\lambda} P_b} = 1 \quad (7.36)$$

This can now be solved for $K_{SNR=1}$.

$$K_{SNR=1} = \frac{\sqrt{4eB_n}}{\sqrt{R_{\lambda} P_b}} \quad (7.37)$$

It can be seen that there is an inverse relationship between K and both the responsivity of the photodiode and the background power. An increase in either of these would cause an increase in the frequency resolution. Obviously the saturation level of the diode limits how much P_b can be increased. In the case of the two detectors used in the experimental system this limits the power to 196 μ W for the small detector and 7.16 mW for the larger one.

Having assumed that the gap size in Eq (7.25) is zero, i.e. $g = 0$, it is possible to derive an equation for the best possible frequency resolution, using

$$P_{DIFF} = P_1 \frac{2}{\sqrt{2\pi}} \frac{\delta x}{\sigma_t} \quad (7.38)$$

since $P_1 = \frac{P_b}{Q(\frac{g}{2})}$ and $Q(0) = \frac{1}{2}$ then

$$P_{DIFF} = \frac{4P_b}{\sqrt{2\pi}} \frac{\delta x}{\sigma_t} \quad (7.39)$$

using Eq. (7.5) gives

$$P_{DIFF} = P_b \frac{8\sqrt{2\pi}\sigma_o}{\lambda f_1} \delta x \quad (7.40)$$

and since $\delta x = \frac{\lambda f_1}{V_a} \delta f$ then

$$P_{DIFF} = P_b \frac{8\sqrt{2\pi}\sigma_o}{V_a} \delta f \quad (7.41)$$

$$\frac{P_{DIFF}}{P_b} = \frac{8\sqrt{2\pi}\sigma_o}{V_a} \delta f \quad (7.42)$$

which can be rearranged and expressed in terms of K

$$\delta f = \frac{V_a}{8\sqrt{2\pi}\sigma_o} K \quad (7.43)$$

so the minimum resolvable frequency for a given system with a unity SNR is found using Eq. (7.37)

$$\delta f_{\min} = \frac{V_a}{8\sqrt{2\pi}\sigma_o} \sqrt{\frac{4eB_n}{R_\lambda P_b}} \quad (7.44)$$

From this it can be seen that there are various system parameters affecting the frequency resolution. The most prominent are the acoustic velocity of the Bragg cell, the standard deviation of the Gaussian beam in the AO cell and the diffracted laser power. The simplest way to increase the resolution is to increase the diameter of the beam in the AO cell σ_o . Figure 7.6 shows how the difference output voltage increases with frequency for three different beamwidths (0.25mm, 0.49mm and 1.49mm). It can be seen that as the beamwidth increases so does the slope of Figure 7.6 and hence the shot noise limited resolution improves. The experimental set-up has a beamwidth of 0.49 mm. From Figure 7.6 the output crosses the shot noise signal at 19Hz, this is verified in Eq. (7.47).

Unfortunately increasing σ_o increases the acoustic transit time τ , which has been shown in Eq. (4.47) to be inversely proportional to the bandwidth of the system. Decreasing the acoustic velocity of the waves will also result in lowering the minimum detectable frequency deviation, although the slow shear mode of the TeO₂ crystal has the slowest available acoustic velocity. The final parameter that can easily be changed in Eq. (7.44) is the background power P_b . A plot of laser power against frequency resolution for $R_\lambda = 0.35$ A/W and $B_n = 800$ kHz is shown in Figure 7.7, as expected from Eq. (7.44) the resolution improves as the laser power increases.

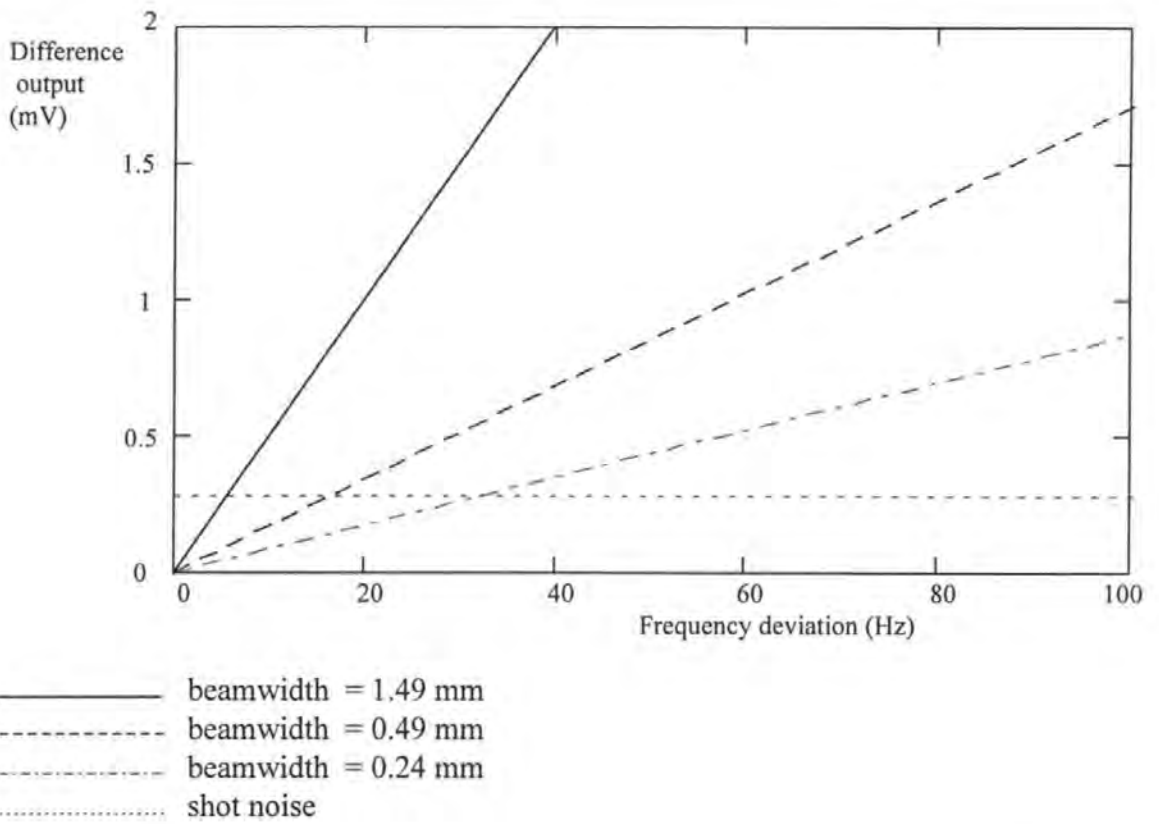


Figure 7.6 Graph showing the effect of increasing the beamwidth in the AO cell

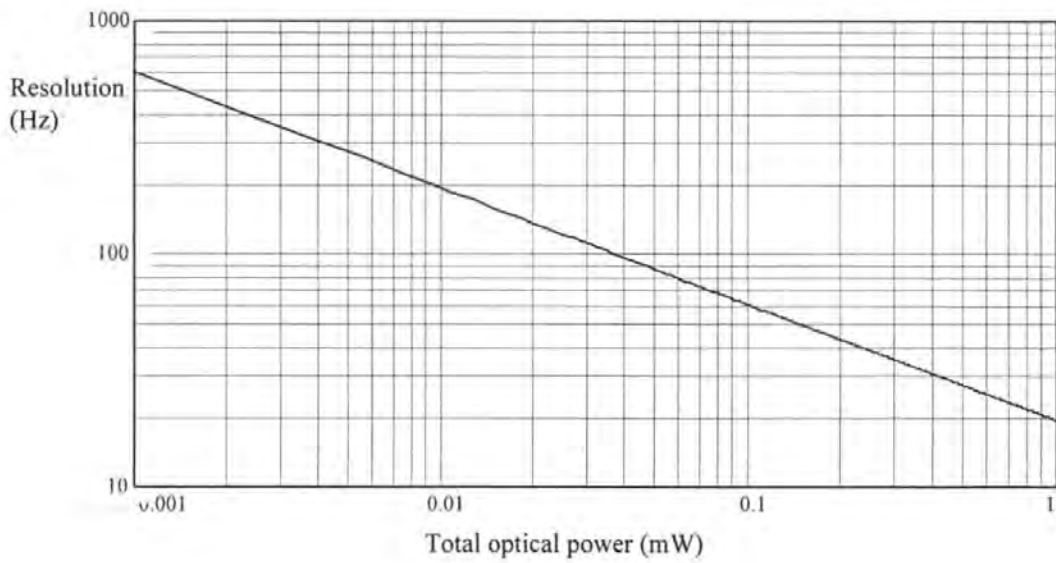


Figure 7.7 System resolution versus diffracted light power

We can also rearrange the shot noise formula Eq. (7.35) to give an expression which links SNR and frequency resolution.

$$K = \sqrt{\frac{4eB_n}{R_\lambda P_b}} \sqrt{SNR} \quad (7.45)$$

therefore

$$\delta f_{\min} = \frac{V_a}{4\sigma_o} \sqrt{\frac{eB_n}{2\pi R_\lambda P_b}} \sqrt{SNR} \quad (7.46)$$

If Eq. (7.46) is compared to Brooks [2] for his analysis of the knife edge we find that the bi-cell reduces the minimum detectable frequency by $1/\sqrt{2}$. For the parameters being used this would give

$$\delta f_{\min} = 19\sqrt{SNR} \quad (7.47)$$

7.3.2 Effect of a finite gap size

If a finite gap size is assumed Eq. (7.38) is no longer valid as all the terms involving g in Eq. (7.25) must now be taken into consideration. This would make the analysis too complicated, so it was decided to ascertain the effect of the gap size on the SNR of the system by resolving the power series approximation of Eq. (7.25) and the Gaussian integrals of Eqs.(7.14) and (7.15) numerically using Mathcad. Figure 7.8 shows how the SNR drops as the gap size increases for a frequency deviation of 19 Hz. As can be seen this graph also agrees with Eq. (7.47) as when the gap is zero the SNR is 1.

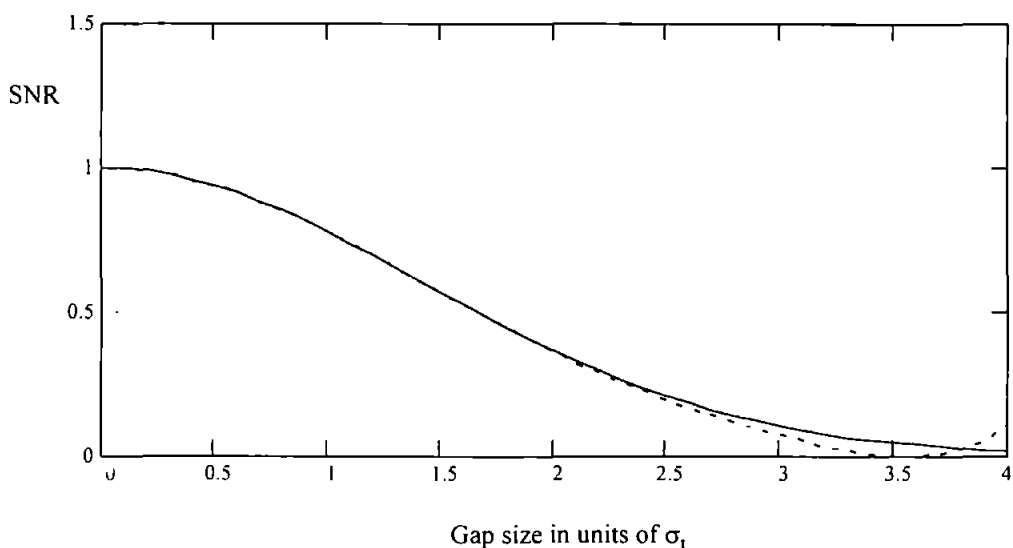


Figure 7.8 Graph showing how the assumption made for P_{DIFF} compares with the actual values

The solid line was calculated using P_{DIFF} as $P_L - P_R$ from Eqs. (7.14) and (7.15) whereas the dotted line was calculated using the approximation of Eq. (7.25). It can be seen that the approximation of Eq. (7.25) is accurate up to a gap size of around $2.5 \sigma_t$.

7.4 Effect of noise on an FM carrier signal

This section sets out to show how Gaussian noise on the incoming signal affects the performance of the system. The action of individual components in the system means that it is impractical to attempt a purely analytical solution to the noise performance.

The elements in the system that cause the complications to the analytical solution are the AO cell, the limiter and the bi-cell detector ; the limiter clips any signal that exceeds a predetermined voltage causing discontinuities on the signal, the noisy clipped signal is first averaged or integrated over the time period fixed by the beamwidth of the laser in the bi-cell, and the power spectrum of the signal is then spatially integrated in two parts over the area of the two detectors in the bi-cell, before the sum and difference of these signals is taken.

Therefore the Mathcad model of the system, described in chapter 6 has been used to simulate the response of the system to various noisy signals. The results of this section show how the optimum level of clipping is dependant on both the frequency deviation, δf , and the SNR of the signal at the input to the system. It also shows that the overall SNR loss of the system is proportional to δf and the clipping level. The validity of these results is substantiated with the experimental results shown in Appendix D. These results show the similarity between the output of the model and the experimental system in response to various noisy signals.

In each of the following sections the output SNR was calculated as follows; an unmodulated carrier plus noise signal was fed into the model, the variance of this signal calculated and stored. A signal containing modulation was then fed through the model, the output from this was used to calculate the average noise power of the output signal. The signal power was then divided by noise power to calculate SNR_{out} .

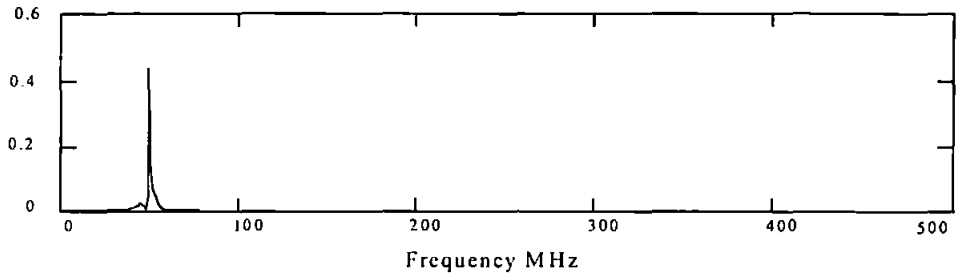
This method of calculating the SNR makes the assumption that the system is linear and as I have just stated it is not, for the reasons given above. Because of this, although the trends of the results will be correct, the absolute values will not be correct.

Finally as shown in section 6.3 because Gaussian or white noise has power across the entire frequency spectrum (Figure 6.4), a bandpass filter is used to try to cut out as much of this noise as possible. Obviously the narrower the filter the better as far as this is concerned, so that the signal to noise ratio at the input is as high as possible. The problem being that the filter has to be wide enough to pass the modulation spectrum, normally considered to be at least T_b , where T_b is the data rate of the modulation, MHz. The input SNR values given, correspond to noise bandlimited to 1 MHz

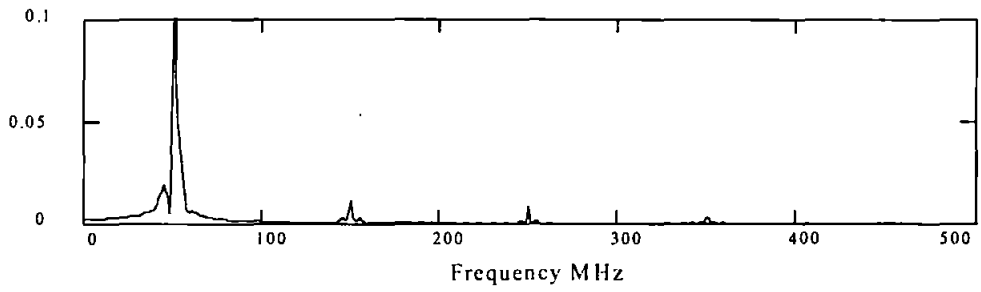
7.4.1 The effect of clipping on the spectrum of a noisy signal.

Because noise is always ultimately going to be the limiting factor in any communication system, the study and mathematical description of its behaviour have become an integral part of statistical communication theory. Of particular relevance to this system, is the effect on the power spectrum of Gaussian noise of a 'clipper' or 'limiter' that chops off extreme values of noise in a wave. This work was started by Van Vleck and Middleton in 1943 [23] who looked at the effect of extreme clipping, and clipping at arbitrary levels. The analysis that follows agrees with the results they published for the demodulator system. They showed that the ratio of energy in the noise sidebands to that in the carrier increases as the signal is clipped harder and harder.

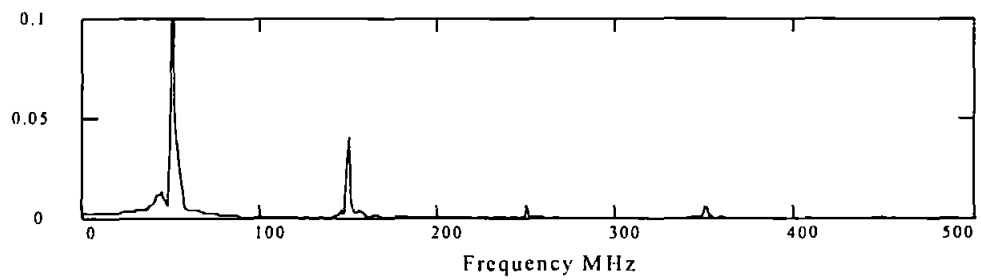
In order to explain how the change in energy from the carrier to the sidebands affects this system we look at Figure 7.9 a,b,c,d and e. These diagrams show how the amount of clipping affects the distribution of energy, between the sidebands and the carrier component of the signal, as different levels of clipping are used. The levels of clipping being used limits the signal to 100%, 80%, 60%, 40%, and 20% of the maximum respectively. It is clear that as the signal is clipped harder more energy is transferred into the sidebands. The plots b,c,d, and e have all been limited to 0.1 on the amplitude scale so that it is easier to see the harmonics. Plot a is shown normally as it has no harmonics and shows more clearly how much of the signal is contained in the centre frequency.



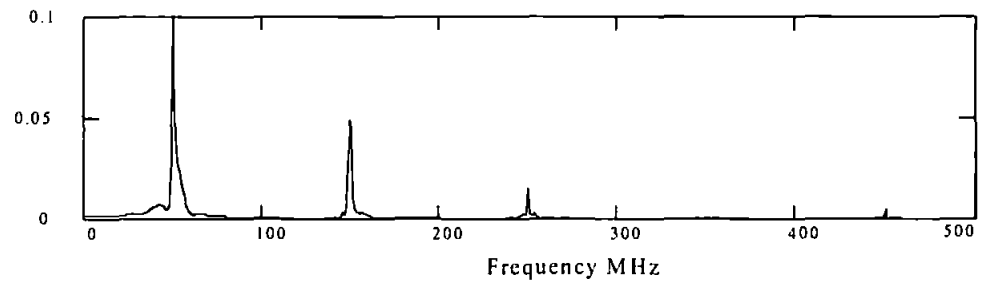
(a)



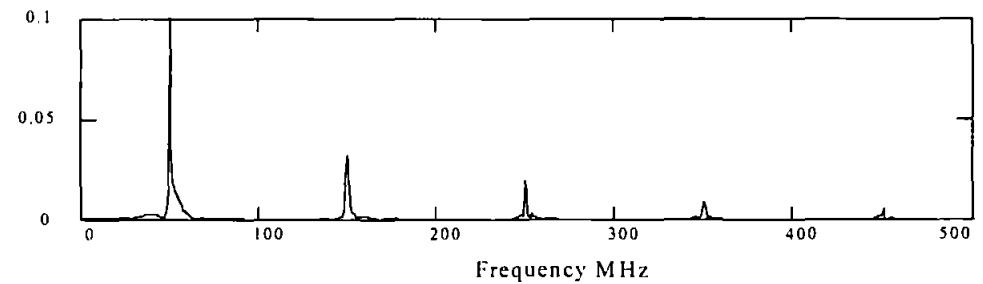
(b)



(c)



(d)



(e)

Figure 7.9 The effect of clipping on the frequency spectrum of the signal
(a)100%, (b)80%, (c)60%, (d)40%, (e)20%.

7.4.2 The optimum clipping level

In order to find out if there was an optimum clipping level, an unmodulated carrier signal was fed into the model and the output signal to noise ratio (SNR_{out}) was calculated from the variance and mean of the output signal. The SNR_{out} was plotted against the level of clipping, for three separate levels of input carrier to noise ratio (CNR_{in}) of the carrier signal, shown in Figure 7.10.

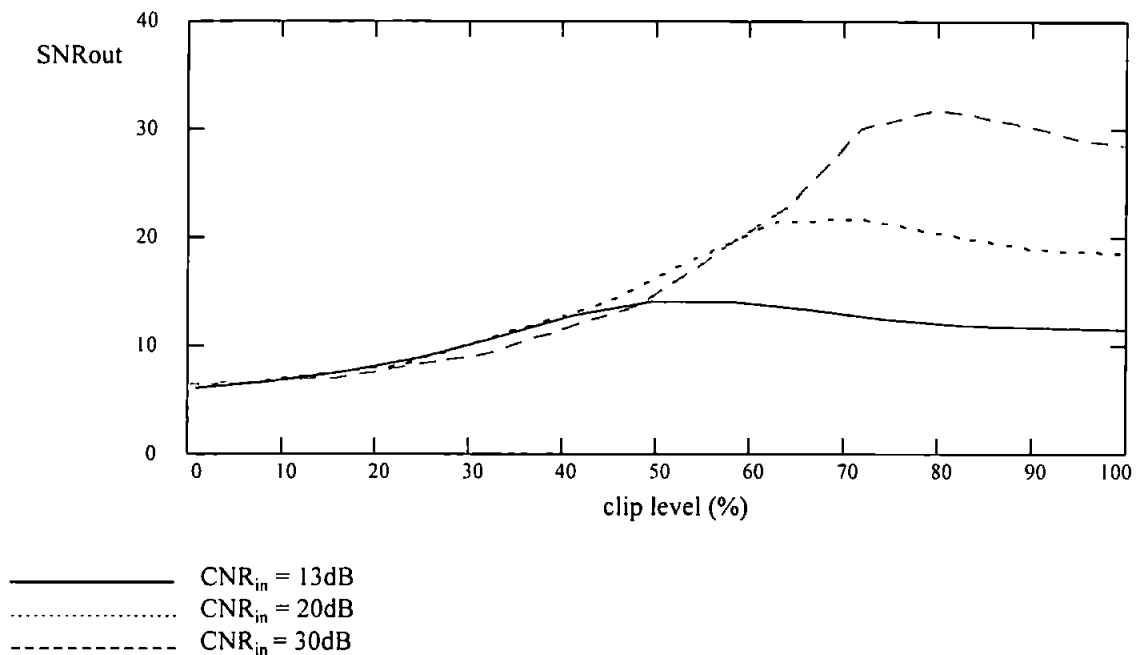


Figure 7.10 The effect of clipping on the output SNR

It should be noted in Figure 7.10 and all subsequent plots containing clip level, that 100% = no clipping .

Figure 7.10 shows clearly that there is an optimum level for clipping a signal and it is proportional to the CNR_{in} . It is also clear that it is better to clip a signal too little than too much. Figure 7.11 shows this relationship between the optimum level of clipping on the signal and CNR_{in} . It was plotted with the deviation, δf , set at 220 kHz. The minimum clipping level for any frequency with a CNR_{in} above 40 dB is seen to be 95%, as the CNR_{in} drops the amount that the signal has to be clipped increases quite markedly.

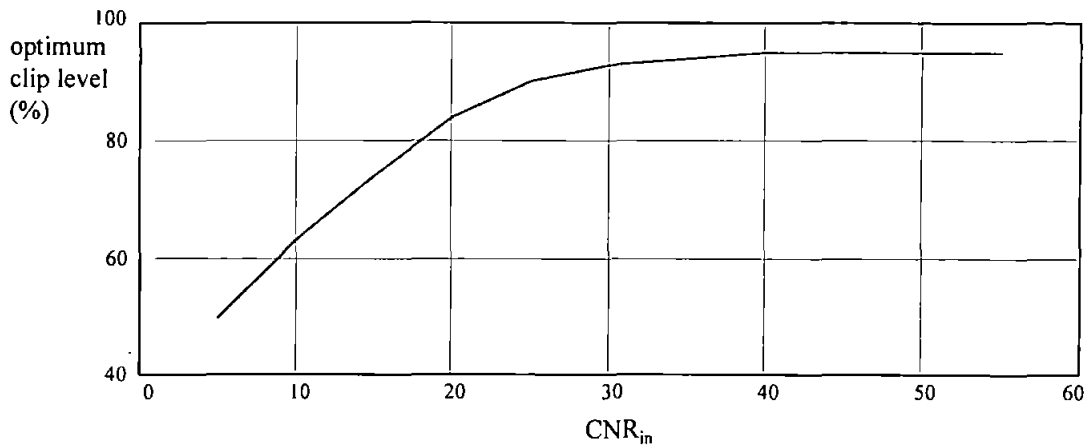


Figure 7.11 Graph showing how the optimum clipping level changes with CNR_{in}

The minimum clipping level itself is not fixed, but is dependant on the value of δf being used in the modulated signal. If a lower value of δf had been used the curve shown in Figure 7.11 would be shifted down by an amount determined by Figure 7.12. This curve shows the relationship between the minimum clip level at high SNR_{in} levels and the deviation δf .

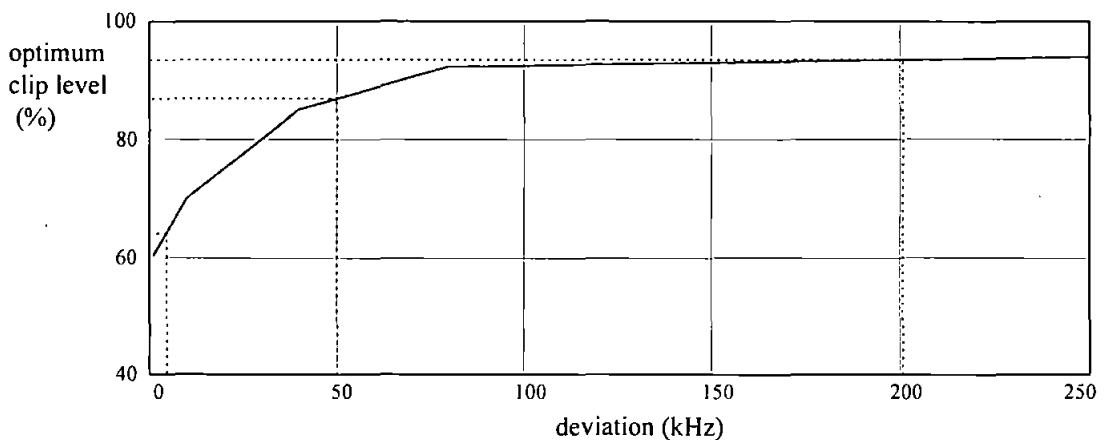


Figure 7.12 Graph showing how the clipping level is affected by the frequency deviation δf .

This means that the plot shown in Figure 7.11 will be shifted on the y-axis depending on the frequency deviation of the signal. Figure 7.13 shows this for three different values of δf .

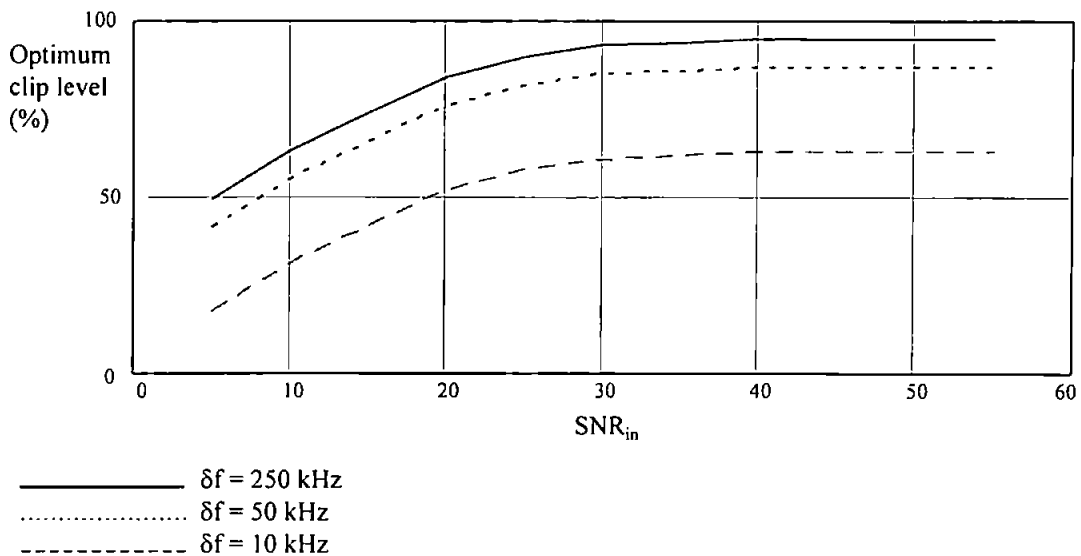


Figure 7.13 Graph showing how Figure 7.12 affects Figure 7.11.

7.4.3 System SNR loss

At this point it was necessary to decide whether the advantages gained from clipping outweighed the disadvantages. Figure 7.14 shows three CNR_{in} vs SNR_{out} plots, taken for a δf of 250 kHz; one with no clipping, one where the clipping has been set to 85% and the other using adaptive clipping where the optimum clipping level is decided for each CNR_{in} . This graph shows that even with the adaptive clipping there is a 1.6dB gain over no clipping at all, and for a fixed level of clipping there is a risk of losing out over an unclipped signal if CNR_{in} is not known to within 10dB

Figure 7.15 Shows how the SNR loss (i.e. the difference between the CNR_{in} and the SNR_{out}) between the input and output of the system depends on the size of the frequency deviation δf . This plot was calculated using no clipping of the input signal. From this graph the expected degradation of the signal as it is demodulated by the system can be accurately predicted for any given frequency deviation. The reason for the lack of linearity at the top of the plot is due to the transfer function of the bi-cell which ceases to be linear at the higher frequencies, see section 7.2. Obviously if clipping had been used the plot would be shifted up or down depending on the level of clipping and the CNR_{in} .

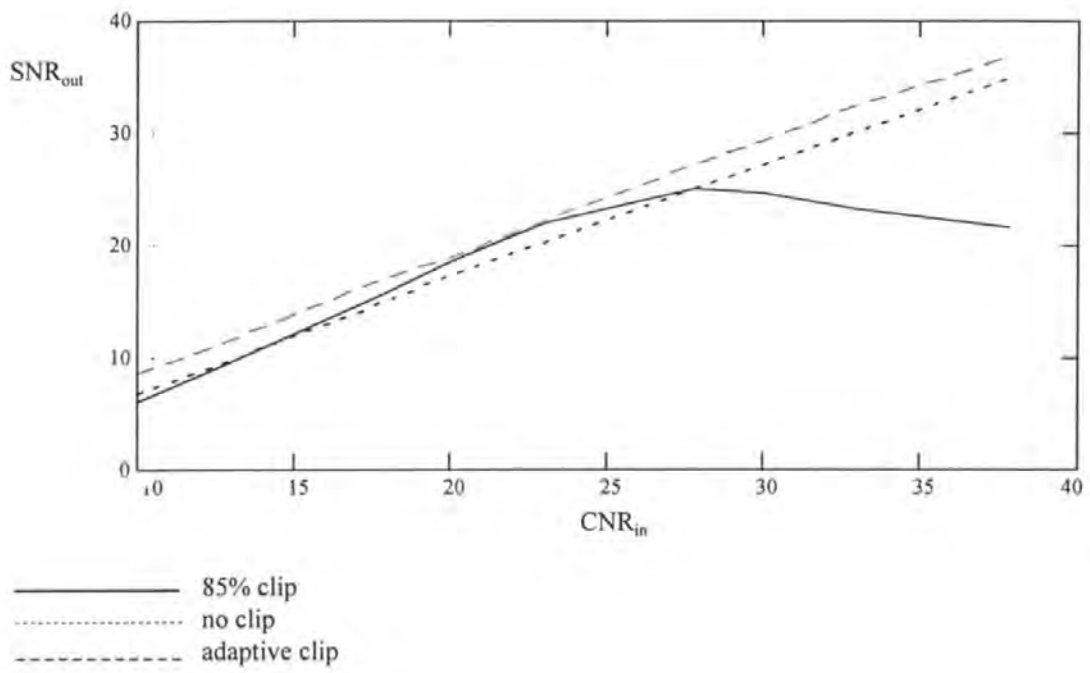


Figure 7.14 The affect of different clipping levels on SNR_{out} as SNR_{in} varies

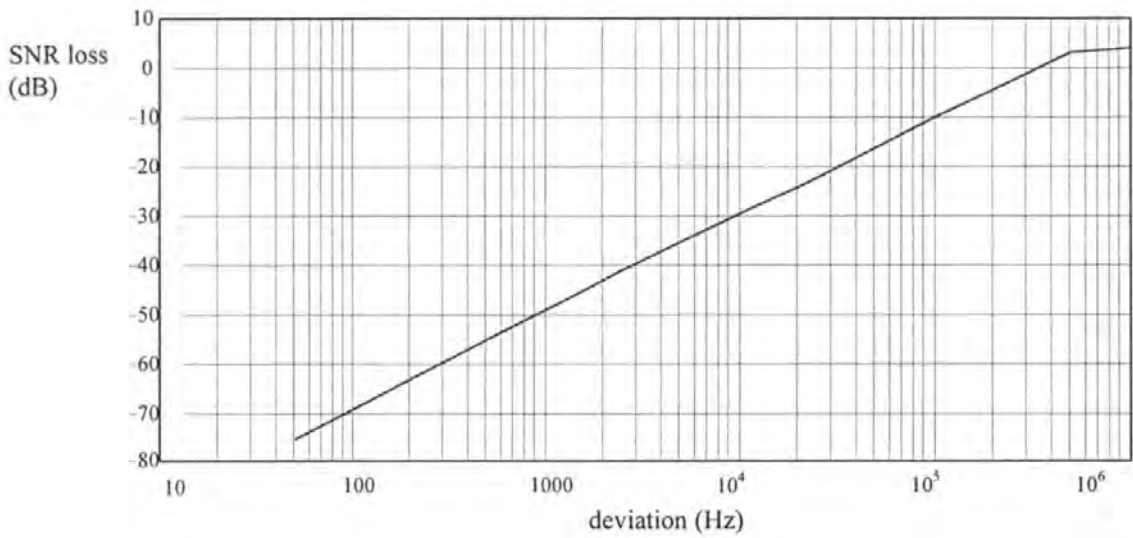


Figure 7.15 SNR loss versus deviation δf .

7.5 Summary and conclusions

Having derived the useful relationship between δx and δf for the system (Eq. (7.2)) in section 7.1, section 7.2 goes on to show the effect of different gap sizes on the modulation transfer function Figure 7.3, and verifying these results using Eq. (7.25) which confirms that the linear range of the output increases with the gap size.

Section 7.3 derives Eq. (7.44) which shows how the parameters P_b , σ_o and V_a are related to the minimum detectable frequency deviation. Figure 7.6 and Figure 7.7 show how increasing σ_o and P_b respectively improve the systems resolution. Finally by using the parameters from the practical system in Eq. (7.46) a value for the minimum detectable frequency is calculated as

$$\delta f = 19\sqrt{\text{SNR}}$$

We now move onto section 7.4 which looks at the effect of putting noise on the carrier signal. Firstly Figure 7.11 shows that the effect of clipping a signal too hard is much worse than not clipping a signal at all. With this in mind, an optimum level of clipping was calculated for each SNR_m and each δf . Figure 7.12 shows how δf affects the position of the maximum clipping level.

Figure 7.14 shows the effect of clipping on the SNR loss of the system, adaptive clipping clearly improves the SNR loss, but the result of getting the clipping level wrong is shown to be drastic.

It has been shown by Brooks [2] that because the difference output subtracts any AM noise common to both detectors on the bi-cell, the bi-cell system exhibits a degree of AM rejection, given by

$$\text{AMrejection}(dB) = 10 \log \left(\frac{V_a}{8\sigma_o \sqrt{2\pi} \delta f} \right) \quad (7.49)$$

which in the case of this system gives

$$\text{AMrejection}(dB) = 54 - 10 \log(\delta f) \quad (7.50)$$

which gives positive values of AM rejection up to frequency deviations of 250 kHz.

It was decided not to clip the incoming signal, when the system is being used solely as an FM demodulator, and rely on the inherent AM rejection of the difference channel. This means Figure 7.15 showing how the SNR loss is related to δf is may be used for all signals to predict the SNR_{out} for a known CNR_{in} .

8. PM System analysis

The system is able to detect phase changes on the carrier signal because of their effect on its power spectral density (PSD) shown in the diffracted laser beam. It has been shown by Reeve and Houghton [3] that the Fourier transform (the effect of the lens) of the signal windowed in the AO cell causes the PSD to spread its power away from the centre of the diffracted beam toward the edges at the detector. It will be shown in chapter 9 that the symmetry of the spread of power away from the centre of the beam is related directly to the size of the phase shift applied.

It is possible to detect this distortion of the PSD on the sum and difference channels of the bi-cell. The difference channel responds to the non symmetrical distortion of the PSD and the sum channel responds to the spreading of light away from the gap of the bi-cell where it is lost, and onto the detectors.

This chapter analyses and in most cases develops theory for several areas of the PM demodulation process, these are:

1. The variation of the system output for discrete phase changes between $\pm\pi$ rads.
2. The effect of the gap size on the demodulation of phase changes for the sum and difference channels.
3. The minimum phase shift detectable by the sum and difference channels.
4. The effect of introducing noise onto the carrier signal, on the response of the system, and optimum levels for clipping these 'noisy' signals.

8.1 Variation of output of bicell system for discrete phase shift

Consider the situation when a sinusoidal carrier of temporal angular frequency ω rads/sec containing a single phase shift ϕ radians is applied to an AO cell, whose acoustic velocity is V_a . The peak output from the system occurs when the phase shift of ϕ rads is in the centre of the Bragg cell aperture. This is when the maximum distortion of the PSD takes place (see chapter 9). The signals in the left and right sides of the AO cell aperture at this instant can be represented as

$$f_l(x) = \cos(kx - \frac{\phi}{2}) \cdot w_l(x) \quad \text{and} \quad f_r(x) = \cos(kx + \frac{\phi}{2}) \cdot w_r(x) \quad (8.1)$$

where $w_l(x)$ and $w_r(x)$ are the left and right side window functions and $k = \omega/V_a$. Figure 8.1 shows the window for a Gaussian function. In the optical system the window function will normally be Gaussian because of the Gaussian beam profile of the laser but this is not important in this analysis. All we need to assume is that the window function is symmetrical about the centre of the window ($x=0$) so that $w_l(x) = w_r(-x)$.

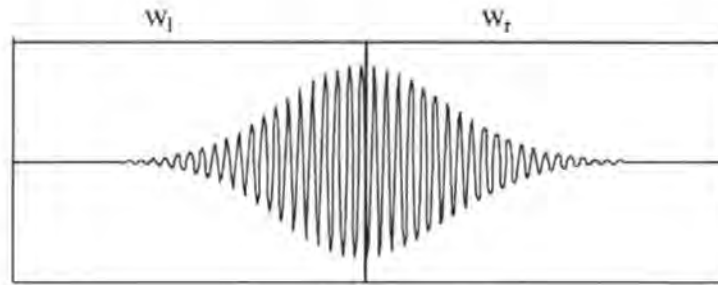


Figure 8.1 Gaussian window function for w_l and w_r .

In this case the Fourier transform of $w_l(x)$ is merely the complex conjugate of the transform of $w_r(x)$. The Fourier transform of the combined left and right parts of the signal is therefore of the form

$$F(u) = W(u) \exp(j\frac{\phi}{2}) + W^*(u) \exp(-j\frac{\phi}{2}) \quad (8.2)$$

where $W(u)$ is the Fourier transform of the right side window function suitably shifted to take account of the carrier frequency term and u is the spatial co-ordinate in the Fourier transform plane at the detector. Writing $W(u)$ as $R(u) + jI(u)$ we have

$$F(u) = [R(u) + jI(u)] \exp(j\frac{\phi}{2}) + [R(u) - jI(u)] \exp(-j\frac{\phi}{2}) \quad (8.3)$$

$$= R(u) \left[\exp(j\frac{\phi}{2}) + \exp(-j\frac{\phi}{2}) \right] + jI(u) \left[\exp(j\frac{\phi}{2}) - \exp(-j\frac{\phi}{2}) \right] \quad (8.4)$$

$$= 2R(u)\cos\left(\frac{\phi}{2}\right) - 2I(u)\sin\left(\frac{\phi}{2}\right) \quad (8.5)$$

The power spectral density is therefore

$$P(u) = 4R^2(u)\cos^2\left(\frac{\phi}{2}\right) + 4I^2(u)\sin^2\left(\frac{\phi}{2}\right) - 8R(u)I(u)\sin\left(\frac{\phi}{2}\right)\cos\left(\frac{\phi}{2}\right) \quad (8.6)$$

$$= 2R^2(u)[1 + \cos\phi] + 2I^2(u)[1 - \cos\phi - 4R(u)I(u)\sin\phi] \quad (8.7)$$

$$= 2R^2(u) + 2I^2(u) + 2[R^2(u) - I^2(u)]\cos\phi - 4R(u)I(u)\sin\phi \quad (8.8)$$

The outputs of the left and right hands element of the bicell are respectively

$$s_L = k \int_{-\infty}^{-g/2} P(u) du \quad \text{and} \quad s_R = k \int_{g/2}^{\infty} P(u) du \quad (8.9)$$

where g is the gap between the bicell elements and k is a system constant, giving

$$s_L = k \int_{-\infty}^{-g/2} [2R^2(u) + 2I^2(u) + 2[R^2(u) - I^2(u)]\cos\phi - 4R(u)I(u)\sin\phi] du \quad (8.10)$$

and

$$s_R = k \int_{g/2}^{\infty} [2R^2(u) + 2I^2(u) + 2[R^2(u) - I^2(u)]\cos\phi - 4R(u)I(u)\sin\phi] du \quad (8.11)$$

Remembering that $R(u)$ is an even function and $I(u)$ is an odd function it follows that $R^2(u)$ and $I^2(u)$ are even functions and $R(u)I(u)$ is an odd function. The above equations may therefore be written as

$$s_L = a_1 + a_2 \cos\phi + a_3 \sin\phi \quad \text{and} \quad s_R = a_1 + a_2 \cos\phi - a_3 \sin\phi \quad (8.12)$$

where

$$a_1 = k \int_{g/2}^{\infty} 2R^2(u) + 2I^2(u) du = k \int_{-g/2}^{-g/2} 2R^2(u) + 2I^2(u) du \quad (8.13)$$

$$a_2 = k \int_{g/2}^{\infty} 2[R^2(u) - I^2(u)]du = k \int_{-g/2}^{-g/2} 2[R^2(u) - I^2(u)]du \quad (8.14)$$

$$a_3 = k \int_{g/2}^{\infty} 4R(u)I(u) du = -k \int_{-g/2}^{-g/2} 4R(u)I(u) du \quad (8.15)$$

Taking the sum and difference of the outputs of the bicell elements gives

$$P_{SUM}(\phi) = 2(a_1 + a_2 \cos\phi) \quad \text{and} \quad P_{DIFF}(\phi) = 2a_3 \sin\phi \quad (8.16)$$

Solving the equations for a_1 , a_2 , and a_3 numerically for a Gaussian window, using Mathcad, (see Appendix C) gives a positive value for a_1 and a_3 and a negative value for a_2 . Figure 8.2 shows the numerical solutions of Eq. (8.16) for the peak deviations in the sum and difference outputs for a series of phase shifts between $-\pi$ and $+\pi$ radians.

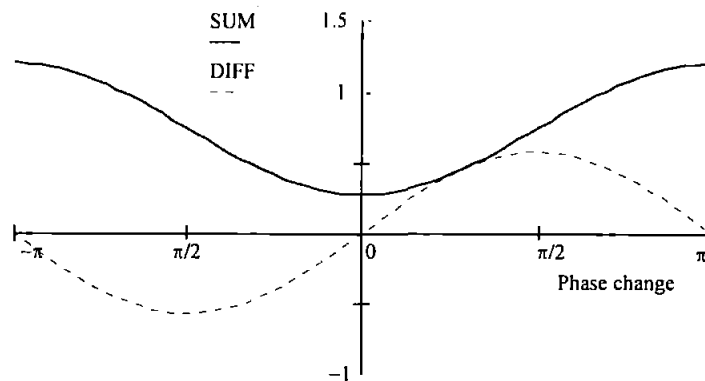


Figure 8.2 numerical solution of equation 8.16.

8.2 Optimum gap size for phase demodulation

When using the system to demodulate PSK signals rather than FSK signals we have to look at the effect of the gap size of the bi-cell in relation to the standard deviation of the beam at the detector, σ_1 . Figure 8.3 shows the light intensity distribution at the bi-cell detector when phase changes of 0 , $\pi/4$, $\pi/2$, and π are at the centre of the AO cell window. The size of the gap shown is $3\sigma_1$. Clearly the signal from each detector element will vary if the gap size is changed.

The trace with the maximum amplitude shows the normal Gaussian beam with no phase change present. The next trace down shows how a $\pi/4$ change affects the shape of the Gaussian, and the next is the response to a $\pi/2$ shift. Finally the solid trace at the bottom shows the symmetrical response that occurs when a phase shift of π is in the centre of the cell

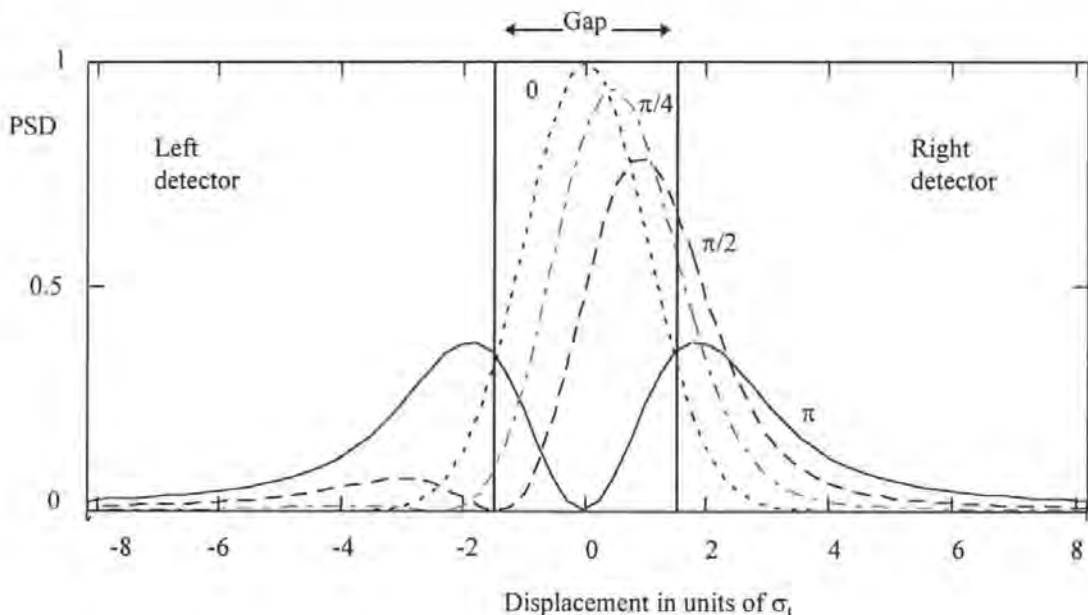


Figure 8.3 Power spectral density of the Gaussian for phase changes of 0 , $\pi/4$, $\pi/2$, and π in the centre of the Gaussian window of the AO-cell

In order to find the optimum gap size for the bi-cell in relation to the standard deviation of the beam at the detector σ_1 a number of graphs were drawn. All simulated noise was taken off the model and carriers with phase changes of 0 , $\pi/4$, $\pi/2$, and π were used as input signals to the system for a number of different gap sizes.

The output level caused by a phase change in the centre of the Gaussian aperture was subtracted from the output level for the carrier only and plotted against the various bi-cell gap sizes.

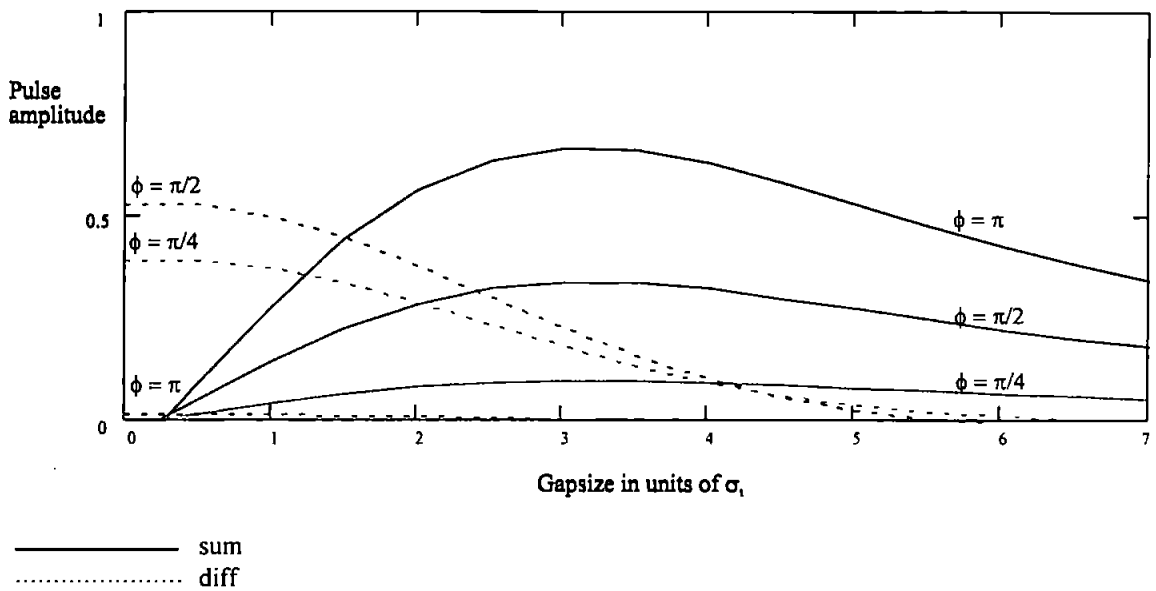


Figure 8.4 Pulse amplitude versus gap size

Figure 8.4 shows how the amplitude of the spikes, shown in Figure 6.16, which will be shown to be produced by instantaneous phase shifts (chapter 9) are affected by the size of the gap between the detectors with respect to the standard deviation of the Gaussian beam at the detector σ_t . The solid lines represent the sum output and the dotted lines represent the difference. The relationship was plotted for three different phase shifts; $\pi, \pi/2$ and $\pi/4$. It can be seen from Figure 3.2. that the optimum gap size for the difference output would be zero, whereas the sum output gains its maximum level for a gap size of $3 \sigma_t$. It was decided that a good compromise would be to set the gap size to be between $2 \sigma_t$ and $3 \sigma_t$. The mathcad file used to generate Figure 8.4 can be found in appendix C.

8.3 Shot noise limited resolution for PM

8.3.1 Sum channel

In a similar way to the frequency modulation analysis, section 7.3, this section looks at the smallest instantaneous phase change that can be detected by the demodulator system. The output voltage from either the sum or difference channel when the phase change is in the centre of the AO cell, is subtracted from the normal output from each channel when no modulation is on the carrier. This leaves the change in voltage caused by the phase change.

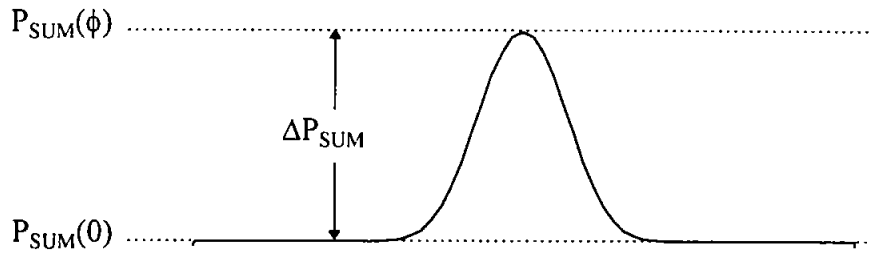


Figure 8.5 Graph showing ΔP_{SUM} , $P_{SUM}(\phi)$, and $P_{SUM}(0)$.

From Eq. (8.4) it can therefore be written that

$$\Delta P_{DIFF} = P_{DIFF}(\phi) - P_{DIFF}(0) = 2P_1 a_3 \sin(\phi) - 2P_1 a_3 \sin(0) \quad (8.17)$$

and

$$\Delta P_{SUM} = P_{SUM}(\phi) - P_{SUM}(0) = 2P_1 (a_1 + a_2 \cos(\phi)) - 2P_1 (a_1 + a_2 \cos(0)) \quad (8.18)$$

where P_1 is the diffracted optical power, ϕ is the phase change and a_1 , a_2 and a_3 are constants given in Eq. (8.13), (8.14) and (8.15). The sum and difference are then divided by the shot noise giving

$$SNR_{SUM} = \frac{(\Delta P_{SUM} R_\lambda)^2}{2R_\lambda e B_n P_b} \quad (8.19)$$

and

$$SNR_{DIFF} = \frac{(\Delta P_{DIFF} R_\lambda)^2}{2R_\lambda e B_n P_b} = \frac{(k P_b R_\lambda)^2}{2R_\lambda e B_n P_b} \quad (8.20)$$

where P_b is the total optical power falling on the two detectors when the phase change is in the centre of the AO cell, this is therefore given by $P_{SUM}(\phi)$.

$$P_b = P_{SUM}(\phi) = 2P_1(a_1 + a_2 \cos(\phi)) \quad (8.21)$$

In order to find the minimum detectable phase change, we continue as for the FM case.

$$\Delta P_{SUM} = 2P_1 a_2 (\cos(\phi) - 1)) \quad (8.22)$$

using Eq. (8.21) gives

$$\Delta P_{SUM} = \frac{2P_b a_2 (\cos(\phi) - 1))}{2(a_1 + a_2 \cos(\phi))} \quad (8.23)$$

therefore

$$K_S = \frac{\Delta P_{SUM}}{P_b} = \frac{a_2 (\cos(\phi) - 1))}{a_1 + a_2 \cos(\phi)} \quad (8.24)$$

as K_S for SNR =1 is given by Eq. (7.37)

$$K_{S_{SNR=1}} = \sqrt{\frac{4eB_n}{R_\lambda P_b}} \quad (8.25)$$

Eq. (8.24) can be written

$$\sqrt{\frac{4eB_n}{R_\lambda P_b}} = \frac{a_2 (\cos(\phi) - 1))}{a_1 + a_2 \cos(\phi)} \quad (8.26)$$

substituting for P_b

$$\frac{4eB_n}{R_\lambda 2P_1(a_1 + a_2 \cos(\phi))} = \frac{a_2^2 (\cos(\phi) - 1))^2}{a_1 + a_2 \cos(\phi)^2} \quad (8.27)$$

which is equal to

$$\frac{2eB_n}{R_\lambda P_1} = \frac{a_2^2 (\cos(\phi) - 1))^2}{a_1 + a_2 \cos(\phi)} \quad (8.28)$$

collecting the $\cos(\phi)$ terms together gives

$$2eB_n(a_1 + a_2 \cos(\phi)) = R_\lambda P_1 a_2^2 (\cos(\phi) - 1))^2 \quad (8.29)$$

$$2eB_n a_1 + 2eB_n a_2 \cos(\phi) = R_\lambda P_1 a_2^2 (\cos(\phi)^2 - 2 \cos(\phi) + 1) \quad (8.30)$$

which can be written as a quadratic

$$R_\lambda P_1 a_2^2 \cos(\phi)^2 - (2R_\lambda P_1 a_2^2 - 2eB_n a_2) \cos(\phi) + R_\lambda P_1 a_2^2 - 2eB_n a_1 = 0 \quad (8.31)$$

which can be solved for $\cos(\phi)$. Two roots are produced, which when the values for a_1 , a_2 and a_3 , numerically calculated using mathcad are substituted in gives one reasonable and one impossible value for $\cos(\phi)$. It is possible, as for the FM analysis, to get an expression which links SNR and minimum detectable phase shift.. This is done by rearranging Eq. (7.36) to give Eq. (7.45)

$$K = \sqrt{\frac{4eB_n}{R_\lambda P_b}} \sqrt{SNR} . \quad (8.32)$$

We can then substitute this in Eq. (8.25) and thus the reasonable root of Eq. (8.31) can be written in terms of the system SNR and thus a value for $\phi_{\min(\text{sum})}$ calculated.

Using the normal system parameters, as given in chapter 5, gives

$$\phi_{\min(\text{sum})} = \frac{\pi}{30} \sqrt{SNR} \quad (8.32)$$

8.3.2 Difference channel

Similarly for the difference output we get

$$\Delta P_{DIFF} = P_1 2a_3 (\sin(\phi)) \quad (8.33)$$

using Eq. (8.21) gives

$$\Delta P_{DIFF} = \frac{P_b 2a_3 (\sin(\phi))}{2(a_1 + a_2 \cos(\phi))} \quad (8.34)$$

therefore

$$K_D = \frac{\Delta P_{DIFF}}{P_b} = \frac{a_3 (\sin(\phi))}{a_1 + a_2 \cos(\phi)} \quad (8.35)$$

which can be rearranged and expressed in terms of K_D

$$\frac{a_1 + a_2 \cos(\phi)}{a_3} K_D = \sin(\phi) \quad (8.36)$$

so the minimum resolvable phase for a given system with a unity SNR is found using Eq. (7.37) from

$$\sin(\phi_{\min}) = \frac{a_1 + a_2 \cos(\phi)}{a_3} \sqrt{\frac{4eB_n}{R_\lambda P_b}} \quad (8.37)$$

Again values for a_1 , a_2 and a_3 , calculated using mathcad are substituted in and linking the SNR and minimum phase for the difference. In the case of the difference we can assume that as ϕ_{\min} is small $\cos(\phi) \approx 1$ so that

$$\sin(\phi_{\min}) = \frac{a_1 + a_2}{a_3} \sqrt{\frac{4eB_n}{R_\lambda P_b}} \sqrt{SNR} \quad (8.38)$$

which using the normal system parameters gives

$$\phi_{\min(\text{diff})} = \frac{\pi}{9166} \sqrt{SNR} \quad (8.39)$$

8.4 The effect of clipping on PM

When considering the response of the system to phase modulation the first point to be noted is that both the sum and the difference channels are used to demodulate the signal. The response of the difference channel to band limited Gaussian noise will be identical to that when the system is being used as an FM demodulator. Therefore it is only necessary to consider the effect noise will have on the sum output.

Figure 8.6 shows the relationship between the optimum level of clipping on the signal and the CNR of the signal at the input to the system CNR_{in} . The optimum clipping level for any frequency with a CNR_{in} above 40 dB is seen to be 70 %, and again as in the case of the difference channel, as the CNR_{in} falls the amount that the signal has to be clipped increases quite markedly.

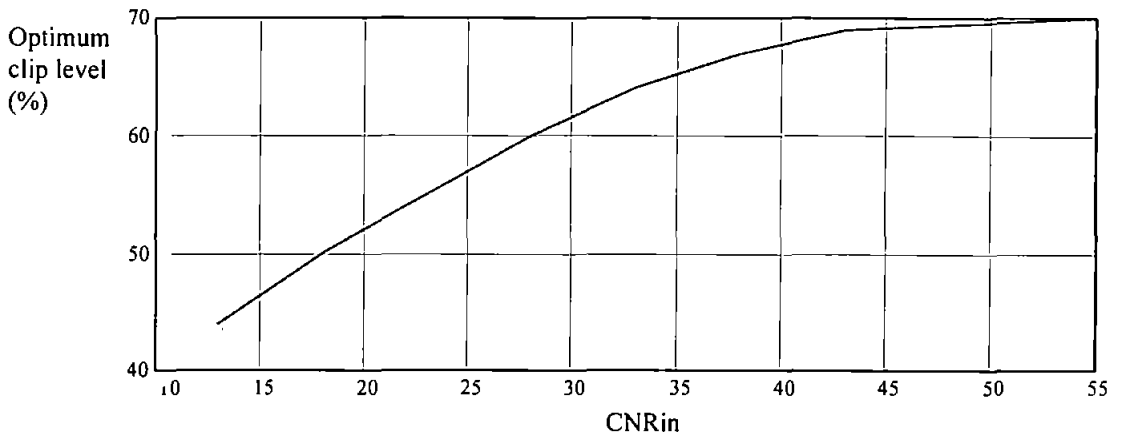


Figure 8.6 Optimum clipping level versus CNR_{in}

By comparing Figure 8.6 to Figure 7.10, which shows the optimum clip level of the difference output versus the CNR_{in} , it can be seen that the overall shape of the curves are similar although the curve for the sum falls off at half the rate as shown in Figure 8.7.

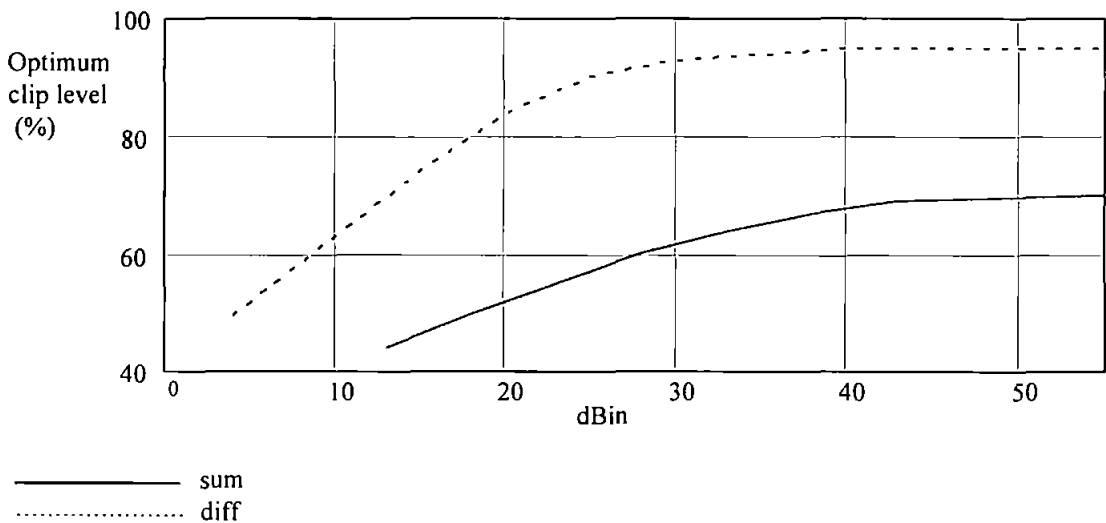


Figure 8.7 Graph showing how the optimum clipping level for the sum channel differs from the optimum clipping level for the difference channel.

As with the difference channel, it was decided to look at what was being gained by clipping the signal. Figure 8.8 shows three CNR_{in} to SNR_{out} plots, taken for a phase change of $\pi/2$ rad; one with no clipping, one where the clipping has been set to 65% and the other using adaptive clipping where the optimum clipping level is decided for each CNR_{in} .

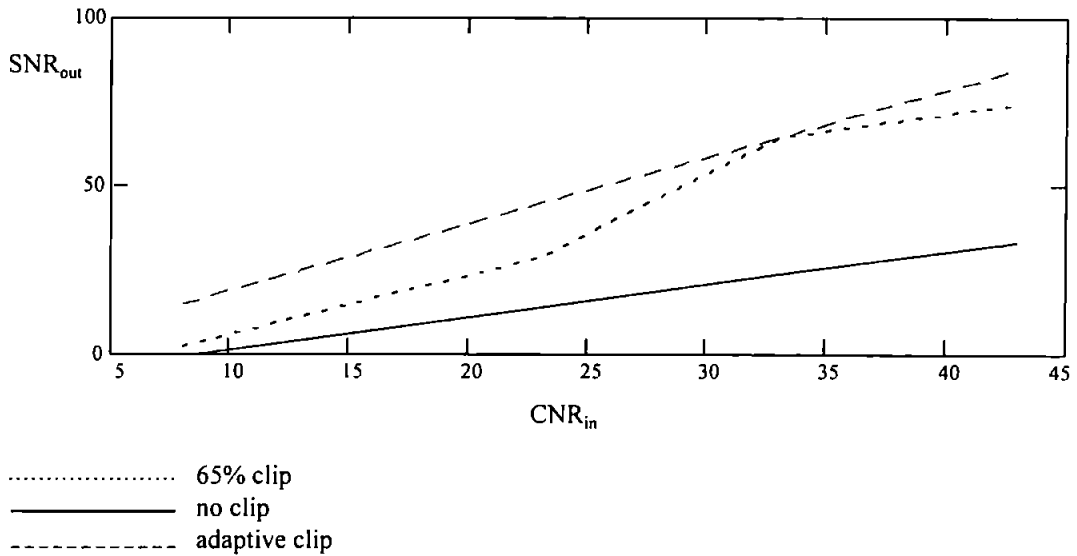


Figure 8.8 Graph showing the effect of different levels of clipping SNR_{out} versus SNR_{in} .

This graph shows that with the adaptive clipping the SNR has a gradient of 2 whereas the gradient of the slope for no clipping is 1. It can also be seen from Figure 8.8 that even a constant level of clipping is preferable to none at all

8.5 Summary and conclusions

This chapter has shown how the AO demodulator performs when it is being used as a phase demodulator. Section 8.1 derived equations relating the instantaneous phase shift ϕ to the output of the system. Concluding that the sum and difference of the outputs of the bicell elements gives

$$P_{SUM}(\phi) = 2(a_1 + a_2 \cos\phi) \quad \text{and} \quad P_{DIFF}(\phi) = 2a_3 \sin\phi \quad (8.16)$$

where ϕ is the discrete phase shift and a_1 , a_2 , and a_3 are constants calculated from Eqs. (8.13), (8.14) and (8.15) respectively.

Section 8.2 goes on to show the optimum gap size of the bi-cell in terms of the standard deviation of the laser beam at the detector, σ_l . Figure 8.4 shows that there is a conflict between the optimum gap size for the difference channel and the sum channel. It was decided that a good compromise would be a gap size of between $2\sigma_l$ and $3\sigma_l$

The shot noise limited resolution of section 8.3 derives two equations for the minimum detectable phase changes, one for the difference channel and one for the sum channel. For the parameters used in the practical system the minimum detectable phase shift for the sum channel is

$$\phi_{\min(\text{sum})} = \frac{\pi}{30} \sqrt{\text{SNR}}$$

and for the difference channel is

$$\phi_{\min(\text{diff})} = \frac{\pi}{9166} \sqrt{\text{SNR}}$$

Finally in section 8.4 the effect of various levels of clipping of the carrier signal (CNR_{in}) on the output signal to noise ratio (SNR_{out}) are presented. It is shown that the level of clipping required for the sum is greater than the level required for the difference channel. It is also shown that any level of clipping improves SNR_{out} . Obviously the signal can only be clipped once so there has to be a trade off between the performance of the two channels. For purposes such as Doppler detection, (see chapter 9), and FM signals the difference channel contains all of the useful information, so obviously the system would be set up to optimise its performance. As a surveillance receiver the information is contained on both channels, but as using Eq. (8.16) for $P_{\text{DIFF}}(\phi)$ it is theoretically possible to calculate the phase shift from the amplitude of the spike, it would seem reasonable to optimise the clipping level for the difference channel again.

9. Simulated results from the model

The mathematical model described in chapter 6 was used to simulate the response of the AO demodulator to a variety of modulated signals, these are; discrete phase shift of π , $\pm \pi/2$, $\pm \pi/4$ and $\pm 3\pi/4$; frequency shift keying signals; phase shift keying signals; a pulse doppler signal; and a carrier signal containing AM noise.

The model (the listings of which can be found in appendix C) created these modulated signals and simulated the effect of each of the components, described in chapter 5, on the overall output of the system. These results were then used to explain exactly what was going on in the system and why the output of the system responded in the way it did to different input signals.

It is also shown how it is possible to decode the waveforms produced by the sum and difference channels in response to the digitally modulated inputs. The simulation results gained from the software were based on a 50 MHz carrier signal modulated by the appropriate form of modulation. In each case the model was used to produce a plot showing the effect of the modulation on the shape of the Gaussian beam profile during the transition stages, and the sum and difference output of the bi-cell. The plots of the beam profile show five representations of the diffracted beam as the change in modulation (be it frequency or phase). These five plots show the effect on the beam as the change in modulation; 1) approaches the AO window, 2) is one quarter the way through the AO window, 3) is half way through the AO window, 4) is three quarters the way through the AO window, 5) has passed all the way through and out the other side.

9.1 Digital phase modulation

This section shows how instantaneous phase shifts of π , $\pm \pi/2$, $\pm \pi/4$ and $\pm 3\pi/4$ affect the power spectral density, PSD, of the diffracted beam and hence the effect on the sum and difference output channels of the system. It is shown that the system can accurately identify all of these individual phase shifts by examination of the sum and difference channels.

9.1.1 Phase shift of π .

A π phase shift is put onto the 50 MHz carrier signal, the effect of this on the shape of the beam at the detector can be clearly seen in Figure 9.1 with the intensity dipping to zero in the centre of the beam (when the phase change is halfway through the cells aperture). This effect was previously described by Reeve and Houghton [3].

Power Spectral Density

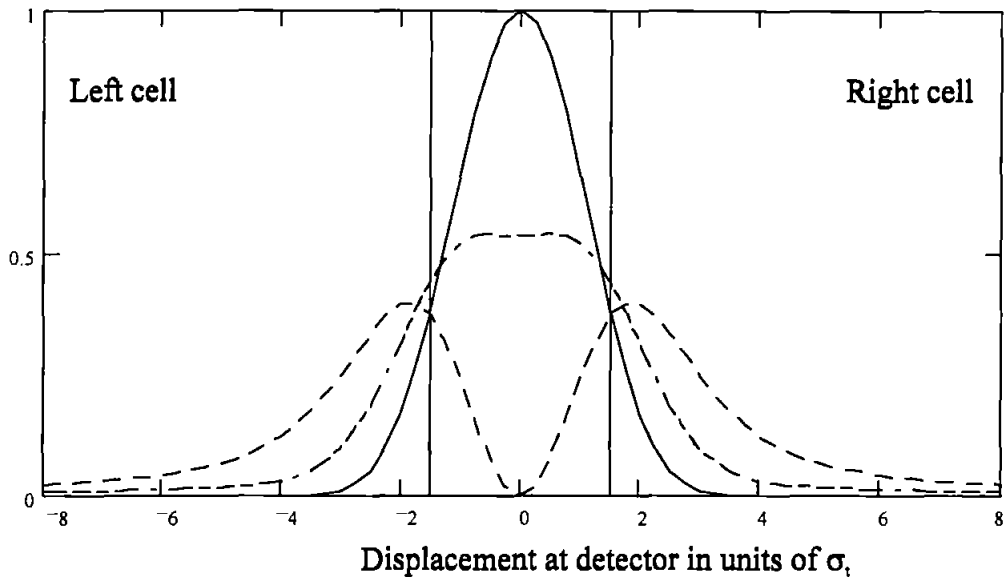


Figure 9.1 Simulation of beam spectral density function in response to BPSK input signal.

The system output shown in Figure 9.2 shows how the sum of the bi-cells outputs (upper trace) increases as the phase change goes through the cell due to the power being taken away from the gap between the two cells and spread onto the active areas. As the change in distribution is symmetrical there is no change on the difference channel.

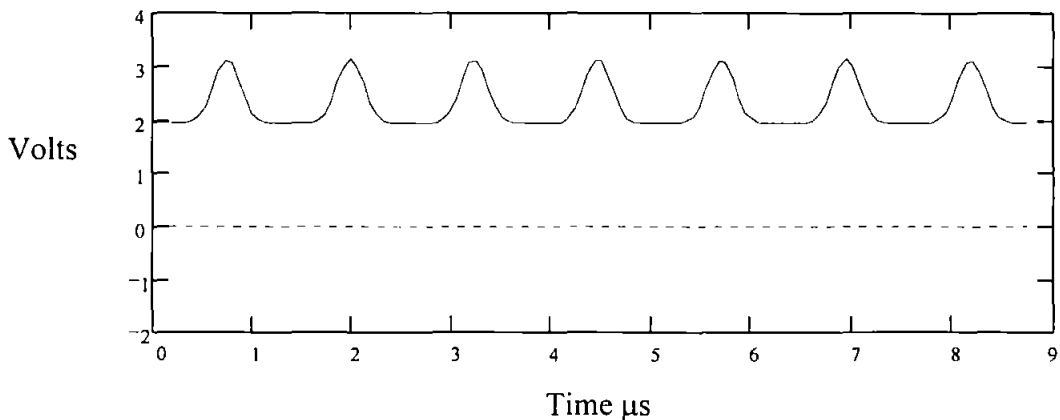


Figure 9.2 Simulation response to π PSK input, on a 50 MHz carrier frequency.
upper trace : sum. lower trace : difference.

9.1.2 Phase shift of $\pi/2$

Figure 9.3 and Figure 9.4 show how the spreading of the intensity described above is no longer symmetrical but is shifted to one side or other of the centre of the beam according to whether the phase change is $\pi/2$ or $-\pi/2$.

Power Spectral Density

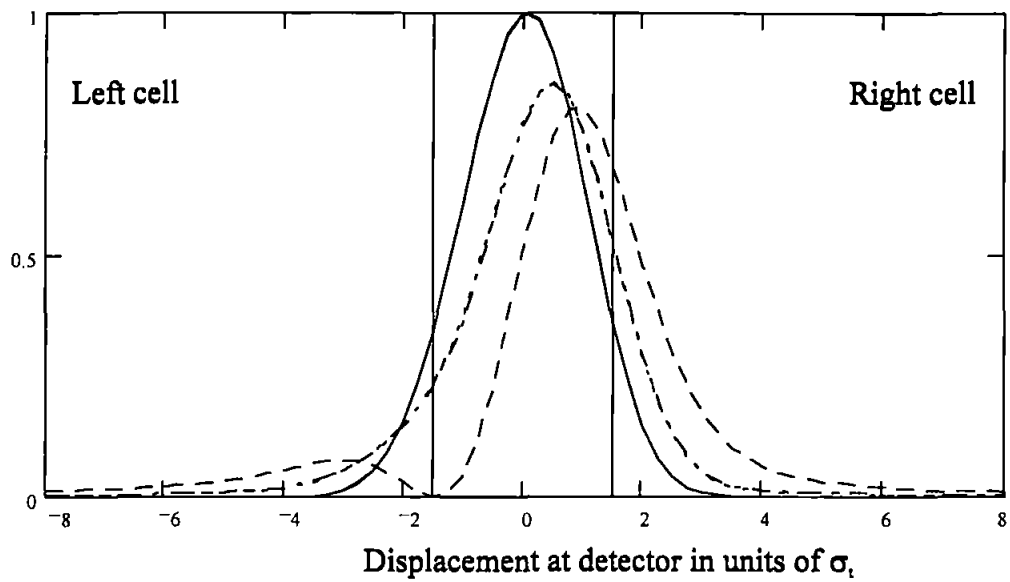


Figure 9.3 Simulation of beam spectral density function in response to $+\pi/2$ input signal.

Power Spectral Density

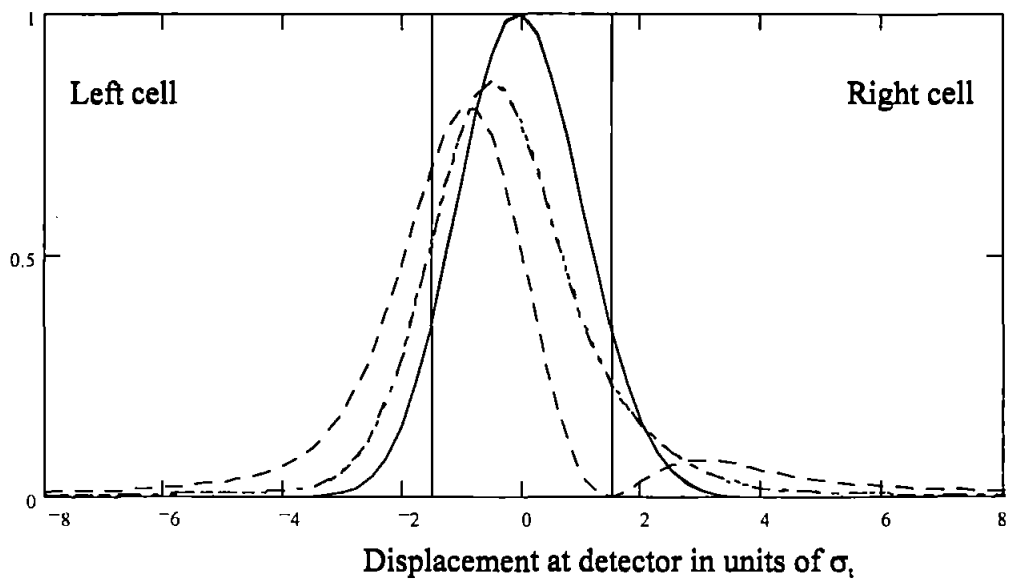


Figure 9.4 Simulation of beam spectral density function in response to $-\pi/2$ input signal.

Figure 9.5 shows that the sum still increases as the phase affects the shape of the pulse although not as much as for the π phase change, this time the difference is also affected due to the non symmetry of Figure 9.4 and Figure 9.3. A positive spike on the difference channel indicates a phase change of $\pi/2$ and a negative spike indicates a phase change of $-\pi/2$.

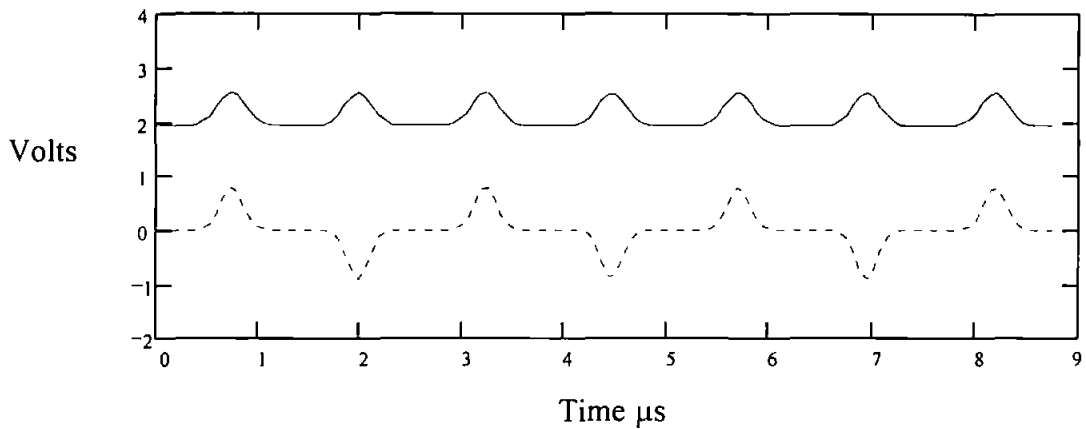


Figure 9.5 Simulation response to $+\pi/2$ and $-\pi/2$ input on a 50 MHz carrier frequency.
upper trace : sum. lower trace : difference.

9.1.3 $\pm \pi/4$ and $\pm 3\pi/4$ phase shifts

Rather than show all four PSD's for $\pm \pi/4$ and $\pm 3\pi/4$, here are shown the PSD's for $-\pi/4$ and $-3\pi/4$ only. As in section 9.1.2 for the $\pm\pi/2$ phase shifts the PSD's for $+\pi/4$ and $+3\pi/4$ are simply mirror images of Figure 9.6 and Figure 9.7.

Power Spectral Density

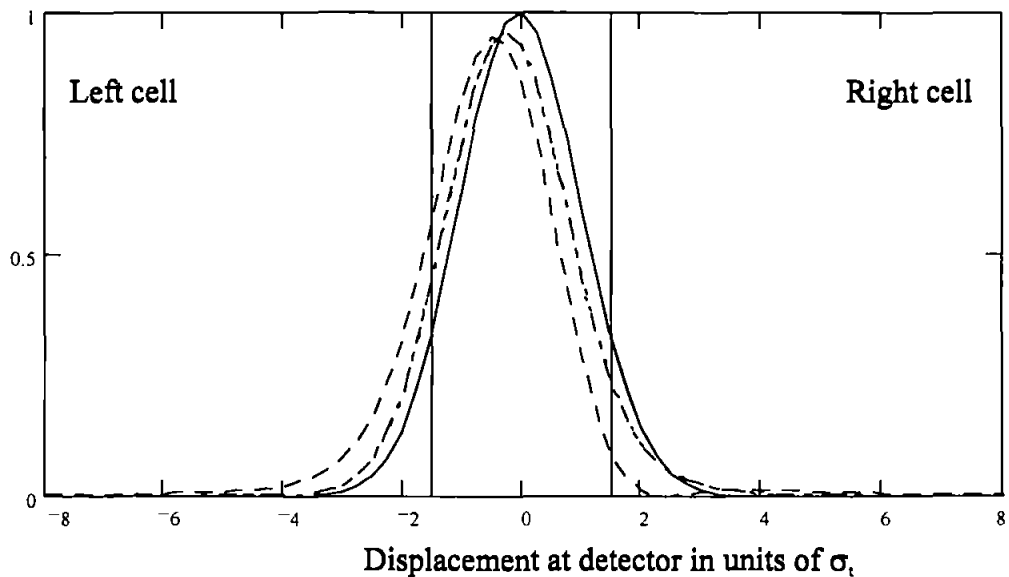


Figure 9.6 Simulation of beam spectral density function in response to $-\pi/4$ input signal.

Power Spectral Density

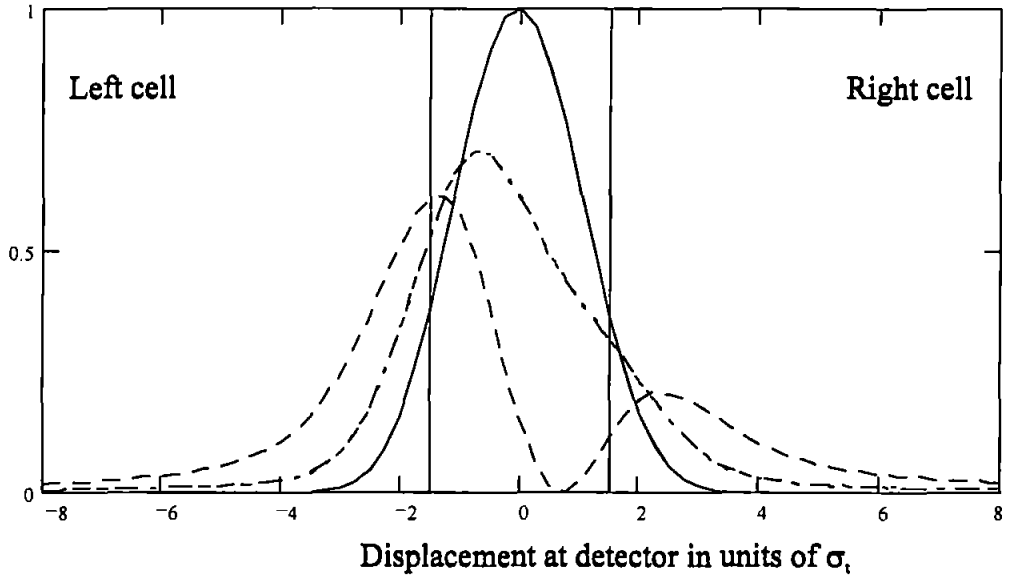


Figure 9.7 Simulation of beam spectral density function in response to $-3\pi/4$ input signal.

The system output shown in Figure 9.8 shows how the sum of the bi-cells outputs (upper trace) is proportional the phase change due to the different amounts of power being taken away from the gap between the two cells and spread onto the active areas. Again positive and negative spikes represent $+$ and $-$ phase changes of $\pi/4$ and $3\pi/4$.

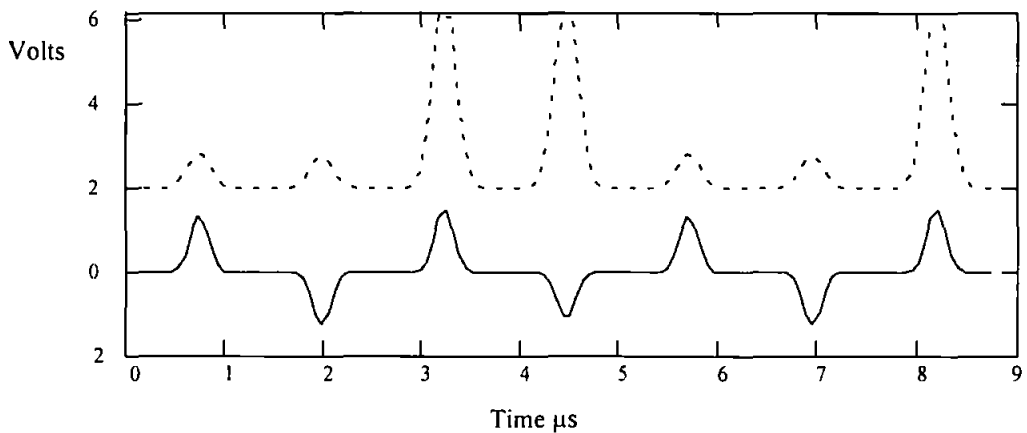


Figure 9.8 A 50 MHz carrier modulated by $\pm\pi/4$ and $\pm3\pi/4$.
upper trace : sum of bi-cell. lower trace : difference of bi-cell

9.1.4 Summary

Section 9.1 has shown that the PSD of the beam and hence the output of the system have different responses to each of the phase changes applied. It is therefore possible to identify

individually each of the phase changes. The distinguishing outputs on the sum and difference channels are shown in Table 9.1. It should be remembered that a_2 , calculated numerically in chapter 8, is always negative.

Phase shift	Sum	Difference
π	tallest spike	Constant
$\pm\pi/2$	medium size spike $\propto a_1 + a_2 \cos(\phi)$	\pm spike $\propto a_3 \sin(\phi)$
$\pm\pi/4$	small spike $\propto a_1 + a_2 \cos(\phi)$	\pm spike $\propto a_3 \sin(\phi)$
$\pm 3\pi/4$	tall spike $\propto a_1 + a_2 \cos(\phi)$	\pm spike $\propto a_3 \sin(\phi)$

Table 9.1 Summary of the effect of phase shifts on the sum and difference channels

9.2 Digital frequency modulated signals

Frequency shift keying (FSK) is binary frequency modulation of the analogue carrier. Thus a voltage controlled oscillator can be used with the two voltage levels of the data, shifting the carrier to two discrete frequencies, one of which represents binary 1 and the other binary 0. In a simple system no care is taken at the transition points to preserve the phase, this results in phase discontinuities at these transition points. Systems that do preserve the phase at these transitions are called continuous phase - FSK (CP-FSK).

9.2.1 Continuous Phase - Frequency Shift Keying (CP-FSK)

A 50 MHz carrier signal was deviated by ± 250 kHz. Figure 9.9 shows the shape of the diffracted beam at the detector does not change very much, except that it broadens slightly when the transition between the two frequencies is in the centre of the acousto-optic cells aperture. The only effect is to shift the position of the beam along the axis by an amount proportional to the frequency deviation. This is an example of a CP-FSK signal. If there is any constant voltage change on the difference output it indicates a change in frequency from the carrier frequency. The system output shown in Figure 9.10 is an example of a CP-FSK signal with alternate positive and negative frequency changes.

Power Spectral Density

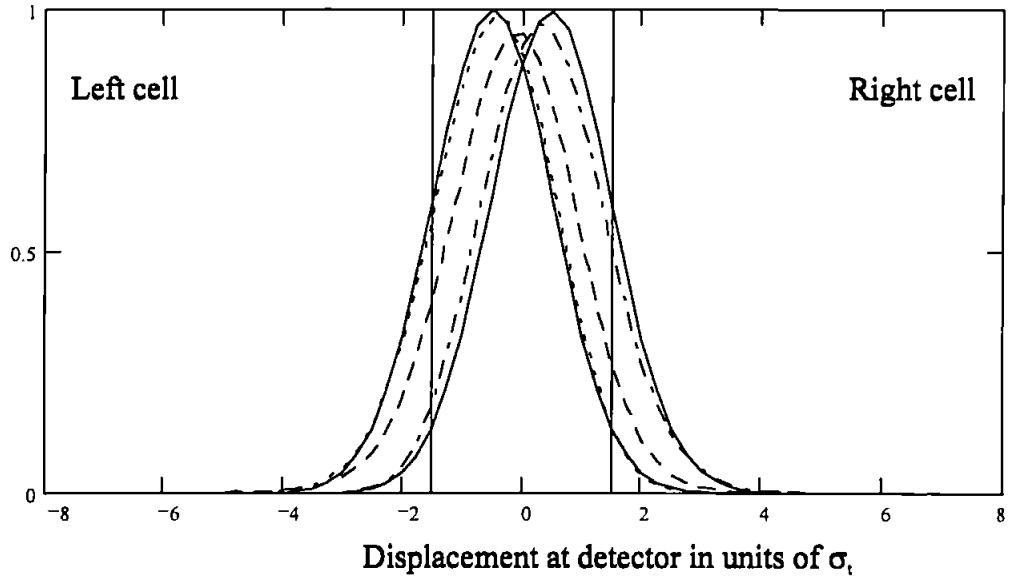


Figure 9.9 Simulation of beam spectral density function in response to CP-FSK input signal.

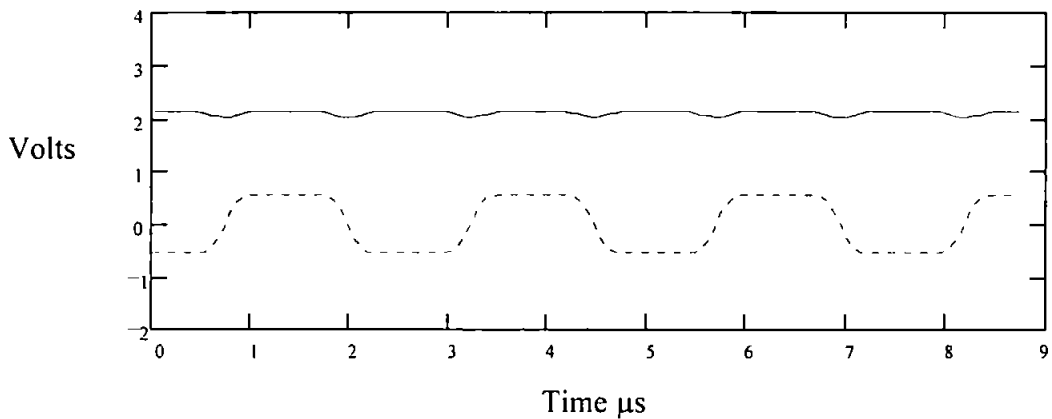


Figure 9.10 Simulation response to CP-FSK input on 50 MHz carrier frequency.
upper trace : sum. lower trace : difference.

9.2.2 Frequency shift keying (FSK)

The result of the phase discontinuities of normal FSK can be clearly seen by the distortion of the PSD in Figure 9.11, this causes the pulses on both the sum and difference at the transition points of Figure 9.12.

Power Spectral Density

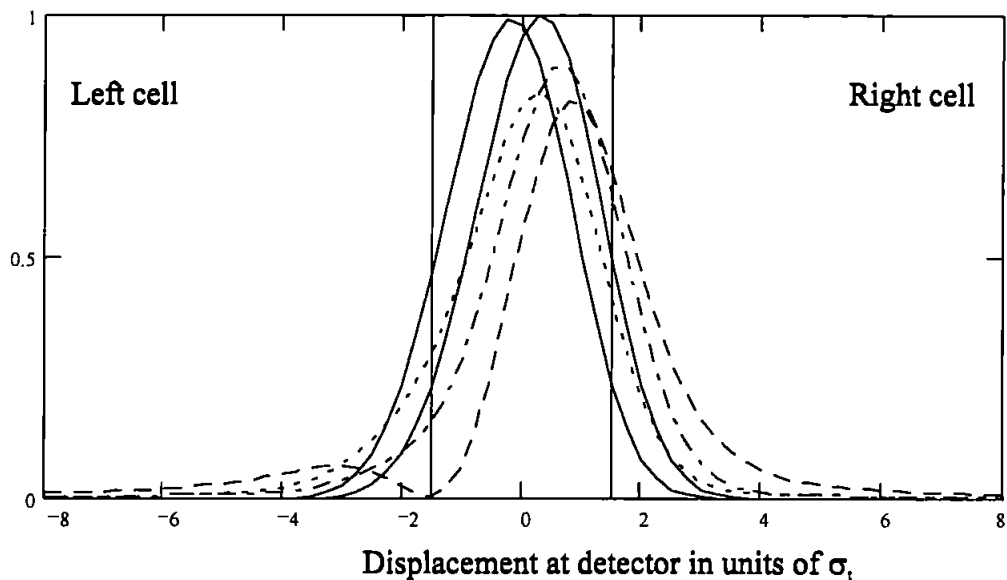


Figure 9.11 Simulation of beam spectral density function in response to FSK input signal.

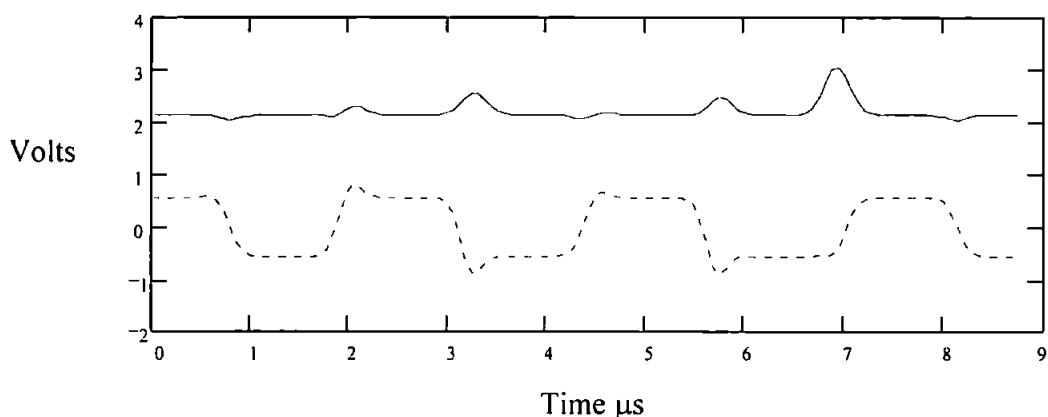


Figure 9.12 Simulation response to FSK input on 50 MHz carrier frequency, pulses on the sum caused by phase changes during frequency transitions. Upper trace : sum. lower trace : difference.

9.3 Practical Phase Shift Keying signals

This section presents the outputs from the various PSK modulation techniques discussed in section 2.3. In PSK the phase of the carrier signal is switched between two or more values in response to a binary message. The majority of practical digital modulations use two-dimensional signal constellations in which the first dimension is the cosine carrier signal and the second is the sine carrier signal of the same frequency. These rely on accurate phase reference in order to keep them orthogonal, a scheme that needs a reference is called a coherent modulation. Conversely a scheme that can work without a phase reference is

called an incoherent modulation. Because the AO demodulator will have no idea of the bit rate of any of the signals it is demodulating, in all these examples the bit rate is assumed to be the time between the two closest changes of modulation. Over a long enough signal sample this will be true.

9.3.1 Binary Phase Shift Keying (BPSK) / Differential phase shift keying (DPSK)

For binary modulation a 180° phase shift is often used because it simplifies the modulator design, this is known as phase-reversal keying (PRK), or BPSK. No phase shift denotes binary 0 and a π phase shift denotes a binary 1. In a DPSK scheme, the data are encoded into the transition from interval to interval. Differential encoding uses the rule that there is no change in the output state if a 1 is present at the input and there is a change if a 0 is present.

BPSK and DPSK signals can be identified by a mixture of spikes and no change on the sum channel and nothing on the difference channel. With reference to the results of section 9.1 it can be seen that the wave form of Figure 9.13 was created by phase changes of π , 0, π , π , 0, π , π . The BPSK codeword that produced this output was 1011011, a DPSK codeword producing the same output would be 001001 due to the encoding discussed in section 2.3.3, see Table 9.2

Output phase	π	0	π	π	0	π	π
DPSK codeword	0	0	1	0	0	1	

Table 9.2 Decoding a DPSK waveform.

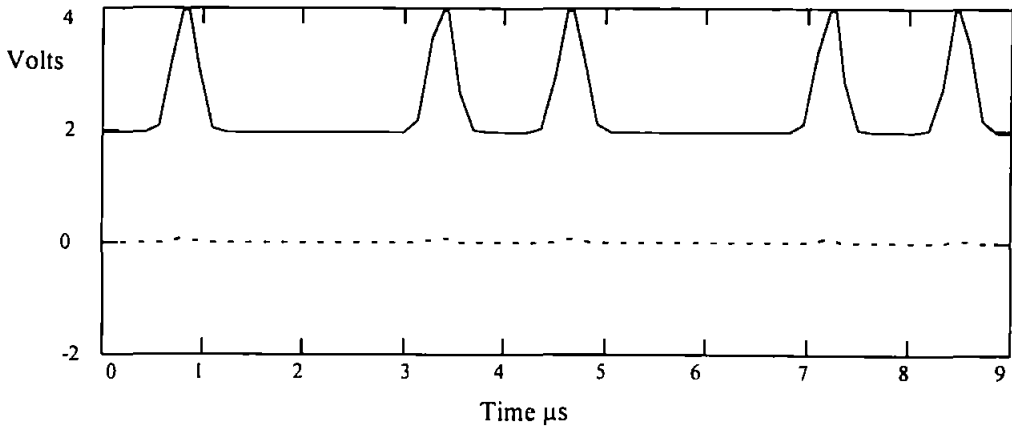


Figure 9.13 Simulation results of phase changes using π and 0.

9.3.2 Quadrature phase shift keying (QPSK)

As described in section 2.3.4, a QPSK signal has a maximum phase shift in any one bit of π . QPSK modulation carries four symbols, each with a different phase. These phases are spaced by 90° and normally are $\psi = \{45^\circ, 135^\circ, 225^\circ, 315^\circ\}$, which correspond to 00, 10, 11, 01 respectively. The example of a QPSK signal shown in Figure 9.14 is a result of the instantaneous phase shifts $\pi/2, \pi, -\pi/2, \pi, \pi/2, -\pi/2$ (From section 9.2). If we assume that the original state of the signal was 00 or $\pi/4$, then we can write the QPSK phase states as $3\pi/4, 7\pi/4, 5\pi/4, \pi/4, \pi/4, 3\pi/4, \pi/4$. Thus we can recreate the codeword 10 01 11 00 00 10 00.

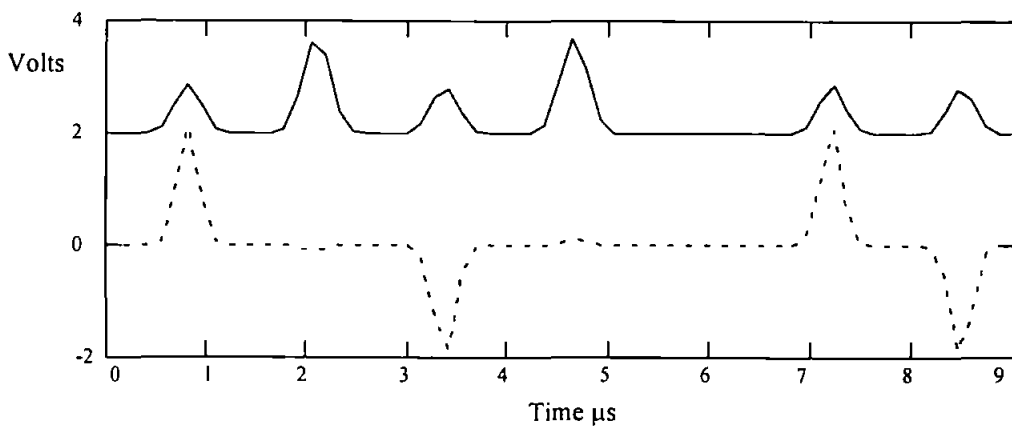


Figure 9.14 Simulation response to a QPSK signal

9.3.3 Offset quadrature phase shift keying (OQPSK)

OQPSK is similar to QPSK except that the carrier phase transitions are transmitted in two periods. This results in instantaneous carrier phase transitions of only $\pm\pi/2$ from the previous phase state, as compared to QPSK (and BPSK) that contain π transitions. Again by looking at section 9.1. it can be seen that Figure 9.15 which was created by instantaneous phase changes of $-\pi/2, 0, \pi/2, \pi/2, \pi/2, 0, -\pi/2$. Again assuming an initial phase of 00 or $\pi/4$, these would result from the transmitted signal phase $7\pi/4, 7\pi/4, \pi/4, 3\pi/4, 5\pi/4, 5\pi/4, 3\pi/4$. Which according to section 2.3.4 translates to $01\ 01\ 00\ 10\ 11\ 11\ 10$, which would make the values for a^I and a^Q

$$\begin{array}{r} a^I \quad 0\ 0\ 1\ 1 \\ a^Q \quad 1\ 0\ 1\ 0 \end{array}$$

This is shown more clearly in Table 9.3. The binary digit in bold the 'corresponding binary' row is the one which is changed by either the I or Q channel alternately

	initial phase	a^I	a^Q	a^I	a^Q	a^I	a^Q	a^I	a^Q
Recorded phase		$-\pi/2$	0	$\pi/2$	$\pi/2$	$\pi/2$	0	$-\pi/2$	
accumulative phase	$\pi/4$	$7\pi/4$	$7\pi/4$	$\pi/4$	$3\pi/4$	$5\pi/4$	$5\pi/4$	$3\pi/4$	
corresponding binary	00	01	01	00	10	11	11	10	
I channel		0		0		1		1	
Q channel			1		0		1		

Table 9.3 Decoding the OQPSK waveform

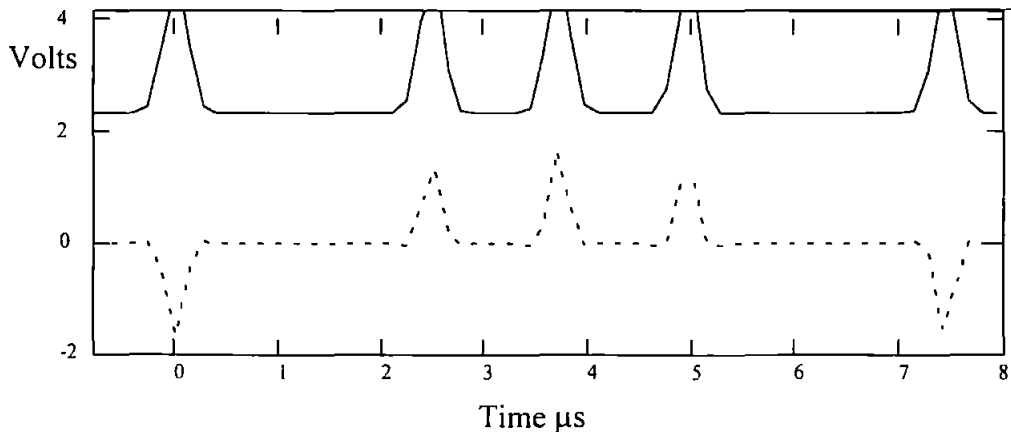


Figure 9.15 Simulation response of an OQPSK signal

9.4 Truth Table

The truth table shown in Table 9.1 characterises the type of waveform that will be produced on the sum and difference channels in response to each form of modulation investigated in section 9.3. Using this table it is possible to identify the type of modulation detected by the system from the waveforms.

(i) CP-FSK. CP-FSK signals are characterised by a shift in level on the difference channel while the sum remains constant. Unlike the case for PSK signals where the output is a spike which only occurs while the phase shift is within the laser window, the level change persists for as long as the frequency remains constant. If there is no phase discontinuity when the frequency changes, as in continuous phase FSK or MSK, then only the level change is observed. The magnitude of the level change, and hence the detectability of the signal, is proportional to the change in frequency.

(ii) ESK. As for CPFSK signals are characterised by a shift in level on the difference channel while the sum remains constant. The difference being a phase discontinuity at the frequency change results in spikes on both the sum and difference.

(iii) BPSK. Assuming that the two phase shifts are 0 and π radians this is characterised by a constant difference channel with a spike on the sum channel at each phase shift.

(iv) QPSK. The four phase shifts are 0, $\pm\pi/2$ and π radians; therefore the possible phase shifts are also 0, $\pm\pi/2$ and π radians. A spike on the sum channel indicates the presence of a phase shift and the corresponding state of the difference channel indicates the nature of the change. The occurrence of all three phase shifts identifies the type of modulation.

(iv) Offset QPSK. Here the only possible phase shifts are $\pm\pi/2$ radians. The absence of the π radians phase shifts identifies the type of modulation.

Modulation	Sum	Difference
FSK	glitches due to ϕ changes	\propto frequency and glitches due to ϕ changes
CP-FSK	Constant	\propto frequency, no glitches
BPSK	Spike	Constant
QPSK	Spike $\propto \phi$	\pm spike
OQPSK	Spike	\pm spike

Table 9.4 Relating the response of the sum and difference channels to the forms of modulation

9.5 Pulse Doppler measurement

Pulse doppler radar as explained in chapter 3 uses the doppler frequency shift produced by moving targets. The recorded doppler shifts can either be used to calculate the relative speed of the object or more commonly to separate small moving targets from undesired stationary targets (clutter).

In order to simulate the returning signals from a pulse doppler radar two pulses were created using the model, one without simulated doppler shift and the other with 10 kHz of frequency shift. Firstly a 2 μ s pulse of a 50 MHz carrier signal is applied to the system, the sum channel shows that a pulse has been detected and the effect of no frequency shift on the difference output is a straight line, Figure 9.17. If however we simulate some doppler shift on the pulse by raising or lowering the frequency of the carrier signal by 10 kHz, we get the trace shown in Figure 9.18. Again the sum channel indicates the presence of a pulse but the difference trace is raised or lowered by an amount proportional to the change in frequency. Figure 9.16 shows how the diffracted beam behaves as the pulse moves into the Gaussian window and travels through the AO cell. Using Eq. (3.1) and assuming that the original transmitted frequency of the radar was 9 GHz before being mixed down to 45 MHz we find that the velocity represented by 10 kHz is

$$v_r = \frac{c f_d}{2 f_o} = \frac{3 * 10^8 * 10 * 10^3}{2 * 9 * 10^9} = 166 \text{ m/s} \quad (9.1)$$

It may be noted that the bi-cell gap has been narrowed, in order to improve the performance of the system for small frequency measurement. In each case the pulse on the

top trace identifies that there is a signal present, while the height of the bottom pulse above or below zero is proportional to the change in frequency. The spikes seen on the difference trace are due to phase discontinuities at the beginning and end of each pulse.

Power Spectral Density

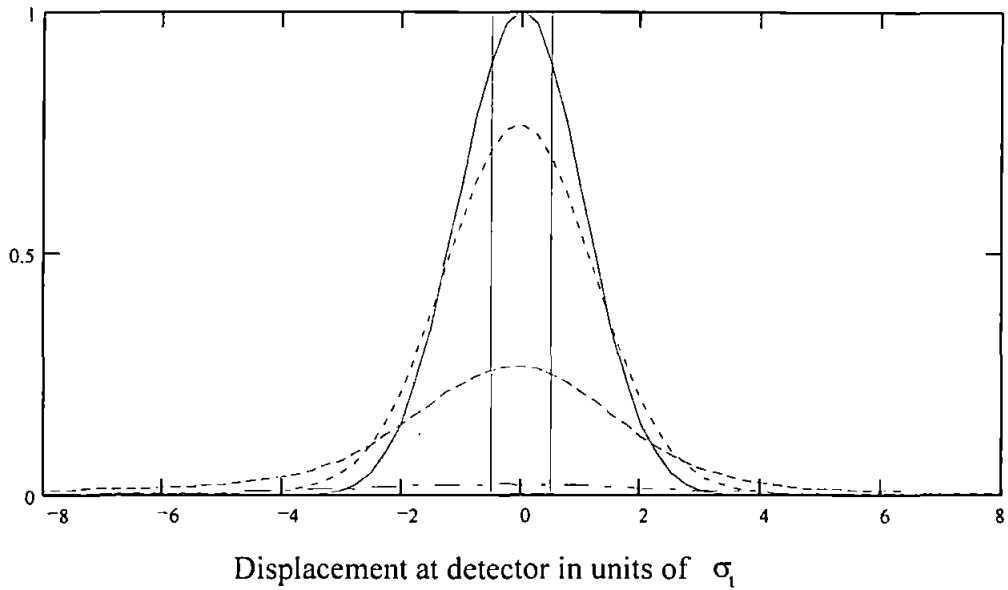


Figure 9.16 Simulation of beam spectral density function in response to a 2 μ s pulse of a 50 MHz

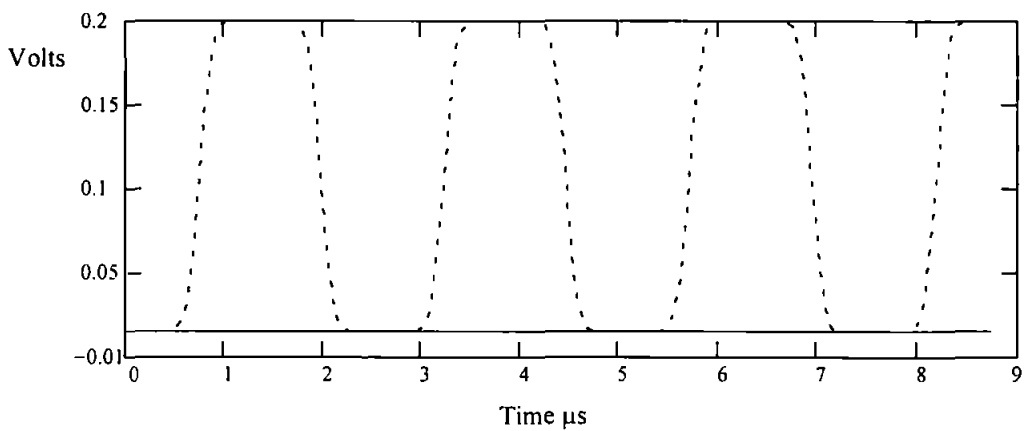


Figure 9.17 A 2 μ s pulse of a 50 MHz
top trace : sum output of bi-cell divided by 50. bottom trace : difference output of bi-cell

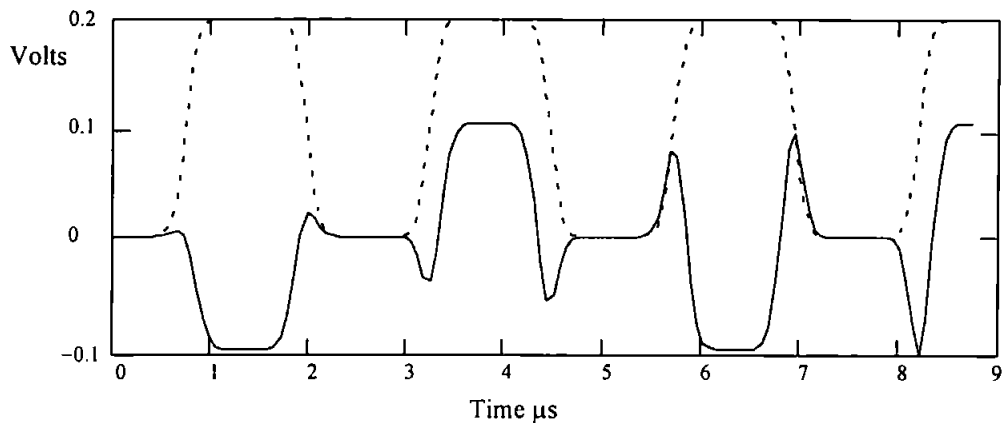


Figure 9.18 A 2 μ s pulse of a \pm 50.01 MHz
top trace : sum output of bi-cell divided by 50. bottom trace : difference output of bi-cell

Skolnik gives an equation for the accuracy of frequency (doppler-velocity) measurement [9] for a perfectly rectangular pulse as

$$\delta f = \frac{\sqrt{3}}{\pi\tau(2E/N_0)^{1/2}} \quad (9.2)$$

where δf in this case is the rms error in frequency measurement, τ is the pulse width and $2E/N_0$ is the signal to noise ratio. The solid line of Figure 9.19 shows is a plot of Eq. (9.2) for a 1 μ s pulse and signal to noise ratios of between 10 and 40 dB. The second trace is the calculated rms frequency error from the AO demodulator model. This trace was produced by calculating the rms error for 6 values of SNR. The rms error was calculated by producing a 1 μ s pulse with the appropriate noise, taking the standard deviation of the signal when the AO window is filled with the pulse, and dividing it by the mean shift caused by a given frequency deviation. From these values the rms error is calculated, for a number of pulses and the average value taken. It is clear that the AO demodulator has a smaller frequency error. For example an SNR of 20 dB gives an rms frequency error of around 55 kHz for Eq. (9.2) whereas the model predicts an error of 22.5 kHz for the AO demodulator, an improvement of almost two and half times.

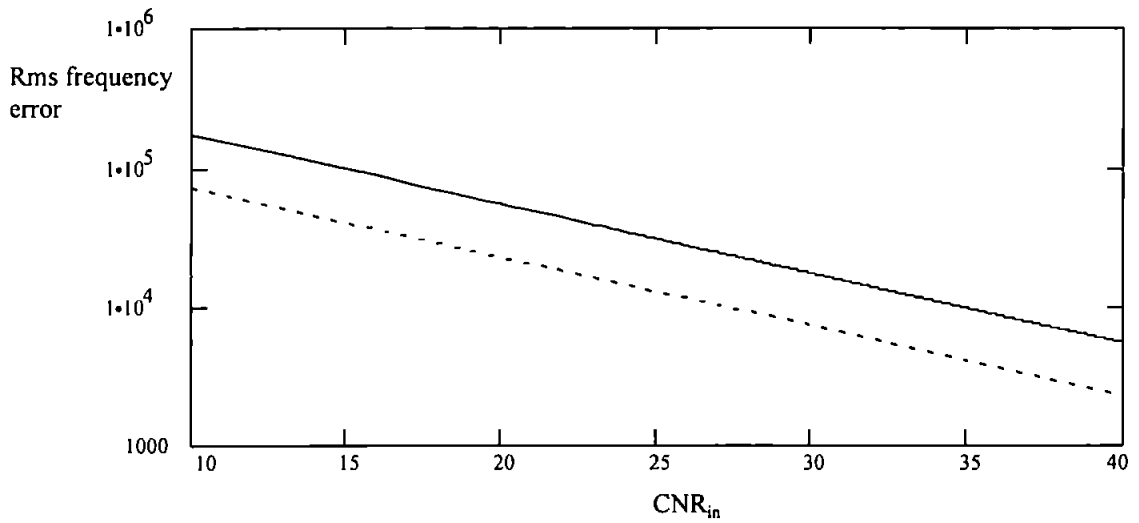


Figure 9.19 Plots showing the improvement in rms frequency error of the AO demodulator for a 1 μs pulse

The rms error is still large even with the improvement that the AO system gives, therefore either high SNR's are needed or longer pulses will have to be used. Obviously if the duration of the pulse is lengthened the rms error will be reduced, as shown in Figure 9.20 for a 2 μs pulse. Again the top trace is calculated from Eq. (9.2) and the lower trace is the predicted response of the AO demodulator from the model.

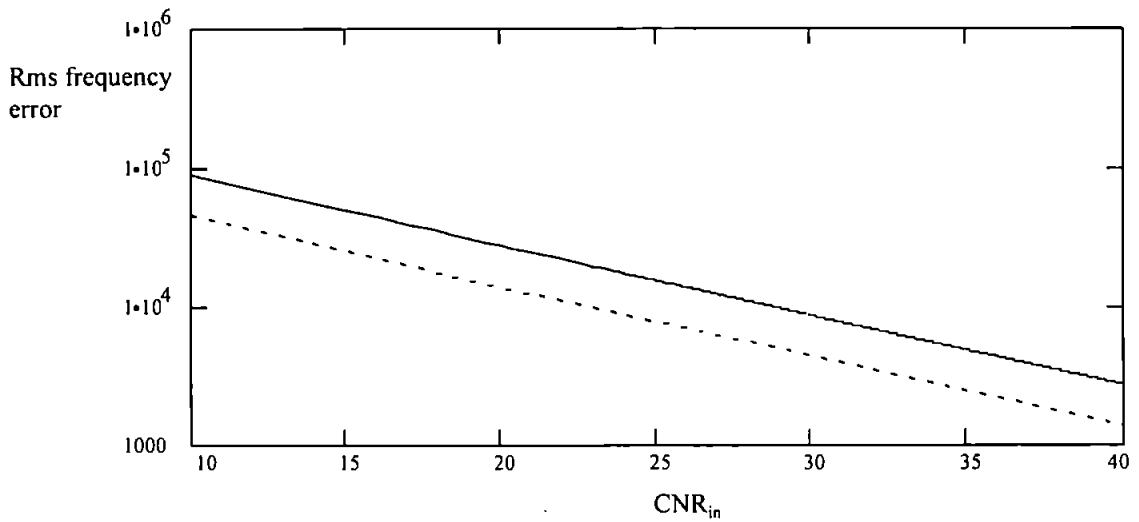


Figure 9.20 Plots showing the improvement in rms frequency error of the AO demodulator for a 2 μs pulse

9.6 AM noise analysis

An example of the AM noise suppression of the system can be seen in Figure 9.21 the top trace shows the AM signal being added to the unmodulated carrier signal and the bottom

trace shows the difference output of the bi-cell. AM and laser intensity noise rejection is at a maximum at the undeviated carrier frequency. The laser SNR (normally quoted in dB's) is the ratio of steady state power to noise power and can be expressed [2]

$$\text{Laser SNR} = 10 \log \left(\frac{\text{average power}}{\text{noise power}} \right) \quad (9.3)$$

The laser SNR will be unchanged as the beam is diffracted by the AO cell, therefore the beam on the detector will have an identical SNR. The laser intensity noise will therefore manifest itself as AM noise at the detector which will be suppressed by the AM rejection of the system. The AM rejection is related to the frequency deviation δf by Eq. (7.49). In this case the AM noise suppression is 34 dB. This is an important result for the pulse doppler measurement as the frequency deviation is measured on the difference channel.

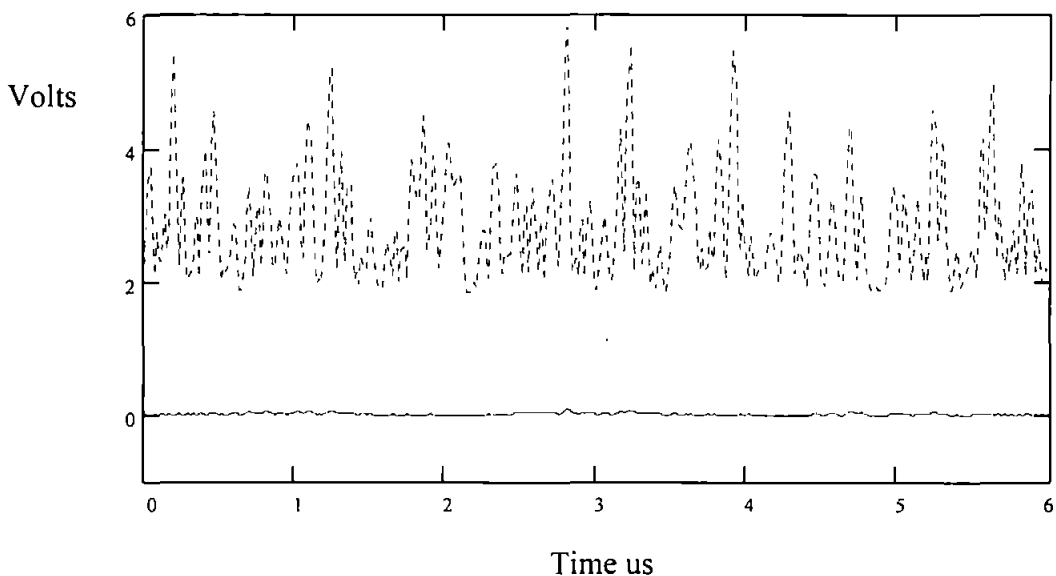


Figure 9.21 Input signal 50 MHz, no modulation, 10 MHz AM noise.
Top trace : AM noise. Bottom trace : difference output from bi-cell .

9.7 System response to phase changes

In order to determine how the system output changed in response to different phase differences, the Mathcad model was used. The relationship between the amplitude of the sum and difference output signals when a phase change, ϕ , is in the centre of the Gaussian window, to that when only the carrier is present, was plotted for a number of phase values between 0 and π . Figure 9.22 and Figure 9.23.

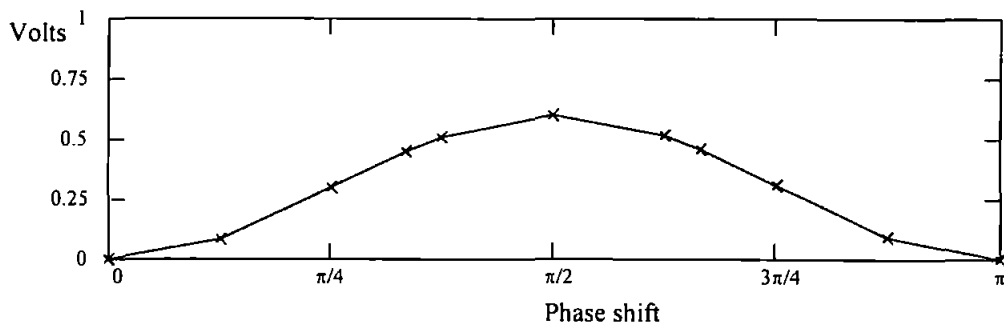


Figure 9.22 Simulated phase response of the difference channel.

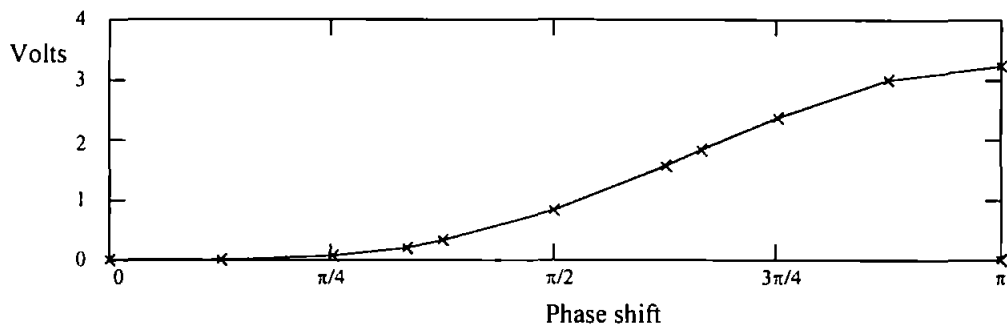


Figure 9.23 Simulated phase response of the sum channel.

The plots were reproduced more accurately using another Mathcad model which plotted 100 points of the phase between $-\pi$ and $+\pi$. On these results was superimposed sine wave and a k-cosine wave as derived in section 8.1, to show how the theoretical results compared with the output of the model, Figure 9.24. and Figure 9.25. The similarity of the two plots shows that the model confirms the theoretical results. Experimental verification is demonstrated in section 10.1.

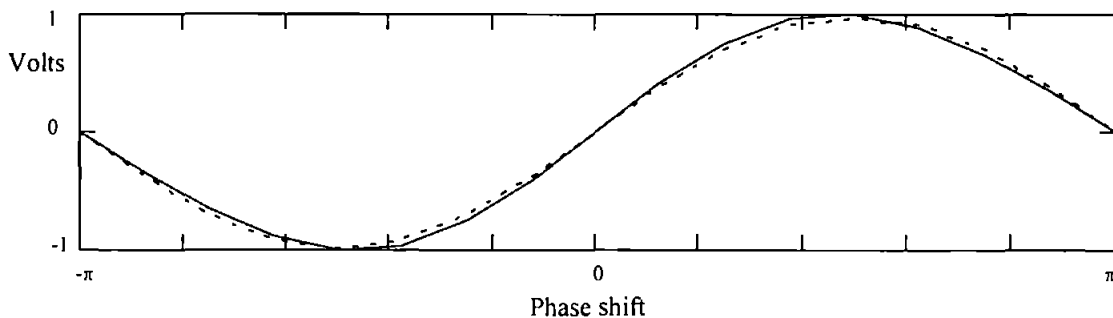


Figure 9.24 Numerically calculated phase response for the difference channel.

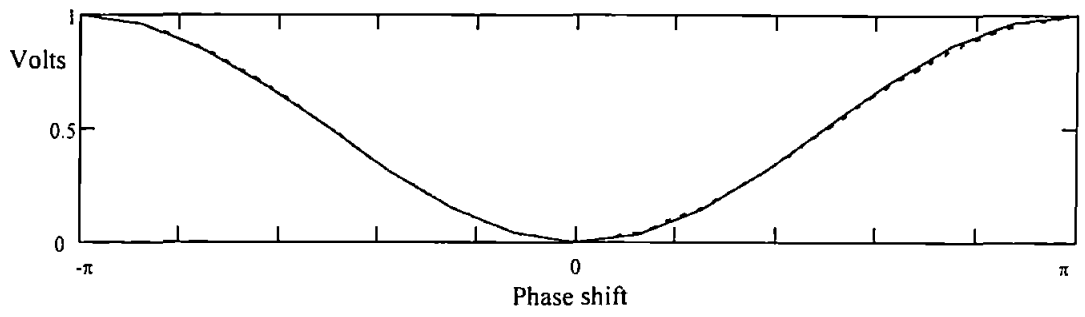


Figure 9.25 Numerically calculated phase response for the sum channel.

10. Experimental results

The results shown in this chapter were all taken from the experimental set-up described in chapter 5. The appropriate signals were generated, either straight from the 2045 signal generator or on the computer and then down loaded onto the 2045. The system was set-up for either FM or surveillance (FM and PM) purposes by changing the focal length of the lens, in order to change the relative gap size of the detector. The stored output waveforms were then transferred back to the computer from data 6100, and plotted using Mathcad.

10.1 Modulation transfer function

A chirped signal was applied to the AO cell, in order to sweep the beam across the bi-cell detector. The beam was swept from $-2\sigma_t$ to $2\sigma_t$ which is equal to the manufacturers quoted beamwidth at the e^{-2} point. To calculate the frequency span needed for the chirp to move the beam by $4\sigma_t$, it is necessary to go back to Eq. (7.2).

$$\delta x = \frac{\lambda l_f}{V_a} \delta f$$

knowing that $\delta x = 4\sigma_t$ and substituting in for σ_t , Eq. (7.5) gives

$$\delta f = \frac{V_a}{\pi \sigma_o} \quad (10.1)$$

which, substituting in for the laser and AO cell being used gave a required frequency span for the chirp of 1.6 MHz.

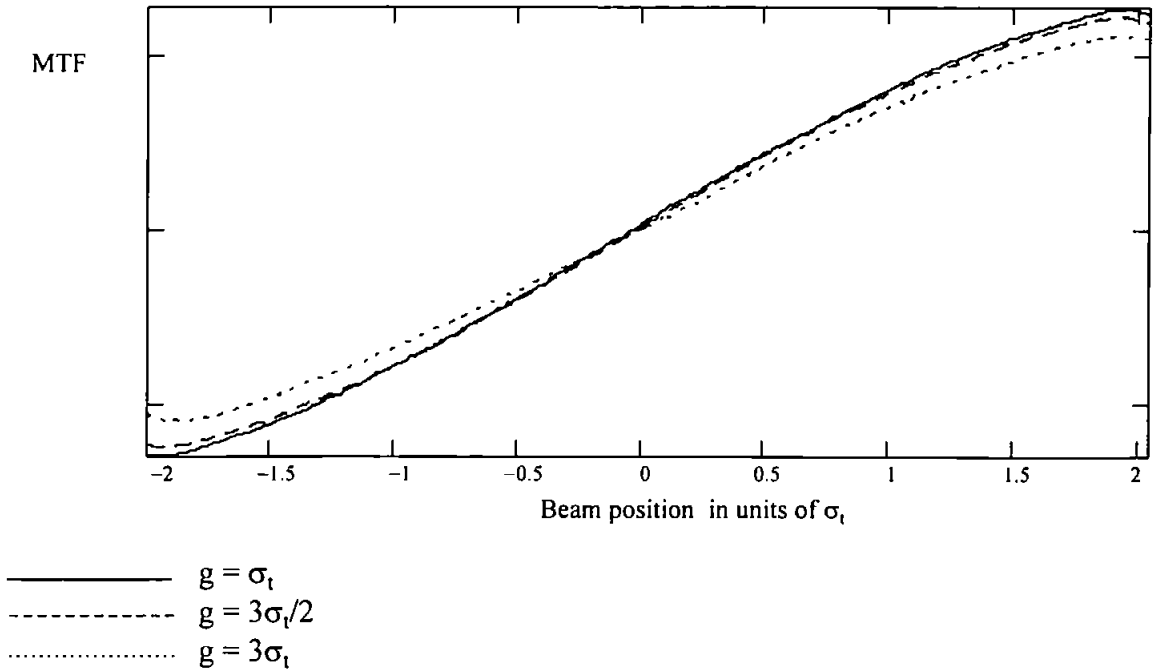


Figure 10.1 modulation transfer function for varying gap sizes

As the AO cell has a centre frequency of 45 MHz this gave a starting frequency for the chirp of 44.2 MHz.

The Modulation transfer function shown in Figure 10.1 was plotted for 30, 20 and 10 cm focal length lenses giving values for σ_t of 123 μm , 82 μm and 41 μm , using a bi-cell with a gap size of 127 μm , this gives relative gap sizes of σ_t , $3\sigma_t/2$ and $3\sigma_t$.

This compares very well with the results shown in Figure 7.3 of the analysis of the system. It can be seen that as the size of the gap size is decreased relative to σ_t the linear range of the system is increased.

10.2 Phase transfer function

The signal generator was set up to give a range of phase shifts from zero to π in steps of $\pi/8$ separated by 1 μs . The result of these phase shifts are shown in Figure 10.2 and Figure 10.3 for the sum and difference channels respectively. The solid line linking the peaks of the sum output is the $a_3\sin\theta$ curve, shown in figure 9.23 and derived in section 8.1. Similarly the solid line linking the peaks of the difference output is the $a_1+a_2\cos\theta$ shown in figure 9.22 and derived in section 8.1. Clearly there is close agreement between these results.

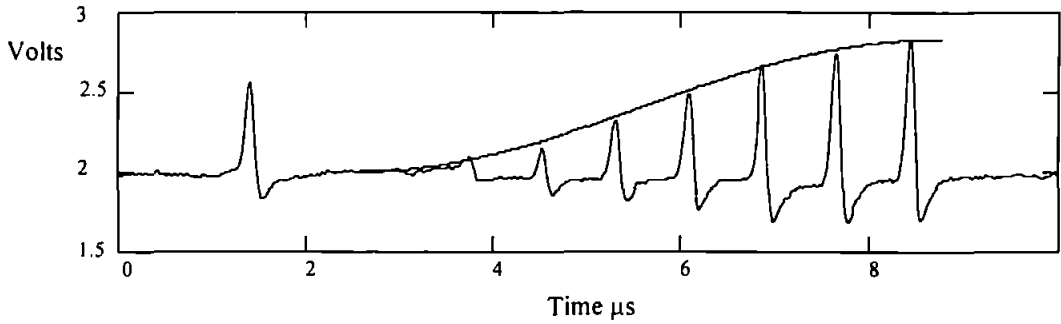


Figure 10.2 Experimental verification of Eq. (8.16). (sum)

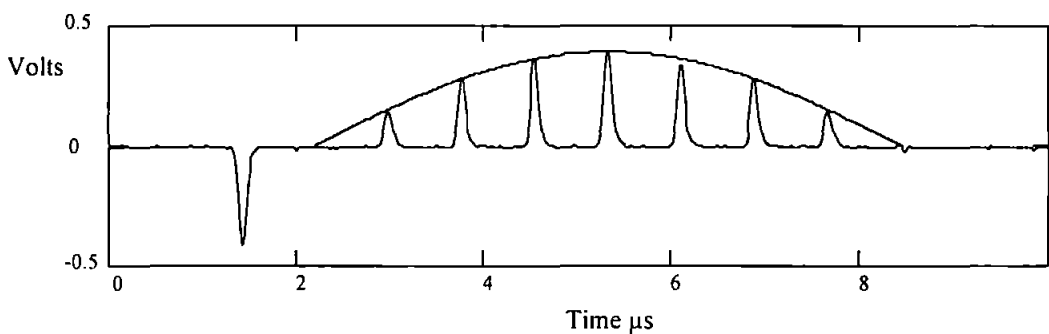


Figure 10.3 Experimental verification of Eq. (8.16). (diff)

10.3 Digital modulation

In this section results are presented from the breadboard system to demonstrate their agreement with the modelled results shown in the previous section. The bi-cell has a gap size of $127 \mu\text{m}$ and was used in conjunction with a lens of focal length 10 cm . Using Eq. (7.5) the value of σ_t can be calculated as $41 \mu\text{m}$, therefore the bicell gap is close to $3\sigma_t$.

Signals for analysis were generated using the Analogic 2045 programmable arbitrary waveform synthesiser so that precise frequencies and phase shifts could be obtained. This section compares the performance of the experimental system in response to digitally modulated signals. The actual signals generated by the 2045 are exactly the same as those used in section 7.5 for the computer model. The sampled signal data generated in Mathcad is downloaded on to the 2045 via the IEEE6400 link. In each of Figure 10.4 to Figure 10.10 showing the results of the digital modulation, the upper trace is the sum and the lower trace is the difference of the bicell outputs

10.3.1 Digital phase modulated signals

Section 9.1 showed how the different phase shifts produced different outputs from the models sum and difference channels. This section presents the experimental results in the same form as section 9.1 for these various phase shifts. The overshoot on the downward edge of the spikes on the sum channel caused by the response of the detectors in the bi-cell system. By slowing up their response time these can be lost, but obviously at the expense of the bandwidth of the system. Figure 10.4 shows the response to a series of π phase changes, Figure 10.5 shows the response to a series of $\pm \pi/2$ phase changes and finally Figure 10.6 shows the response to $\pm \pi/4$ and $\pm 3\pi/4$ repeated once. When compared with figures 9.2, 9.5 and 9.8 respectively it can be seen that the results are in very good agreement.

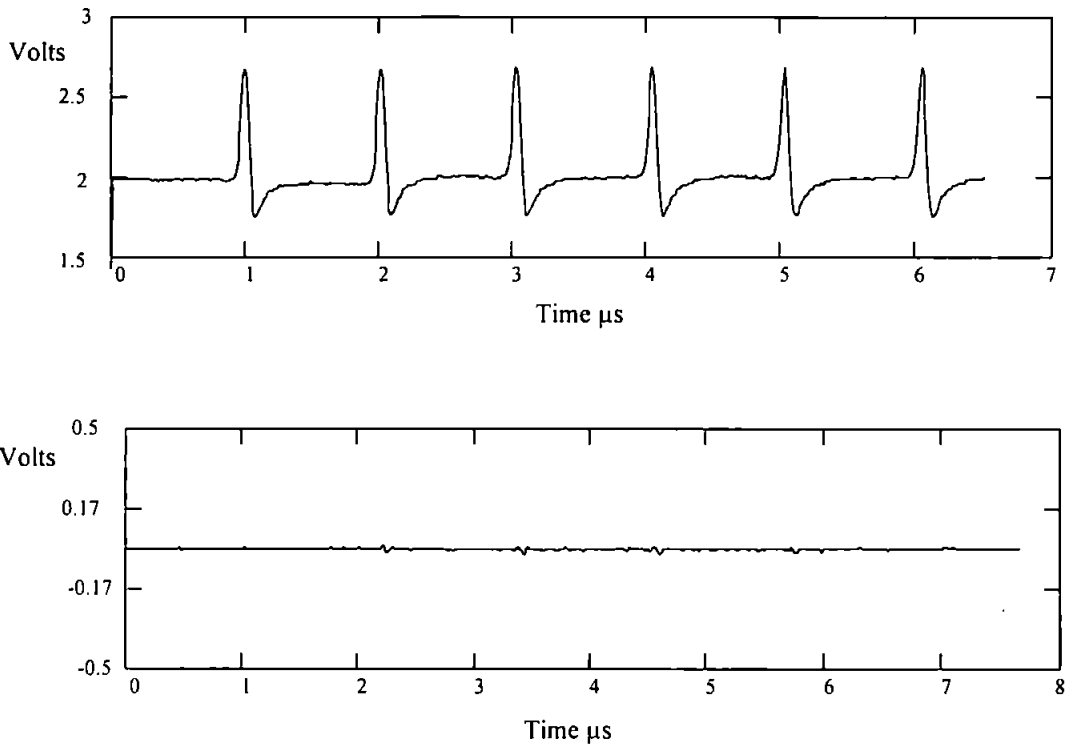


Figure 10.4 Experimental response to a π phase shift. Top trace : sum. bottom trace : difference.

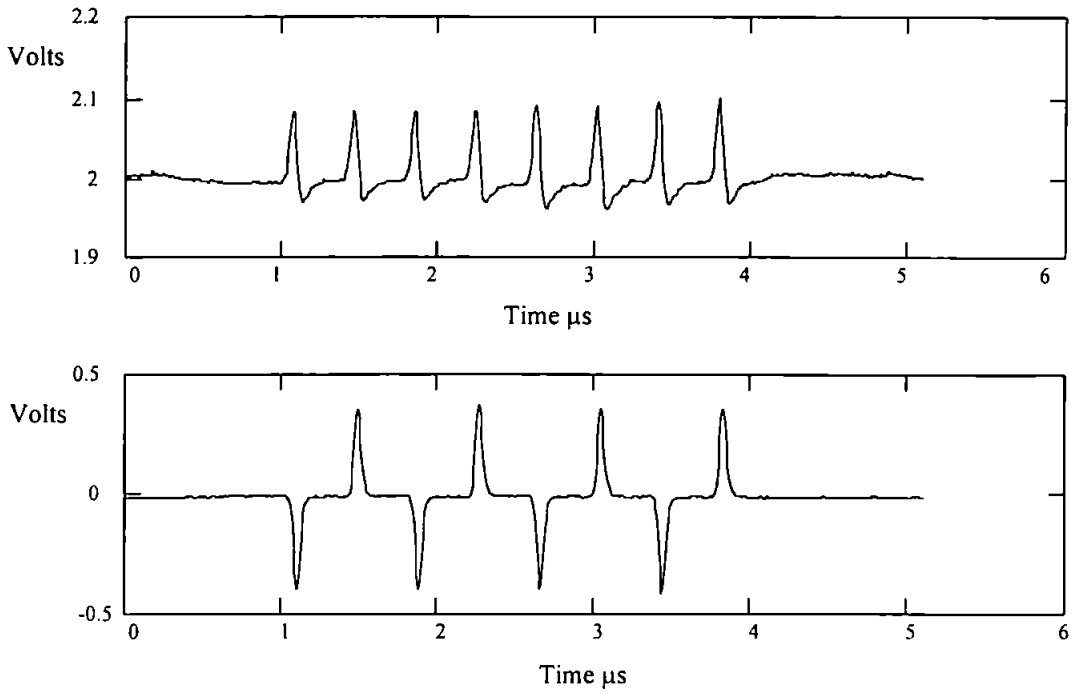


Figure 10.5 Experimental response to phase shifts of $\pm\pi/2$. Top trace : sum. bottom trace : difference.

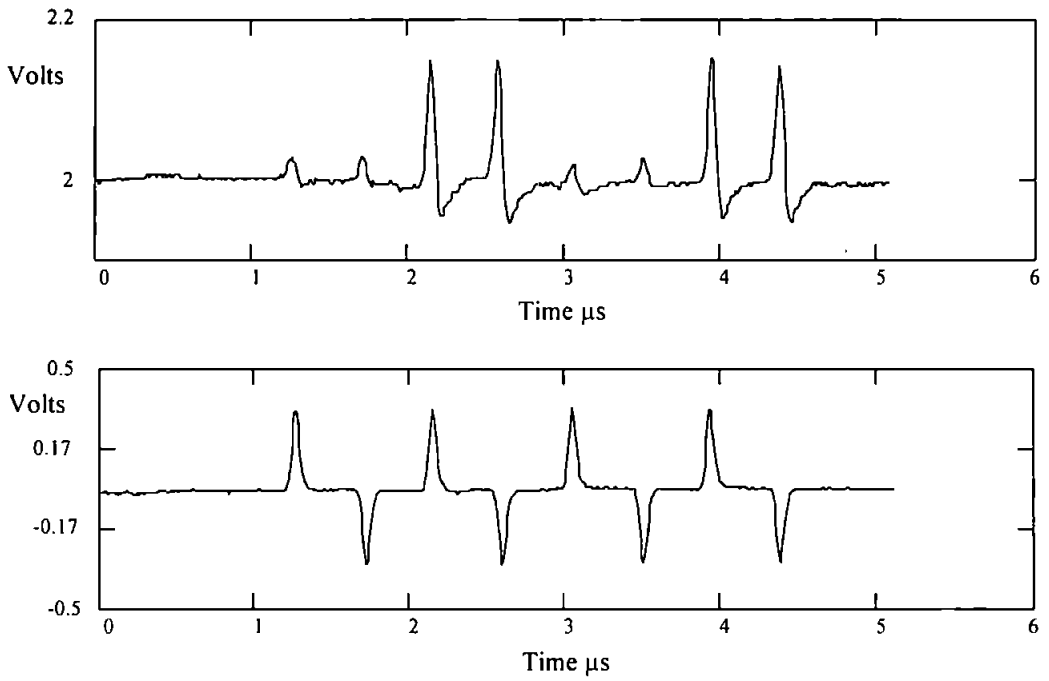


Figure 10.6 Experimental response to $\pm\pi/4, \pm 3\pi/4$ phase shifts. Top trace : sum. bottom trace : difference.

10.3.2 Digital frequency modulated signals

10.3.2.a Continuous Phase - Frequency Shift Keying (CP-FSK)

The CP-FSK signal was generated on the PC ensuring that no phase changes occurred when the frequency changed. The frequency deviation applied was ± 25 kHz and the period was $2.5 \mu\text{s}$, Figure 10.7 . This result should be compared with the CP-FSK signal used on the model shown in figure 9.10.

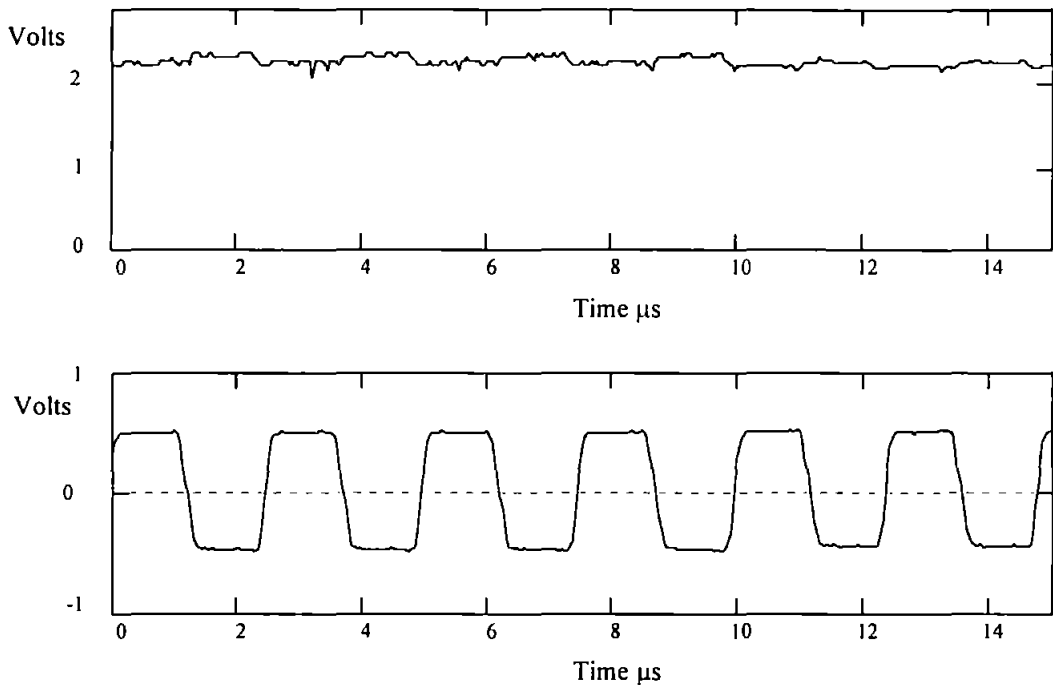


Figure 10.7 Experimental response to a CP-FSK signal. Top trace : sum. bottom trace : difference.

10.3.2.b Frequency Shift Keying (FSK)

In generating the normal FSK signal no care was taken in maintaining phase at the transition points. Hence the random phase changes shown by the spikes at these points, on both the sum and difference outputs graphs. As for the CP-FSK the frequency deviation applied was ± 25 kHz and the period was $2.5 \mu\text{s}$, Figure 10.8. Again this backs up the results of the model shown in figure 9.12.

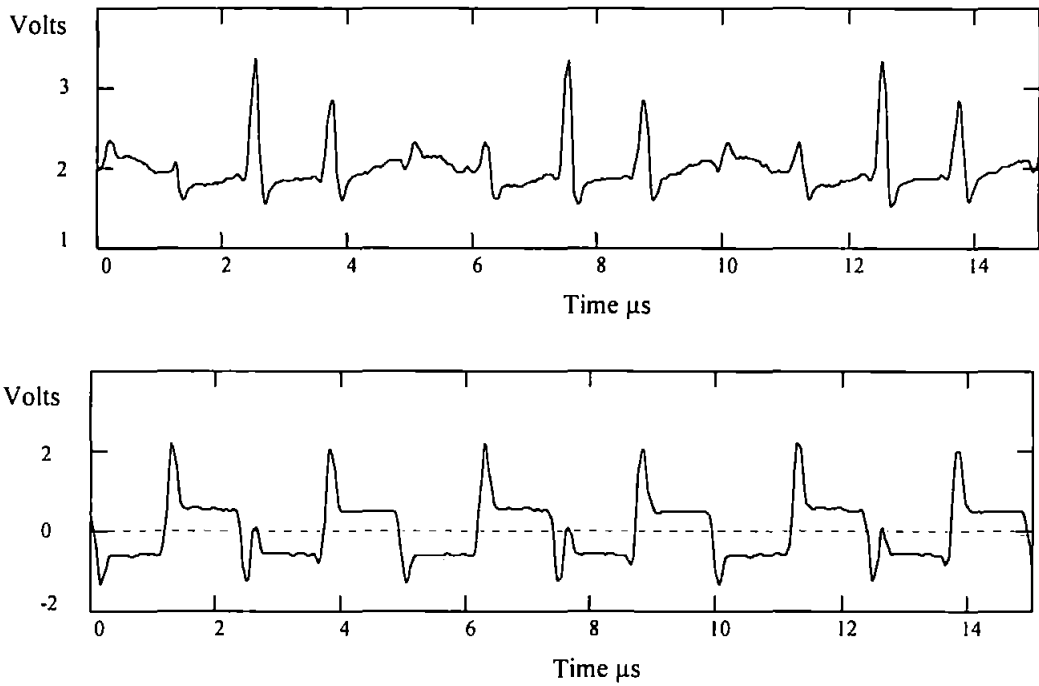


Figure 10.8 Experimental response to an FSK signal. Top trace : sum. bottom trace : difference.

10.3.3 Practical Phase Shift Keying (PSK) signals

10.3.3.a Binary Phase Shift Keying (BPSK)

The output for a signal containing phase shifts of 0 and π radians is shown in Figure 10.9. The BPSK codeword that produced this output was 1011011 where a peak represents 1 and no peak represents zero, whereas the DPSK codeword would be 001001 due to the encoding discussed in section 2.3.3. These are the same signals used for the model in section 9.3.1 again very close agreement can be seen between the two sets of results.

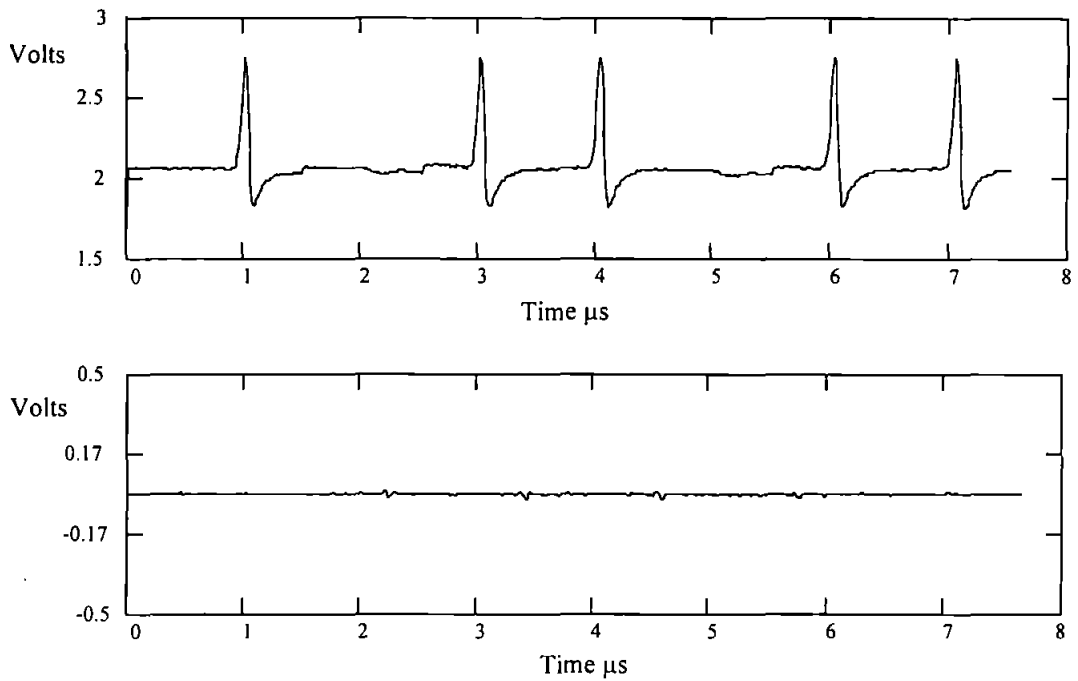


Figure 10.9 Experimental response to a BPSK signal. Top trace : sum. bottom trace : difference.

10.3.3.b Quadrature Phase Shift Keying (QPSK)

The output for a signal containing phase shifts of $0, \pi/2, \pi, -\pi/2$ radians is shown in Figure 10.1. As the phase changes shown are the instantaneous phase changes relative to the previous change, the phase changes shown are cumulative. i.e. the phase changes are

$$\pi/2, \pi, -\pi/2, \pi, 0, \pi/2, -\pi/2$$

which makes the actual transmitted phase states assuming the original state of the signal as for the modelled results of section 9.3.2

$$3\pi/4, 7\pi/4, 5\pi/4, \pi/4, \pi/4, 3\pi/4, \pi/4$$

Which again following the conventional encoding technique (section 2.3.4) would be the codeword

10 01 11 00 00 10 00

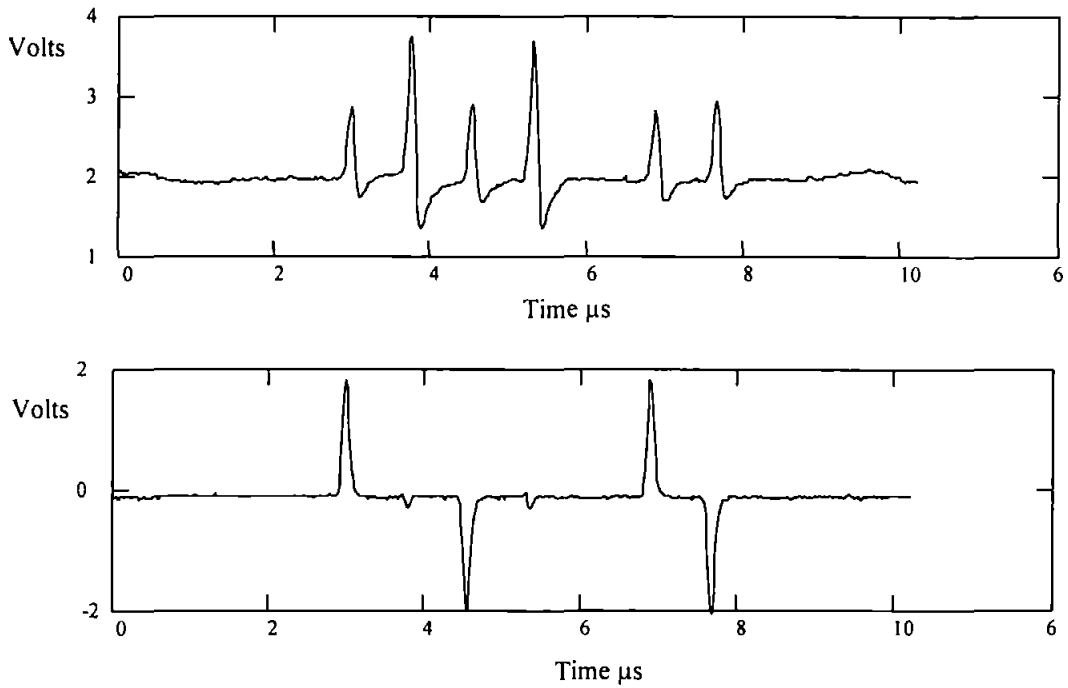


Figure 10.10 Experimental response to a QPSK signal. Top trace : sum. bottom trace : difference.

Clearly there is very close agreement between the results obtained from the model and those from the breadboard system.

10.3.3.c Offset Quadrature Phase Shift Keying (OQPSK)

The output for a signal containing phase shifts of $\pm \pi/2$ radians is shown in Figure 10.11. The phase shifts here are $-\pi/2, 0, \pi/2, \pi/2, \pi/2, 0, -\pi/2, -\pi/2$. It is necessary to assume an initial phase for the system, as for the results of section 9.3.3 it is assumed to be binary 00 i.e. $\pi/4$. The presence of a phase change ($\pm \pi/2$) on the signal denotes a change in state by either the I or the Q channel alternatively. Obviously no phase change means that the channel has not changed state. Table 10.1 decoding an OQPSK output from the system shows how the codeword can be decoded from the output waveforms, a more detailed explanation of the decoding can be found in section 9.3.3.

phase change	$-\pi/2$	0	$\pi/2$	$\pi/2$	$\pi/2$	0	$-\pi/2$	$-\pi/2$
channel	I	Q	I	Q	I	Q	I	Q
input signal	0	1	0	0	1	1	1	0

Table 10.1 decoding an OQPSK output from the system

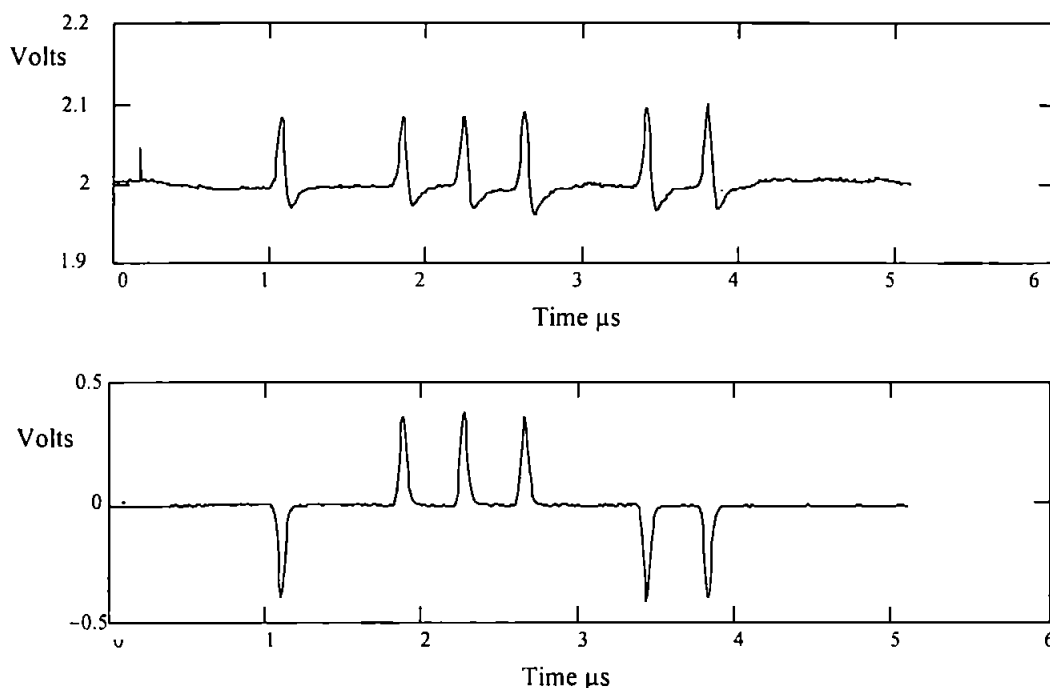
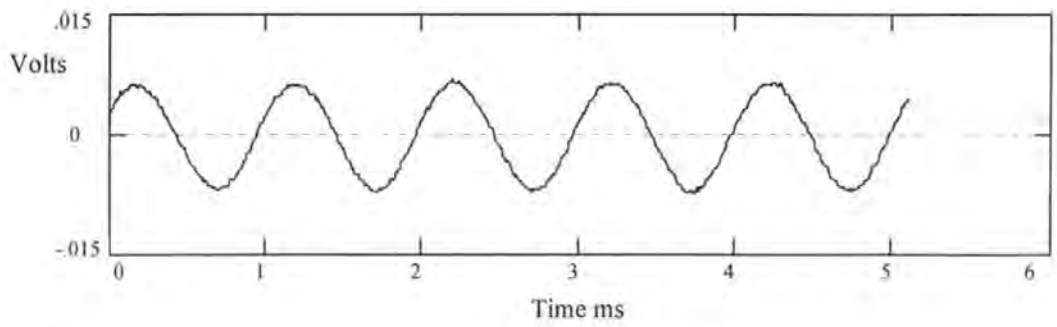


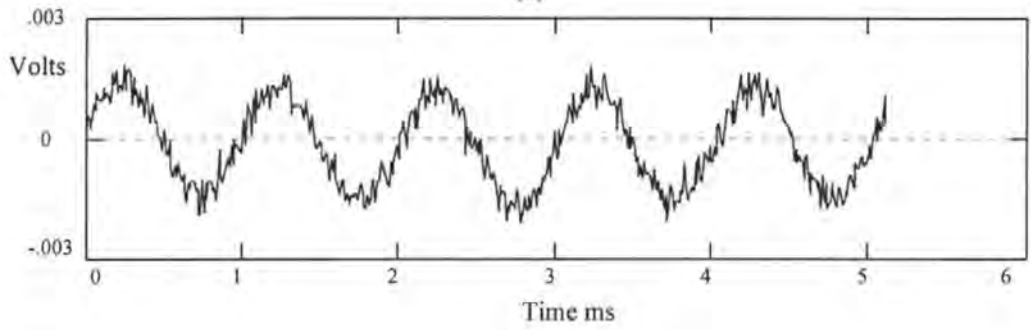
Figure 10.11 Experimental response to an OQPSK signal. Top trace : sum. bottom trace : difference.

10.4 Shot noise limited frequency resolution

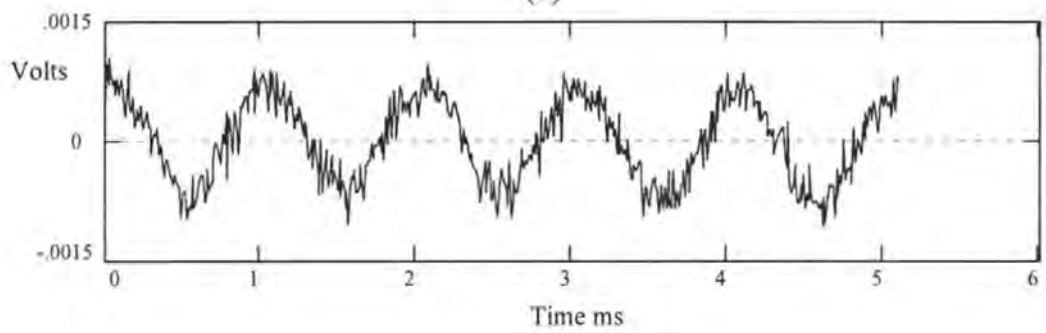
For the frequency resolution results the smaller bi-cell was used as its gap size was only 10 μm , the lens had a focal length of 15 cm. Using Eq. (7.5) the value of σ_t was therefore 60 μm , therefore the bicell gap is close to $\sigma_t/6$. A Marconi 2022E signal source was programmed to give a 45 MHz carrier signal. FM modulation at 1 kHz with a variable deviation width was used as a test signal. Figure 10.12 (a), (b), (c), and (d) show the difference channel output for frequency deviations of 1kHz, 100 Hz, 50 Hz and 20 Hz respectively. The shot noise clearly begins to mask the signals at the lower frequency deviations, and the 20 Hz signal is barely distinguishable above the noise.



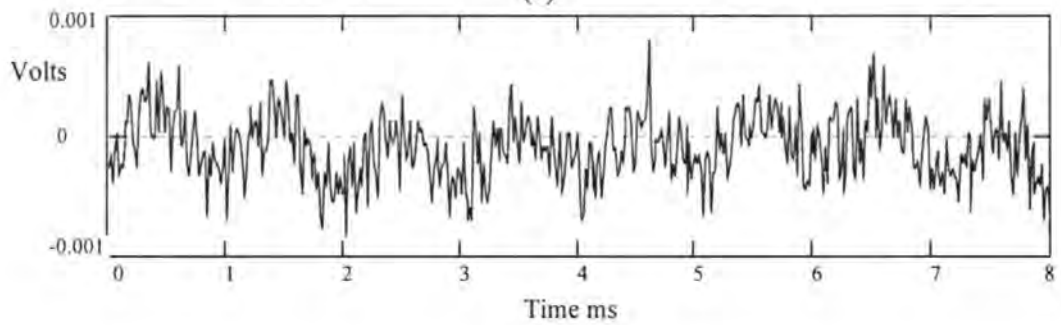
(a)



(b)



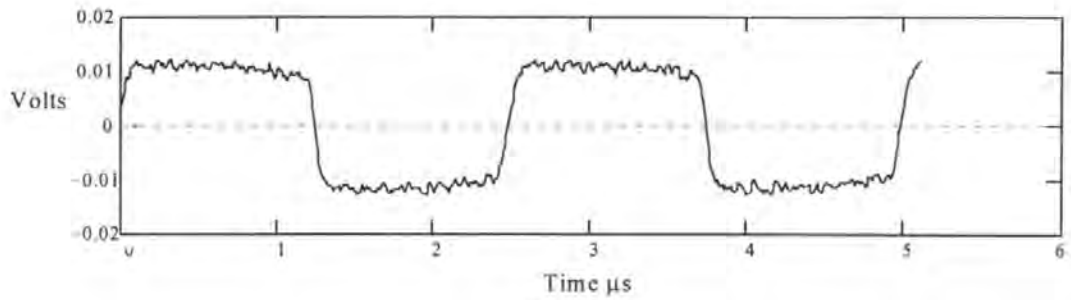
(c)



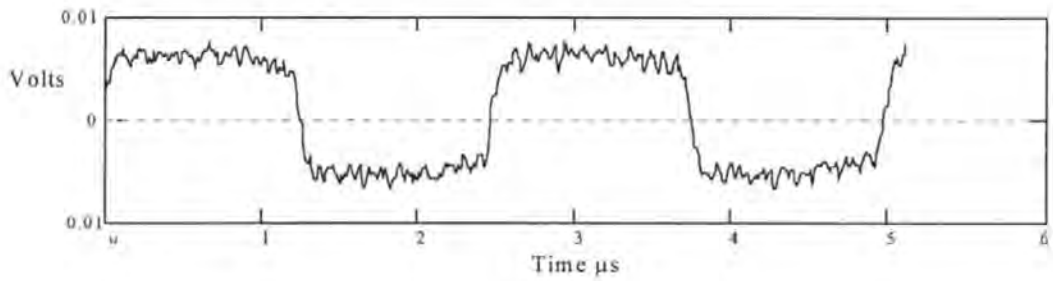
(d)

Figure 10.12 Graphs showing a 1 kHz sin wave with deviations of
 (a) 1 kHz, (b) 100 Hz, (c) 50 Hz, and (d) 20 Hz

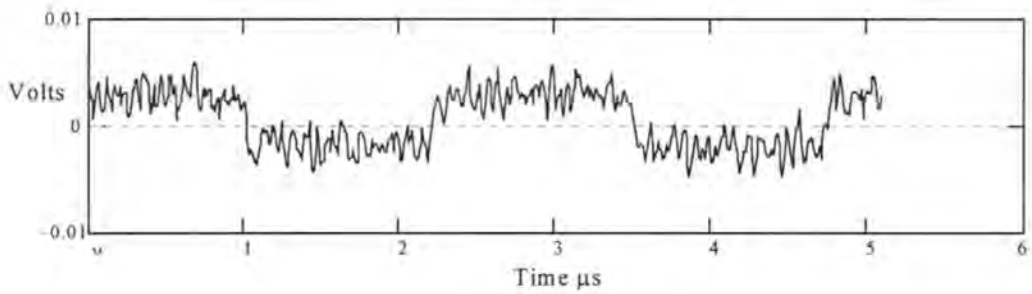
Figure 10.13 used signals generated on the 2045 signal generator to create FM signals of frequency $f_c \pm \delta f$.



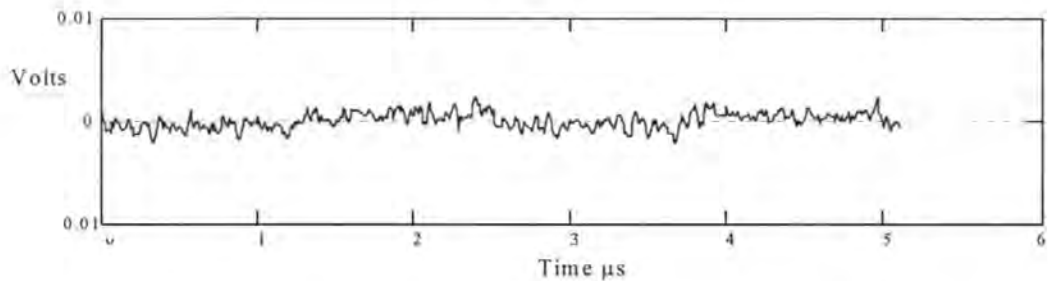
(a)



(b)



(c)



(d)

Figure 10.13 Plots showing how an FSK signal is shot noise limited for deviations of
 (a) 1 kHz (b) 500 Hz (c) 100 Hz (d) 50 Hz

Thus essentially these are FSK signal but using very small deviations, for Figure 10.13(a) $\delta f = 1$ kHz, Figure 10.13(b) has $\delta f = 500$ Hz, Figure 10.13(c) has $\delta f = 100$ Hz and finally for Figure 10.13(d) $\delta f = 50$ Hz. Again the shot noise limit of the system can be seen in Figure 10.13(d) where $\delta f = 50$ Hz.

10.5 Shot noise limited phase resolution

In section 8.3 the minimum detectable phase change was calculated to be $\pi/30$ on the sum output and $\pi/9166$ on the difference output. Figure 10.14 shows the sum and difference response to phase changes of $\pi/8$, $\pi/16$, $\pi/32$, $\pi/64$. Similarly Figure 10.15 shows the response to phase changes of $\pi/512$, $\pi/1024$, $\pi/2048$, $\pi/4096$. These show that the theory presented in section 8.3 is of the right order for the sum and difference channels, where the minimum values were calculated to be $\pi/30\sqrt{\text{SNR}}$ and $\pi/9166\sqrt{\text{SNR}}$.

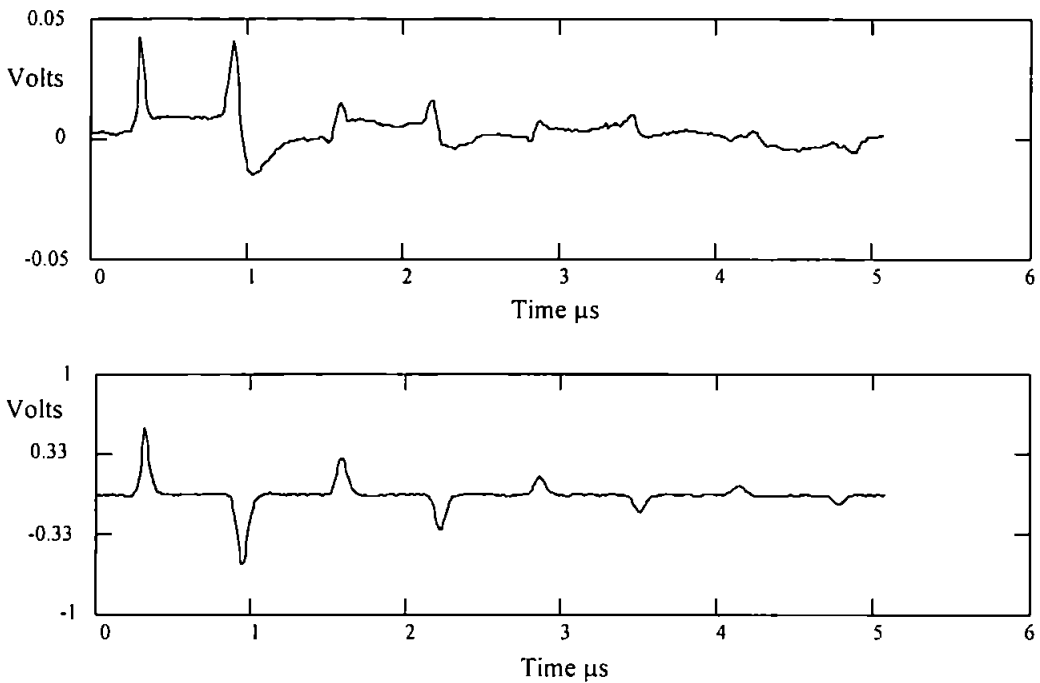


Figure 10.14 Experimental response to phase shifts of $\pi/8$, $\pi/16$, $\pi/32$, and $\pi/64$. top trace : sum. bottom trace : difference.

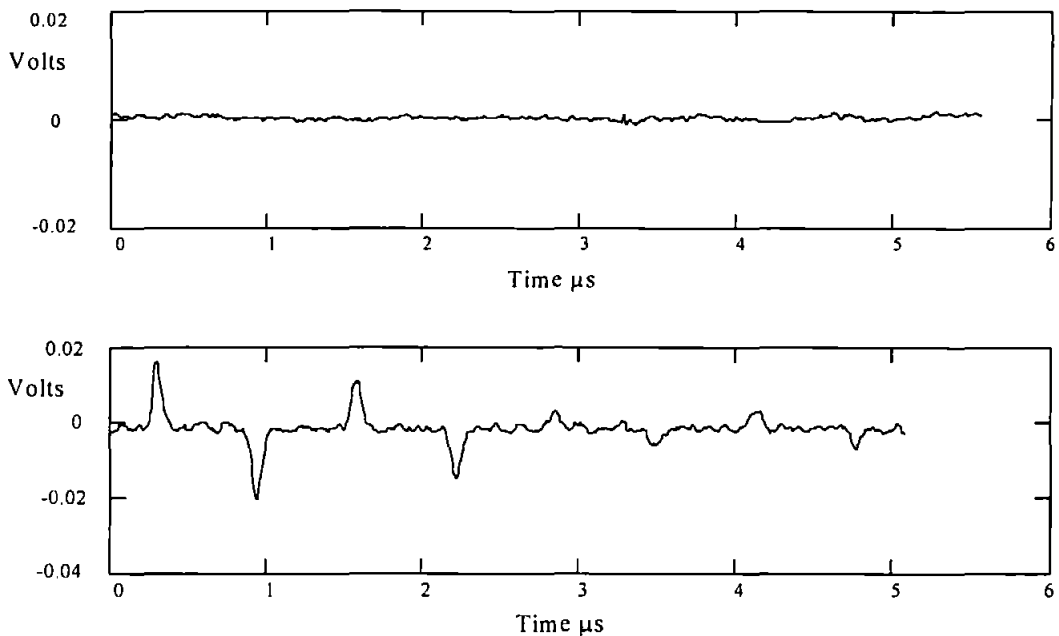


Figure 10.15 Experimental response to phase shifts of $\pi/512$, $\pi/1024$, $\pi/2048$, and $\pi/4096$. top trace : sum. Bottom trace : difference.

10.6 Pulse Doppler measurement

As in section 9.5 if we simulate some doppler shift on the pulse by raising or lowering the frequency of the carrier signal by 10 kHz the difference trace is raised or lowered by an amount proportional to the change in frequency, Figure 10.16. Again this compares well with the results of the model shown in Figure 9.18.

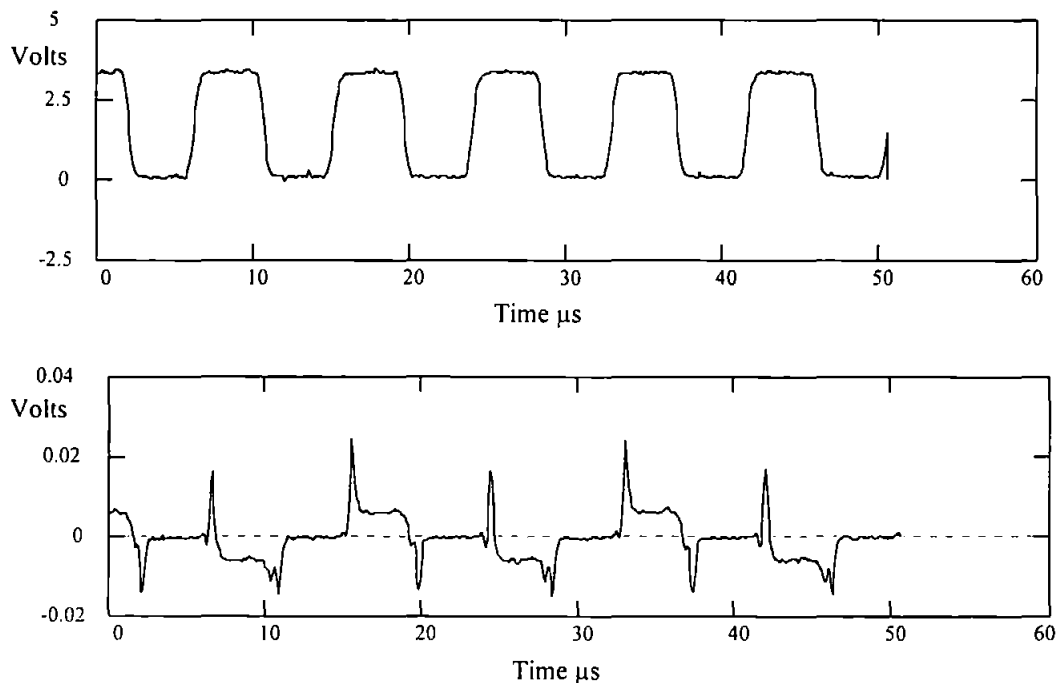


Figure 10.16 $5\mu\text{s}$ pulses of $45\text{ MHz} \pm 10\text{ kHz}$ signal separated by $5\mu\text{s}$. Top trace : difference. Bottom trace : sum

11. Conclusions

Before the overall conclusions are drawn this chapter emphasises the important results and conclusions that have been drawn from this study of the AO demodulator system. Again the operation of the system has been split into different sections, frequency modulation, phase modulation and digital modulation. Each area has been considered individually as they perform in different ways, using different characteristics of the system and relying on different parameters to optimise their performance.

The first section considers the frequency modulation operation of the AO demodulator, its limitations, how to interpret its results and how to optimise its performance. The next two sections consider the phase modulation and the digital communications operation of the system in the same ways as for the FM conclusions. Finally before the overall conclusions, the recommendations for future work details where the areas of interest lie for future investigation into the AO demodulator.

11.1 FM AO demodulator

Firstly it is important to note that the analysis for the frequency modulation assumes that at any one time only one phase shift is in the Gaussian laser window at the AO cell. This obviously limits the data rate at which the system can operate to the reciprocal of the transit time (time for the acoustic wave to travel through the beam). The analysis of the FM performance of the system started by looking at the effect of the gap size on the linear range of the system. It showed in section 7.2 that by increasing the gap size of the detector relative to the standard deviation of the beam at the detector the linearity of the system is improved over the frequency range used to generate its modulation transfer function MTF. This was confirmed experimentally in section 10.1, where the MTF was plotted for three different gap sizes. This improvement in linearity is gained at the expense of the overall system sensitivity.

It has been shown theoretically (Eq. (7.46)), using the model (Figure 7.6) and experimentally (section 10.4) that the AO demodulator is capable of resolving frequency deviations of around 20 Hz on a 50 MHz carrier for carrier to noise ratios of above 80 dB.

The effect of increasing the laser power and the width of the Gaussian laser window in the AO cell are also shown to improve the frequency resolution of the system in section 7.3

The noise analysis for FM demodulation showed how the level of clipping required was affected by the carrier to noise ratio at the input to the system, CNR_{in} , and the frequency deviation of the signal δf . Firstly it was shown that the effect of clipping a signal too hard is much worse than not clipping a signal at all. With this in mind, an optimum level of clipping was calculated for each CNR_{in} and different frequency deviations. The effect of clipping on the SNR loss of the system is also demonstrated, it shows that adaptive clipping improves the SNR loss, but the result of getting the clipping level wrong is shown to reduce the SNR_{out} by as much as 10 dB. The conclusion drawn from all this is that, unless the system had an estimate of the CNR_{in} of within ± 5 dB, it would perform better with no limiter at all.

The pulse response of the system (section 9.5) shows the ability to resolve small frequency changes on a single pulse, the minimum resolvable size of a pulse for the system being decided by the cell access time, τ . The pulse response has also been compared with the performance of existing pulse doppler demodulation techniques as described in Skolnik [9]. It was shown that the AO demodulator offered a 150% improvement over the standard rms error equation given in Skolnik.

Finally the ability of the system to suppress AM noise [2] on the signal at the detector is demonstrated, this is one reason why the system can demodulate doppler pulses with a greater accuracy than existing systems.

11.2 Phase modulation

Again it is important to note that the analysis for the phase response of the system, as for the FM analysis, assumes that at any one time only one phase shift is in the Gaussian laser window at the AO cell. The analysis of the phase response of the system first derived equations relating the instantaneous phase shift ϕ to the output of the system, concluding that the sum and difference of the outputs of the bicell elements gives

$$P_{SUM}(\phi) = 2(a_1 + a_2 \cos\phi) \quad \text{and} \quad P_{DIFF}(\phi) = 2a_3 \sin\phi$$

By looking at the graph produced to identify the optimum gap size for the system, Figure 8.4, it can be seen that there is a conflict between the best size for FSK signals and the best size for phase modulated signals. FSK requires the gap to be as small as possible to gain the biggest pulse, whereas the maximum for phase modulated signals appears when the size of the gap is between $2 \sigma_t$ and $3 \sigma_t$.

The shot noise limited resolution of section 8.3 derives two equations for the minimum detectable phase changes, one for the difference channel and one for the sum channel. For the parameters used in the practical system the minimum detectable phase shift for the sum channel is

$$\phi_{\min(\text{sum})} = \frac{\pi}{30} \sqrt{\text{SNR}}$$

and for the difference channel is

$$\phi_{\min(\text{diff})} = \frac{\pi}{9166} \sqrt{\text{SNR}}$$

The minimum detectable phase shift of the difference channel is better than that of the sum channel because the initial slope of a sine wave from zero is one whilst that of a cosine wave is zero (Figure 8.2). Thus the output signal from the difference channel will climb above the shot noise level for a smaller value of phase shift than the sum channel.

Finally the effect of various levels of clipping of the carrier signal for a given carrier to noise ratio (CNR_{in}) on the output signal to noise ratio (SNR_{out}) are presented. It is shown that the level of clipping required for the sum is greater than the level required for the difference channel. It is also shown that any level of clipping improves SNR_{out} .

11.3 Digital modulation

The analysis of the response of the system to digitally modulated signals, such as FSK and PSK, centred around predicting the system response using the model and then verifying these predictions with the experimental set-up. The modelled and experimental results show that the system output for each type of signal has a distinctive signature. Signals with a phase change of π radians cause a spike on the sum channel with the difference remaining constant; signals with phase changes of $\pm\pi/2$ cause equal sized spikes on the

sum channels and equal but opposite polarity spikes on the difference. Signals with phase shifts of $\pm\pi/4$ or $\pm3\pi/4$ can be shown to give spikes on the sum channel related to the phase shift (Eq 8.16), and the polarity of the spike on the difference again gives its sign. FSK signals in which there is no phase discontinuity at the frequency transition give a change in the difference channel proportional to the frequency shift with no change in the sum. FSK signals with an arbitrary phase shift at the frequency transition give the same result but with additional spikes due to the phase shifts; the size of the spike on the sum channel is dependent on the phase shift and the polarity of the spike on the difference gives its sign. Using these results it is possible to distinguish between the following types of digital modulation.

(i) BPSK. Assuming that the two phase states are 0 and π radians this is characterised by a constant difference channel with a spike on the sum channel at each phase shift.

(ii) DPSK. As with BPSK the two phase states are 0 and π radians characterised by a constant difference channel with a spike on the sum channel at each phase shift, although for DPSK the decoding of the output will differ.

(iii) QPSK. The four phase states are 0, $\pm\pi/2$ and π radians; therefore the possible phase shifts are also 0, $\pm\pi/2$ and π radians. A spike on the sum channel indicates the presence of a phase shift and the corresponding state of the difference channel indicates the nature of the change. The occurrence of all three phase shifts identifies the type of modulation.

(iv) Offset QPSK. Here the only possible phase shifts are $\pm\pi/2$ radians. The absence of the π radians phase shifts identifies the type of modulation. The signal processing required to decode OQPSK would be more complicated than for the other forms of modulation, due to the encoding technique.

(v) FSK. FSK signals are characterised by a shift in level on the difference channel while the sum remains constant. Unlike the case for PSK signals where the output is a spike which only occurs while the phase shift is within the laser window, the level change persists for as long as the frequency remains constant. If there is no phase discontinuity when the frequency changes, as in continuous phase FSK or MSK, then only the level changed is observed. A phase discontinuity at the frequency change results in spikes on both the sum and difference channels. Thus not only is the system capable of identifying the presence of FSK signals, it can also indicate the type of FSK modulation being used. The magnitude of the level change, and hence the detectability of the signal, is proportional

to the change in frequency. For an MSK signal the frequency change is $2\delta f = 1/2T_b$, where T_b is the interval between frequency shifts. In the experimental example shown T_b was 5 μs so that the frequency shift was 100 kHz. Since it has been shown that this type of system is capable of detecting frequency changes of the order of 20 Hz, detectability is not considered to be a problem.

11.4 Future work

The analysis of the AO demodulator has, to all intents and purposes, been covered by this work. The model written can readily be used to simulate the response of the system to any signals not mentioned in this thesis. Future work would need to centre on the practical applications of the demodulator system, i.e. setting up the system to receive real signals such as PSK, FSK, pulse doppler and CW radar. In this way the practicality of using this system in environments outside the laboratory can be judged.

The step that is not covered by this thesis is the signal processing of the output waveforms from the system;

- (i) For the radar type applications this would involve selecting a threshold voltage such that the probability of false alarm was acceptable to the application involved.
- (ii) For the digital communication application of the system, the signal processing would have to make a number of decisions based upon the results shown in section 9; firstly it would have to recognise that a signal is present, it would then look at both the sum and difference channels to decide whether the modulation is FSK or PSK. For the signal to be FSK the difference channel would have to cross a threshold level for a given duration in order to differentiate between a shift in frequency and a phase spike. Finally having decided which form of modulation is on the signal being received the system must attempt to decode the message being transmitted.

It might also be possible to develop modulation methods, using the versatility of the system i.e. its ability to demodulate such small frequency and phase deviations, such that only an AO demodulator would have the ability to detect all the information contained on a signal. This would be very useful for secure communication type applications.

11.5 Overall conclusions

It is concluded that using the optical system described, together with some detection and logic circuits, it is possible to identify and decode a number of types of digitally modulated signals, without any a priori knowledge apart from their carrier frequency.

The ability of the system to handle both frequency and phase modulated signals is particularly valuable. Although apparently very simple, the system performs functions that would be difficult to achieve electronically in real time. In summary these functions are as follows.

- (i) The signal propagating through the AO cell is windowed by the Gaussian profile of the laser beam. The time window depends upon the laser beamwidth and the acoustic velocity in the AO cell; by focusing the beam into the AO cell, time windows down to a few nanoseconds are achievable. This places an upper limit on the data rates that can be processed since only one transition may occur within the window.
- (ii) The light distribution at the detector is proportional to the instantaneous Fourier transform of the windowed signal.
- (iii) The response of each element of the detector is proportional to the instantaneous power in the windowed signal over frequency bands defined by the size and position of the elements. In effect the system responds in real time to variations in the spectral content of the signal as the frequency and/or phase shifts propagate through the laser beam window.
- (iv) Taking the sum and difference of the signals from the bicell elements results in distinctive signatures for the different types of modulation. AO cells are currently available for operation at carrier frequencies from around 30 MHz (tellurium dioxide) to 3 GHz (gallium phosphide). Acoustic velocities vary from 617 m/s for tellurium dioxide to 6320 m/s for gallium phosphide. To perform a similar operation at the lower end of this frequency range might be possible using DSP techniques; at the upper end it would not. The properties of AO cells allow the system to be tuned over an octave bandwidth merely by moving the detector.

The effect of clipping on both the sum and difference channels has been shown in sections 7.4 and 8.4. This showed that the optimum level of clipping a signal for the sum channel requires harder limiting than that required for the difference channel. Obviously the signal

can only be clipped once so there has to be a trade off between the performance of the two channels. For purposes such as Doppler detection, (see chapter 9), and FM signals the difference channel contains most of the useful information, so obviously the system would be set up to optimise its performance. As a surveillance receiver the information is contained on both channels, but as using Eq. (8.16) for $P_{\text{DIFF}}(\phi)$ it is theoretically possible to calculate the phase shift from the amplitude of the difference spike, it would seem reasonable to optimise the clipping level for the difference channel again.

Finally it is concluded that the AO demodulator system has the potential for being a versatile solution to electronic support measures (ESM) requirements for both radar and communications applications

APPENDIX A

1. Matched Filters

In a number of systems a deterministic signal $f(t)$ is transmitted and received, along with noise $n(t)$ at the receiver. The problem that the receiver has, is to decide at time t_0 , whether there is signal and noise present or if there is just noise. Matched filters are used to maximise the signal to noise ratio of signal power to average noise power, and hence enhance the receiver's decision. Here is a brief overview of such filters.

Consider an arbitrary linear time invariant filter with impulse response and transfer function $h(t)$ and $H(\omega)$, respectively. The response of $f_o(t)$ generated by the application of $f(t)$ to the filter's input is

$$f_o(t) = \frac{1}{2\pi} \int_{-\infty}^{\infty} F(\omega)H(\omega)e^{j\omega t} d\omega \quad (\text{A1.1})$$

where $f(t) \leftrightarrow F(\omega)$

Average output noise power N_o is

$$N_o = \frac{1}{2\pi} \int_{-\infty}^{\infty} \zeta_{NN}(\omega)|H(\omega)|^2 d\omega \quad (\text{A1.2})$$

where $\zeta_{NN}(\omega)$ is the power density spectrum of the noise $n(t)$ represented by the random process $N(t)$. The ratio of the signal power at time t_0 to average noise power, which we wish to maximise, is

$$\left(\frac{S_o}{N_o}\right) = \frac{\left|\left(\frac{1}{2\pi}\right) \int_{-\infty}^{\infty} F(\omega)H(\omega)e^{j\omega t_0} d\omega\right|^2}{\left(\frac{1}{2\pi}\right) \int_{-\infty}^{\infty} \zeta_{NN}(\omega)|H(\omega)|^2 d\omega} \quad (\text{A1.3})$$

By applying Schwarz's inequality, we have

$$\left(\frac{S_o}{N_o}\right) \leq \frac{1}{2\pi} \int_{-\infty}^{\infty} \frac{|F(\omega)|^2}{\zeta_{NN}(\omega)} d\omega \quad (\text{A1.4})$$

The maximum occurs only when we choose the optimum transfer function as

$$H_{opt}(\omega) = \frac{1}{2\pi C} \frac{F^*(\omega)e^{-j\omega t_0}}{\zeta_{NN}(\omega)} e^{-j\omega t_0} \quad (A1.5)$$

It is called a matched filter because its transfer function depends on the signals spectrum $F(\omega)$. If the signal is changed, the optimum filter must be changed.

In the special case of white noise where $\zeta_{NN}(\omega) = N_o / 2$ (constant) at all frequencies and

$$\frac{|f_o(t_0)|^2}{n_o^2(t)} \leq \frac{1}{\pi\eta} \int_{-\infty}^{\infty} |F(\omega)|^2 d\omega = \frac{E}{\eta / 2} \quad (A1.6)$$

where E is the energy in $f(t)$ for a 1-ohm load, the optimum filter transfer function is

$$H_{opt}(\omega) = \frac{1}{N_o\pi C} F^*(\omega)e^{-j\omega t_0} \quad (A1.7)$$

Its impulse is readily found to be

$$h_{opt}(\omega) = \frac{1}{N_o\pi C} f^*(t_0 - t) \quad (A1.8)$$

If $f(t)$ is real, this optimum impulse response is a replica of $f(t)$ centred at t_0 but running backwards in time. At the point $t = t_0$, the signal output of the matched filter is given by substituting Eq. (A1.7) in Eq. (A1.1) with $1/N_o\pi C = 1$:

$$f_o(t_0) = \frac{1}{2\pi} \int_{-\infty}^{\infty} |F(\omega)|^2 d\omega = E \quad (A1.9)$$

Thus the output of the matched filter at the point $t = t_0$ is independent of the particular waveform, but depends on the signal energy. The mean square noise output of the matched filter is [Eq. (A1.9) in Eq. (A1.6)]

$$\overline{n_o^2(t)} = E \frac{\eta}{2} \quad (A1.10)$$

An alternative realisation of the matched filter is as follows. Let the input to the matched filter be $y(t) = f(t) + n(t)$ and the corresponding output be

$$\begin{aligned} g(t) &= y(t) \otimes f^*(t_m - t) = f^*(t_m - t) \otimes y(t) \\ &= \int_{-\infty}^{\infty} f^*(t_m - \xi) y(t - \xi) d\xi. \end{aligned} \quad (A1.11)$$

We let $\zeta = t_m - \xi$, so that Eq. (A1.12) becomes

$$g(t) = \int_{-\infty}^{\infty} f^*(\zeta)y(\zeta + t - t_m)d\zeta$$

$$= r_{fy}(t - t_m), \quad (\text{A1.12})$$

where

$$r_{fy}(\tau) = \int_{-\infty}^{\infty} f^*(\zeta)y(\zeta + \tau)d\zeta \quad (\text{A1.13})$$

is the time cross-correlation function for energy signals. Noting that $y(t) = f(t) + n(t)$, we find

$$g(t) = r_f(t - t_m) + r_{fn}(t - t_m), \quad (\text{A1.14})$$

where

$$r_f(\tau) = \int_{-\infty}^{\infty} f^*(\zeta)f(\zeta + \tau)d\zeta \quad (\text{A1.15})$$

is the time-autocorrelation function for energy signals. If the cross-correlation between $f(t)$ and $n(t)$ is zero, then the peak output $g(t_m)$ is given by $r_f(0)$.

The incoming waveform $y(t)$ is multiplied by $f(t)$, this requires that the signal $f(t)$ be known a priori and either stored in memory or supplied from another source.

2. Carrier recovery in QPSK

Since QPSK and QAM are coherent systems, their receivers require locally generated coherent carriers. A common method of carrier recovery uses a modified Costas loop, as illustrated in Figure A1. The network has phase ambiguities at multiples of $\pi/2$. Performance of Costas loops can be optimised by special selection of filters at the carrier product device outputs or by using integrate-and-dump filters.

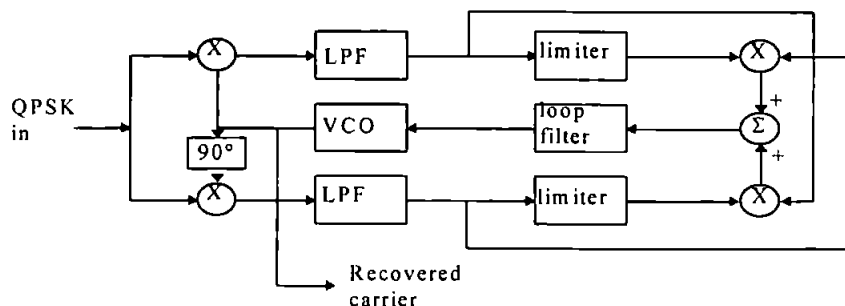


Figure A1 The Costas loop.

3. Probability of error in transmission

To begin this introduction to probability of error, we will assume that the binary levels at the receiver are 0 and A and not use the matched filter. The observed waveform at the receiver $y(t)$ also contains additive noise $n(t)$ so that at a time $t = t_1$ the signal could either be

$$y(t_1) = A + n(t_1) \quad (\text{signal present}) \quad (\text{A3.1})$$

or

$$y(t_1) = n(t_1) \quad (\text{no signal}) \quad (\text{A3.2})$$

Because $n(t_1)$ is random it is necessary to use probability to decide whether the signal is present or absent.

To calculate the probability of error (i.e. the probability that the receiver say a signal present when it is not or vice versa), we first need a decision threshold designated by μ . We assume that the noise $n(t_1)$ is Gaussian distributed with zero mean value and a mean-square value of

$$\overline{n^2(t_1)} = \sigma^2 \quad (\text{A3.3})$$

Using the standard equation for a Gaussian distribution we can write the probability density function of the input when there is no signal present as

$$p_0(y) = \frac{1}{\sqrt{2\pi}\sigma} e^{-y^2/(2\sigma^2)} \quad (\text{A3.4})$$

The probability density function of the input when the signal is present is also Gaussian, but has a mean value equal to A

$$p_1(y) = \frac{1}{\sqrt{2\pi}\sigma} e^{-(y-A)^2/(2\sigma^2)} \quad (\text{A3.5})$$

These probability density functions are shown in Figure A2.

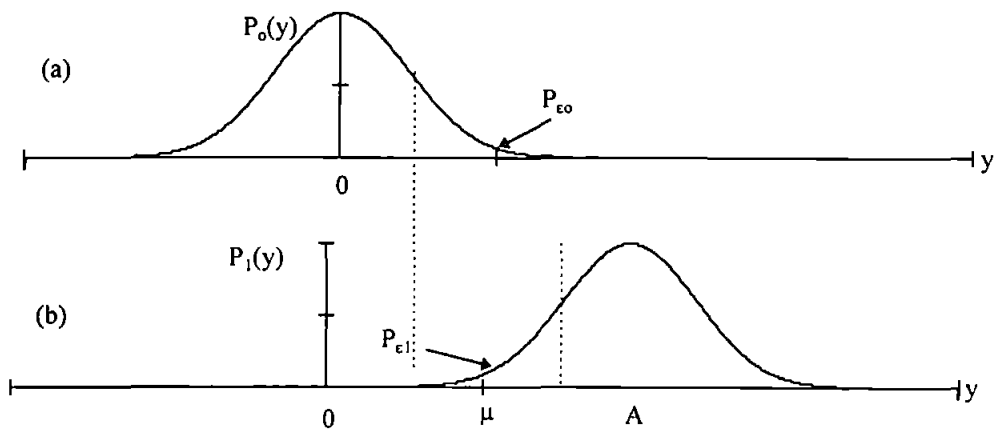


Figure A2 Probability density functions for the binary decision case

It can be seen that there are times when $y > \mu$ even though the signal is absent, these are called false alarms. The probability of false alarm designated by $P_{\epsilon o}$, can be written as

$$P_{\epsilon o} = \int_{\mu}^{\infty} \frac{1}{\sqrt{2\pi}\sigma} e^{-y^2/(2\sigma^2)} dy \quad (A3.6)$$

In the same way if $y < \mu$ when the signal is present, this is termed a false dismissal. The probability here given by $P_{\epsilon i}$ is

$$P_{\epsilon i} = \int_{\mu}^{\infty} \frac{1}{\sqrt{2\pi}\sigma} e^{-(y-A)^2/(2\sigma^2)} dy \quad (A3.7)$$

If we now define the net probability of error as being

$$P_{\epsilon} = 1/2 (P_{\epsilon o} + P_{\epsilon i}) \quad (A3.8)$$

Which holds so long as the binary levels (zero or one) are equiprobable.

In this case it is obvious from Figure A2 that the sum of these two areas will be a minimum if

$$\mu = A/2 \quad (A3.9)$$

As a result of symmetry we can write

$$P_{\epsilon} = \int_{\mu}^{\infty} \frac{1}{\sqrt{2\pi}\sigma} e^{-y^2/(2\sigma^2)} dy \quad (A3.10)$$

With the change of variable $z = y/\sigma$, this becomes

$$P_{\varepsilon} = \int_{\mu/\sigma}^{\infty} \frac{1}{\sqrt{2\pi}\sigma} e^{-z^2/2} dz \quad (\text{A3.11})$$

This can also be written, in terms of the function $Q(x)$, which has its values tabulated for convenience, as

$$P_{\varepsilon} = Q(\mu/\sigma) \quad (\text{A3.12})$$

Inserting the decision threshold $\mu = A/2$, we obtain

$$P_{\varepsilon} = Q[A/(2\sigma)] \quad (\text{A3.13})$$

The probability of error is dependant on the signal-to-noise ratio at a given time. Because the matched filter discussed in A1 is the best system to maximise the peak-signal-to-noise ratio in the presence of white noise. This case is now considered.

The matched filter is designed to maximise the SNR at time $t = t_m$ and we shall assume that $t_m = T$. It can readily be shown that the output of the matched filter at time $t_m = T$ is E , the energy in $f(t)$, giving

$$y(T) = E + n_o(T) \quad (\text{signal present}) \quad (\text{A3.14})$$

or

$$y(T) = n_o(T) \quad (\text{signal absent}) \quad (\text{A3.15})$$

A comparison of Eqs. (A3.14) and (A3.15) with Eqs. (A3.1) and (A3.2) shows that this problem has already been solved with A being replaced by E , and

$$\sigma^2 = \overline{n_o^2(t)} = \frac{E\eta}{2}, \quad (\text{A3.16})$$

where $\eta/2$ is the (two-sided) power spectral density of the white noise input to the matched filter. Substituting E for A and $\sqrt{(E\eta/2)}$ for σ in Eq. (A3.13) gives the probability of error for matched filter detection as

$$P_{\varepsilon} = Q\left(\sqrt{\frac{E}{2\eta}}\right) \quad (\text{on-off binary}) \quad (\text{A3.17})$$

The polar binary case follows in the same way except that the output of the matched filter is

$$y(T) = \pm E + n_o(T) \quad (\text{A3.18})$$

substituting $2E$ for A and $\sqrt{(E\eta/2)}$ for σ in Eq. (A3.13) gives

$$P_{\varepsilon} = Q\left(\sqrt{\frac{2E}{\eta}}\right) \quad (\text{polar binary}) \quad (\text{A3.19})$$

4. Likelihood Ratio

The radar detection problem is a binary hypothesis-testing problem in which H_0 denotes that no target is present and H_1 is the hypothesis that a target is present. The Neyman Pearson [9] method of optimality maximises the probability of detection P_D for a given probability of false alarm P_{fa} by comparing the likelihood ratio [Eq. (A4.1)] to an appropriate threshold T which determines the P_{fa} . A target is declared present if

$$L(x_1, \dots, x_n) \frac{p(x_1, \dots, x_n | H_1)}{p(x_1, \dots, x_n | H_0)} \geq T \quad (\text{A4.1})$$

where $p(x_1, \dots, x_n | H_1)$ and $p(x_1, \dots, x_n | H_0)$ are the joint probability density functions of the n samples x_i under the conditions of target presence and target absence respectively.

APPENDIX B

Derivation of optical Fourier transform

Figure B1 illustrates the light distribution $\phi(x,y)$ in the plane (x,y) due to the distribution $\psi(u,v)$ in the plane (u,v) . Each point P in the (u,v) plane is considered as a point source, the distribution in the (x,y) plane is therefore the sum of the spherical waves from each source.

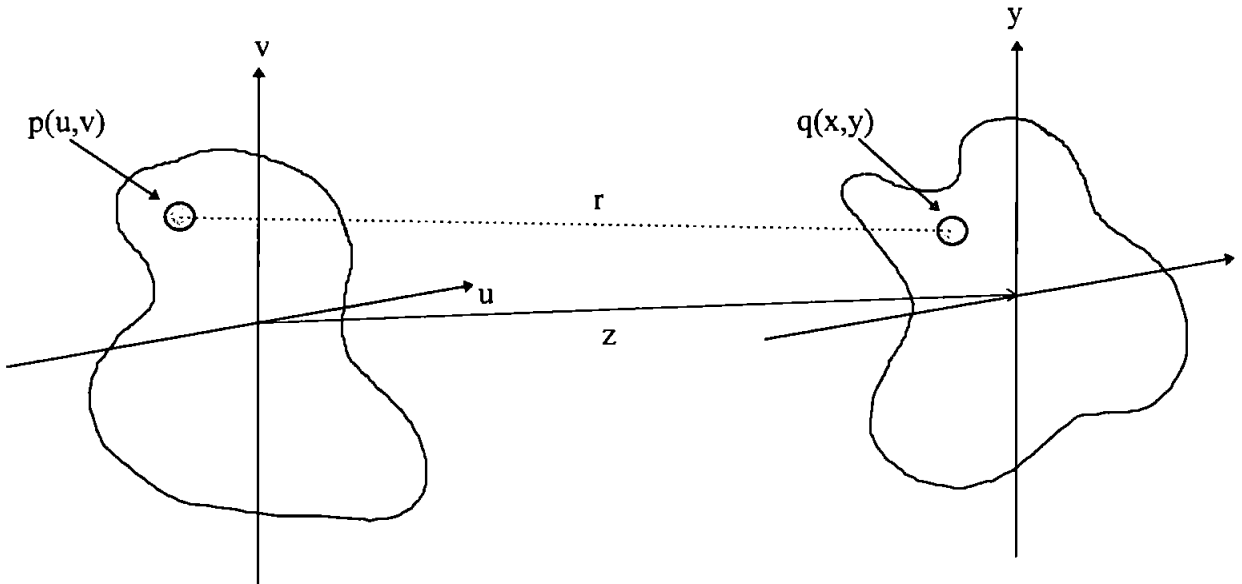


Figure B1 Spatial light distribution at point $q(x,y)$ due to point source at point $p(u,v)$

This can be expressed as

$$\phi(x,y) = k \iint \frac{\psi(u,v)}{r} e^{-jkr} du dv \quad (\text{B.1})$$

where k is a constant, r is the distance between two points and k is the wave number. If we keep close to the origin and assume that the distance between the (u,v) and (x,y) planes is large then the divisor r can be taken as a constant z , the distance between the planes. The r in the exponent must be evaluated

$$r^2 = (x-u)^2 + (y-v)^2 + z^2 \quad (\text{B.2})$$

$$= x^2 + y^2 + z^2 + u^2 + v^2 - 2ux - 2vy \quad (\text{B.3})$$

if we let $x^2 + y^2 + z^2 = R^2$ then

$$r = R \sqrt{1 + \frac{u^2 + v^2}{R^2} - \frac{2ux - 2vy}{R^2}} \quad (\text{B.4})$$

$$\approx R \left[1 + \frac{u^2 + v^2}{2R^2} - \frac{ux - vy}{R^2} + \dots \right] \quad (\text{B.5})$$

$$R + \frac{u^2 + v^2}{2R} - \frac{ux - vy}{R} + \dots \quad (\text{B.6})$$

therefore

$$\phi(x, y) = \frac{k}{2} \iint \psi(u, v) e^{-jkR} e^{-j \frac{k(u^2 + v^2)}{2R}} e^{j \frac{k(ux + uv)}{R}} du dv \quad (\text{B.7})$$

A lens has the effect on an optical system [19]

$$e^{j \frac{k(u^2 + v^2)}{2l_f}} \quad (\text{B.8})$$

thus a lens where $l_f = R$ cancels the term

$$e^{-j \frac{k(u^2 + v^2)}{2R}} \quad (\text{B.9})$$

therefore in the focal plane of the lens

$$\phi(x, y) = \frac{k}{2} e^{-jkR} \iint \psi(u, v) e^{j \frac{k(ux + uv)}{l_f}} du dv \quad (\text{B.10})$$

$$= k' \iint \psi(u, v) e^{j \frac{2\pi(ux + uv)}{\lambda l_f}} du dv \quad (\text{B.11})$$

which is a Fourier transform between the (u, v) and (x, y) planes.

For the analysis of the system it is necessary to know how the Fourier transform affects the intensity distribution of the Gaussian profile. It is well known that a Gaussian profile is still Gaussian after the action of a Fourier transform, but we need to know the effect on the scaling factor σ . In order to do this we must first apply our transform to a Gaussian profile. The intensity profile of a one dimensional Gaussian spatial intensity profile is

$$I_o = e^{-\frac{u^2}{2\sigma_o^2}} \quad (\text{B.12})$$

where σ_o is the beam width standard deviation in the AO cell. The amplitude profile is therefore

$$A_o = \sqrt{I_o} \quad (\text{B.13})$$

which can be written as

$$A_o = e^{-\frac{1}{2} \frac{u^2}{2\sigma_o^2}} \quad (\text{B.14})$$

$$A_o = e^{-\frac{u^2}{4\sigma_o^2}} \quad (\text{B.15})$$

If we now take the Fourier transform in 1-D via the optical Fourier transform

$$A_t = \int A_o e^{-\left(\frac{2\pi}{\lambda f} ux\right)} du \quad (\text{B.16})$$

which gives the Amplitude profile in the focal plane A_t (i.e. the at the detector) as

$$A_t = e^{-\left(\frac{2\pi\sigma_o}{\lambda f}\right)^2 x^2} \quad (\text{B.17})$$

since the detector measures the intensity we must find the intensity of the transformed Gaussian

$$I_t = e^{-2\left(\frac{2\pi\sigma_o}{\lambda f}\right)^2 x^2} \quad (\text{B.18})$$

which simplifies to

$$I_t = e^{-\frac{8\pi^2\sigma_o^2}{\lambda^2 f^2} x^2} \quad (\text{B.19})$$

We can now equate the exponent of the transformed intensity profile we can find σ_t , the standard deviation of the transformed Gaussian, using Eqs.(D.12) and (D.19)

$$\frac{8\pi^2\sigma_o^2}{\lambda^2 f^2} = \frac{1}{2\sigma_t^2} \quad (\text{B.20})$$

which can be rearranged to give

$$\sigma_t = \frac{\lambda f}{4\pi\sigma_o} \quad (\text{B.21})$$

This is the standard deviation of a transformed Gaussian expressed in terms of the optical Fourier transform parameters and the original intensity profile standard deviation.

APPENDIX C

MATHCAD Files

1. AO demodulator model

set up sampling

$$N := 4096 \quad f_s := 400 \cdot 10^6 \quad i := 0..N-1 \quad I_i := i \quad t_i := \frac{I_i}{f_s} \quad n := 0.. \frac{N}{2} \quad f_n := \frac{n}{N} \cdot f_s$$
$$T_s := 50 \cdot 10^6 \quad f_{1n} := \frac{n}{T_s}$$

definitions and functions

$$\text{LaserDev} := \frac{0.49 \cdot 10^{-3}}{4}$$

$$V_a := 617$$

$$\text{StdDevTime} := \frac{\text{LaserDev}}{V_a}$$

$$\text{LaserPower} := 15 \cdot 10^{-3}$$

$$\text{Responsivity} := 0.35$$

$$\text{StdDevPoints} := \text{StdDevTime} \cdot f_s$$

$$\text{DiffractionEff} := 0.5$$

$$\text{TransimpGain} := 1.5 \cdot 10^3$$

$$\text{StdDevPoints} = 79.417$$

$$\lambda := 830 \cdot 10^{-9}$$

$$\text{electron} := 1.6 \cdot 10^{-19}$$

$$\text{rect}(x) := \Phi(x + 0.5) - \Phi(x - 0.5)$$

$$\text{fact}(x) := 10^{\frac{x}{10}}$$

$$\text{gauss } x, \sigma := \frac{1}{\sqrt{2 \cdot \pi \cdot \sigma^2}} \cdot e^{-\frac{\frac{\text{LaserDev}}{\text{StdDevPoints}} \cdot x^2}{2 \cdot \sigma^2}}$$

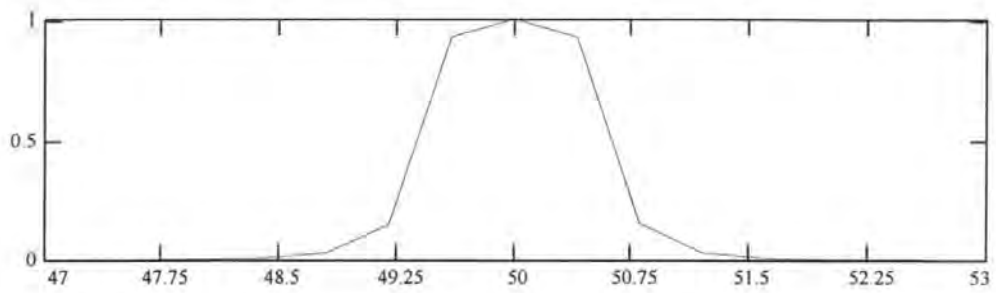
create bandpass AWGN

$$f_c := 50 \cdot 10^6$$

$$Bw := 1 \cdot 10^6$$

$$P := \text{iirpass butter}(4), \frac{f_c - \frac{Bw}{2}}{400 \cdot 10^6}, \frac{f_c + \frac{Bw}{2}}{400 \cdot 10^6}$$

$$x := 0, 0.001.. .5$$

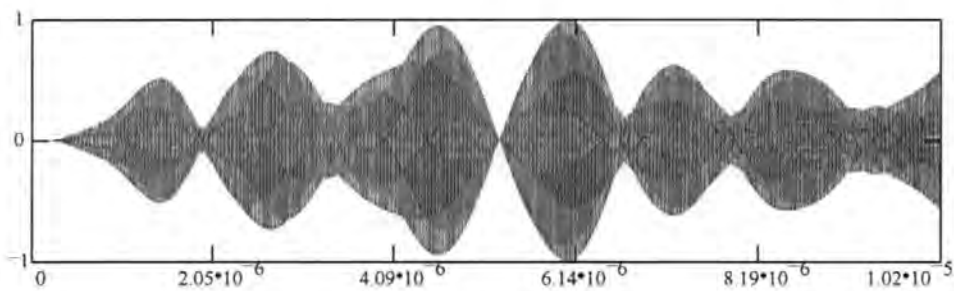


create bandlimited gaussian noise

$B_n = 1$ $\eta = 2$ $N_i = \eta \cdot B_n \cdot 20$ $N_i = 40$ $\sigma_n = \sqrt{N_i}$ `noise = gaussn(N)`

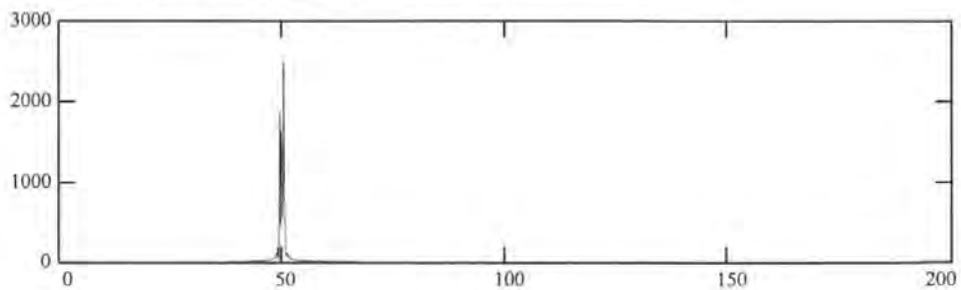
`noise = $\sigma_n \cdot \sqrt{\frac{f_s}{2 \cdot B_n}}$ \cdot response(gaussn(N), P, 4096)`

`noise = (noise - mean(noise))` `mean(noise) = $-1.545 \cdot 10^{-13}$`



Bandwidth of bandlimited noise

`NOISE = FFT(noise)`



Creating signals

carrier signal

$$k := 0..N-1 \quad f_0 := 50 \cdot 10^6$$

$$\text{carrier}_k = \sin[2 \cdot \pi \cdot (f_0) \cdot t_k]$$

step frequency change

$$\text{diff} = 100 \cdot 10^3$$

$$k = 0.. \frac{N}{8} - 1 \quad \text{st1}_k = \cos[2 \cdot \pi \cdot (f_0 - \text{diff}) \cdot t_k] \quad k = \frac{N}{8}.. \frac{N}{4} - 1 \quad \text{st1}_k = \cos[2 \cdot \pi \cdot (f_0 + \text{diff}) \cdot t_k]$$

$$k = \frac{N}{4}.. \frac{3 \cdot N}{8} - 1 \quad \text{st1}_k = \cos[2 \cdot \pi \cdot (f_0 - \text{diff}) \cdot t_k] \quad k = \frac{3 \cdot N}{8}.. \frac{N}{2} - 1 \quad \text{st1}_k = \cos[2 \cdot \pi \cdot (f_0 - \text{diff}) \cdot t_k]$$

$$k = \frac{N}{2}.. \frac{5 \cdot N}{8} - 1 \quad \text{st1}_k = -\cos[2 \cdot \pi \cdot (f_0 - \text{diff}) \cdot t_k] \quad k = \frac{5 \cdot N}{8}.. \frac{3 \cdot N}{4} - 1 \quad \text{st1}_k = -\cos[2 \cdot \pi \cdot (f_0 + \text{diff}) \cdot t_k]$$

$$k = \frac{3 \cdot N}{4}.. \frac{7 \cdot N}{8} - 1 \quad \text{st1}_k = -\cos[2 \cdot \pi \cdot (f_0 - \text{diff}) \cdot t_k] \quad k = \frac{7 \cdot N}{8}.. N - 1 \quad \text{st1}_k = \cos[2 \cdot \pi \cdot (f_0 - \text{diff}) \cdot t_k]$$

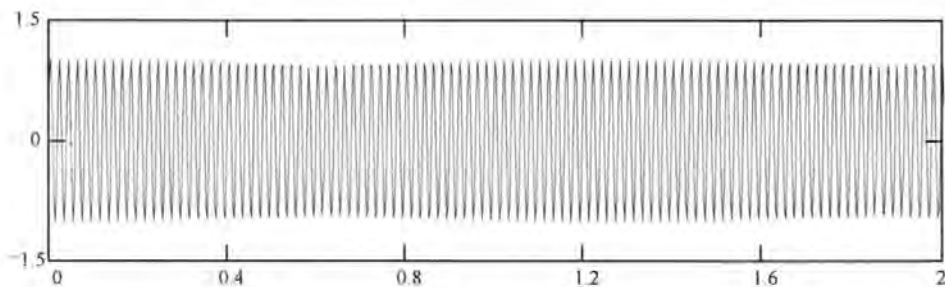
$$k = 0.. \frac{N}{8} - 1 \quad \text{st}_k = \sin[2 \cdot \pi \cdot (f_0 - \text{diff}) \cdot t_k] \quad k = \frac{N}{8}.. \frac{N}{4} - 1 \quad \text{st}_k = -\sin[2 \cdot \pi \cdot (f_0 + \text{diff}) \cdot t_k]$$

$$k = \frac{N}{4}.. \frac{3 \cdot N}{8} - 1 \quad \text{st}_k = -\sin[2 \cdot \pi \cdot (f_0 - \text{diff}) \cdot t_k] \quad k = \frac{3 \cdot N}{8}.. \frac{N}{2} - 1 \quad \text{st}_k = \sin[2 \cdot \pi \cdot (f_0 + \text{diff}) \cdot t_k]$$

$$k = \frac{N}{2}.. \frac{5 \cdot N}{8} - 1 \quad \text{st}_k = \sin[2 \cdot \pi \cdot (f_0 - \text{diff}) \cdot t_k] \quad k = \frac{5 \cdot N}{8}.. \frac{3 \cdot N}{4} - 1 \quad \text{st}_k = \sin[2 \cdot \pi \cdot (f_0 + \text{diff}) \cdot t_k]$$

$$k = \frac{3 \cdot N}{4}.. \frac{7 \cdot N}{8} - 1 \quad \text{st}_k = -\sin[2 \cdot \pi \cdot (f_0 - \text{diff}) \cdot t_k] \quad k = \frac{7 \cdot N}{8}.. N - 1 \quad \text{st}_k = \sin[2 \cdot \pi \cdot (f_0 + \text{diff}) \cdot t_k]$$

input signal



$$\text{out} = \text{st} - \text{st1}$$

combining signal with noise(SNRin is in dB)

SNRin := 30 var(noise) = 4.782·10⁷ var(out) = 1

$$A = \sqrt{10^{\frac{\text{SNRin}}{10}} \cdot \frac{\text{var}(\text{noise})}{\text{var}(\text{out})}} \quad \text{var} \frac{\text{noise}}{A} = 0.001 \quad 10 \cdot \log \frac{\text{var}(\text{out})}{\text{var} \frac{\text{noise}}{A}} = 30$$

$$s_i = \frac{\text{noise}_i}{(A)} + \text{out}_i$$

eb = var(out)·1.275·10⁻⁶

$$\text{No} := \frac{\text{var} \frac{\text{noise}}{A}}{\text{Bw}} \quad 10 \cdot \log \frac{\text{eb}}{\text{No}} = 31.055$$

clipping

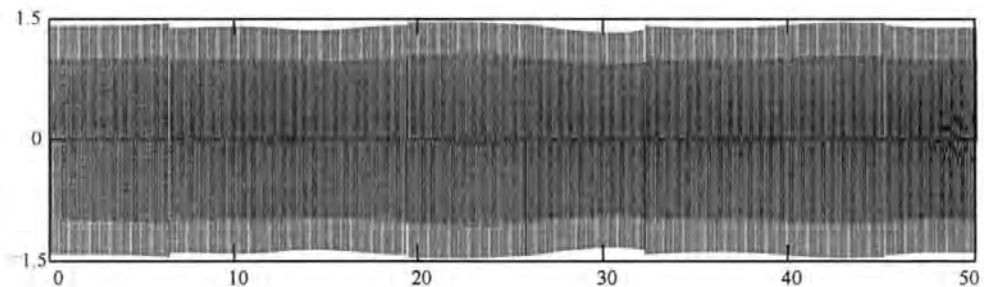
clip = max(s)·1 s_i = if s_i>clip, clip, s_i s_i = if s_i<- clip, clip, s_i

set up Gaussian window with time shift

h = 0..2047 g = $\sqrt{\text{gauss } 512 - 1, \frac{\text{LaserDev}}{2}}$

G = FFT(g) τ = 41

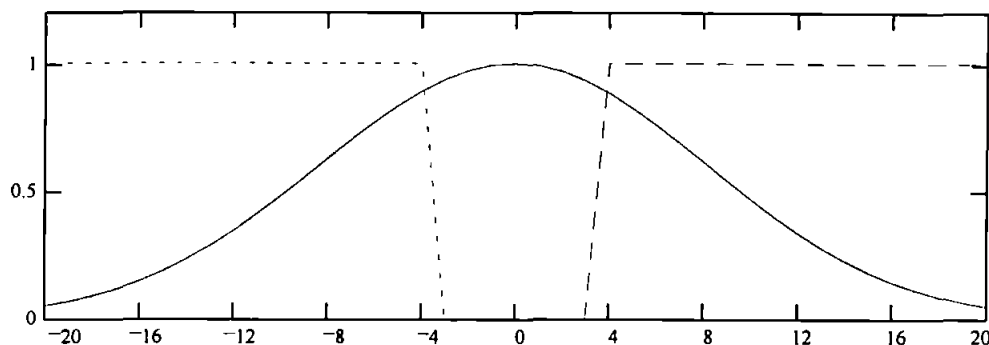
$a = \text{s} \cdot \text{IFFT} \left(G \cdot e^{-j \cdot 2 \cdot \pi \cdot \tau \cdot 10^6} \right)$ a = $\frac{a}{\text{max}(a)}$ last(s) = 4.095·10³
 last(G) = 2.048·10³



calculating power spectrum of gaussian windowed signal, and setting up windows for the bi-cell

$$P := \left[\left| \text{FFT recenter } \vec{a} \right|^2 \right] \quad W1 := \text{rect} \frac{f1 - 9.56 \cdot 10^{-6}}{1.2 \cdot 10^{-6}} \quad W2 := \text{rect} \frac{f1 - 10.92 \cdot 10^{-6}}{1.2 \cdot 10^{-6}}$$

$$z := \max(P) \quad z = 2.959 \cdot 10^{-4}$$



$$\text{BeamInt} := \text{LaserPower} \cdot \text{DiffractionEff}$$

$$\text{BeamInt} = 0.007$$

expressions for spatially integrated intensity of light on each photodiode as functions of time shift

$$C1(\tau) := \sum \left[\left| \left[\text{FFT } s \cdot \text{IFFFT } G \cdot e^{-j \cdot 2 \cdot \pi \cdot f1 \cdot 10^6 \cdot \tau} \right] \right|^2 \cdot W1 \right]$$

$$C2(\tau) := \sum \left[\left| \left[\text{FFT } s \cdot \text{IFFFT } G \cdot e^{-j \cdot 2 \cdot \pi \cdot f1 \cdot 10^6 \cdot \tau} \right] \right|^2 \cdot W2 \right]$$

calculate difference outputs for a set of different time shifts

$$K := 132 \quad k := 0..K \quad \tau_k := \frac{k}{3} - 4 \quad \text{OPC2} := \overline{C2(\tau)} \quad \text{OPC1} := \overline{C1(\tau)}$$

$$\text{noise1} := \sqrt{\text{OPC1} \cdot \text{Responsivity} \cdot \text{electron} \cdot \text{Bw}}$$

$$\text{noise2} := \sqrt{\text{OPC2} \cdot \text{Responsivity} \cdot \text{electron} \cdot \text{Bw}}$$

$$\text{noise1} := \text{noise1} \cdot \sqrt{2}$$

$$\text{noise2} := \text{noise2} \cdot \sqrt{2}$$

$$k := 0, 2..132$$

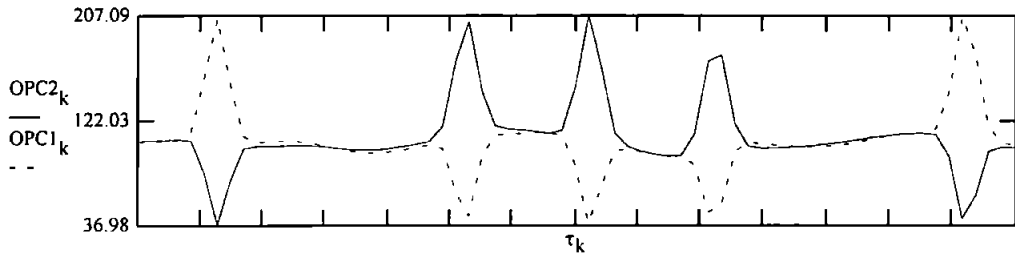
$$\text{noise1}_k := -\text{noise1}_k$$

$$\text{noise2}_k := -\text{noise2}_k$$

$$OPC1 := ((OPC1 \cdot \text{Responsivity}) + \text{noise1}) \cdot \text{TransimpGain} \cdot \overline{\text{BeamInt}}$$

$$OPC2 := ((OPC2 \cdot \text{Responsivity}) + \text{noise2}) \cdot \text{TransimpGain} \cdot \overline{\text{BeamInt}}$$

graph showing the outputs of each detector cell

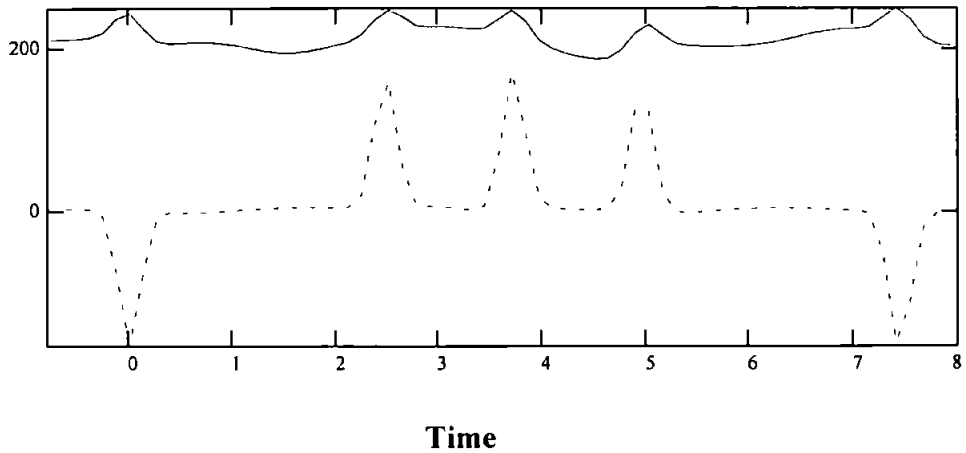


$$OPS := \overline{(OPC2 - OPC1)}$$

$$OPS1 := \overline{(OPC2 + OPC1)}$$

graph showing the sum and the difference of the two cells

Volts



SNR, standard deviation, variance, and mean of output signals

$$10 \cdot \log \left[\frac{(27)^2}{\text{var}(OPS1)} \right]_0$$

$$\text{var}(OPS1) = 238.896$$

$$\text{stdev}(OPS1) = 15.456$$

$$\text{mean}(OPS1) = 213.302$$

$$10 \cdot \log \left[\frac{(66)^2}{\text{var}(OPS)} \right]_0$$

$$\text{var}(OPS) = 2.91 \cdot 10^3$$

$$\text{stdev}(OPS) = 53.944$$

$$\text{mean}(OPS) = 4.36$$

2. Creating the power spectral density plots

definitions and functions

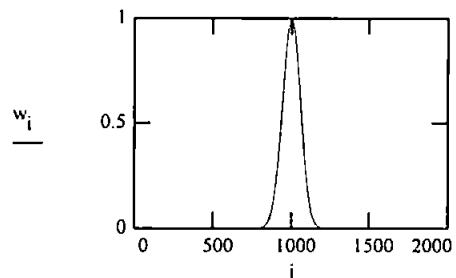
$$\sigma := 0.1225 \cdot 10^{-3} \quad V_a := 617 \quad \sigma v := \frac{\sigma}{V_a}$$

$$dt := \frac{\sigma v}{40} \quad fs := \frac{1}{dt} \quad \frac{\sigma v}{dt} = 40 \quad fs = 2.015 \cdot 10^8$$

$$i := 0..1999$$

creating the gaussian beam

$$w_i := \sqrt{\exp\left[-\frac{((i - 1000) \cdot dt)^2}{2 \cdot \sigma v^2}\right]}$$



defining the signal with modulation change

carrier frequency

$$f := \frac{fs}{4}$$

frequency shift

$$fd := \frac{f \cdot 0}{100}$$

phase shift

$$\phi := \pi$$

$$j := 0..1999$$

$$y_j := \cos(2 \cdot \pi \cdot (f - fd) \cdot j \cdot dt)$$

$$j := 2000..3999$$

$$y_j := \cos(2 \cdot \pi \cdot (f + fd) \cdot j \cdot dt + \phi)$$

moving the signal across the gaussian in 5 steps

$$q := 0..4 \quad i := 0..1999$$

$$s_{i,q} := w_i \cdot y_{i + 879 + q \cdot 60}$$

taking the Fourier transform of the Gaussian multiplied by the signal

$$S^{<q>} := \text{recenter CFFT } s^{<q>}$$

$$S^{<q>} := \text{mag } S^{<q>}$$

$$S := \vec{S^2}$$

scaling the displacement axis

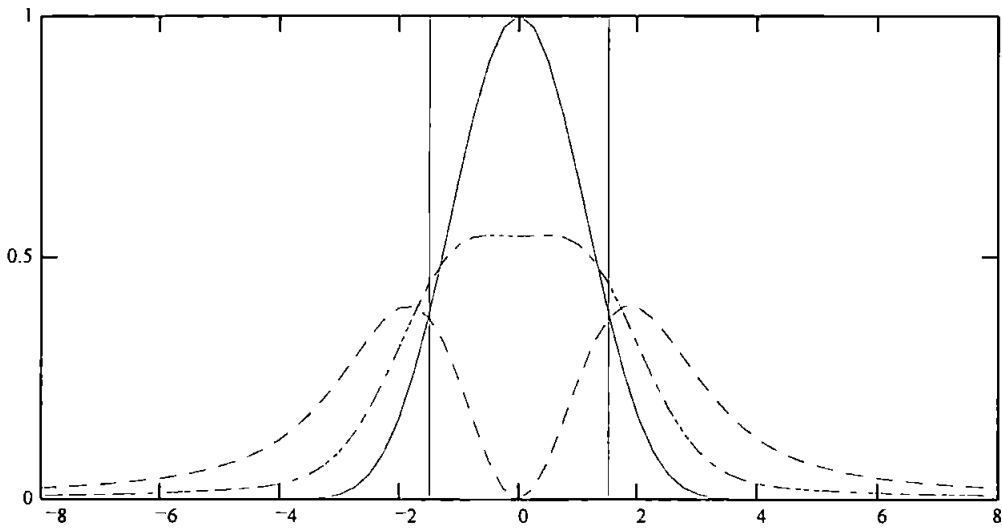
$$j := 1000..1999 \quad p := \max(S) \quad fr_j := \frac{fs \cdot (j - 1000)}{2000} \cdot 10^{-6}$$

$$S := \frac{\overrightarrow{S}}{p} \quad x\sigma_j := \frac{4 \cdot \pi \cdot \sigma \cdot fr_j}{V_a} \cdot 10^6 \quad m := x\sigma_{1499} \quad x\sigma := (\overrightarrow{x\sigma - m})$$

$$j := 1467..1531$$

Change in beam profile in response to a QPSK signal

Power Spectral Density



Displacement at detector

3. Calculating the optimum gap size for FSK and PSK modulation

definitions and functions

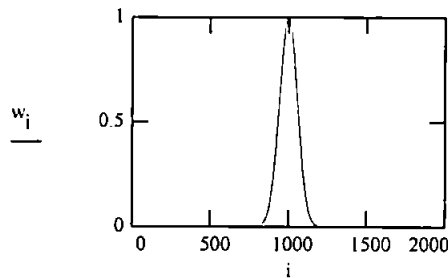
$$\sigma := 0.1225 \cdot 10^{-3} \quad V_a := 617 \quad \sigma v := \frac{\sigma}{V_a}$$

$$dt := \frac{\sigma v}{40} \quad fs := \frac{1}{dt} \quad \frac{\sigma v}{dt} = 40 \quad fs = 2.015 \cdot 10^8$$

generating the Gaussian beam

$$i := 0..1999$$

$$w_i := \sqrt{\exp\left[-\frac{((i - 1000) \cdot dt)^2}{2 \cdot \sigma v^2}\right]}$$



generating the modulating signal

carrier frequency

$$f := \frac{fs}{10}$$

frequency shift

$$fd := \frac{f \cdot 0}{200}$$

phase shift

$$\phi := \frac{\pi}{4}$$

$$j := 0..1999$$

$$y_j := \cos(2 \cdot \pi \cdot (f - fd) \cdot j \cdot dt)$$

$$j := 2000..3999$$

$$y_j := \cos(2 \cdot \pi \cdot (f - fd) \cdot j \cdot dt + \phi)$$

multiplying the signal by the Gaussian

$$i := 0..1999$$

$$s_i := w_i \cdot y_{i+999}$$

taking the Fourier transform of the signal and Gaussian

$$S := \text{recenter}(\text{CFFT}(s))$$

$$S := \text{mag}(S)$$

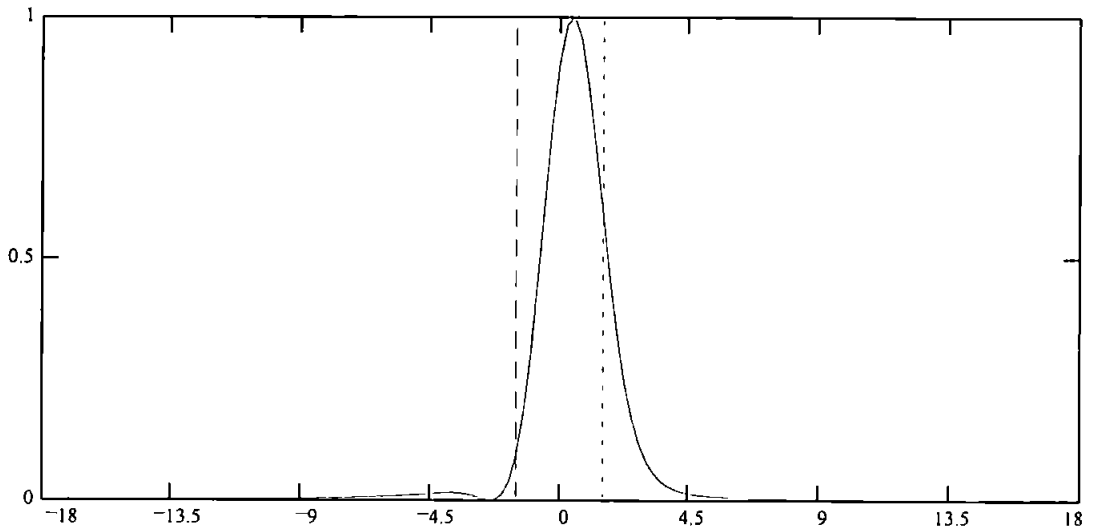
$$S := \vec{S^2}$$

scaling the displacement axis

$$j := 1000..1999 \quad fr_j := \frac{fs \cdot (j - 1000)}{2000} \cdot 10^{-6} \quad p := \max(S)$$

$$S := \frac{\overrightarrow{S}}{p} \quad x\sigma_j := \frac{4 \cdot \pi \cdot \sigma \cdot fr_j}{V_a} \cdot 10^6 \quad m := x\sigma_{1199} \quad x\sigma := \overrightarrow{(x\sigma - m)}$$

power spectral density



displacement at the detector

$$S := \frac{S}{\sum S} \quad x\sigma_{1100} = -24.881 \quad j := 0..20 \quad q_j := j$$

summing the light falling on each cell

$$LHS_j := \sum_{a=1000}^{1199 - q_j} S_a \quad RHS_j := \sum_{a=1199 + q_j}^{1398} S_a$$

calculating the sum and difference

$$\text{Sum} := LHS + RHS$$

$$\text{Diff} := RHS - LHS$$

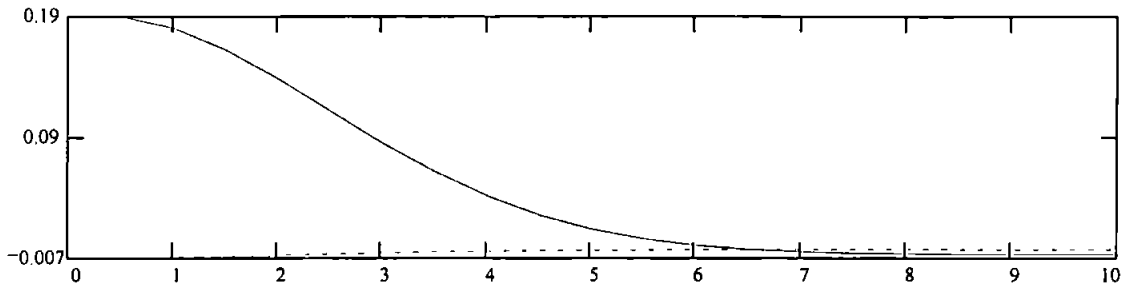
$$\text{WRITEPRN}(\text{sum}) := \text{Sum}_0$$

$$\text{WRITEPRN}(\text{diff}) := \text{Diff}_0$$

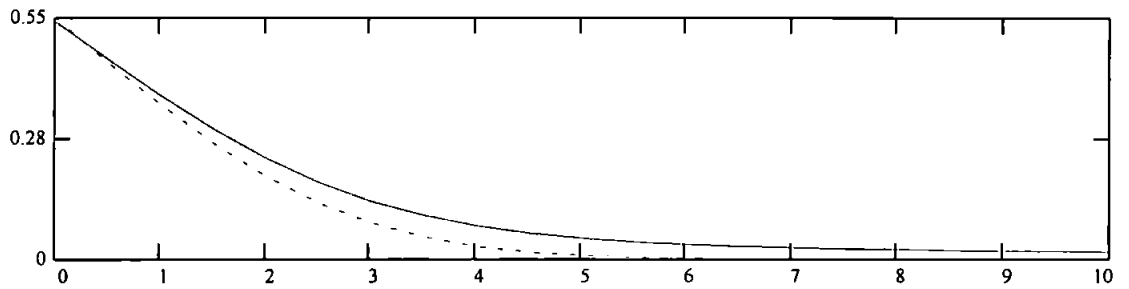
$$\text{nsum} := \text{READPRN}(\text{sum})$$

$$\text{ndiff} := \text{READPRN}(\text{diff})$$

Difference



Sum



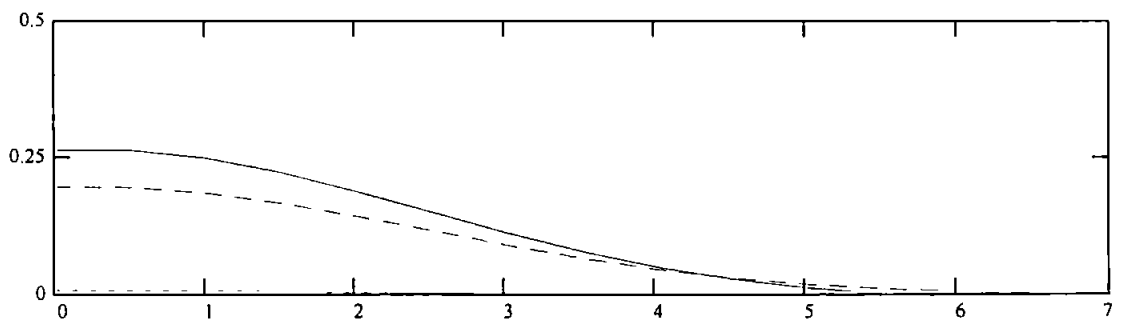
subtracting the background voltage from the pulse amplitude voltage

$$\text{Sum} := \text{Sum} - \text{nsum} \quad \text{Diff} := \text{Diff} - \text{ndiff}$$

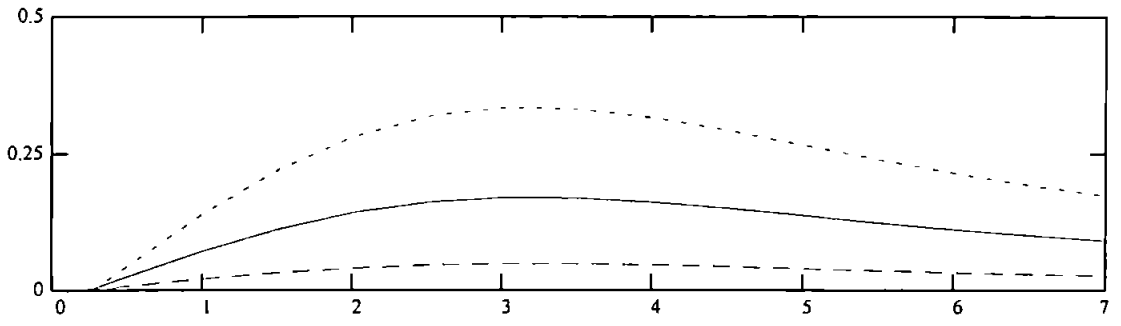
loading the data for each form of modulation

```
WRITEPRN(sum3) := Sumo      WRITEPRN(diff3) := Diffo  
sum1 := READPRN(sum1)      diff1 := READPRN(diff1)  
sum2 := READPRN(sum2)      diff2 := READPRN(diff2)  
sum3 := READPRN(sum3)      diff3 := READPRN(diff3)
```

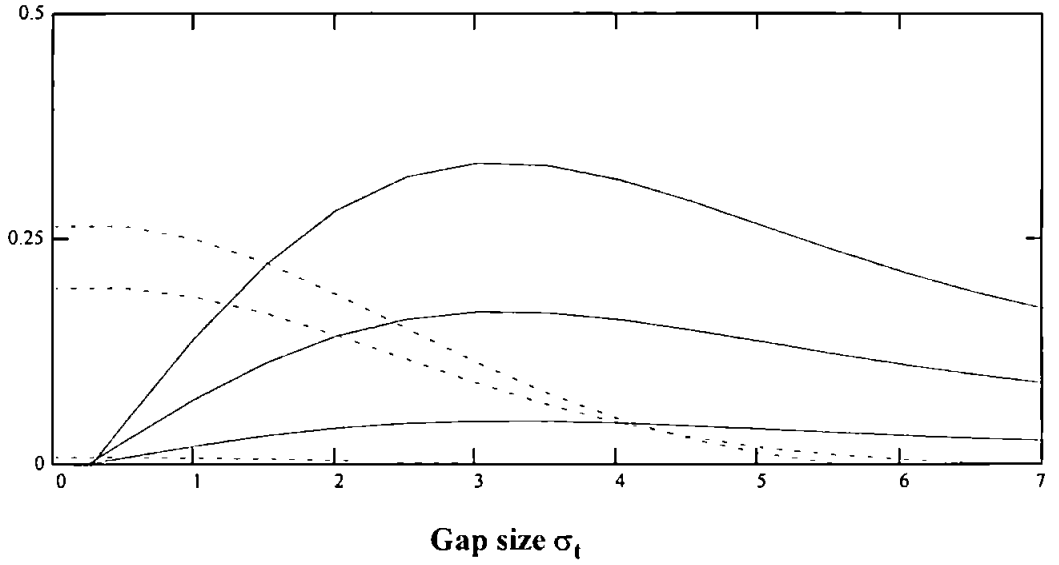
Difference



Sum



**Pulse
amplitude
mV**



4. Effect of gap size on the linearity of the MTF

definitions and functions

$$lf := 0.05 \quad \lambda := 632.8 \cdot 10^{-9} \quad Va := 617 \quad i := 0..100$$

$$\sigma t := 20 \cdot 10^{-6}$$

$$\delta x_i := \frac{i}{100} \cdot \sigma t$$

$$gap := 1.5 \cdot \sigma t$$

$$g := gap$$

calculating the light falling on the left and right cells as the position of the gap is moved across the Gaussian beam

$$Psl_i := \int_{-8 \cdot \sigma t + \frac{gap}{2}}^{\delta x_i - \frac{gap}{2}} \frac{1}{\sqrt{2 \cdot \pi \cdot \sigma t^2}} \cdot e^{-\frac{x^2}{2 \cdot \sigma t^2}} dx$$

$$Psr_i := \int_{\delta x_i + \frac{gap}{2}}^{8 \cdot \sigma t - \frac{gap}{2}} \frac{1}{\sqrt{2 \cdot \pi \cdot \sigma t^2}} \cdot e^{-\frac{x^2}{2 \cdot \sigma t^2}} dx$$

calculating the difference in optical power between the left and right cell

$$Psdiff := Psl - Psr$$

$$i := 0..100$$

$$\delta x_i := \frac{i \cdot \sigma t}{100}$$

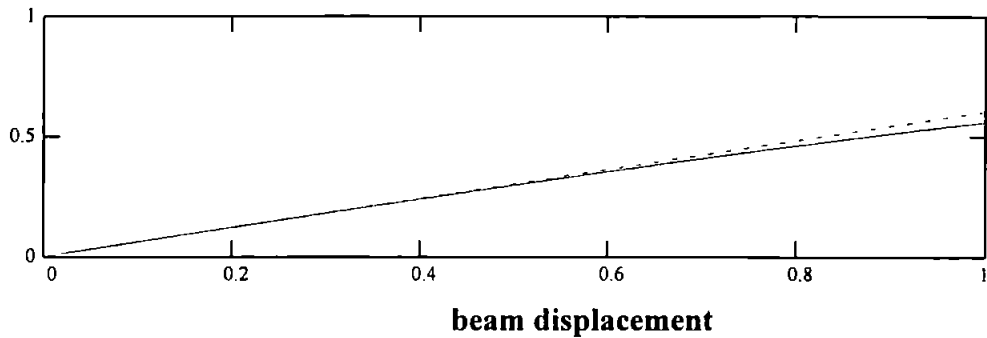
power series approximation of the difference in optical power between the two cells

$$\delta x \sigma t_i := \frac{1}{1536} \cdot \delta x_i \cdot \frac{24 \cdot g^4 \cdot \sigma t^2 - g^6 - 384 \cdot g^2 \cdot \sigma t^4 + 3072 \cdot \sigma t^6}{\sigma t^7}$$

$$Psl_i := \frac{1}{\sqrt{2 \cdot \pi}} \cdot \delta x \sigma t_i$$

graph showing the approximated and calculated, difference values as the gap is moved across the beam

optical power



calculating the error between the two methods

$$\delta f_i := \frac{\frac{\delta x_i}{\sigma t} \cdot (\lambda \cdot l f \cdot \sigma t)}{V_a}$$

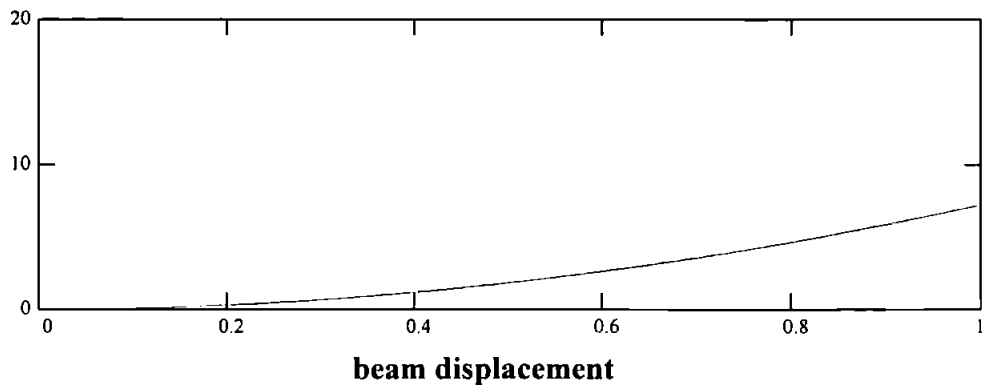
$$P_{sdiff_0} := 10^{-15}$$

$$P_{error} := 1 - \left[\frac{P_{sdiff}}{P_s} \right] \cdot 100$$

$$P_{s_0} := 10^{-15}$$

graph showing the error between the two method

error
%



load previously stored error plots for diferent gap sizes

WRITEPRN(error1) := Perror

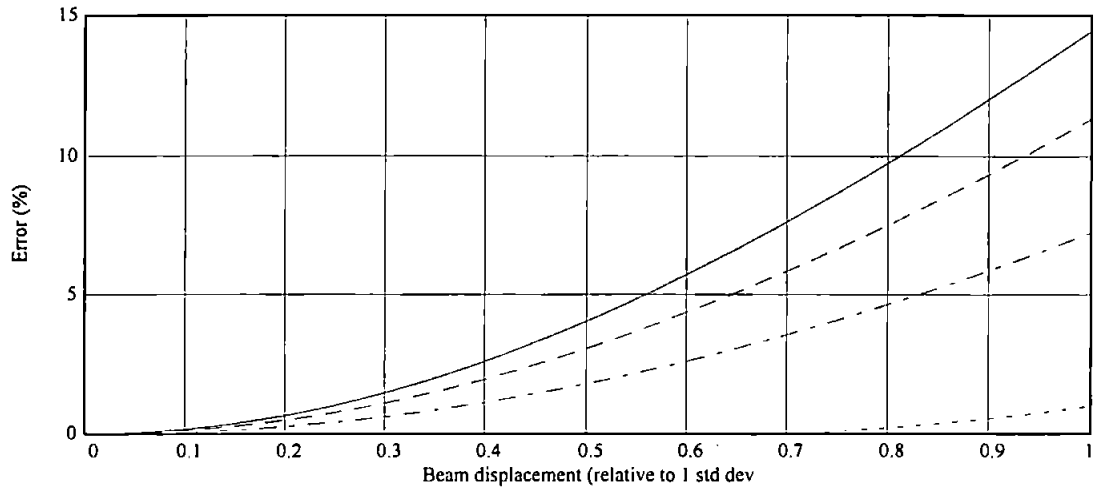
a := READPRN(error)

c := READPRN(error2)

b := READPRN(error1)

d := READPRN(error3)

graph showing how the %age error decreases as the gap size increases



5. MTF for varying gap sizes

definitions and functions

$$lf := 0.05 \quad \lambda := 632.8 \cdot 10^{-9} \quad Va := 617$$

$$\sigma_t := 20 \cdot 10^{-6}$$

calculating the power of the light falling on the left and right cells as the gap is move across the Gaussian

$$i := 0..500 \quad \delta x_i := \frac{4 \cdot \sigma_t \cdot i}{500} - 2 \cdot \sigma_t \quad \text{gap} := 2 \cdot \sigma_t$$

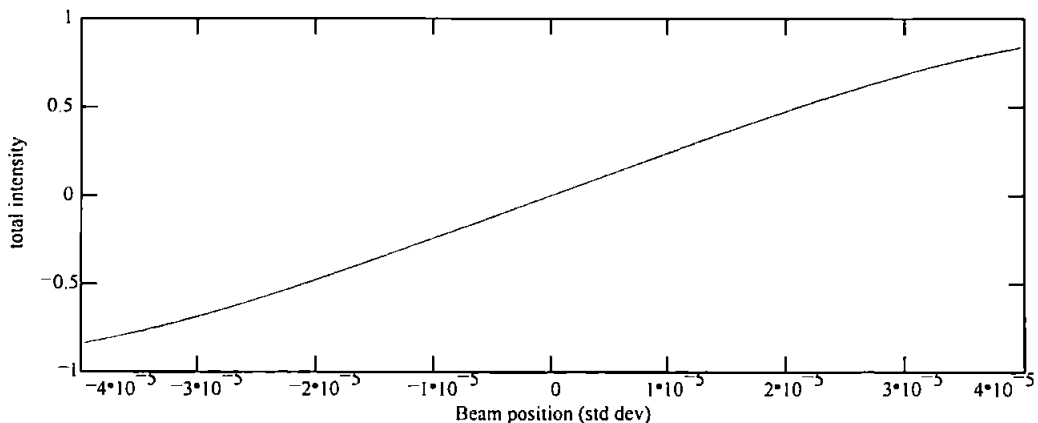
$$Psl_i := \int_{-8 \cdot \sigma_t + \frac{\text{gap}}{2}}^{\delta x_i - \frac{\text{gap}}{2}} \frac{1}{\sqrt{2 \cdot \pi \cdot \sigma_t^2}} \cdot e^{-\frac{x^2}{2 \cdot \sigma_t^2}} dx$$

$$Psr_i := \int_{\delta x_i + \frac{\text{gap}}{2}}^{8 \cdot \sigma_t - \frac{\text{gap}}{2}} \frac{1}{\sqrt{2 \cdot \pi \cdot \sigma_t^2}} \cdot e^{-\frac{x^2}{2 \cdot \sigma_t^2}} dx$$

calculating the difference between the power of the light falling on the left and right cells

$$i := 0..500 \quad Psdiff := Psl - Psr \quad \text{WRITEPRN}(\text{gap1}) := Psdiff$$

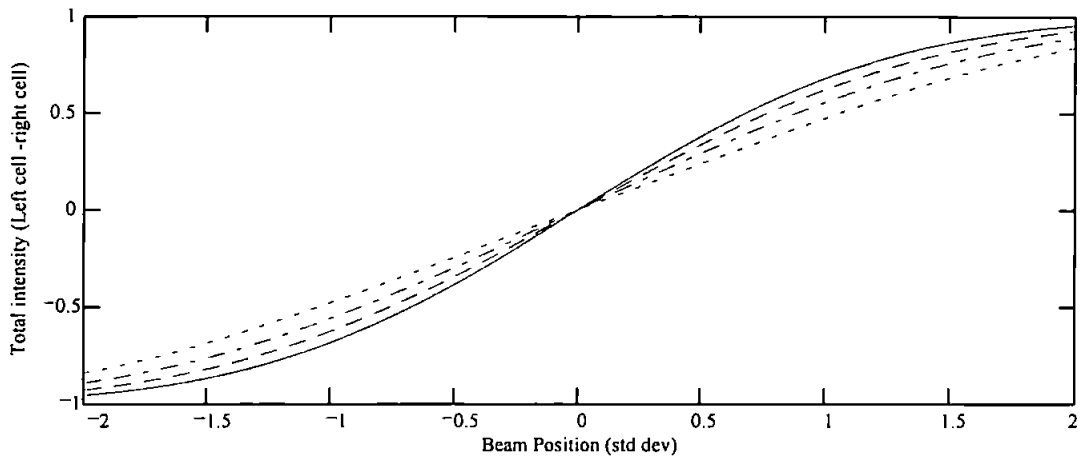
the MTF of the bicell system for a given gap size



loading stored MTF plots of varying gap sizes

```
a := READPRN(gap)      c := READPRN(gap2)
b := READPRN(gap1)     d := READPRN(gap3)
```

graph showing the MTF of the system for different gap sizes



6. Calculating values for a1 a2 and a3

set up sampling

$$N := 2048 \quad f_s := 200 \cdot 10^6 \quad i := 0..N-1 \quad I_i := i \quad t_i := \frac{I_i}{f_s}$$

definitions and functions

$$\text{LaserDev} := \frac{0.49 \cdot 10^{-3}}{4}$$

$$V_a := 617$$

$$\text{StdDevTime} := \frac{\text{LaserDev}}{V_a}$$

$$\text{StdDevPoints} := \text{StdDevTime} \cdot f_s$$

$$\text{gauss } x, \sigma := \frac{1}{\sqrt{2 \cdot \pi \cdot \sigma^2}} \cdot e^{-\frac{\frac{\text{LaserDev}}{\text{StdDevPoints}} \cdot x^2}{2 \cdot \sigma^2}}$$

create half the Gaussian

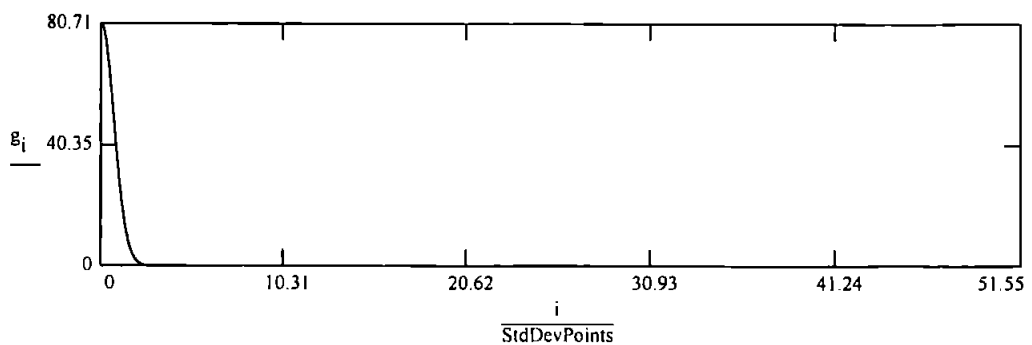
$$g := \sqrt{\text{gauss } 512 - 1, \frac{\text{LaserDev}}{2}} \quad j := 511..2047$$

$$g_{j-511} := g_j$$

take Fourier transform of the Gaussian

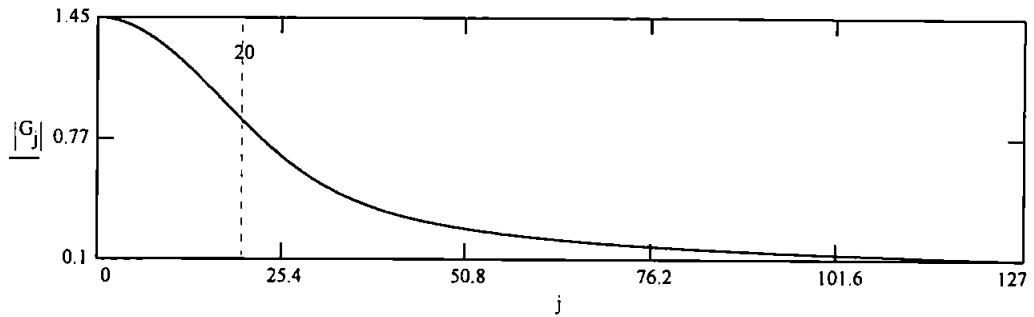
$$G := \text{FFT } \text{recenter } \vec{g}$$

plot of the Gaussian



plot of the Fourier transform of the gaussian

j := 0..127



summing the Fourier transform of the Gaussian minus the portion lost in the gap

$$G := \frac{G}{\sum G} \quad a := \sum_{b=21}^{1024} G_b$$

taking the real and imaginary parts of the above summation

$$I := \text{Im}(a) \quad R := \text{Re}(a)$$

calculating the values of the constants a1 a2 and a3 as given by the theory

$$a1 := 2 \cdot R^2 + I^2 \quad a2 := 2 \cdot R^2 - I^2 \quad a3 := -4 \cdot R \cdot I$$

$$a1 = 0.723 \quad a2 = -0.49 \quad a3 = 0.531$$

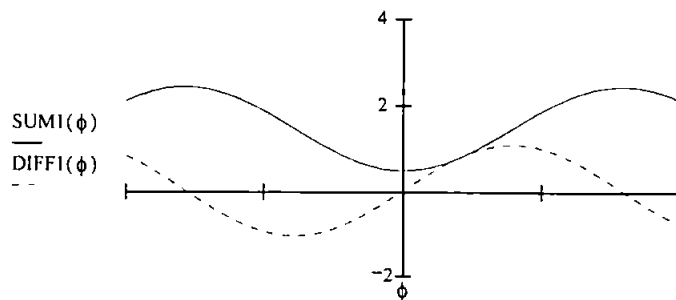
$$\phi := 0$$

plotting the sum and difference responses for phase varying instantaneous phase shifts

$$\phi := -4, -3.9..5$$

$$\text{SUM1}(\phi) := 2 \cdot (a1 + a2 \cdot \cos(\phi))$$

$$\text{DIFF1}(\phi) := 2 \cdot a3 \cdot \sin(\phi)$$



7. Sum and difference response to instantaneous phase shifts

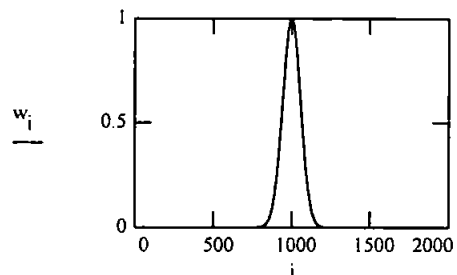
definitions and functions

$$\sigma := 0.1225 \cdot 10^{-3} \quad V_a := 617 \quad \sigma v := \frac{\sigma}{V_a} \quad dt := \frac{\sigma v}{40} \quad fs := \frac{1}{dt}$$

create Gaussian

$$i := 0..1999$$

$$w_i := \sqrt{\exp\left[-\frac{((i - 1000) \cdot dt)^2}{2 \cdot \sigma v^2}\right]}$$



create signals

carrier frequency

$$f := \frac{fs}{4}$$

frequency shift

$$fd := \frac{f \cdot 0}{200}$$

phase shift

$$q := 0..16$$

$$\phi_q := \frac{q \cdot \pi}{8} - \pi$$

$$j := 0..1999$$

$$y_{j,q} := \cos(2 \cdot \pi \cdot (f - fd) \cdot j \cdot dt)$$

$$j := 2000..3999$$

$$y_{j,q} := \cos[2 \cdot \pi \cdot (f - fd) \cdot j \cdot dt + \phi_q]$$

multiply signal by the Gaussian

$$i := 0..1999$$

$$s_{i,q} := w_i \cdot y_{i+999,q}$$

take the Fourier transform of the signal and Gaussian

$$S^{<q>} := \text{recenter CFFT } s^{<q>}$$

$$S^{<q>} := \text{mag } S^{<q>}$$

$$S := S^2$$

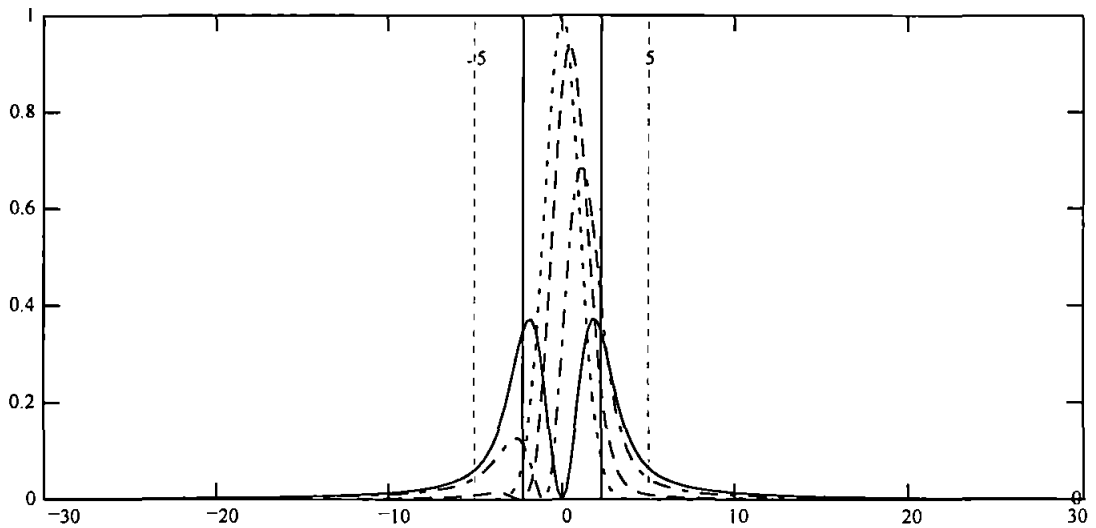
$$j := 1000..1999 \quad fr_j := \frac{fs \cdot (j - 1000)}{2000} \cdot 10^{-6} \quad p := \max(S)$$

$$b := 0..200 \quad S := \frac{\overrightarrow{S}}{p}$$

scaling the displacement axis

$$x\sigma_j := \frac{4 \cdot \pi \cdot \sigma \cdot fr_j}{V_a} \cdot 10^6 \quad m := x\sigma_{1499} \quad x\sigma := \overrightarrow{(x\sigma - m)}$$

graph showing the how the PSD of the beam is affected by the phase shifts



summing across the left and right cells, gapsize going from 2 to 10 stddevs

$$X := 1..5$$

$$LHS_{q,X} := \sum_{a=1300}^{1499-(X)} S_{a,q} \quad RHS_{q,X} := \sum_{a=1499+(X)}^{1701} S_{a,q}$$

$$\begin{aligned} \text{Sum} &:= LHS + RHS & \text{Diff} &:= RHS - LHS & D\text{matt}_q &:= \sin \phi_q \\ & & & & S\text{matt}_q &:= 1 - \cos \phi_q \end{aligned}$$

$$\begin{aligned} \text{Sum}^{<1>} &:= \text{Sum}^{<1>} - \max \text{Sum}^{<1>} & \text{Sum}^{<1>} &:= \frac{\text{Sum}^{<1>}}{\min \text{Sum}^{<1>}} & \text{Diff}^{<1>} &:= \frac{\text{Diff}^{<1>}}{\max \text{Diff}^{<1>}} \end{aligned}$$

$$\text{Sum}^{<2>} := \text{Sum}^{<2>} - \max \text{Sum}^{<2>}$$

$$\text{Sum}^{<2>} := \frac{\text{Sum}^{<2>}}{\min \text{Sum}^{<2>}}$$

$$\text{Diff}^{<2>} := \frac{\text{Diff}^{<2>}}{\max \text{Diff}^{<2>}}$$

$$\text{Sum}^{<3>} := \text{Sum}^{<3>} - \max \text{Sum}^{<3>}$$

$$\text{Sum}^{<3>} := \frac{\text{Sum}^{<3>}}{\min \text{Sum}^{<3>}}$$

$$\text{Diff}^{<3>} := \frac{\text{Diff}^{<3>}}{\max \text{Diff}^{<3>}}$$

$$\text{Sum}^{<4>} := \text{Sum}^{<4>} - \max \text{Sum}^{<4>}$$

$$\text{Sum}^{<4>} := \frac{\text{Sum}^{<4>}}{\min \text{Sum}^{<4>}}$$

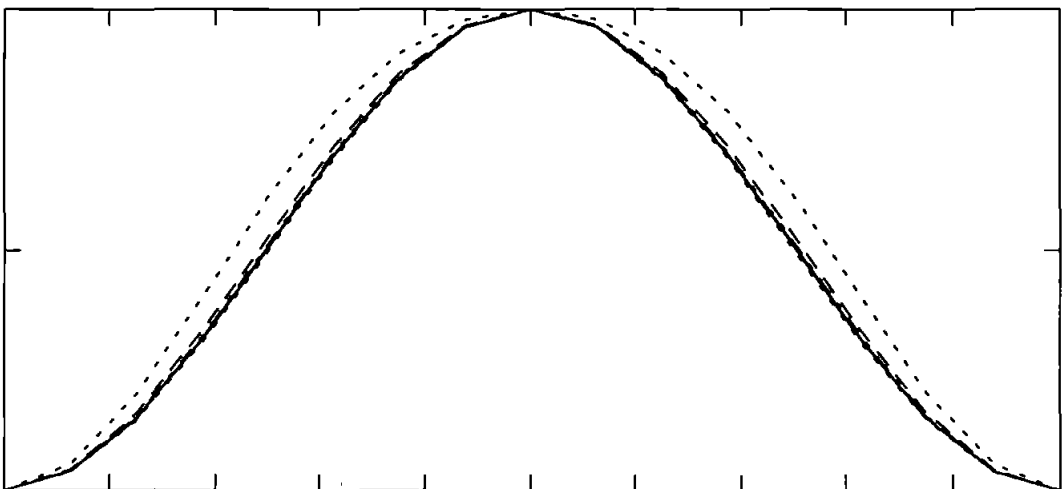
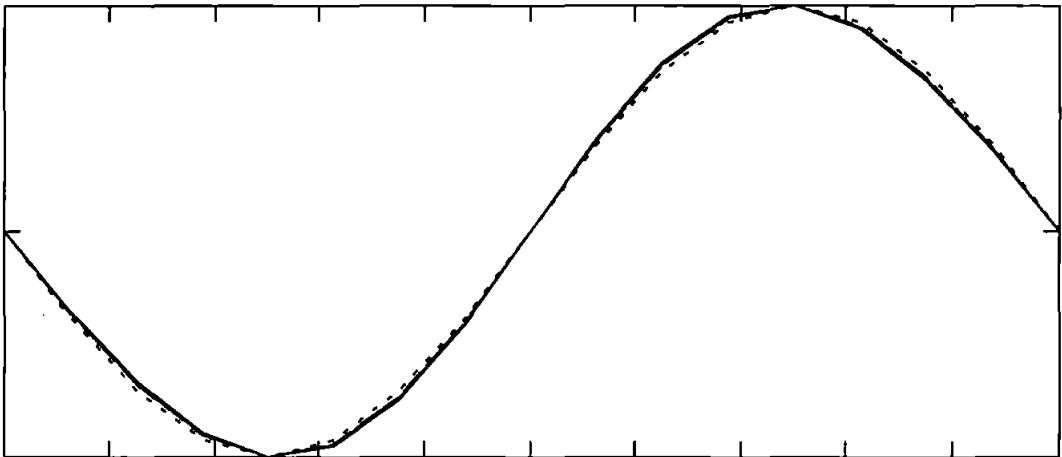
$$\text{Diff}^{<4>} := \frac{\text{Diff}^{<4>}}{\max \text{Diff}^{<4>}}$$

$$\text{Sum}^{<5>} := \text{Sum}^{<5>} - \max \text{Sum}^{<5>}$$

$$\text{Sum}^{<5>} := \frac{\text{Sum}^{<5>}}{\min \text{Sum}^{<5>}}$$

$$\text{Diff}^{<5>} := \frac{\text{Diff}^{<5>}}{\max \text{Diff}^{<5>}}$$

plots of the phase response of the difference and sum channels, for different gap sizes



APPENDIX D

Response to bandlimited gaussian noise.

In sections 7.4 and 8.4 signals were created to represent the type of bandlimited noise that would appear on the system. These signals were fed into the model in order to try to analyse how the system responded. The results from the system were then used to create the graphs of SNR and clipping levels. Presented in this section are six examples of the output from the sum and difference channels from the model and the experimental setup, for comparison. Both systems used exactly the same signal as the signal created for the model was downloaded onto the 2045 used to drive the AO cell.

The signals were all filtered by a 1 MHz bandpass filter with a centre frequency of 50 MHz. The signals in Figure D.1 and Figure D.2 had a carrier to noise ratio of 35 dB, Figure D.3 and Figure D.4 had a carrier to noise ratio of 25 dB, Figure D.5 and Figure D.6 had a carrier to noise ratio of 15 dB. The final two set of results also had carrier to noise ratios of 15 dB, this time the signals were also clipped. Figure D.7 and Figure D.8 were clipped at 80% of the maximum signal, and Figure 17 and Figure D.10 were clipped at 60%.

In all cases it obvious that the model and experimental signal compare very well, with little difference in their variances. These results backup the modeled noise analysis for FM and PM described in sections 7.4 and 8.4, for the clipping levels required and SNR loss of the system .

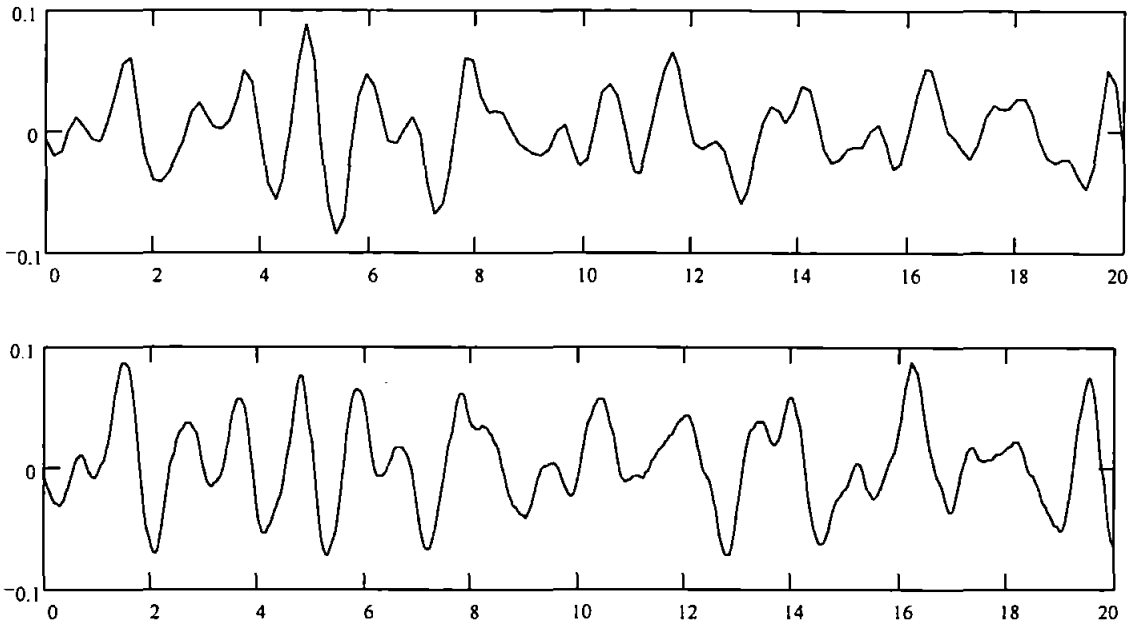


Figure D.1 Difference output for a 45 MHz carrier signal with CNR_{in} of 35 dB. Top trace : model. Bottom trace : experimental

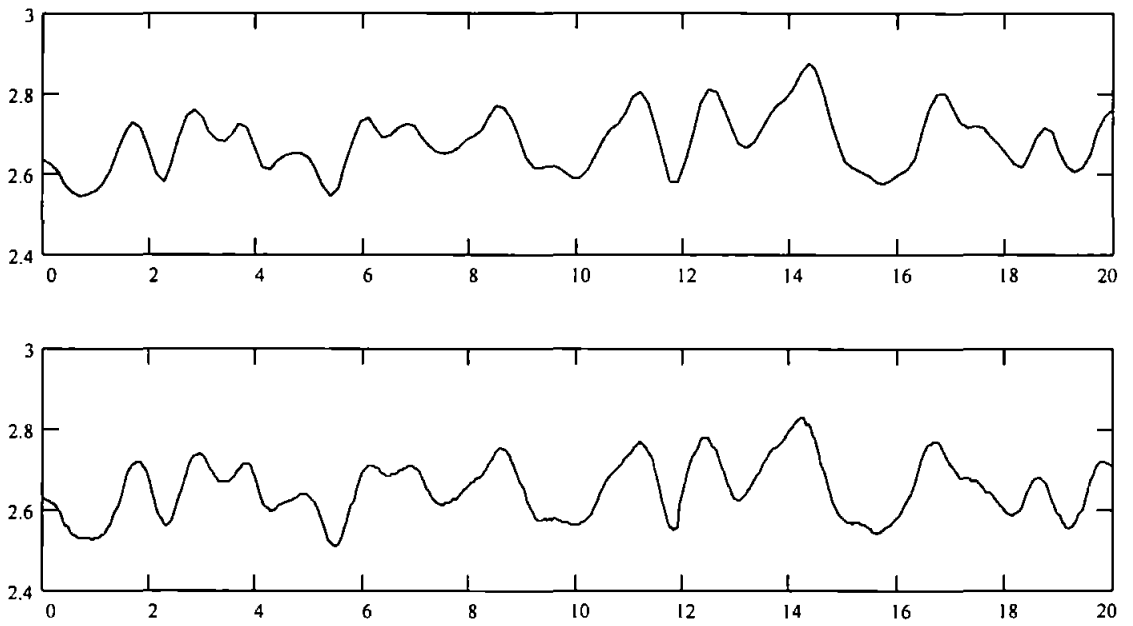


Figure D.2 Sum output for a 45 MHz carrier signal with CNR_{in} of 35 dB. Top trace : model. Bottom trace : experimental

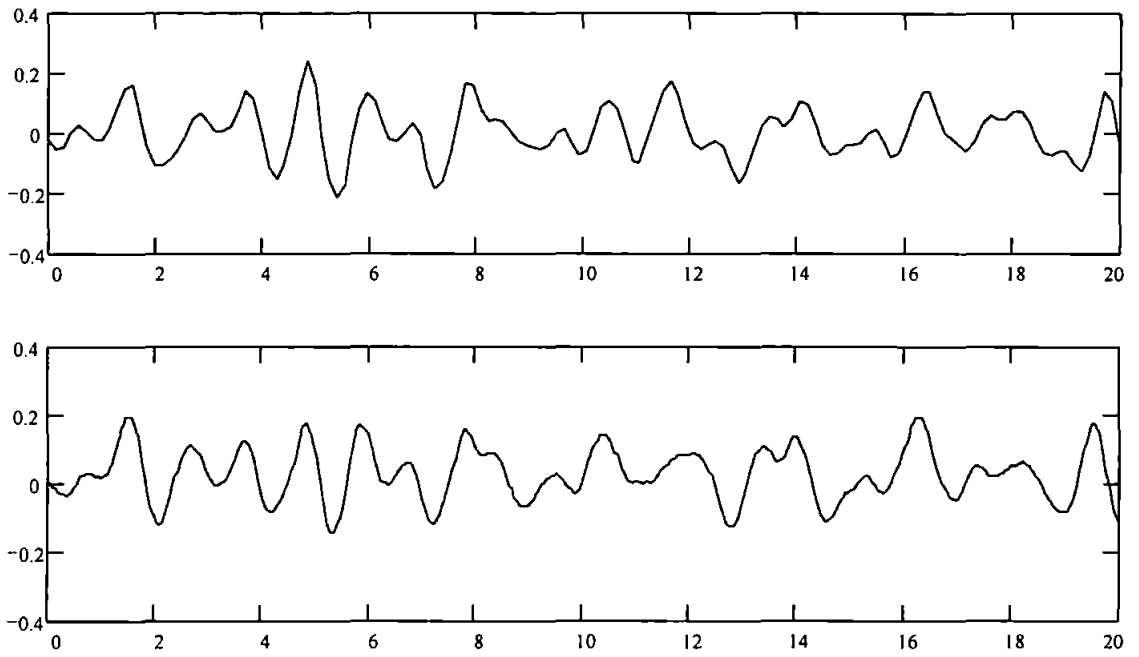


Figure D.3 Difference output for a 45 MHz carrier signal with CNR_{in} of 25 dB. Top trace : model. Bottom trace : experimental

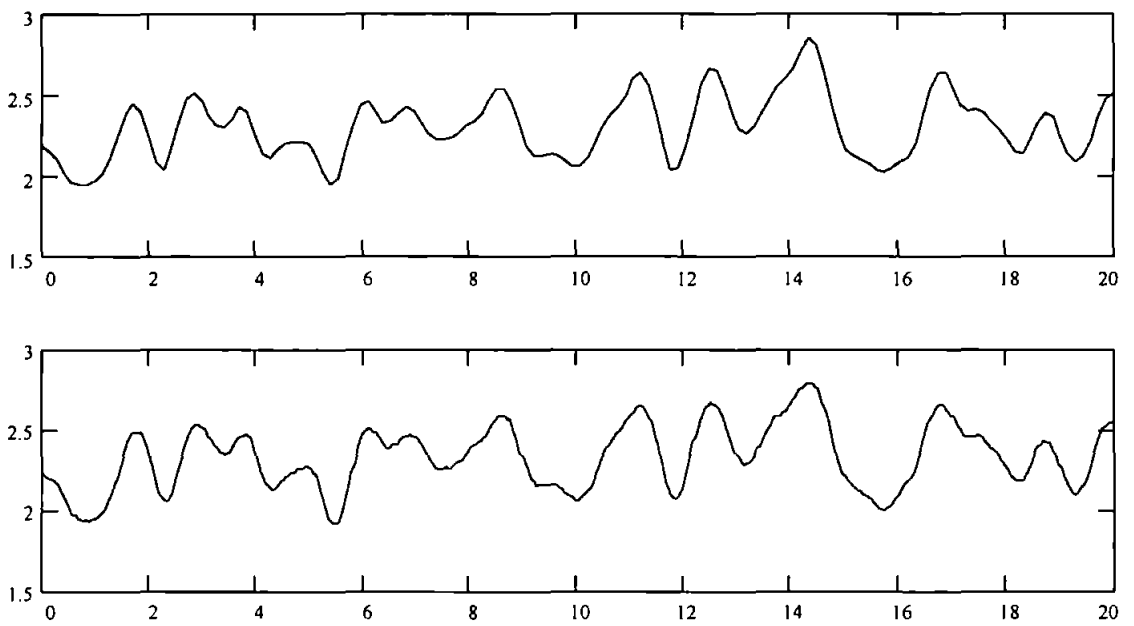


Figure D.4 Sum output for a 45 MHz carrier signal with CNR_{in} of 25 dB. Top trace : model. Bottom trace : experimental

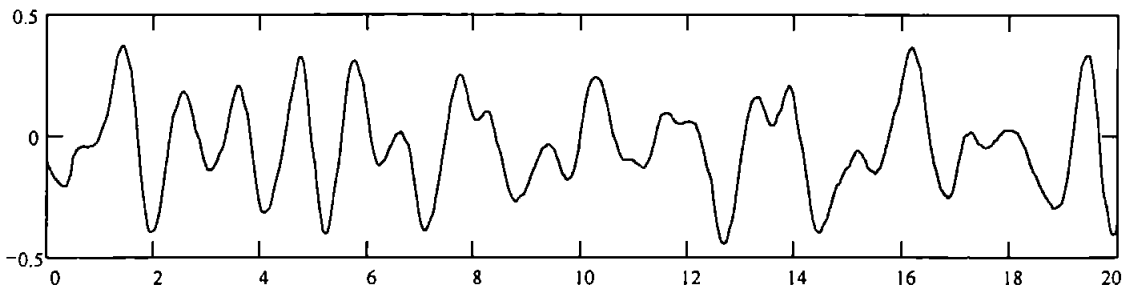
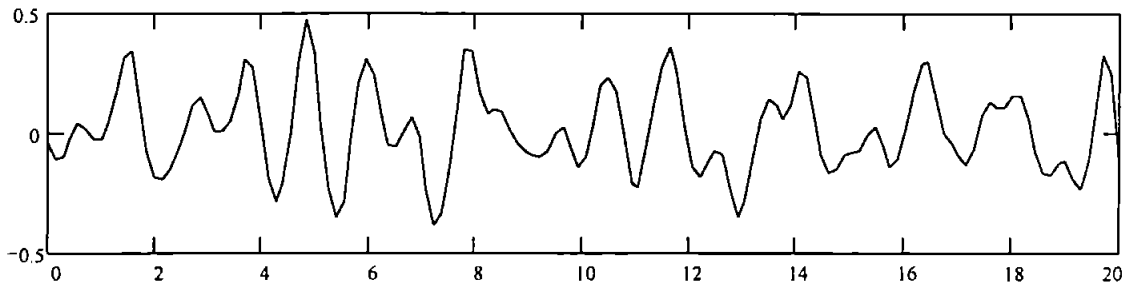


Figure D.5 Difference output for a 45 MHz carrier signal with CNR_{in} of 15 dB. Top trace : model. Bottom trace : experimental

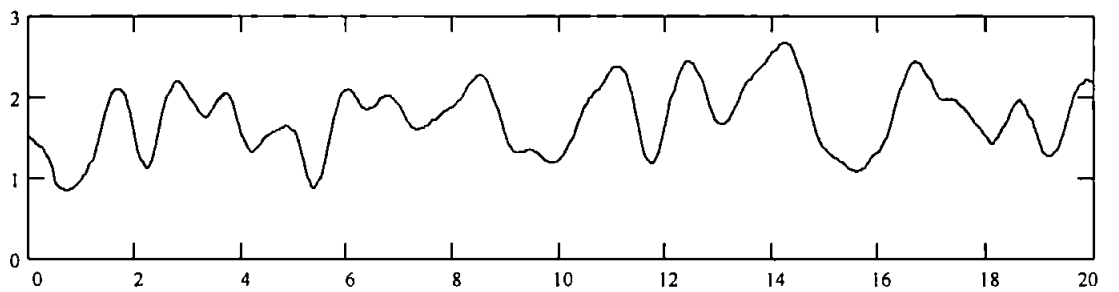
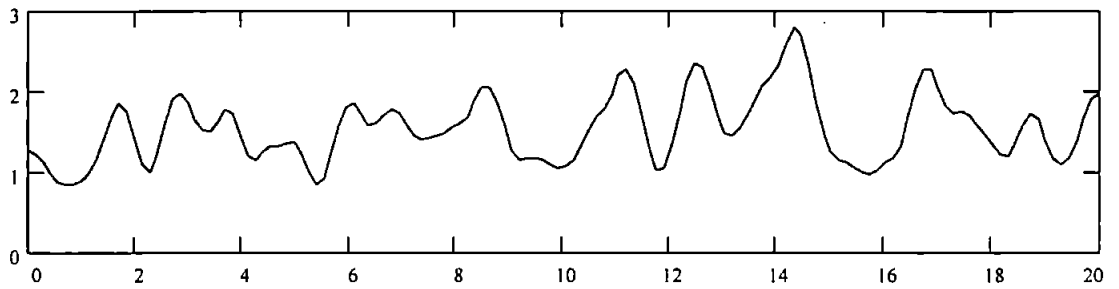


Figure D.6 Sum output for a 45 MHz carrier signal with CNR_{in} of 15 dB. Top trace : model. Bottom trace : experimental

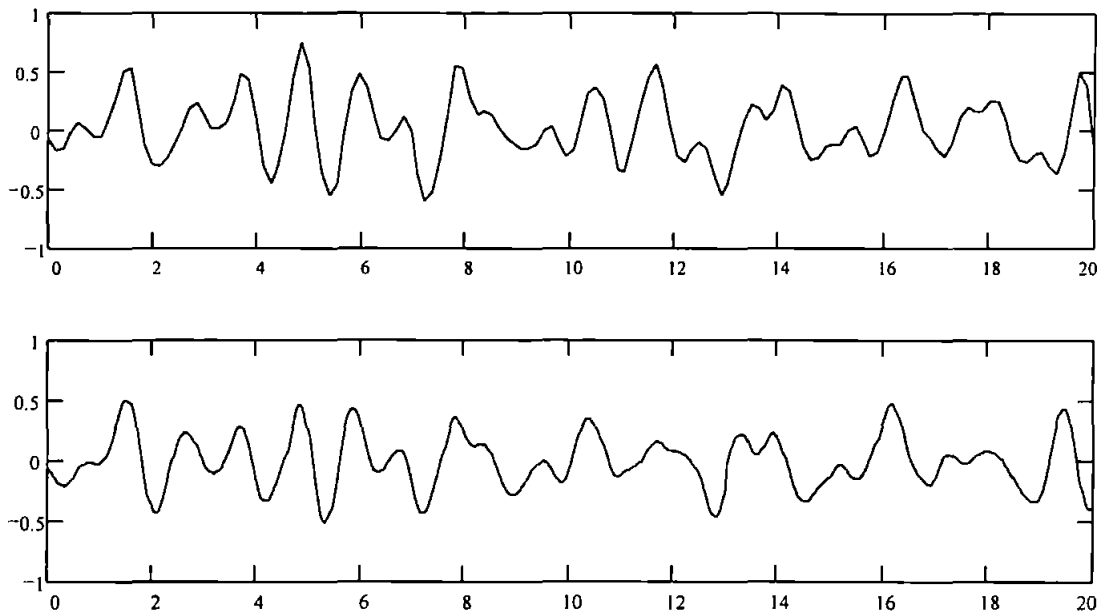


Figure D.7 Difference output for a 45 MHz carrier signal with CNR_{in} of 15 dB and 80% clip level. Top trace : model. Bottom trace : experimental

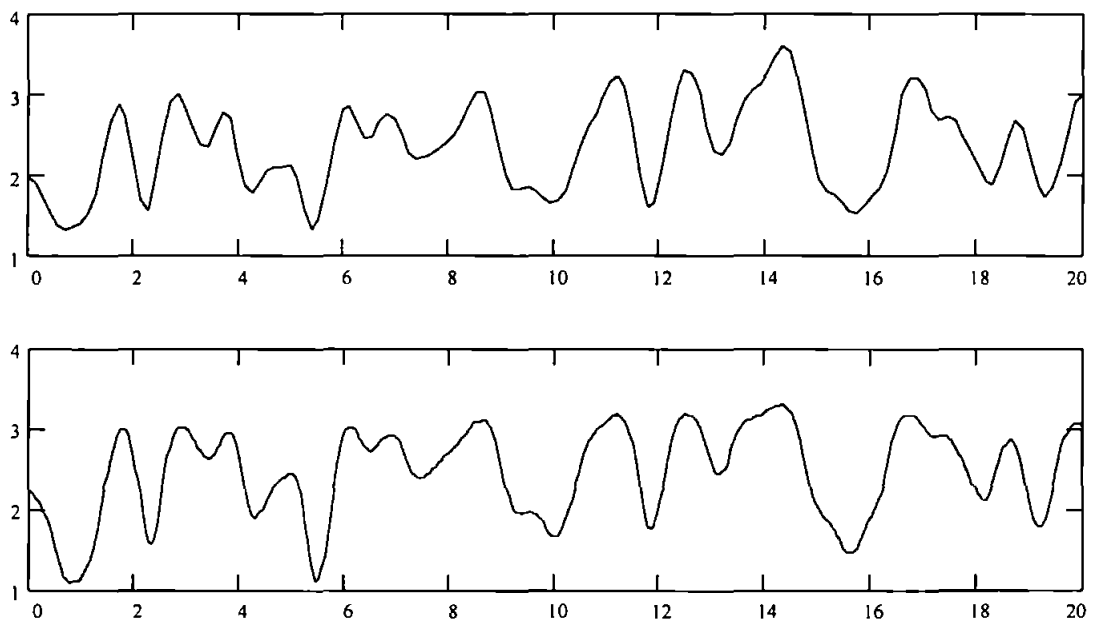


Figure D.8 Sum output for a 45 MHz carrier signal with CNR_{in} of 15 dB and 80% clip level. Top trace : model. Bottom trace : experimental

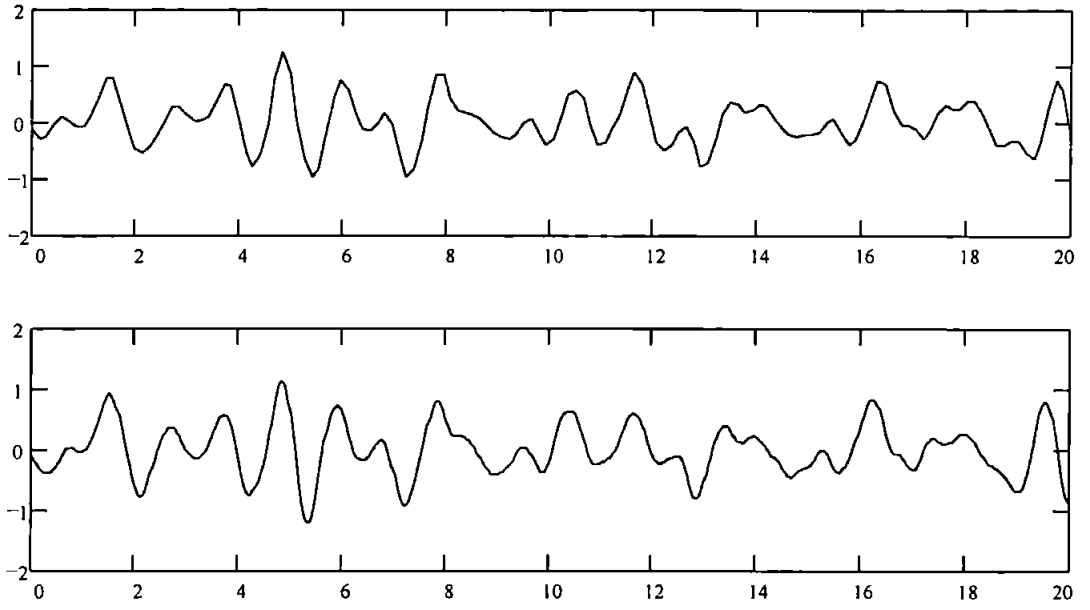


Figure 17 Difference output for a 45 MHz carrier signal with CNR_{in} of 15 dB and 60% clip level. Top trace : model. Bottom trace : experimental

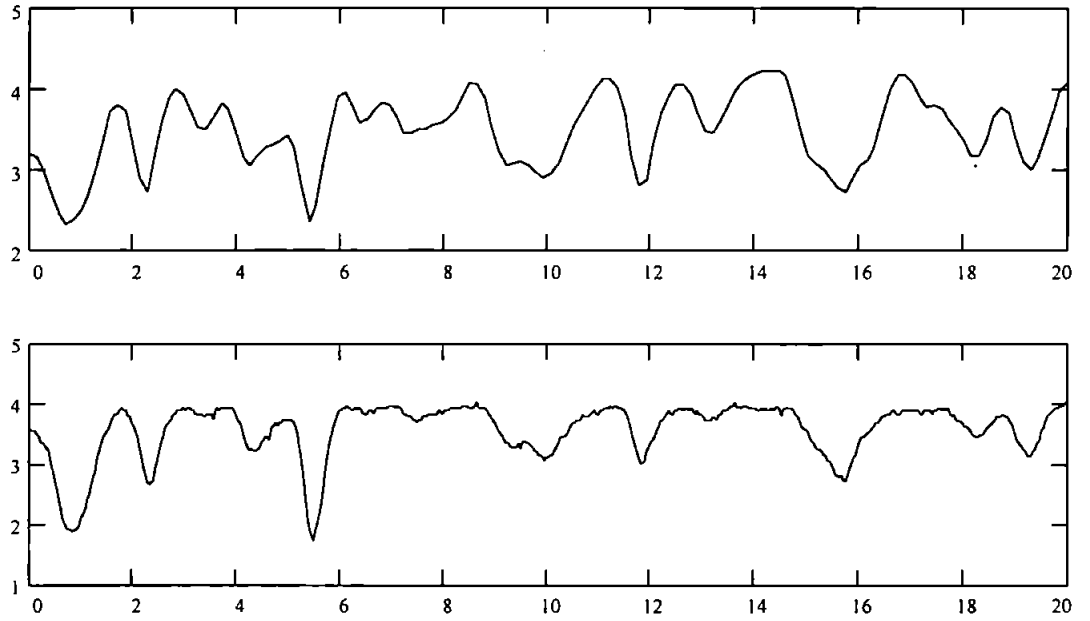


Figure D.10 Sum output for a 45 MHz carrier signal with CNR_{in} of 15 dB and 60% clip level. Top trace : model. Bottom trace : experimental

References

- [1]. Pieper R.J. and Poon T.C. 'An acousto-optic FM receiver demonstrating some principles of modern signal processing.' IEEE Transactions on Education, E-28, 1, 11-17, 1985.
- [2]. Brooks P. 'Acousto-Optic FM demodulation.' Thesis for PhD, University Of Southampton, 1994.
- [3]. Reeve C.D. and Houghton A.W. 'Optical method for detecting biphasic coded signals.' Electronics Lett, 27, 1379-1381, 1991
- [4]. Sremler, F.G. 'Introduction to Communication systems' Addison-Wesley 1990.
- [5]. Kenedy G. 'Electronic Communication Systems 2nd ed.' McGraw-Hill Auckland 1981.
- [6]. Stark, H. Tuteur, F.B. Anderson, J. B. 'Modern electrical communications analog, digital, and optical systems 2nd ed.' Prentice-Hall International Editions 1988.
- [7]. Song, B. Lee I.S. 'A digital FM demodulator for FM, TV and wireless' IEEE Trans. on circ. and sys. II : Vol 42, No. 12 December pp821-825 1995.
- [8]. Peebles, P.Z. 'Digital communication systems' Prentice-Hall International Editions 1987.
- [9]. Skolnik, M. 'Introduction to radar systems 2nd ed.' McGraw-Hill 1981.
- [10]. Department of Defense, Joint chiefs of staff, 'Dictionary of military and associated terms, JCS pub-1, September 1974.
- [11]. Davies, C. L. Hollands, P. 'Automatic Data processing for ESM' IEE Proc. Vol 129, pt F, No 3, p164, June 1982.
- [12]. Brillouin, L. 'Diffusion de la lumiere et des rayons x par un corps transparent homgene' Ann. Physique, Vol 17, p88 1922.
- [13]. Debeye, P. And Sears, F.W. 'On the scattering of light by supersonic waves' Proc. Nat. Acad. Sci. US Vol 18, p409 1932.
- [14]. Raman, C.V. and Nath, N.S. 'Diffraction of light by high frequency sound waves Parts I and II' Proc. Indian Acad. of Sci. Vol 2, October 1935, pp406-420, 'Diffraction of light by supersonic waves part III' Vol 3 Jan 1936, pp459-456, 'Generalised theory' Vol 4, pp222-242 1936.
- [15] Yariv, A 'Optical electronics' Holt Saunders, International editions, pp 392-394 1985

- [16]. Oliver, F.J.W. 'Bessel function of integer order' in Abramowitz, M. and Stegun, I.A. eds. 'Handbook of mathematical functions' Dover, New York, p721 1965.
- [17]. Korpel A 'Acousto-optics' Marcel Decker, New York 1988.
- [18]. Klein, W.R., Cook, B.D. 'Light diffraction by ultrasonic gratings' *Acoustica*, Vol 15, pp67-74 1965.
- [19]. Vanderlugt, A. 'Optical signal processing' Wiley-Interscience 1992.
- [20]. Young, E.H. Yao, S-K. 'Design considerations for acousto-optic devices' *Proc. IEEE*, Vol. 69, p54 1981.
- [21]. Brooks, P. Reeve, C.D. 'Limitations in acousto-optic FM demodulators' *IEE Proc.-Optoelectron.*, Vol. 142, No. 3, June 1995. Pp 149-156.
- [22]. Stearns, S. David, Ruth, D. 'Signal processing algorithms' Prentice Hall,
- [23]. VanFleck, J.H. Middleton, D. 'The spectrum of clipped noise' *Proc. IEEE*, Vol. 54, No 1, pp2-19 1966.
- [24]. Xu, J. Stroud, R. 'Acousto-Optic Devices Principles, design and applications' Wiley-Interscience 1992.

BIBLIOGRAPHY

Nathenson F. E. 'Radar design principles' McGraw Hill 1991.

Killen H. B. 'Digital communication with fibre optics and satellite applications' Prentice Hall 1988.

Peebles P. Z. 'Probability, random variables, and random signal principles' McGraw Hill 1993.

Wiley R.G. 'Electronic Intellegence: The Interception of radar signals' Artech House 1985

Edde B. 'Radar principles, technology, applications' Prentice Hall 1993

Young P. 'Electronic Communication Techniques', Macmillan 1994.

OPTICAL TECHNIQUE FOR IDENTIFICATION AND DECODING OF DIGITALLY MODULATED SIGNALS IN SURVEILLANCE RECEIVERS

M Hicks and C D Reeve

University of Plymouth, UK

ABSTRACT

An acousto-optic technique for identifying and decoding various unknown types of digitally modulated signals is described. The performance of the system, which uses a bicell photodiode detector assembly, is modelled. It is shown that the output of the system, which consists of the sum and difference of the signals from the two bicell elements, is different and easily identifiable for each of the following modulation types: BPSK, QPSK, offset-keyed QPSK, differential QPSK, continuous-phase FSK (including MSK) and non continuous-phase FSK. Preliminary experimental results from an optical breadboard system are presented which are in good agreement with the modelled results.

INTRODUCTION

There is a variety of techniques currently in use for digital modulation of communications signals. These fall under the broad headings of amplitude, frequency and phase shift keying (ASK, FSK and PSK) but many variations exist, such as phase reversal keying (PRK), quaternary phase shift keying (QPSK), offset-keyed QPSK and minimum shift keying (MSK). These techniques are used, not only in general communications applications but also in spread spectrum systems; similar techniques are also used in low probability of intercept radar. A co-operating receiver will know the details of the type of modulation being employed and will have the appropriate matched filter and demodulation systems. A general purpose surveillance receiver, on the other hand, will have no a priori knowledge of the signal characteristics. The requirements for such a receiver would be threefold: (i) to detect the presence of a signal and measure its carrier frequency, (ii) to identify the type of modulation being used, and (iii) to demodulate/decode the signal. The first of these requirements can be achieved using scanning superhet or channelised receivers but automatic techniques for (ii) and (iii) are more difficult. We present a simple optical technique for identifying different types of digital modulation that also effectively demodulates the signal and enables decoding. We concentrate on FSK and PSK modulation and their variations. ASK is obviously very easy to identify, by this method and others, and is therefore rarely used for the types of transmission that a surveillance receiver would be interested in. In PSK and

FSK signals the amplitude is constant so any receiver that detects only variations in the power of the signals will see no modulation. It is only when the signals are examined in the frequency domain that the modulation becomes evident. A convenient way of monitoring changes in the frequency domain is to use an acousto-optic (AO) device to spatially modulate a laser beam with the signal and then to use the Fourier transform properties of a lens. Such a system will operate in real time at carrier frequencies from around 20 MHz to several GHz, depending on the type of AO cell used. The power spectrum is examined using a bicell detector; that is two photodiodes separated by a small gap. The output from the two elements of the bicell detector show how the power in the signal varies within two frequency bands defined by the size and position of the elements. Comparison of the sum and difference of the signals from the two detectors enables the different types of modulation to be identified. We present results from computer simulations of the system, showing how the spectrum of the signal changes as the frequency and phase shifts pass through the laser beam window in the AO cell and how the sum and difference of the outputs from the bicell detector are different for the different modulation types. Preliminary results from a practical system are presented that are in good agreement with the simulation.

SYSTEM ARCHITECTURE

A schematic diagram of the system is shown in Figure 1. Similar systems, using only a single photodiode detector, have been described by Pieper and Poon [1] and Brooks and Reeve [2] for FM demodulation and by Reeve and Houghton [3] for demodulation of BPSK signals. The detector assembly employed in this case is a bicell device (Figure 2) consisting of two photodiodes separated by a narrow gap of width g . The signal under investigation is applied to the AO cell. The properties of AO cells are well known; a good review is given by Korpel [4]. A narrow laser beam passing through the cell is deflected through an angle proportional to the signal carrier frequency. In this first order diffracted light the beam is spatially modulated by the signal instantaneously in that part of the cell that is illuminated by the laser beam. The spatial distribution of light amplitude in the focal plane of the lens is therefore proportional to the Fourier transform of that part of the signal within the window formed by the laser beam passing through the AO cell. Since the photodiodes respond to the light intensity, their output will be proportional to the power spectral density of the signal integrated over the illuminated part of the

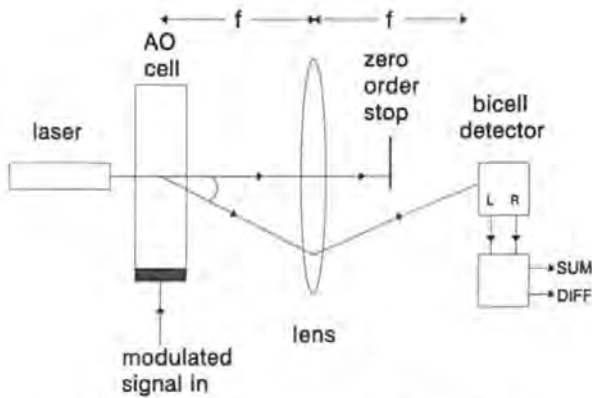


Figure 1. The acousto-optic demodulator

detector. The system therefore monitors changes in the power in the windowed signal over two frequency bands defined by the size and position of the bicell elements. The signal from the left and right elements of the bicell detector are:

$$s_L = K \int_{-\infty}^{\frac{g}{2}} |F(x)|^2 dx \quad \text{and} \quad s_R = K \int_{\frac{g}{2}}^{\infty} |F(x)|^2 dx \quad (1)$$

where K is a constant and $F(x)$ is the spatial light distribution in the focal plane of the lens, which is proportional to the Fourier transform of the windowed signal. These equations do not lend themselves easily to an analytic solution; the response of the system has therefore been studied using a computer model.

MODELLING RESULTS

The model was written in such a way that particular system parameters such as the focal length of the lens, the laser wavelength, the dimensions of the bicell detector and the AO cell parameters could be easily changed to study different arrangements. It is assumed that the laser beam intensity profile is Gaussian (corresponding to a laser with a single TEM_{00} transverse mode) with a standard deviation σ_0 in the x -direction i.e. perpendicular to the bicell gap. The standard deviation in the y -direction may or may not be the same but since we integrate over the complete range of y values its precise value is not important. If the signal within this Gaussian window in the AO cell is a constant amplitude tone of frequency f , it may be shown that the intensity profile of the light in the focal plane of the lens is also Gaussian with standard deviation σ_t given by

$$\sigma_t = \frac{\lambda l_f}{4\pi\sigma_0} \quad (2)$$

where λ is the wavelength of the light and l_f is the focal length of the lens and that the angle θ through which the first order diffracted light is deflected is given by

$$\sin\theta \approx \theta = \frac{\lambda}{V_a} f \quad (3)$$

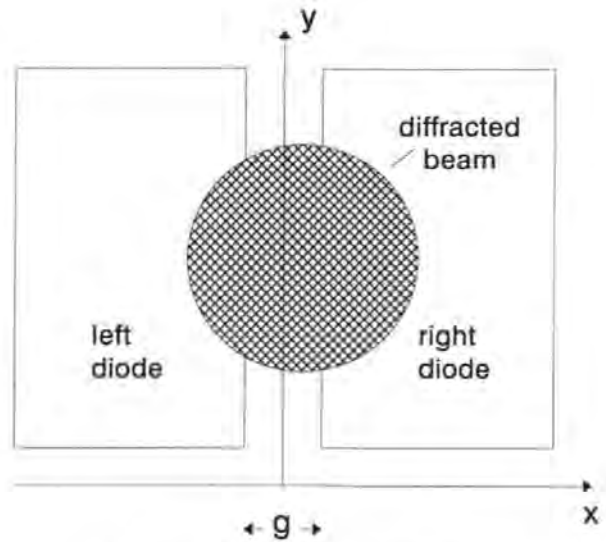


Figure 2. The bicell detector assembly

where V_a is the acoustic velocity in the AO cell. The displacement δx of the diffracted spot at the detector due to a change in frequency δf is therefore

$$\delta x = l_f \delta\theta = \frac{\lambda l_f}{V_a} \delta f \quad (4)$$

Dividing eqn (3) by eqn (1) we obtain

$$\frac{\delta x}{\sigma_t} = \frac{4\pi\sigma_0}{V_a} \delta f \quad (5)$$

This ratio, which expresses lateral deviation of the diffracted spot at the detector, due to a given change in frequency, in terms of the spot size, is independent of the laser wavelength and the focal length of the lens. It is convenient therefore to express all dimensions at the detector as a multiple of σ_t .

The signal applied to the AO cell is assumed to be of constant amplitude with changes of frequency and/or phase occurring at unspecified intervals; the time window defined by the laser beam in the AO cell is assumed to be sufficiently short that only one change in frequency or phase is within the window at any given time. The laser beam width is usually quoted as the distance between the $1/e^2$ points on the Gaussian profile, which is equivalent to $4\sigma_0$. In fact the beam is not truncated at the $1/e^2$ points. In the model the laser beam is represented as having a width of $6\sigma_0$, which yields results which are virtually indistinguishable from those obtained assuming an infinitely wide Gaussian. We have calculated how the power spectral density of the windowed signal varies as the transition in frequency and/or phase moves through the window. These are shown in Figure 3. Five positions of the transition have been used: (i) $x = -3\sigma_0$ i.e. as it enters the window - solid line, (ii) $x = -1.5\sigma_0$ - dotted line, (iii) $x = 0$ i.e. at the centre of the window - dashed line, (iv) $x = 1.5\sigma_0$ - dot-dash line, and (v) $x = 3\sigma_0$ i.e. as it leaves the window - solid line. In the cases where only the phase is changing only three of these will be visible

since (i) and (ii) are identical to (iv) and (v). The horizontal axis is distance at the detector as a multiple of σ_T . The vertical lines denote the edges of the bicell elements assuming a gap of $3\sigma_T$. It is assumed that, for signals where only the phase changes, the centre line of the bicell gap corresponds to the carrier frequency; for FSK signals the centre line corresponds to the centre frequency f_0 , so that the frequencies transmitted are $f_0 \pm \delta f$. Figure 3 shows results for: a) a phase shift of π radians, b) a phase shift of $+\pi/2$ radians (the result for a $-\pi/2$ radian shift is a mirror image about $d = 0$), c) a frequency shift with no phase discontinuity at the frequency transition, d) a frequency shift with an arbitrary phase shift at the frequency transition.

Figure 4 shows the modelling results for the sum and difference of the outputs from the two bicell elements using a bicell gap of $3\sigma_T$ for various types of signal. In Figure 4(a) the output for a BPSK signal with a phase shift of π radians shows that the difference remains essentially constant (zero) while the sum reaches a maximum when the phase shift is at the centre of the window. The reason for this behaviour is readily understood by studying Figure 3(a). Before the phase shift enters the window most of the light energy is concentrated in the gap; as the phase shift traverses the window the power spectral density broadens and dips at the centre shifting more light onto the bicell elements increasing the sum; however since the power spectral density remains symmetrical about the centre the difference is always zero. Figure 4(b) shows the response for a signal with phase shifts of $\pm\pi/2$. In this case the sum reaches a maximum when the phase shift is at the centre of the window but now the difference goes either positive or negative depending on the sign of the phase change because the power spectral density does not remain symmetrical. The response for a continuous phase FSK (or MSK) signal is shown in Figure 4(c); in this case the sum is essentially constant while the difference changes by an amount proportional to the frequency shift. The output for an FSK signal in which the frequency change is accompanied by an arbitrary phase shift is shown in Figure 4(d); the response is basically the same as for the previous case except that a spike occurs in both the sum and difference signals proportional to the magnitude/sign of the phase shift.

EXPERIMENTAL RESULTS

We present some preliminary results from a breadboard system to demonstrate their agreement with the modelled results shown in the previous section. The system consisted of: a frequency stabilised 1 mW Helium Neon laser with wavelength 633 nm and $1/e^2$ beamwidth 0.49 mm; a tellurium dioxide slow shear mode AO cell with time aperture 50 μ s and acoustic velocity 617 m/s; a 50 mm focal length biconvex lens; a

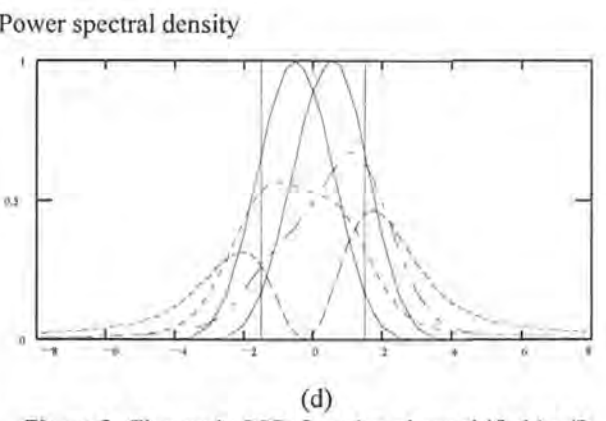
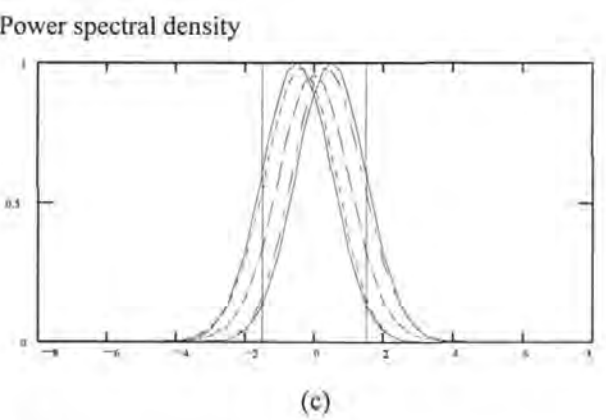
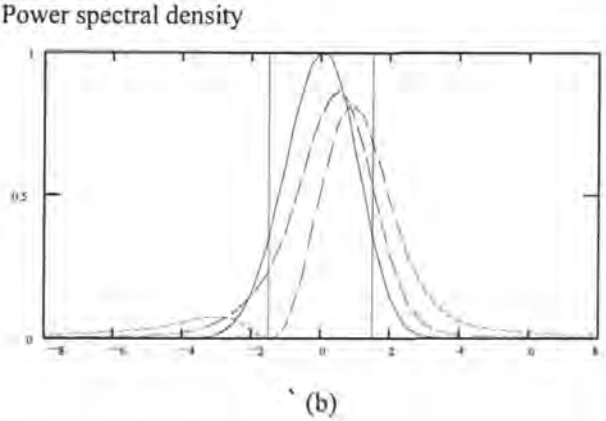
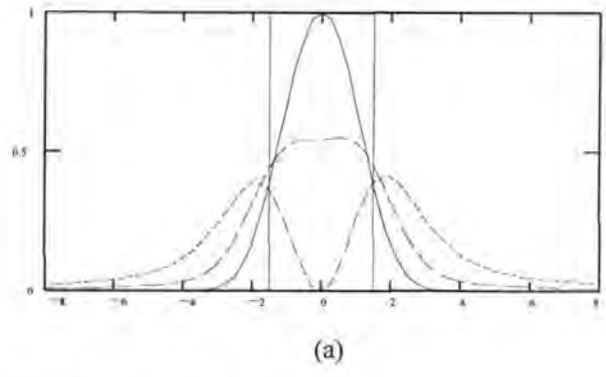


Figure 3. Change in PSD for: a) π phase shift, b) $\pi/2$ phase shift, c) CP-FSK, d) FSK with phase shift. Horizontal scale: displacement at bicell in units of σ_T

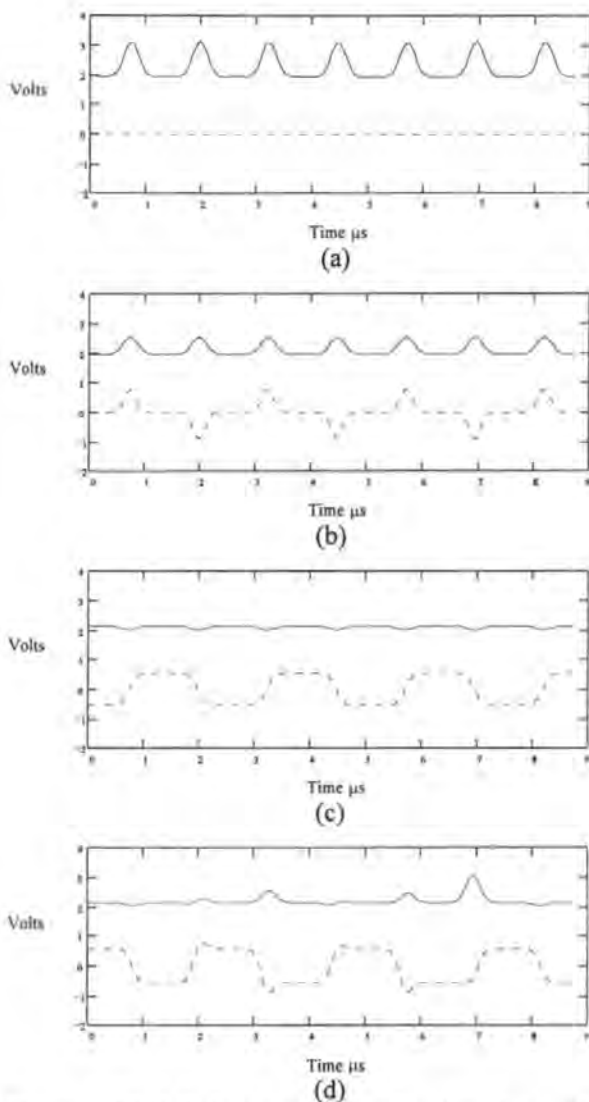


Figure 4. Modelled system output for a) π phase shift, b) $\pm\pi/2$ phase shift, c) continuous phase FSK, d) FSK with arbitrary phase shifts.

detector consisting of a bicell photodiode with a gap of $85\ \mu\text{m}$ with each element connected via trans-impedance and buffer amplifiers to a waveform analyser, which performs the sum and difference operations. Using eqn (1) the value of σ_t was $21\ \mu\text{m}$, therefore the bicell gap is close to $4\sigma_t$. Signals for analysis were generated using a programmable arbitrary waveform synthesiser so that precise frequencies and phase shifts could be obtained. The output for a signal containing phase shifts of $\pm\pi/2$ radians is shown in Figure 5(a). Figure 5(b) shows the output from a continuous phase FSK signal. In each case the upper trace is the sum and the lower trace is the difference of the bicell outputs. Clearly there is very close agreement between the results obtained from the model and those from the breadboard system. Results for other signals agree equally well.

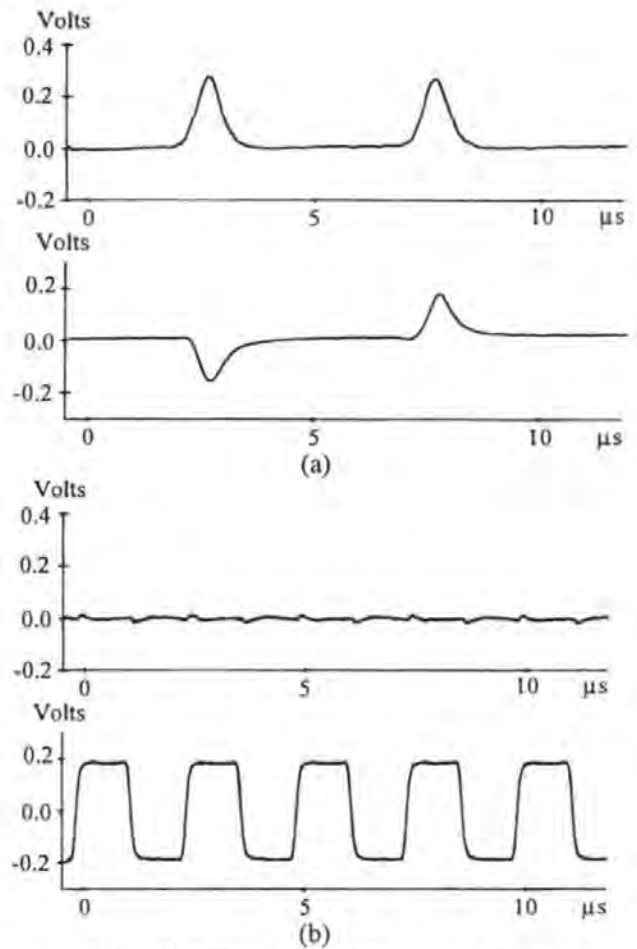


Figure 5. Experimental system output for a) $\pm\pi/2$ phase shift, b) continuous phase FSK

DISCUSSION

The modelled and experimental results show that the system output for each type of signal has a distinctive signature. Signals with a phase change of π radians cause a spike on the sum channel with the difference remaining constant; signals with phase changes of $\pm\pi/2$ cause equal sized spikes on the sum channels and equal but opposite polarity spikes on the difference. FSK signals in which there is no phase discontinuity at the frequency transition give a change in the difference channel proportional to the frequency shift with no change in the sum. FSK signals with an arbitrary phase shift at the frequency transition give the same result but with additional spikes due to the phase shifts; the size of the spike on the sum channel is proportional to the phase shift and the polarity of the spike on the difference gives its sign. Signals with phase shifts of $\pm\pi/4$ or $\pm3\pi/4$ (not illustrated) can be shown to give spikes on the sum channel proportional to the phase shift and the polarity of the spike on the difference again gives its sign. Using these results it is possible to distinguish between the following types of digital modulation.

(i) BPSK. Assuming that the two phase states are 0 and π radians this is characterised by a constant difference channel with a spike on the sum channel at each phase shift.

(ii) QPSK. The four phase states are 0, $\pm\pi/2$ and π radians; therefore the possible phase shifts are also 0, $\pm\pi/2$ and π radians. A spike on the sum channel indicates the presence of a phase shift and the corresponding state of the difference channel indicates the nature of the change. The occurrence of all three phase shifts identifies the type of modulation.

(iii) Offset-keyed QPSK. Here the only possible phase shifts are $\pm\pi/2$ radians. The absence of the π radians phase shifts identifies the type of modulation.

(iv) FSK. FSK signals are characterised by a shift in level on the difference channel while the sum remains constant. Unlike the case for PSK signals where the output is a spike which only occurs while the phase shift is within the laser window, the level change persists for as long as the frequency remains constant. If there is no phase discontinuity when the frequency changes, as in continuous phase FSK or MSK, then only the level change is observed. A phase discontinuity at the frequency change results in spikes on both the sum and difference channels. Thus not only is the system capable of identifying the presence of FSK signals, it can also indicate the type of FSK modulation being used. The magnitude of the level change, and hence the detectability of the signal, is proportional to the change in frequency. For an MSK signal the frequency change is $2\delta f = 1/2T_b$, where T_b is the interval between frequency shifts. In the experimental example shown T_b was 5 μ s so that the frequency shift was 100 kHz. Since it has been shown [2] that this type of system is capable of detecting frequency changes of the order of 100 Hz, detectability is not considered to be a problem.

(v) Differential QPSK. Four phase shifts are possible namely $\pm\pi/4$ and $\pm3\pi/4$. In all the previous cases identification has depended upon merely detecting a change from zero in either or both channels. For differential QPSK it is necessary to distinguish between two different level spikes in the sum channel corresponding to phase shifts of $\pi/4$ or $3\pi/4$. Although not difficult this raises the complexity of the detection system and will tend to increase the signal to noise ratio required for reliable detection.

CONCLUSIONS

It is concluded that using the optical system described, together with some simple detection and logic circuits, it is possible to identify and decode a number of types of digitally modulated signals, without any a priori knowledge apart from their carrier frequency. The ability of the system to handle both frequency and phase modulated signals is particularly valuable. Although apparently very simple, the system performs functions

that would be difficult to achieve electronically in real time. In summary these functions are as follows.

(i) The signal propagating through the AO cell is windowed by the Gaussian profile of the laser beam. The time window depends upon the laser beamwidth and the acoustic velocity in the AO cell; by focusing the beam into the AO cell, time windows down to a few nanoseconds are achievable. This places an upper limit on the data rates that can be processed since only one transition may occur within the window. (ii) The light distribution at the detector is proportional to the instantaneous Fourier transform of the windowed signal. (iii) The response of each element of the detector is proportional to the instantaneous power in the windowed signal over frequency bands defined by the size and position of the elements. In effect the system responds in real time to variations in the spectral content of the signal as the frequency and/or phase shifts propagate through the laser beam window.

(iv) Taking the sum and difference of the signals from the bicell elements results in distinctive signatures for the different types of modulation. AO cells are currently available for operation at carrier frequencies from around 30 MHz (tellurium dioxide) to 3 GHz (gallium phosphide). Acoustic velocities vary from 617 m/s for tellurium dioxide to 6320 m/s for gallium phosphide. To perform a similar operation at the lower end of this frequency range might be possible using DSP techniques; at the upper end it would not. The properties of AO cells allow the system to be tuned over an octave bandwidth merely by moving the detector.

REFERENCES

1. Pieper R J and Poon T-C, 1985, "An acousto-optic FM receiver demonstrating some principles of modern signal processing." *IEEE Trans*, E-28, 1, 11-17
2. Brooks and Reeve C D, 1995, "Limitations in acousto-optic FM Demodulators" *IEE Proc-J*, in press
3. Reeve C D. and A W Houghton, 1991, "Optical method for detecting biphase coded signals." *Electronics Lett*, 27, 1379-1381
4. Korpel A, 1981, "Acousto-optics - a review of fundamentals." *Proc. IEEE*, 69, 48-53

ACKNOWLEDGEMENT

This work was supported by a research agreement with the Defence Research Agency.

Copyright © HMSO, London, 1995

An acousto-optic system for frequency and phase demodulation

M Hicks and C D Reeve

School of Electronic Communication and Electrical Engineering
University of Plymouth, Drake Circus, Plymouth, PL4 8AA, UK

ABSTRACT

An acousto-optic technique for identifying and decoding various unknown types of digitally modulated signals is described. The performance of the system, which uses a bicell photodiode detector assembly, is modelled. It is shown that the output of the system, which consists of the sum and difference of the signals from the two bicell elements, is different and easily identifiable for each of the following modulation types: BPSK, QPSK, offset-keyed QPSK, differential QPSK, continuous-phase FSK (including MSK) and non continuous-phase FSK. Preliminary experimental results from an optical breadboard system are presented which are in good agreement with the modelled results.

1. INTRODUCTION

There is a variety of techniques currently in use for digital modulation of communications signals. These fall under the broad headings of amplitude, frequency and phase shift keying (ASK, FSK and PSK) but many variations exist, such as phase reversal keying (PRK), quaternary phase shift keying (QPSK), offset-keyed QPSK and minimum shift keying (MSK). These techniques are used, not only in general communications applications but also in spread spectrum systems; similar techniques are also used in low probability of intercept radar. A co-operating receiver will know the details of the type of modulation being employed and will have the appropriate matched filter and demodulation systems. A general purpose surveillance receiver, on the other hand, will have no a priori knowledge of the signal characteristics. The requirements for such a receiver would be threefold: (i) to detect the presence of a signal and measure its carrier frequency, (ii) to identify the type of modulation being used, and (iii) to demodulate/decode the signal. The first of these requirements can be achieved using scanning superhet or channelised receivers but automatic techniques for (ii) and (iii) are more difficult. We present a simple optical technique for identifying different types of digital modulation that also effectively demodulates the signal and enables decoding. We concentrate on FSK and PSK modulation and their variations. ASK is obviously very easy to identify, by this method and others, and is therefore rarely used for the types of transmission that a surveillance receiver would be interested in. In PSK and FSK signals the amplitude is constant so any receiver that detects only variations in the power of the signals will see no modulation. It is only when the signals are examined in the frequency domain that the modulation becomes evident. A convenient way of monitoring changes in the frequency domain is to use an acousto-optic (AO) device to spatially modulate a laser beam with the signal and then to use the Fourier transform properties of a lens. Such a system will operate in real time at carrier frequencies from around 20 MHz to several GHz, depending on the type of AO cell used. The power spectrum is examined using a bicell detector; that is two photodiodes separated by a small gap. The output from the two elements of the bicell detector show how the power in the signal varies within two frequency bands defined by the size and position of the elements. Comparison of the sum and difference of the signals from the two detectors enables the different types of modulation to be identified. We present results from computer simulations of the system, showing how the spectrum of the signal changes as the frequency and phase shifts pass through the laser beam window in the AO cell and how the sum and difference of the outputs from the bicell detector are different for the different modulation types. Preliminary results from a practical system are presented that are in good agreement with the simulation.

SYSTEM ARCHITECTURE

A schematic diagram of the system is shown in Figure 1. Similar systems, using only a single photodiode detector, have been described by Pieper and Poon [1] and Brooks and Reeve [2] for FM demodulation and by Reeve and Houghton [3] for demodulation of BPSK signals. The detector assembly employed in this case is a bicell device (Figure 2) consisting of two photodiodes separated by a narrow gap of width g . The signal under investigation is applied to the

AO cell. The properties of AO cells are well known; a good review is given by Korpel [4]. A narrow laser beam passing through the cell is deflected through an angle proportional to the signal carrier frequency. In this first order diffracted light the beam is spatially modulated by the signal instantaneously in that part of the cell that is illuminated by the laser beam. The spatial distribution of light amplitude in the focal plane of the lens is therefore proportional to the Fourier transform of that part of the signal within the window formed by the laser beam passing through the AO cell. Since the photodiodes respond to the light intensity, their output will be proportional to the power spectral density of the signal integrated over the illuminated part of the

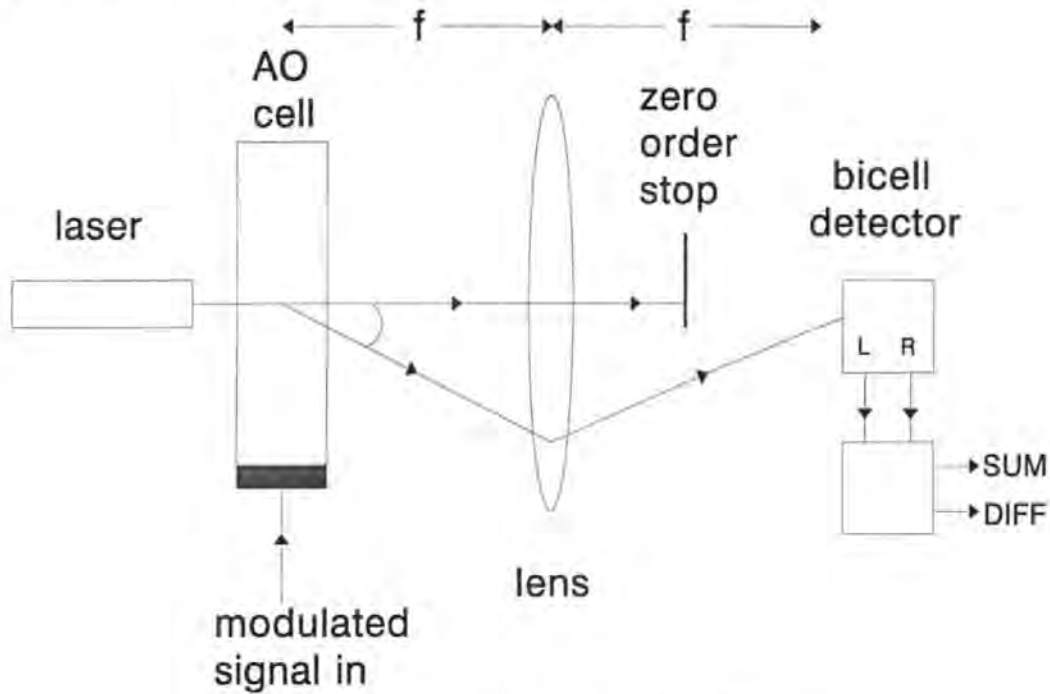


Figure 1. The acousto-optic demodulator

detector. The system therefore monitors changes in the power in the windowed signal over two frequency bands defined by the size and position of the bicell elements. The signal from the left and right elements of the bicell detector are:

$$s_L = K \int_{-x}^{\frac{x}{2}} |F(x)|^2 dx \quad \text{and} \quad s_R = K \int_{\frac{x}{2}}^x |F(x)|^2 dx \quad (1)$$

where K is a constant and $F(x)$ is the spatial light distribution in the focal plane of the lens, which is proportional to the Fourier transform of the windowed signal. These equations do not lend themselves easily to an analytic solution; the response of the system has therefore been studied using a computer model.

MODELLING RESULTS

The model was written in such a way that particular system parameters such as the focal length of the lens, the laser wavelength, the dimensions of the bicell detector and the AO cell parameters could be easily changed to study different arrangements. It is assumed that the laser beam intensity profile is Gaussian (corresponding to a laser with a single TEM_{00} transverse mode) with a standard deviation σ_0 in the x -direction i.e. perpendicular to the bicell gap. The standard deviation in the y -direction may or may not be the same but since we integrate over the complete range of y values its precise value is not important. If the signal within this Gaussian window in the AO cell is a constant amplitude tone of frequency f , it may be shown that the intensity profile of the light in the focal plane of the lens is also Gaussian with standard deviation σ_1 given by

$$\sigma_t = \frac{\lambda l_f}{4\pi\sigma_o} \quad (2)$$

where λ is the wavelength of the light and l_f is the focal length of the lens and that the angle θ through which the first order diffracted light is deflected is given by

$$\sin\theta \approx \theta = \frac{\lambda}{V_a} f \quad (3)$$

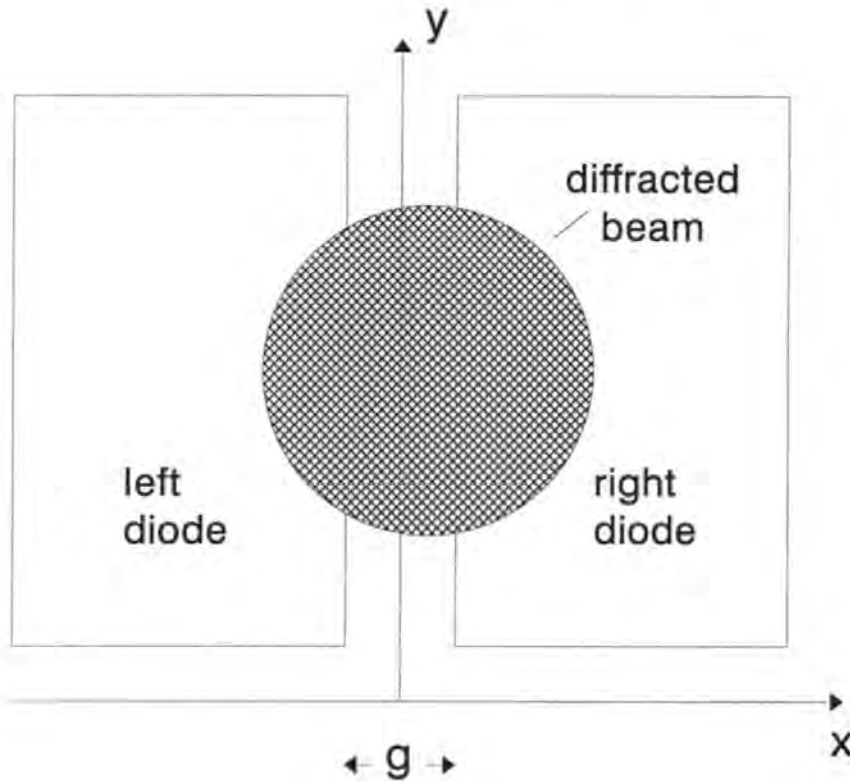


Figure 2. The bicell detector assembly

where V_a is the acoustic velocity in the AO cell. The displacement δx of the diffracted spot at the detector due to a change in frequency δf is therefore

$$\delta x = l_f \delta\theta = \frac{\lambda l_f}{V_a} \delta f \quad (4)$$

Dividing eqn (3) by eqn (1) we obtain

$$\frac{\delta x}{\sigma_t} = \frac{4\pi\sigma_o}{V_a} \delta f \quad (5)$$

This ratio, which expresses lateral deviation of the diffracted spot at the detector, due to a given change in frequency, in terms of the spot size, is independent of the laser wavelength and the focal length of the lens. It is convenient therefore to express all dimensions at the detector as a multiple of σ_t .

The signal applied to the AO cell is assumed to be of constant amplitude with changes of frequency and/or phase occurring at unspecified intervals; the time window defined by the laser beam in the AO cell is assumed to be sufficiently short that only one change in frequency or phase is within the window at any given time. The laser beam width is usually quoted as the distance between the $1/e^2$ points on the Gaussian profile, which is equivalent to $4\sigma_0$. In fact the beam is not truncated at the $1/e^2$ points. In the model the laser beam is represented as having a width of $6\sigma_0$, which yields results which are virtually indistinguishable from those obtained assuming an infinitely wide Gaussian. We have calculated how the power spectral density of the windowed signal varies as the transition in frequency and/or phase moves through the window. These are shown in Figure 3. Five positions of the transition have been used: (i) $x = -3\sigma_0$ i.e. as it enters the window - solid line, (ii) $x = -1.5\sigma_0$ - dotted line, (iii) $x = 0$ i.e. at the centre of the window - dashed line, (iv) $x = 1.5\sigma_0$ - dot-dash line, and (v) $x = 3\sigma_0$ i.e. as it leaves the window - solid line. In the cases where only the phase is changing only three of these will be visible since (i) and (ii) are identical to (iv) and (v). The horizontal axis is distance at the detector as a multiple of σ_t . The vertical lines denote the edges of the bicell elements assuming a gap of $3\sigma_t$. It is assumed that, for signals where only the phase changes, the centre line of the bicell gap corresponds to the carrier frequency; for FSK signals the centre line corresponds to the centre frequency f_0 , so that the frequencies transmitted are $f_0 \pm \delta f$. Figure 3 shows results for: a) a phase shift of π radians, b) a phase shift of $+\pi/2$ radians (the result for a $-\pi/2$ radian shift is a mirror image about $d = 0$), c) a frequency shift with no phase discontinuity at the frequency transition, d) a frequency shift with an arbitrary phase shift at the frequency transition.

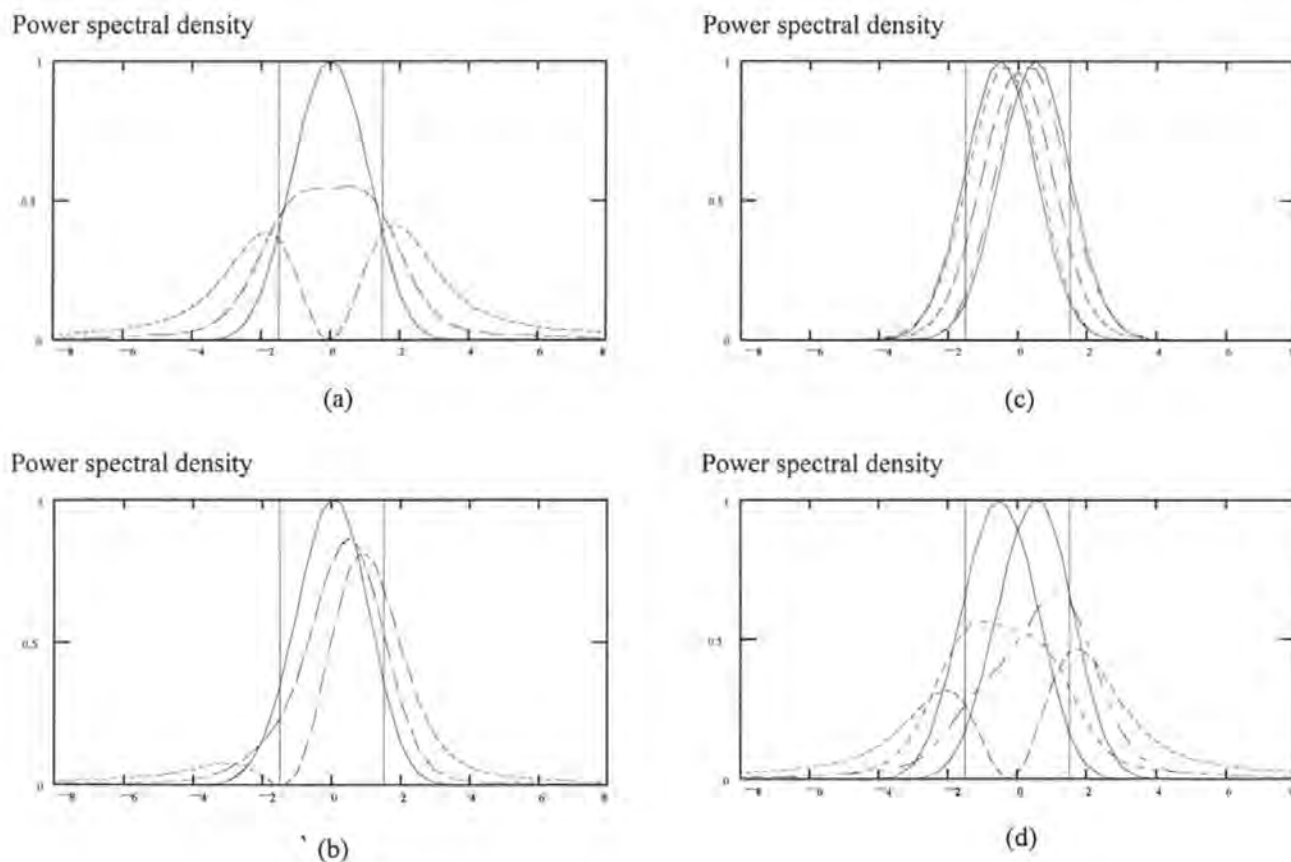


Figure 3. Change in PSD for: a) π phase shift, b) $\pi/2$ phase shift, c) CP-FSK, d) FSK with phase shift. Horizontal scale: displacement at bicell in units of σ_t

Figure 4 shows the modelling results for the sum and difference of the outputs from the two bicell elements using a bicell gap of $3\sigma_t$ for various types of signal. In Figure 4(a) the output for a BPSK signal with a phase shift of π radians shows that the difference remains essentially constant (zero) while the sum reaches a maximum when the phase shift is at the centre of the window. The reason for this behaviour is readily understood by studying Figure 3(a). Before the phase shift enters the window most of the light energy is concentrated in the gap; as the phase shift traverses the window the power spectral density broadens and dips at the centre shifting more light onto the bicell elements increasing the sum; however since the power spectral density remains symmetrical about the centre the difference is always zero. Figure 4(b) shows the response for a signal with phase shifts of $\pm\pi/2$. In this case the sum reaches a maximum when the phase shift is at the centre of the window but now the difference goes either positive or negative depending on the sign of the phase change because the power spectral density does not remain symmetrical. The response for a continuous phase FSK (or MSK) signal is shown in Figure 4(c); in this case the sum is essentially constant while the difference changes by an amount proportional to the frequency shift. The output for an FSK signal in which the frequency change is accompanied by an arbitrary phase shift is shown in Figure 4(d); the response is basically the same as for the previous case except that a spike occurs in both the sum and difference signals proportional to the magnitude/sign of the phase shift.

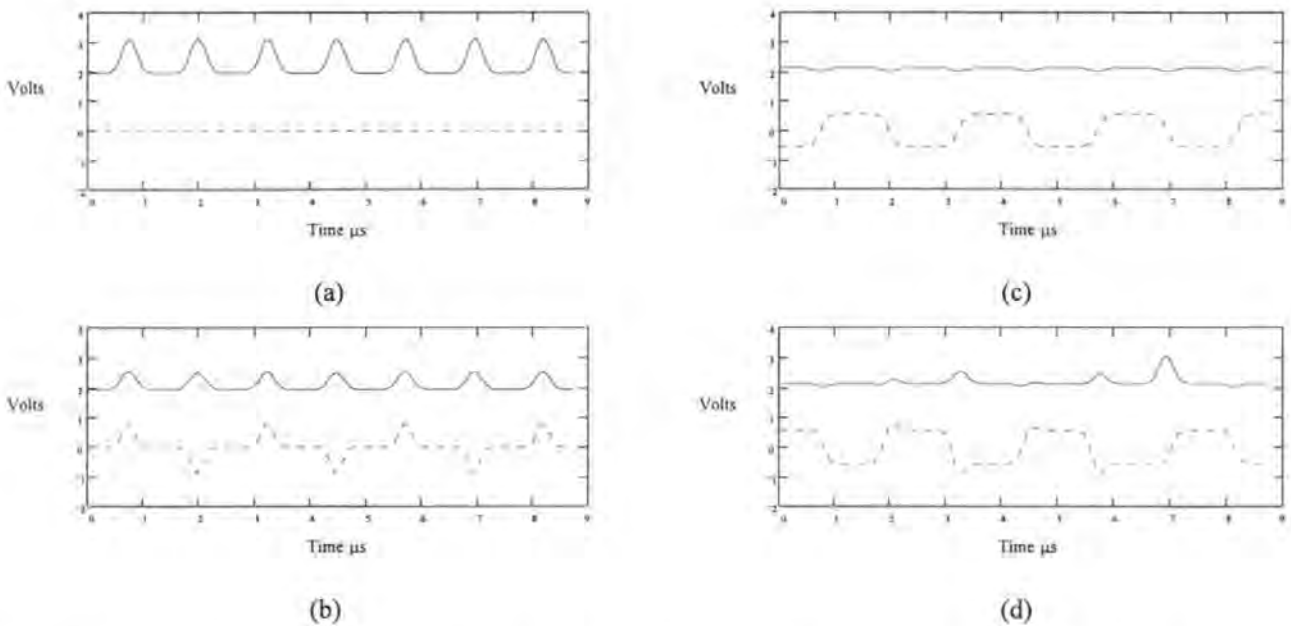


Figure 4. Modelled system output for a) π phase shift, b) $\pm\pi/2$ phase shift, c) continuous phase FSK, d) FSK with arbitrary phase shifts.

From these results it was possible to draw up a truth table (Table 1.) showing what outputs would be expected from the sum and difference in response to each of the main forms of digital modulation.

Modulation	Sum	Difference
FSK	glitches due to ϕ changes	\propto frequency and glitches due to ϕ changes
CP-FSK	Constant	\propto frequency, no glitches
BPSK	Spike	Constant
QPSK	Spike $\propto \phi$	\pm spike
OQPSK	Spike	\pm spike

Table 1. Truth Table

Figure 5. Shows how the amplitude of the spikes produced by phase modulated signals are effected by the size of the gap between the photodetectors with respect to the standard deviation of the gaussian beam at the detector σ_t . The solid lines represent the sum output and the dotted lines represent the difference. The relationship was plotted for three different phase shifts; $\pi, \pi/2$ and $\pi/4$. It can be seen from Figure 5. That the optimum gapsize for the difference output would be zero, whereas the sum output gains its maximum level for a agapsize of $3 \sigma_t$. It was decided that a good compromise would be to set the gapsize to be between 2 and $3 \sigma_t$.

Pulse
amplitude
mV

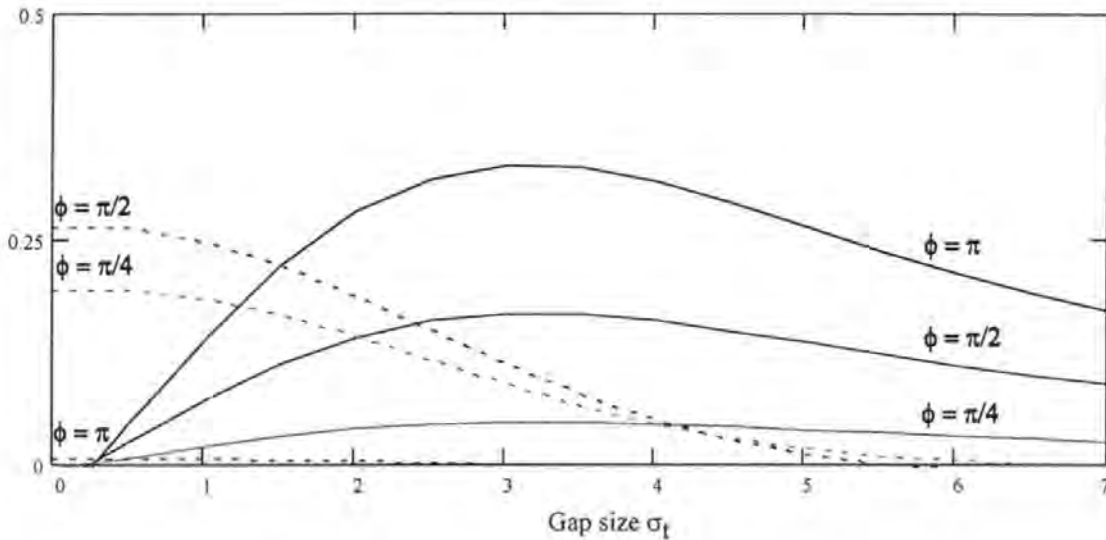


Figure 5. The effect of increasing the gapsize on the amplitude of the output pulse.

EXPERIMENTAL RESULTS

We present some preliminary results from a breadboard system to demonstrate their agreement with the modelled results shown in the previous section. The system consisted of: a frequency stabilised 1 mW Helium Neon laser with wavelength 633 nm and $1/e^2$ beamwidth 0.49 mm; a tellurium dioxide slow shear mode AO cell with time aperture 50 μ s and acoustic velocity 617 m/s; a 50 mm focal length biconvex lens; a detector consisting of a bicell photodiode with a gap of 85 μ m with each element connected via trans-impedance and buffer amplifiers to a waveform analyser, which performs the sum and difference operations. Using eqn (1) the value of σ_t was 21 μ m, therefore the bicell gap is close to $4\sigma_t$. Signals for analysis were generated using a programmable arbitrary waveform synthesiser so that precise frequencies and phase shifts could be obtained. The output for a signal containing phase shifts of $\pm\pi/2$ radians is shown in Figure 5(a). Figure 5(b) shows the output from a continuous phase FSK signal. In each case the upper trace is the sum and the lower trace is the difference of the bicell outputs. Clearly there is very close agreement between the results obtained from the model and those from the breadboard system.

DISCUSSION

The modelled and experimental results show that the system output for each type of signal has a distinctive signature. Signals with a phase change of π radians cause a spike on the sum channel with the difference remaining constant; signals with phase changes of $\pm\pi/2$ cause equal sized spikes on the sum channels and equal but opposite polarity spikes on the difference. FSK signals in which there is no phase discontinuity at the frequency transition give a change in the difference channel proportional to the frequency shift with no change in the sum. FSK signals with an arbitrary phase

shift at the frequency transition give the same result but with additional spikes due to the phase shifts; the size of the spike on the sum channel is proportional to the phase shift and the polarity of the spike on the difference gives its sign. Signals with phase shifts of $\pm\pi/4$ or $\pm3\pi/4$ (not illustrated) can be shown to give spikes on the sum channel proportional to the phase shift and the polarity of the spike on the difference again gives its sign. Using these results it is possible to distinguish between the following types of digital modulation.

(i) BPSK. Assuming that the two phase states are 0 and π radians this is characterised by a constant difference channel with a spike on the sum channel at each phase shift.

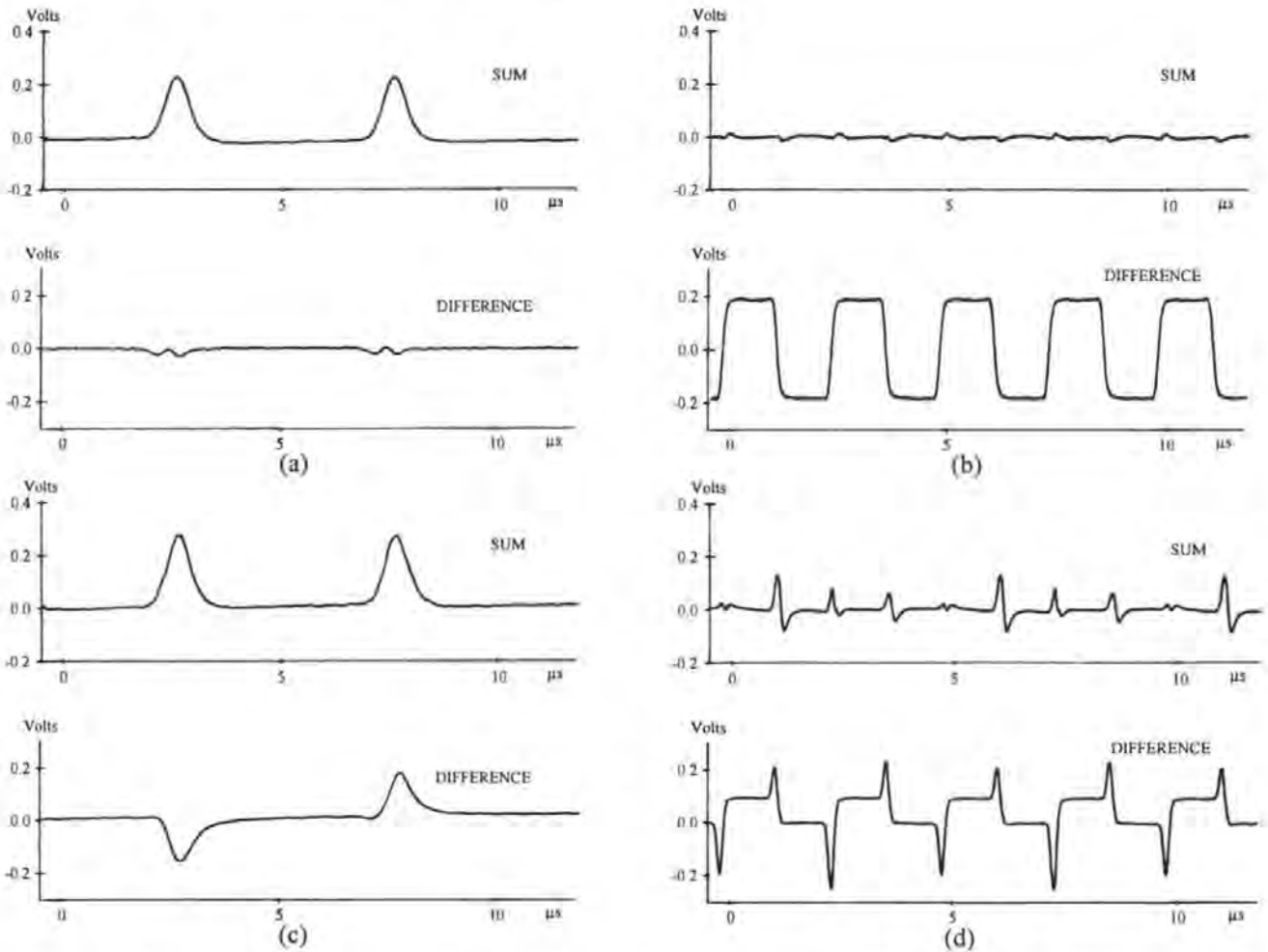


Figure 5. Experimental system output for a) $\pm\pi$ phase shift, b) $\pm\pi/2$ phase shift, c) continuous phase FSK, d) FSK

(ii) QPSK. The four phase states are 0, $\pm\pi/2$ and π radians; therefore the possible phase shifts are also 0, $\pm\pi/2$ and π radians. A spike on the sum channel indicates the presence of a phase shift and the corresponding state of the difference channel indicates the nature of the change. The occurrence of all three phase shifts identifies the type of modulation.

(iii) Offset-keyed QPSK. Here the only possible phase shifts are $\pm\pi/2$ radians. The absence of the π radians phase shifts identifies the type of modulation.

(iv) FSK. FSK signals are characterised by a shift in level on the difference channel while the sum remains constant. Unlike the case for PSK signals where the output is a spike which only occurs while the phase shift is within the laser window, the level change persists for as long as the frequency remains constant. If there is no phase discontinuity when the frequency changes, as in continuous phase FSK or MSK, then only the level change is observed. A phase discontinuity at the frequency change results in spikes on both the sum and difference channels. Thus not only is the

system capable of identifying the presence of FSK signals, it can also indicate the type of FSK modulation being used. The magnitude of the level change, and hence the detectability of the signal, is proportional to the change in frequency. For an MSK signal the frequency change is $2\delta f = 1/2T_b$, where T_b is the interval between frequency shifts. In the experimental example shown T_b was 5 μ s so that the frequency shift was 100 kHz. Since it has been shown [2] that this type of system is capable of detecting frequency changes of the order of 100 Hz, detectability is not considered to be a problem.

(v) Differential QPSK. Four phase shifts are possible namely $\pm\pi/4$ and $\pm3\pi/4$. In all the previous cases identification has depended upon merely detecting a change from zero in either or both channels. For differential QPSK it is necessary to distinguish between two different level spikes in the sum channel corresponding to phase shifts of $\pi/4$ or $3\pi/4$. Although not difficult this raises the complexity of the detection system and will tend to increase the signal to noise ratio required for reliable detection.

CONCLUSIONS

It is concluded that using the optical system described, together with some simple detection and logic circuits, it is possible to identify and decode a number of types of digitally modulated signals, without any a priori knowledge apart from their carrier frequency. The ability of the system to handle both frequency and phase modulated signals is particularly valuable. Although apparently very simple, the system performs functions that would be difficult to achieve electronically in real time. In summary these functions are as follows.

(i) The signal propagating through the AO cell is windowed by the Gaussian profile of the laser beam. The time window depends upon the laser beamwidth and the acoustic velocity in the AO cell; by focusing the beam into the AO cell, time windows down to a few nanoseconds are achievable. This places an upper limit on the data rates that can be processed since only one transition may occur within the window. (ii) The light distribution at the detector is proportional to the instantaneous Fourier transform of the windowed signal. (iii) The response of each element of the detector is proportional to the instantaneous power in the windowed signal over frequency bands defined by the size and position of the elements. In effect the system responds in real time to variations in the spectral content of the signal as the frequency and/or phase shifts propagate through the laser beam window.

(iv) Taking the sum and difference of the signals from the bicell elements results in distinctive signatures for the different types of modulation. AO cells are currently available for operation at carrier frequencies from around 30 MHz (tellurium dioxide) to 3 GHz (gallium phosphide). Acoustic velocities vary from 617 m/s for tellurium dioxide to 6320 m/s for gallium phosphide. To perform a similar operation at the lower end of this frequency range might be possible using DSP techniques; at the upper end it would not. The properties of AO cells allow the system to be tuned over an octave bandwidth merely by moving the detector.

REFERENCES

1. Pieper R J and Poon T-C, 1985. "An acousto-optic FM receiver demonstrating some principles of modern signal processing." *IEEE Trans*, E-28, 1, 11-17
2. Brooks and Reeve C D, 1995, "Limitations in acousto-optic FM Demodulators" *JEE Proc-J*, in press
3. Reeve C D. and A W Houghton, 1991, "Optical method for detecting biphase coded signals." *Electronics Lett*, 27, 1379-1381
4. Korpel A, 1981, "Acousto-optics - a review of fundamentals." *Proc. IEEE*, 69, 48-53

ACKNOWLEDGEMENT

This work was supported by a research agreement with the Defence Research Agency.

SYMBOLGY and ABBREVIATIONS

A	amplitude
A_q	amplitude of qth diffracted order
AM	amplitude modulation
AO	acousto-optic
AOA	angle of arrival
ASK	amplitude shift keying
B	bandwidth (general)
BPSK	binary PSK
B_n	system noise bandwidth
B_{-3dB}	bandwidth (-3 dB)
c	speed of light
CW	continuous wave
CNR	carrier to noise ratio (general)
CP-FSK	continuous phase FSK
CNR_{in}	CNR at system input
dB	decibel
DSP	digital signal processing
DPSK	differential PSK
e	electron charge
E	electric field
ECM	electronic counter measures
ECCM	electronic counter-counter measures
ESM	electronic support measures
EW	electronic warfare
f	frequency
f_c	centre frequency
f_d	doppler frequency
$F(x)$	spatial light distribution
FDM	frequency division multiplex
FFT	fast Fourier transform

FM	frequency modulation
FMOP	FM on pulse
FSK	frequency shift keying
g	gap size
H	height of acoustic cell
IF	intermediate frequency
IFM	instantaneous frequency measurement
i_n	noise current
i_{nL}	noise current from left cell
i_{nR}	noise current from right cell
I_q	intensity of qth diffracted order
i_s	signal current
i_{sL}	signal current from left cell
i_{sR}	signal current from right cell
I_s	intensity profile at AO cell
I_t	intensity profile at detector
k	general constant
K	ratio of signal power to background power
l	optical path length
l_f	focal length of lens
L	acousto-optic interaction length
(L)	longitudinal
LPI	low possibility of intercept
m	modulation index
MSK	minimum shift keying
MTF	modulation transfer function
M_n	acousto-optic figure of merit
n	refractive index (general)
n_o	normal refractive index
OSP	optical signal processing
OQPSK	offset QPSK
p	elasto-optic constant

P_1	optical power in 1st order
P_a	acoustic power
P_b	optical background power at detector
P_{DIFF}	$P_{sR} - P_{sL}$
P_{SUM}	$P_{sR} + P_{sL}$
P_s	optical signal power at detector
P_{sL}	optical signal power on left cell
P_{sR}	optical signal power on right cell
P_{tot}	total diffracted power
P_e	probability of error
PA	pulse amplitude
PM	phase modulation
PW	pulse width
PCM	pulse code modulation
PLL	phase locked loop
PSD	power spectral density
PSK	phase shift keying
PRK	phase reversal keying
PMOP	PM on pulse
Q	acousto-optic figure of merit
QPSK	quaternary PSK
r	propagation vector
RF	radio frequency
R_f	frequency response roll off (dB)
R_l	load resistance
R_λ	diode responsivity
S_L	signal from left detector
S_R	signal from right detector
(SS)	slow shear
SNR	signal to noise ratio
SSB	single side band
SNR_{out}	SNR at system output

t	time
TeO_2	tellurium dioxide
t_p	pulse width
t_r	10% - 90% risetime
T	sampling interval
T_b	bit interval
v	velocity
v_r	radial velocity
V_a	acoustic velocity
w	beam waist diameter
w_0	beam e^{-2} radius
x	spatial variable
y	spatial variable
z	spatial variable
Z	impedance
α	deflection angle
β	FM modulation index
δf	frequency deviation
δx	change in beam position at detector
$\delta\theta$	optical divergence
Δf	frequency bandwidth
Δn	refractive index change
ζ	spatial variable
γ	phase
θ	angle (general)
θ_B	Bragg angle
η	power spectral density
λ	optical wavelength
Λ	acoustic wavelength
ν	optical frequency
ρ	density

σ	standard deviation
σ_0	standard deviation of beam at cell
σ_t	standard deviation of beam at detector
τ	cell access time
ψ	optical phase
ϕ	electrical phase

This copy of the thesis has been supplied on condition that anyone who consults it is understood to recognise that its copyright rests with its author and that no quotation from the thesis and no information derived from it may be published without the author's prior consent.